Precision Coupling Measurements of the Higgs Boson using the $H \rightarrow ZZ^* \rightarrow 4\ell$ decay channel

by

Syed Haider Abidi

A thesis submitted in conformity with the requirements
for the degree of Doctor of Philosophy
Graduate Department of Physics
University of Toronto

Abstract

Precision Coupling Measurements of the Higgs Boson using the $H \to ZZ^* \to 4\ell$ decay channel

Syed Haider Abidi
Doctor of Philosophy
Graduate Department of Physics
University of Toronto
November 2020

The coupling of the Higgs boson to other particles is probed by measuring the production cross sections at the Large Hadron Collider using the ATLAS detector. The present measurement is performed using the $H \to ZZ^* \to 4\ell$ decay channel, with $\ell =$ electron or muon and with datasets corresponding to various integrated luminosities. The inclusive production cross section is measured to be 1.34 ± 0.12 pb, which is in good agreement with the predicted value of 1.33 ± 0.08 pb. The gluon-gluon fusion, the vector boson fusion, the vector boson associated and the top associated production cross sections are measured to be 1.12 ± 0.12 pb, 110 ± 40 fb, 75^{+61}_{-49} fb and 27^{+26}_{-17} fb, respectively. The differential production cross sections are also measured using the Simplified Template cross sections framework. All measurements are in good agreement with the Standard Model predictions. These results are used to measure the Higgs boson coupling to fermions and vector bosons using the κ-framework and to derive constraints on contributions from beyond the Standard Model physics using an effective field theory approach. No significant deviations from the Standard Model are observed.

Acknowledgements

First and foremost, I would like to thank my supervisor, Richard Teuscher. His guidance since very beginning, when I was started in ATLAS as an undergraduate, has been crucial for teaching me how to do physics. He gave me the freedom to pursue any topic that interested me, but was always there to provide guidance and gently nudge me towards a path.

I would also like to thank Robert Orr for hiring a first year engineering student about a decade ago and mentoring him since then. I do not think I gave him too much choice on the second part, but most important lesson I learned from him is that failing is a necessary part of the process.

The research carried out for this thesis would not have been possible without the ATLAS HZZ team. I have meet so amazing people and learned everything I know about Higgs boson analyses for them. Special thank you to Laurelle, Maddie, Verena, RD and Sandra for being part of this long journey.

During every research trip to Geneva, I had an always amazing time with my CERN family: Roberto, Andrea, Antonio, Eleni, Lucia, Gaetano, Monica and Jochen. The crazy pushes for conference deadlines and late nights in B40 followed by a kebab dinner are some of my fondest memories. Thank you for keeping me sane.

The time spent during this research wouldn't have been as enjoyable as it was without Bianca being my partner in crime. You had the perfect balance of pushing us to the brink of exhaustion and then relaxing to the point where the lack of work gave us anxiety.

Thank you Daniel for knowing when to poke me to death and when to be simply there. Also, thank you Yubo for all the support through all the years since high school.

I owe a huge debt of gratitude to Sarah Torrie and Robert Schweitzer for setting me on a path of research and physics. Without them, I would not be standing here.

Finally, I would like to thank my parents, my brother and my family for putting up with me and all the things I subjected them to. This thesis drove all of us a bit crazy.

Contents

Chapter 1

Standard Model Higgs Boson

1.1 Standard Model

1.1.1 Overview

The Standard Model (SM) is a theory that describes the fundamental particles and the interactions between them through the electromagnetic, weak and strong forces. In the SM, there are two types of fundamental particles: fermions and bosons. All the matter particles have half integer spin and are subsequently classified as fermions. These obey Fermi-Dirac statistics and due to the Pauli exclusion principle, cannot occupy the same quantum state. Force mediators, which are bosons, have integer spins and are governed by Bose-Einstein statistics. Unlike fermions, multiple bosons can occupy the same state.

Fermions are further sub-classified into leptons and quarks and they exist in three generations or flavours. Each particle in the subsequent generation is a heavier copy of the previous one. In each generation, the lepton family consists of a charged lepton and an uncharged neutrino. Table 1.1 lists the known leptons according to their generation. Due to the presence of electric charge and weak hypercharge, leptons interact through the electromagnetic and weak force, while neutrinos only couple to the weak force.

Table 1.1: List of leptons and their properties [1]. Note that weak hypercharge depends on the handedness of the particle. For charged leptons, both right-handed (RH) and left-handed (LH) states carry hypercharge. Neutrinos are only LH particles and have a hypercharge.

Generation	Lepton	Mass [MeV]	Electric Charge	Weak hypercharge
First	Electron (e)	0.511	-1	-1 (LH) & -2 (RH)
	Electron-neutrino (ν_e)	$< 2 \times 10^{-3}$	0	-1 (LH)
Second	Muon (μ)	105.7	-1	-1 (LH) & -2 (RH)
	Muon-neutrino (ν_μ)	< 0.19	0	-1 (LH)
Third	Tau (τ)	1776.8	-1	-1 (LH) & -2 (RH)
	Tau-neutrino (ν_τ)	< 18.2	0	-1 (LH)

Quarks are distinguishable from leptons as they have fractional electric charge, carry colour charge and have different mass. The three colour charge states are referred to as ‘red’, ‘green’ and ‘blue’. Table 1.2 lists the experimentally observed quarks and their properties. Due to the presence of colour charge and confinement, quarks interact via the strong force and cannot exist as free particles. Observable states, such as mesons and baryons, occur as colour singlets and the existence of quarks is indirectly inferred from the interactions between colour singlet states. The weak force mixes the quark mass eigenstates and allows a given quark to decay to another quark from a different generation.

Table 1.2: List of quarks and their properties [1]. Note that weak hypercharge depends on the handedness of the particle.

Generation	Quarks	Mass [MeV]	Electric Charge	Weak Hypercharge
First	Up (u)	2.3	$2/3$	$1/3$ (LH) & $4/3$ (RH)
	Down (d)	4.8	$-1/3$	$1/3$ (LH) & $-2/3$ (RH)
Second	Charm (c)	1.3×10^3	$2/3$	$1/3$ (LH) & $4/3$ (RH)
	Strange (s)	95	$-1/3$	$1/3$ (LH) & $-2/3$ (RH)
Third	Top (t)	172.9×10^3	$2/3$	$1/3$ (LH) & $4/3$ (RH)
	Bottom (b)	4.18×10^3	$-1/3$	$1/3$ (LH) & $-2/3$ (RH)

In the SM, each force is mediated by a gauge boson. Table 1.3 lists the forces with their corresponding gauge bosons. Despite there being no consistent quantum model and it being a part of the SM, it is hypothesized that the exchange of a Graviton (G) mediates the gravitational interaction between two particles. The gravitational force is a negligible force at the fundamental particle length scale. The massless photon (γ) is a quantum of the electromagnetic (EM) field and mediates EM interactions between all charged particles. For the weak force, the charged-current interactions are mediated by massive $W^{\pm}$ bosons and the neutral-current interactions by the Z boson. The force carriers for the strong interaction are gluons (g). Unlike other bosons, gluons carry colour charge and occur in 8 colour states. Lastly, the Higgs boson (H) is an excitation of the Higgs field, which couples to particles thereby giving them mass while still preserving gauge symmetry.

Table 1.3: List of gauge bosons and the associated force [1].

Force	Boson	Mass [GeV]	Spin
Strong	Gluon (g)	0	1
Electromagnetic	Photon (γ)	0	1
Weak	$W^{\pm}$	80.4	1
	Z	91.2	1
Gravity	Graviton (G) ?	0	2
Higgs Mechanism	Higgs (H)	125.1	0

Significant effort has been made in the last century to describe the SM within a single theoretical framework. With the exception of gravity, the other three interactions have successfully been encoded using local gauge symmetry and renormalizable quantum field theory. The electromagnetic and the weak forces are combined into an overall electroweak theory (EW) using the $\mathrm{SU}(2)_L \otimes \mathrm{U}(1)_Y$ gauge group. The theory of Quantum Chromodynamics (QCD) and $\mathrm{SU}(3)_C$ describes the strong force. The indices, Y (weak hypercharge) and C (colour), refer to the conserved quantity for the respective gauge transformation, while L indicates that the SU(2) interactions only include left-handed particles. The combination of EW and QCD theories form the basis of the Standard Model.

Quantum Field Theory

In quantum mechanics, a particle is described by a wavefunction, ψ, and its dynamics are governed by the Schrödinger equation. Quantum field theory (QFT) combines special relatively and quantum mechanics by describing particles as an excitation of the field $\phi(x^\mu)$, where x^μ are the space-time coordinates [2–4]. Using the methodology from classical mechanics, the dynamics of this field are calculated by using a Lagrangian density, $\mathcal{L}$, which only depends on ϕ and its space-time derivatives, $\partial_\mu\phi$. The action, S, is defined as:

$$S = \int \mathrm{d}^4\mathrm{x}\ \mathcal{L}(\phi, \partial_\mu\phi). \tag{1.1}$$

The evolution of ϕ from a given initial state is calculated using the principle of least action. The variation in action, δS, is required to be zero along a stationary path. With this, the Euler-Lagrange equation governing the dynamics is derived to be [3]:

$$\partial_\mu \left(\frac{\partial\mathcal{L}}{\partial(\partial_\mu\phi)} \right) - \frac{\partial\mathcal{L}}{\partial\phi} = 0. \tag{1.2}$$

Specifically under gauge transformations, symmetries play an important role in QFT. They are defined as any variation to $\mathcal{L}$ that leaves the final equation of motion invariant. If, under a given transformation, the ϕ field transforms as:

$$\phi \to \phi + \epsilon\delta\phi, \tag{1.3}$$

where ϵ is an infinitesimal parameter and $\delta\phi$ is some deformation of the field, and the Lagrangian is invariant up to a total divergence of a field Λ,

$$\mathcal{L} \to \mathcal{L} + \epsilon\partial_\mu\Lambda^\mu, \tag{1.4}$$

the transformation is considered a symmetry of the system. According to Noether's theorem [4], continuous symmetry of the Lagrangian leads to a current,

$$j^\mu = \frac{\partial\mathcal{L}}{\partial(\partial_\mu\phi)}\delta\phi - \Lambda^\mu, \tag{1.5}$$

which is conserved,

$$\partial_\mu j^\mu = 0. \tag{1.6}$$

Quantum Electrodynamics

The Dirac Lagrangian [2, 4], which represents a free massive spin $\frac{1}{2}$ particle, is given by:

$$\mathcal{L}_D = i\bar{\psi}\gamma^\mu\partial_\mu\psi - m\bar{\psi}\psi, \tag{1.7}$$

where ψ is the spinor field, m is the mass of the particle and γ^μ are the 4 gamma matrices. The γ^μ matrices obey the anticommutation relationship, $\{\gamma^\mu, \gamma^\nu\} = 2\mathrm{g}^{\mu\nu}$. $\mathcal{L}_D$ is invariant under a global U(1) phase transformation:

$$\psi \rightarrow \psi' = e^{iq\theta}\psi. \tag{1.8}$$

This, according to Noether's theorem, creates a conserved current:

$$j^{\mu} = \bar{\psi}\gamma^{\mu}\psi. \tag{1.9}$$

Equation 1.9, when interpreted under the context of classical or QFT framework, leads to the well-known EM continuity equation and the conservation of electric charge.

A more interesting phenomenon emerges when local U(1) transformations are considered. This transformation is given by:

$$\psi \rightarrow \psi' = e^{iq\theta(x)}\psi. \tag{1.10}$$

Due to the presence of a derivative, $\mathcal{L}_D$ is not invariant under this but transforms according to:

$$\begin{aligned} \mathcal{L}_D \rightarrow \mathcal{L}'_D &= ie^{-iq\theta}\bar{\psi}\gamma^{\mu}[e^{iq\theta}\partial_{\mu}\psi + iq(\partial_{\mu}\theta)e^{iq\theta}\psi] - me^{-iq\theta}\bar{\psi}e^{iq\theta}\psi \\ &= \mathcal{L}_D - q\bar{\psi}\gamma^{\mu}(\partial_{\mu}\theta)\psi. \end{aligned} \tag{1.11}$$

However if this symmetry is explicitly required from the Lagrangian, it forces a substitution of ∂_{μ} with its covariant derivative D_{μ}:

$$D_{\mu} = \partial_{\mu} + iqA_{\mu}, \tag{1.12}$$

where A_{μ} is a vector field with its U(1) gauge transformation being defined by:

$$A_{\mu} \rightarrow A'_{\mu} = A_{\mu} - \partial_{\mu}\theta. \tag{1.13}$$

Since a new field was included, its kinematic term must also be added to $\mathcal{L}_D$. This leads to the final form of the Lagrangian, which describes Quantum Electrodynamics (QED):

$$\mathcal{L}_{\text{QED}} = \bar{\psi}\left(i\gamma^{\mu}\partial_{\mu} - m\right)\psi - \frac{1}{4}F_{\mu\nu}F^{\mu\nu} + e\bar{\psi}\gamma^{\mu}\psi A_{\mu}, \tag{1.14}$$

where $F_{\mu\nu} = \partial_{\mu}A_{\nu} - \partial_{\nu}A_{\mu}$ and q has been replaced with the electron charge. The last term in $\mathcal{L}_{\text{QED}}$ is the potential term which represents the coupling of the electron and photon fields with a strength of e.

It should be noted that the above procedure provides a general method to describe interactions between particles in the SM. For QED, by starting with a Lagrangian for a free electron and imposing local U(1) gauge symmetry, it forces the introduction of a photon field and electron-photon coupling, which ultimately leads to EM interactions. Similarly for Quantum Chromodynamics (QCD) and electroweak theory, by imposing local $\text{SU}(3)_C$ and $\text{SU}(2)_L \otimes \text{U}(1)_Y$ gauge symmetry respectively on a free particle Lagrangian, the weak and strong forces between particles naturally arise.

Quantum Chromodynamics

Building upon the use of local gauge symmetry in QED, quarks and the strong force is described using $\text{SU}(3)_C$. The Lagrangian for free quarks is given by:

$$\mathcal{L} = \sum_j \bar{q}_j(i\gamma^\mu \partial_\mu - m_j)q_j, \tag{1.15}$$

where $q_j = (q_j^R, q_j^B, q_j^G)^\mathrm{T}$ is the colour triplet and the index j run overs the 6 quark flavours. Hereafter for simplification, the explicit sum over j is implied.

Under local $\mathrm{SU}(3)_C$, the quark field transforms as:

$$q \to Uq = e^{-ig\theta(x)_a T^a} q, \tag{1.16}$$

where U is a 3×3 unitary matrix, g is the strong coupling constant and $T^a = \frac{\lambda^a}{2}$, with a running from 1 to 8. The T^a matricies are the 8 generators of the $\mathrm{SU}(3)_C$ group and are represented by using the well-known 3×3 traceless Gell-Mann matrices (λ^a). They obey the anti-commutation relation, $[T_a, T_b] = if_{abc}T^c$, where f_{abc} are the structure constants of SU(3) and encode the non-Abelian characteristics of QCD.

By imposing local $\mathrm{SU}(3)_C$ on the free quark Lagrangian, the partial derivative is replaced by the covariant derivative, which is defined as:

$$D_\mu = \partial_\mu + ig\frac{\lambda_a}{2}G_\mu^a \tag{1.17}$$

where G_μ^a is a gluon field with its SU(3) gauge transformation being defined by:

$$G_\mu^a \to G_\mu^a - \frac{1}{g}\partial_\mu \theta^a - f_{bc}^a \theta^b G_\mu^c. \tag{1.18}$$

The kinematic term for the gluon field is given by $\frac{1}{4}G_{\mu\nu}^a G_a^{\mu\nu}$ with:

$$G_{\mu\nu}^a = \partial_\mu G_\nu^a - \partial_\nu G_\mu^a - g f_{bc}^a G_\mu^b G_\nu^c. \tag{1.19}$$

This results in the final QCD Lagrangian being:

$$\mathcal{L}_{\mathrm{QCD}} = \bar{q}\left(i\gamma^\mu \partial_\mu - m\right) q - \bar{q}\left(ig\gamma^\mu \frac{\lambda^a}{2} G_\mu^a\right) q - \frac{1}{4} G_{\mu\nu}^a G_a^{\mu\nu}. \tag{1.20}$$

Comparing Equation 1.15 and Equation 1.20, the first additional term, arising from imposing local gauge symmetry, is the colour charged current and describes the structure of quark-gluon interactions. A closer examination of the second term shows that it is not only the kinematic term for the field, but includes self-interaction terms for gluons. The non-Abelian characteristics of QCD lead to 3- and 4-gluon vertices for gluon-gluon interactions.

Electroweak Theory

The decay of unstable particles, such as pions and muons point to the presence of an additional force with a low-energy coupling that is weaker than those found in QED or QCD. This is due to the observation of longer than expected decay times if only the electromagnetic or strong force were present. Labelled as the weak interaction, this force involves both charged and neutral currents. Charged currents allow the transition between up-type and down-type quarks and the decay of leptons from one generation into another, while neutral currents conserve flavour. Experimental data also indicate that the charged currents maximally violate parity conservation.

For describing the interaction between fermions and the weak force, the fermions are grouped into left-handed (ψ_L) and right-handed particles (ψ_R). These are defined as:

$$\psi_L = P_L\psi = \frac{1}{2}(1-\gamma^5)\psi \tag{1.21}$$

$$\psi_R = P_R\psi = \frac{1}{2}(1+\gamma^5)\psi \tag{1.22}$$

where $\gamma^5 = i\gamma^0\gamma^1\gamma^2\gamma^3$, P_R & P_L are chirality projection operators and ψ is the fermion field. The left-handed fields,

$$\begin{pmatrix} u \\ d \end{pmatrix}_L, \begin{pmatrix} \nu_e \\ e \end{pmatrix}_L, \quad \begin{pmatrix} c \\ s \end{pmatrix}_L, \begin{pmatrix} \nu_\mu \\ \mu \end{pmatrix}_L, \quad \begin{pmatrix} t \\ b \end{pmatrix}_L, \begin{pmatrix} \nu_\tau \\ \tau \end{pmatrix}_L, \tag{1.23}$$

form a doublet with isospin $I = \frac{1}{2}$ and the right-handed fields,

$$u_R, d_R, e_R, \quad c_R, s_R, \mu_R, \quad t_R, b_R, \tau_R, \tag{1.24}$$

are singlets with $I = 0$.

Using the same local gauge symmetry principles as QED and QCD, the electroweak theory is constructed using the $\mathrm{SU}(2)_L \otimes \mathrm{U}(1)_Y$ gauge group. This theory treats electromagnetic and weak forces as different manifestations of the same force. $\mathrm{SU}(2)_L$ couples to particles based on the weak isospin charge (I) and involves left-handed particles, while $\mathrm{U}(1)_Y$ couples through weak hypercharge (Y) and involves particles of both chiralities. Under $\mathrm{SU}(2)_L$, the left-handed doublets are transformed according to:

$$\psi_L \to e^{i\beta^a(x)\frac{\tau_a}{2}}\psi_L, \tag{1.25}$$

where $a = 1, 2, 3$ and τ_a, the well-known Pauli matrices, are the generators of the SU(2) group. Both left-handed and right-handed fields are modified by a factor $e^{i\alpha(x)\frac{Y}{2}}$ when transformed under $\mathrm{U}(1)_Y$.

After imposing local $\mathrm{SU}(2)_L \otimes \mathrm{U}(1)_Y$ invariance on the free particle Lagrangian, as described in Equation 1.7, additional gauge fields are introduced. Specifically, the B_μ field arises due to $\mathrm{U}(1)_Y$ symmetry, while three gauge fields, W^i_μ, are associated to the $\mathrm{SU}(2)_L$ symmetry. The resulting Lagrangian for the electroweak theory is:

$$\mathcal{L} = -\frac{1}{4}W^a_{\mu\nu}W_a^{\mu\nu} - \frac{1}{4}B_{\mu\nu}B^{\mu\nu} + i\bar{\psi}\gamma^\mu D_\mu\psi, \tag{1.26}$$

where $W^a_{\mu\nu}$ and $B_{\mu\nu}$ field tensors are:

$$W^i_{\mu\nu} = \partial_\mu W^i_\nu - \partial_\nu W^i_\mu - g\epsilon_{ijk}W^j_\mu W^k_\nu, \tag{1.27}$$

$$B_{\mu\nu} = \partial_\mu B_\nu - \partial_\nu B_\mu. \tag{1.28}$$

The ϵ_{ijk} variables are the structure constants for SU(2). The covariant derivative is defined as:

$$D_\mu = \partial_\mu + igW^a_\mu\tau_a + ig'\frac{1}{2}B_\mu Y, \tag{1.29}$$

where g' and g are the U(1) and SU(2) coupling constants respectively. Expanding the Lagrangian, the fermion-gauge boson interaction terms are defined by:

$$\mathcal{L}_{\text{int}} = -\bar{\psi}_L \gamma^\mu \left(g' \frac{Y}{2} B_\mu + g \frac{\tau_a}{2} W_\mu^a \right) \psi_L - \bar{\psi}_R \gamma^\mu \left(g' \frac{Y}{2} B_\mu \right) \psi_R. \tag{1.30}$$

As required by the experimental observations, the bosons associated with SU(2) only couple to left-handed fermions while the U(1) boson couples to particles irrespective of their chirality.

The Higgs Mechanism

As shown for QCD and the electroweak theory, local gauge symmetry provides an elegant and consistent method to describe the known fundamental forces. However, a shortcoming of this framework is that the introduction of a quadratic mass term for the boson field breaks the imposed symmetry. For example, if the W_μ^i field had a mass, the electroweak Lagrangian would be modified to:

$$\mathcal{L}' = \mathcal{L} + \frac{1}{2} m_W^2 W_\mu^i W_i^\mu. \tag{1.31}$$

The last term in Equation 1.31 is not invariant under local SU(2). Similarly, the fermion mass term, $m_f(\bar{\psi}_L \psi_R + \bar{\psi}_R \psi_L)$, breaks the local gauge invariance.

To mitigate this problem, the concept of spontaneous symmetry breaking was borrowed from BCS theory [5–7] and applied to the SM. This mechanism was independently proposed [8] in 1964 by Englert and Brout [9], Higgs [10] and subsequently by Guralnik, Hagen and Kibble [11]. It consists of expanding the ground state of a field around a specific non-zero point, which allows the gauge boson field to gain mass while still preserving local symmetry.

Mathematically, an additional $\mathrm{SU}(2)_L$ isospin doublet, ϕ:

$$\phi = \begin{pmatrix} \phi^+ \\ \phi^0 \end{pmatrix} = \frac{1}{\sqrt{2}} \begin{pmatrix} \phi_1 + i\phi_2 \\ \phi_3 + i\phi_4 \end{pmatrix}, \tag{1.32}$$

with $Y = 1$ is considered with its potential term being:

$$V(\phi) = \mu^2 \phi^2 + \lambda \phi^4. \tag{1.33}$$

It leads to the following Lagrangian:

$$\mathcal{L} = (\partial_\mu \phi)^* (\partial^\mu \phi) - V(\phi). \tag{1.34}$$

Similar to the method described before, imposing local $\mathrm{SU}(2)_L \otimes \mathrm{U}(1)_Y$ symmetry gives a modified $\mathcal{L}$:

$$\mathcal{L} = -\frac{1}{4} W_{\mu\nu}^a W_a^{\mu\nu} - \frac{1}{4} B_{\mu\nu} B^{\mu\nu} + (D_\mu \phi)^\dagger (D^\mu \phi) - V(\phi), \tag{1.35}$$

where,

$$D_\mu = \partial_\mu + igW_\mu^a I_a + ig' \frac{1}{2} B_\mu Y. \tag{1.36}$$

For $\mu^2 < 0$, the $V(\phi)$ potential follows the shape shown in Figure 1.1 [12]. The minimum for this function exists on a curve defined by: $\phi_0^2 = \frac{-\mu^2}{\lambda} = \nu^2$. Hence, the physical vacuum or ground state will correspond to a single non-vanishing point along this curve. This is defined as spontaneous symmetry

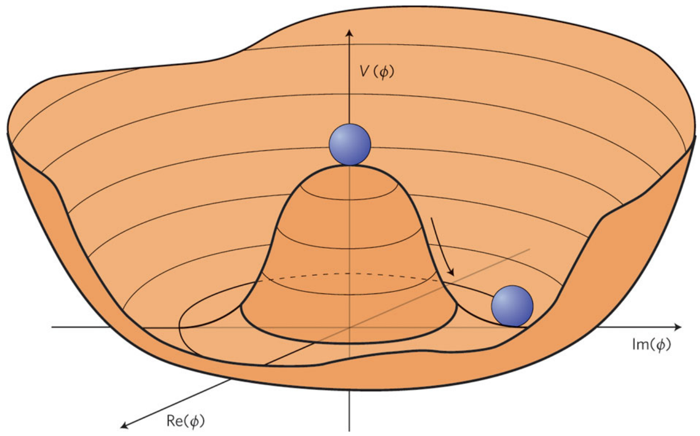

Figure 1.1: The Higgs potential for $\mu^2 < 0$.

breaking. Without any loss of generality, the minimum point can be chosen to be:

$$\phi_0 = \frac{1}{\sqrt{2}}\begin{pmatrix}0\\ \nu\end{pmatrix}. \tag{1.37}$$

The excitation of the ϕ field can be investigated by expanding it around this point. This expansion is defined as:

$$\phi = \frac{1}{\sqrt{2}}e^{i\zeta^a(x)\frac{\tau_a}{2}}\begin{pmatrix}0\\ \frac{\nu+H(x)}{\sqrt{2}}\end{pmatrix}, \tag{1.38}$$

where $\zeta^a(x)$ are three real fields and H is the physical Higgs field. As the Lagrangian is invariant under SU(2), the degree of freedom can be used to remove the $\zeta^a(x)$ fields from the spectrum, as they correspond to unphysical states. After transformation to the Unitarity gauge, the expansion is described by:

$$\phi = \frac{1}{\sqrt{2}}\begin{pmatrix}0\\ \nu + H(x)\end{pmatrix}. \tag{1.39}$$

Substituting this parameterization into the kinetic term leads to:

$$(D_\mu\phi)^\dagger(D^\mu\phi) \rightarrow \frac{1}{2}\partial^\mu H\partial_\mu H + \frac{1}{8}g^2(\nu+H)^2|W_\mu^1 + iW_\mu^2|^2 + \frac{1}{8}(\nu+H)^2|g'W_\mu^3 + gB_\mu|^2. \tag{1.40}$$

The physical charged $W^\pm$ fields are defined as a linear combination of the W_μ^1 and W_μ^2 fields, with

$$W_\mu^\pm = \frac{1}{\sqrt{2}}(W_\mu^1 \mp iW_\mu^2), \tag{1.41}$$

while the neutral Z and photon fields are defined as:

$$\begin{aligned} Z_\mu &= W_\mu^3\cos(\theta_W) - B_\mu\sin(\theta_W),\\ A_\mu &= W_\mu^3\cos(\theta_W) + B_\mu\sin(\theta_W), \end{aligned} \tag{1.42}$$

with

$$\sin(\theta_W) = \frac{g}{\sqrt{g^2 + g'^2}}. \tag{1.43}$$

Expanding Equation 1.40 leads to terms which encode the 3 and 4-vertex interactions of the Higgs boson and the W, Z and γ bosons. Furthermore, the quadratic field terms are interpreted as the mass terms for the gauge bosons, with:

$$M_W = \frac{g\nu}{2}, \tag{1.44}$$

$$M_Z = \frac{\sqrt{g^2 + g'^2}\nu}{2}, \tag{1.45}$$

$$\frac{M_Z}{M_W} = \cos(\theta_W). \tag{1.46}$$

The photon field remains massless. It should be noted that while these mass terms break local gauge symmetry, the overall Lagrangian is still invariant under this transformation.

Similar analysis of other terms in the Lagrangian leads to the description of a Higgs boson with a mass of $m_H = \sqrt{2\lambda}\nu$. While ν can be determined from low-energy muon decay, λ cannot be predicted using the SM. Hence, m_H is a free parameter in the SM. The Higgs potential term leads to the cubic and quartic Higgs self interaction terms.

Fermion masses are also added using the Higgs boson spontaneous symmetry breaking mechanism. This is achieved by adding Yukawa interaction terms to the free fermion field Lagrangian. For example, for the first generation leptons, the Yukawa term corresponds to:

$$\mathcal{L}_{\text{Yukawa}} = -g_e\bar{\psi}_L\phi\psi_R + \text{h.c.}, \tag{1.47}$$

where ψ_L is the left-handed doublet field, ψ_R is the right-handed singlet field and g_e is the Yukawa coupling constant. 'h.c.' is the Hermitian conjugate of the first term. After gauge symmetry breaking, $\mathcal{L}_{\text{Yukawa}}$ is modified to:

$$\mathcal{L}_{\text{Yukawa}} = -\frac{g_e}{\sqrt{2}}\nu(\bar{e}_L e_R + \bar{e}_R e_L) - \frac{g_e}{\sqrt{2}}H(\bar{e}_L e_R + \bar{e}_R e_L). \tag{1.48}$$

The first term is the mass term for the electron with $m_e = \frac{g_e}{\sqrt{2}}\nu$, while the second term leads to the introduction of the Higgs boson-electron vertex for which the coupling is proportional to electron mass. Similar Yukawa interaction terms are introduced for other leptons and quarks. Since no right-handed neutrinos exist in the SM, neutrinos are predicted to be massless after spontaneous symmetry breaking.

1.2 Theoretical constraints on Higgs boson

The existence of a massive scalar Higgs boson is the main prediction of the Higgs mechanism, with its mass being the only free parameter [3, 4, 13, 14]. However, from perturbative calculations of scattering cross-sections and their validity up to a given energy regime, constraints on the mass can be derived. Additional constraints can also be derived by studying the effective running of the Higgs boson quartic coupling, λ, with energy. The Higgs boson couples to all massive particles and affects almost all processes through either direct interactions or higher-order loop corrections. Hence, the Higgs mass can be inferred by fitting precision measurements of various processes.

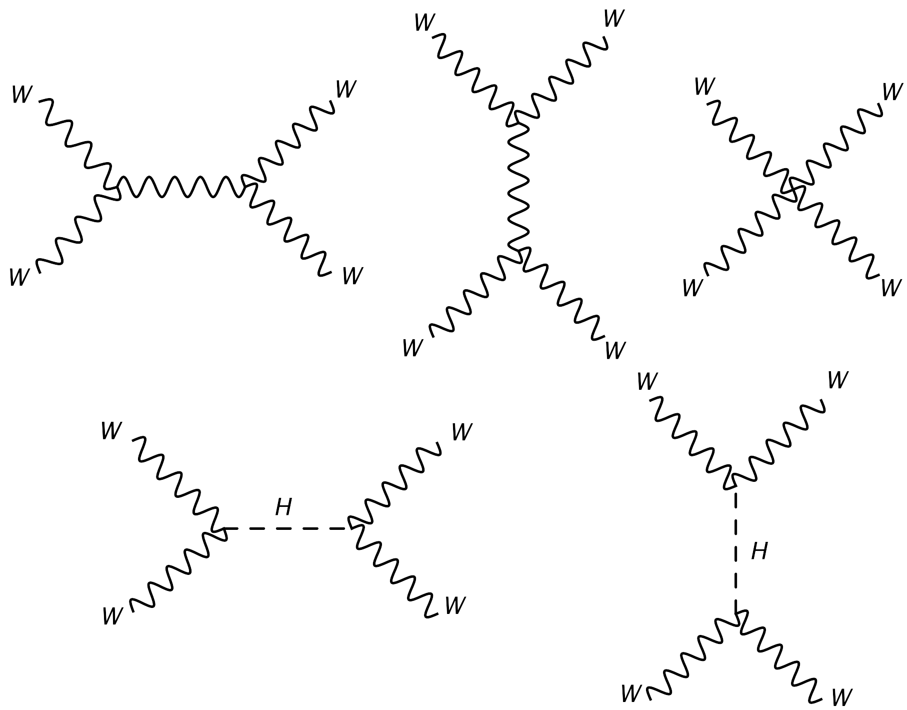

Figure 1.2: Leading order Feynman diagrams for the WW scattering process. The top three diagrams are interactions arising from electroweak theory, while the bottom two diagrams involve the Higgs boson.

Unitarity constraints from Perturbative calculation

Before establishing the electroweak theory, β-decay was described using Fermi's theory of weak interactions. This theory describes low-energy phenomena, as calculations violated unitarity bounds at higher energy. This was solved by the introduction of the electroweak theory where a massive W mediated this decay. Similarly, there are other SM process that would violate unitarity constraints, if interactions involving the Higgs boson are excluded [15].

One such example of this type of interaction is WW scattering [15]. Leading order Feynman diagrams for this process, shown in Figure 1.2, involve γ, Z and H exchange and WW self-interaction diagrams. If all diagrams without the Higgs boson are considered, the contributions from the longitudinal scattering of the bosons cause the process cross-section to grow with energy and violate unitarity.

The Higgs boson s and t channel diagrams interfere destructively, limit the growth of the process cross-section and restore unitarity. An analysis of this process using partial wave decomposition and the optical theorem, shows that this holds only if:

$$\frac{m_H^2}{8\pi\nu} < \frac{1}{2}. \tag{1.49}$$

This leads to an upper limit on the Higgs boson mass:

$$m_H < 870\text{GeV}. \tag{1.50}$$

This is the maximum value for the Higgs boson mass that will allow the WW scattering process to

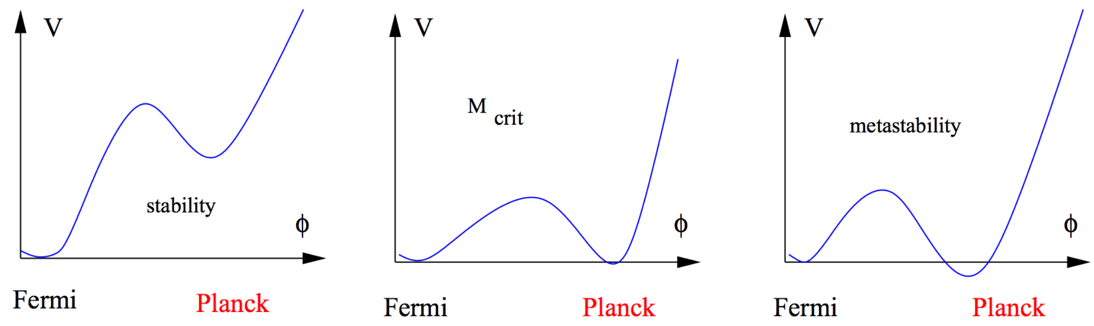

Figure 1.3: The form of the effective potential for the Higgs field ϕ which corresponds to the stable (left), critical (middle) and metastable (right) electroweak vacuum. The form of the effective potential is tightly related to the energy dependence of the Higgs self-coupling constant $\lambda(Q^2)$: the potential is negative almost in the same domain where $\lambda(\phi) < 0$. Adapted from [16].

preserve unitarity to all energy scales.

Triviality and vacuum stability

Higher order loop-corrections to the Higgs boson quartic coupling, λ, lead to a logarithm dependency of λ on the energy scale square, Q^2:

$$\lambda(Q^2) = \lambda(Q_0^2)\left[1 - \frac{3}{4\pi^2}\lambda(Q_0^2)\log\left(\frac{Q^2}{Q_0^2}\right)\right]^{-1}, \tag{1.51}$$

where Q_0 is a reference energy scale. For the coupling to remain finite at all energies, the $\lambda(Q^2)$ must vanish at low energy ($Q << Q_0$). This leads to a trivial, non-interacting theory. However, the positive contribution of loops containing the Higgs boson are m_H dependent and can be cancelled by the negative contributions from the top loops. As such, an upper limit on the Higgs boson mass can be derived if $\lambda(Q^2)$ is required to be finite only up to a given energy. For example, the perturbative regime is valid up to the Planck scale if $m_H < 175$ GeV, while $m_H < 800$ GeV only guarantees validity up ≈ 1 TeV [16, 17].

Lower limits on the Higgs mass can be derived by examining the vacuum stability. For low m_H, the loop corrections involving the top quark dominate and force $\lambda(Q^2)$ to be negative. This can lead to either stable, metastable or unstable configurations of the Higgs potential, as shown in Figure 1.3. Masses larger than 100 GeV allow the vacuum to be stable or metastable up to $Q = 10$ TeV [16–18].

Fit to precision electroweak parameters

Since the Higgs field couples to the weak bosons, the mass of the Higgs boson affects higher order corrections to many electroweak predictions and m_H can be constrained by fitting these parameters. The GFitter program [19] provides such a method. It uses a χ^2 minimization to fit electroweak observables, which have been measured precisely at previous accelerator experiments.

In the SM, higher order corrections to the W mass and the effective electroweak mixing angle have the largest sensitivity for placing limits on m_H. This is due to the experimental determination of these observables with extreme precision. The decay widths of the W and Z provide additional, but relatively

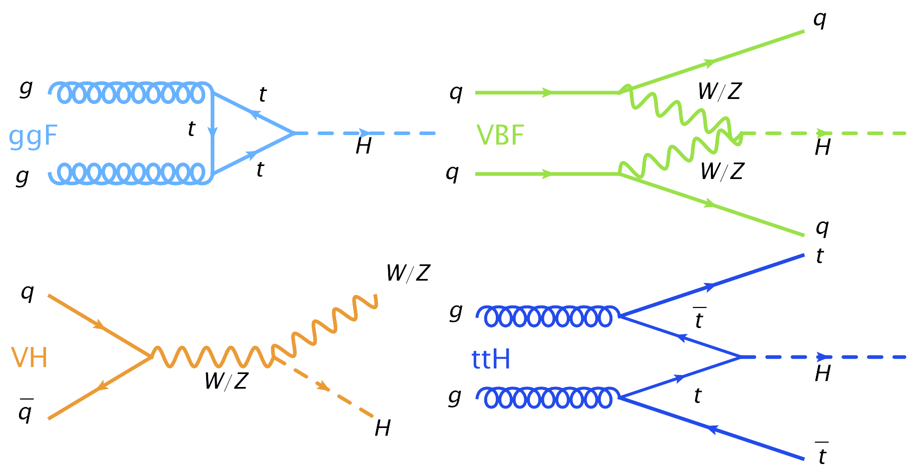

Figure 1.4: Leading order Feynman diagram for Higgs production modes at LHC. ggF production dominates, followed by VBF, VH and ttH respectively.

limited, constraints on the Higgs boson mass.

In the standard fit, the GFitter programs use the electromagnetic, weak and strong coupling constants and the mass of fermions and weak gauge boson. The best fit value for m_H, while simultaneously fitting other SM parameters, is found to be [19],

$$m_H = 91^{+30}_{-23}\text{GeV}. \tag{1.52}$$

Moreover, by including the results from direct Higgs searches at the Large Electron Positron (LEP) and Tevatron colliders, this estimate is improved and yields the best fit for Higgs mass to be [19],

$$m_H = 120^{+12}_{-5}\text{GeV}. \tag{1.53}$$

1.3 Higgs Boson Discovery at LHC

1.3.1 Higgs Boson at the LHC

At the LHC, there are four main modes through which a SM Higgs boson can be produced in a proton-proton collision: gluon-gluon fusion (ggF), vector boson fusion (VBF), vector boson associated production (VH) and top quark associated production (ttH). Figure 1.4 shows the leading order Feynman diagrams for these modes. There are other smaller Higgs boson production methods, such as bottom quark associated production (bbH) and single top quark associated production (tH), which also contribute at the LHC. Once the Higgs boson mass is specified, all other predictions are fixed. Figure 1.5 shows the cross-sections of various production modes for a Higgs boson mass between 120 GeV and 130 GeV at $\sqrt{s} = 13$ TeV [20].

Despite proceeding through a loop at leading order, ggF production has the highest production cross-section at the LHC. This is due to the large Higgs boson-top quark coupling and the large gluon partonic luminosity at the LHC. VBF production has the next largest cross-section. This is followed by VH, ttH and bbH production. Table 1.4 summarizes the predicted cross-section and the associated

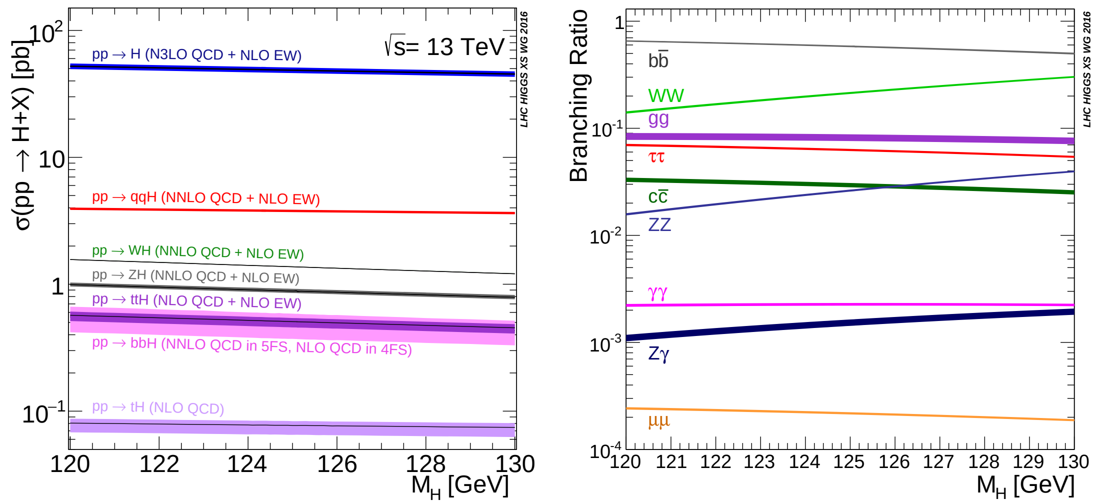

(a) Production cross-section

(b) Decay branching ratio

Figure 1.5: Production cross-section (a) and decay branching ratio (b) as a function of m_H for the Higgs Boson at the LHC [20].

theoretical uncertainty for each of these production modes.

Table 1.4: The predicted SM Higgs boson production cross sections for different production modes at the LHC for $m_H = 125.09$ GeV at $\sqrt{s} = 13$ TeV [20]. The quoted uncertainties correspond to the total theoretical systematic uncertainties calculated by adding in quadrature the QCD scale and PDF+α_s uncertainties. The decay branching ratio (B) with the associated uncertainty for $H \to ZZ^*$ and $H \to ZZ^* \to 4\ell$ with $\ell = e, \mu$, is also given.

Production process	σ [pb]
ggF $(gg \to H)$	48.5 ± 2.4
VBF $(qq' \to Hqq')$	3.78 ± 0.08
WH $(q\bar{q}' \to WH)$	1.369 ± 0.028
ZH $(q\bar{q}/gg \to ZH)$	0.88 ± 0.04
ttH $(q\bar{q}/gg \to t\bar{t}H)$	0.51 ± 0.05
bbH $(q\bar{q}/gg \to b\bar{b}H)$	0.49 ± 0.12
Decay process	B $[\cdot\, 10^{-4}]$
$H \to ZZ^*$	264 ± 6
$H \to ZZ^* \to 4\ell$	1.250 ± 0.027

In the low mass regime, $m_H \sim 125$ GeV, the decay of the Higgs boson is governed by the coupling strength and the available phase space. Figure 1.5 shows the branching ratio for various decay modes as a function of the Higgs boson mass [20]. The largest branching ratio is to $H \to b\bar{b}$, which is followed by the $H \to W^+W^-$ decay. Due to the limited phase space, this decay contains either one or two off-shell W bosons and is highly sensitive to the value of m_H. $H \to gg$, $H \to \tau\tau$ and $H \to c\bar{c}$ have the next largest decay fraction. Similar to ggF production, the $H \to gg$ decay proceeds through a fermion loop diagram at leading order. Despite the larger Higgs-Z boson coupling, $H \to ZZ$ decay has a lower branching ratio when compared to $H \to W^+W^-$. This is due to the comparatively smaller phase space and presence of indistinguishable particles in the final state. Due to the photon being massless, $H \to \gamma\gamma$ also proceeds

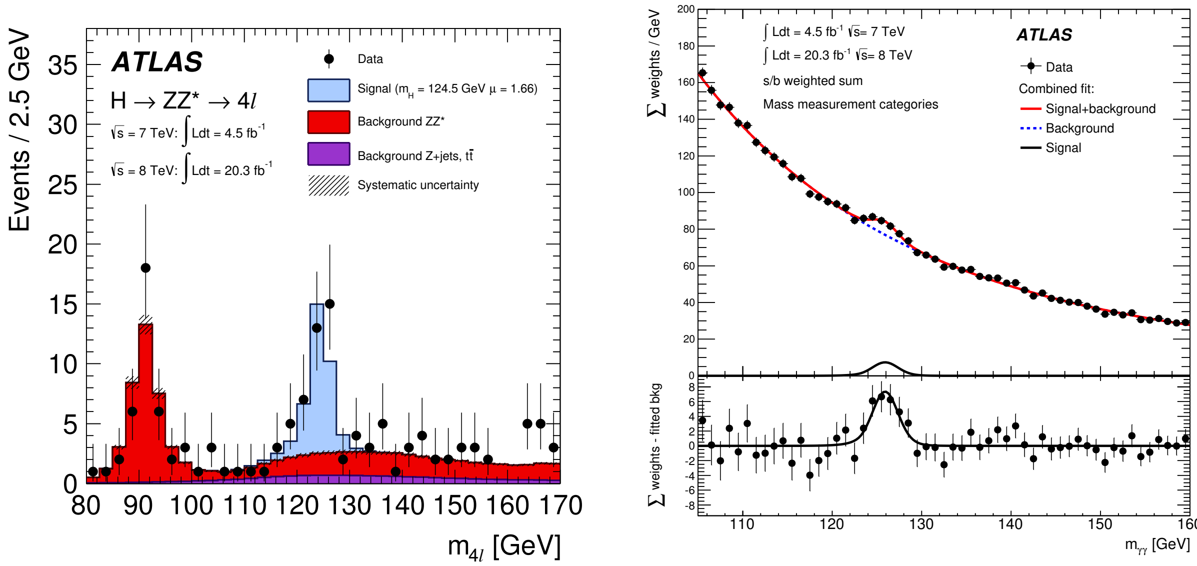

(a) $m_{4\ell}$

(b) $m_{\gamma\gamma}$

Figure 1.6: The observed invariant mass distribution in the (a) $H \to ZZ^* \to 4\ell$ and (b) $H \to \gamma\gamma$ channels [27].

through fermion and W loop diagrams at leading order. There are other smaller Higgs boson decay modes such as $H \to Z\gamma$ and $H \to \mu\mu$.

1.3.2 Higgs Boson Discovery and Experimental Results from LHC Run 1

In the pre-LHC era, the most significant results for direct Higgs searches came from the experiments at the LEP and Tevatron colliders. The LEP collider at CERN excluded the existence of the Higgs boson with $m_H < 114.4$ GeV at 95% confidence level (CL) [21]. These limits were mainly driven by results probing $e^+e^- \to Z \to HZ$. On the other hand, Tevatron searches in the $H \to b\bar{b}$ and $H \to W^+W^-$ channels excluded the possibility of a Higgs boson at 95% CL in the mass range of $100 < m_H < 103$ GeV and $147 < m_H < 180$ GeV and saw a $\approx 3\sigma$ excess over the predicted background in the range $115 < m_H < 140$ GeV [22].

After decades of these direct searches, the Higgs boson was discovered in 2012 and its properties were initially measured by the ATLAS and CMS collaborations during Run 1 of the LHC. The discovery was led by searches in the $H \to ZZ^* \to 4\ell$ and $H \to \gamma\gamma$ decay channels. Figure 1.6 shows the invariant mass distribution in these channels, where a clear contribution from the Higgs boson is observed [23]. By the end of the Run 1, the background-only hypothesis was rejected at greater than a 5σ statistical level for each single channel [23–26].

As stated in Section 1.2, the mass of the Higgs boson is a free parameter in the Standard Model. As such, measuring the mass of the resonance with the highest precision was one of the first experimental goals after the discovery. This measurement was driven by analysis of high-resolution channels, $H \to ZZ^* \to 4\ell$ and $H \to \gamma\gamma$. By combining the ATLAS and CMS Run 1 data, the Higgs boson mass was measured to be $m_H = 125.09 \pm 0.24$ GeV [27, 28]. Figure 1.7 shows a summary of the mass measurement in the individual channels and the subsequent combination of the results.

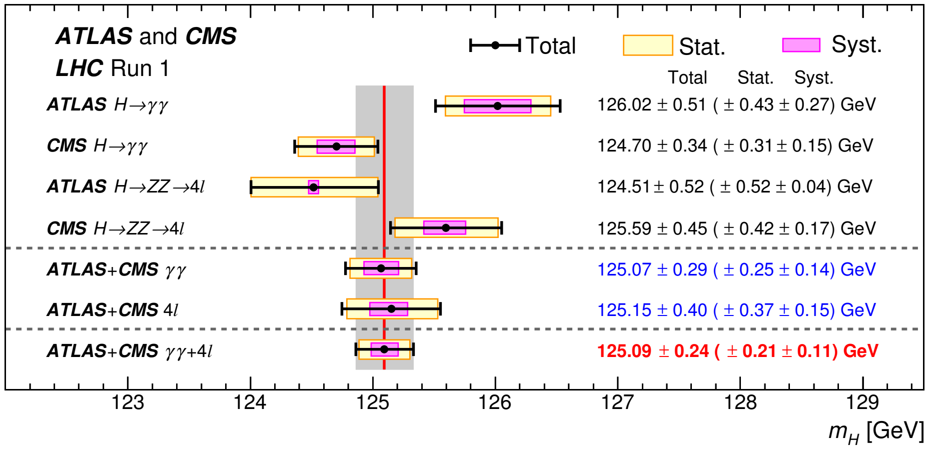

Figure 1.7: Summary of the individual and combination of the Higgs mass measurement in the $H \to ZZ^* \to 4\ell$ and $H \to \gamma\gamma$ decay channels using the ATLAS and CMS detectors [28].

The couplings of the Higgs boson to other Standard Model particles were measured using the observed production cross-section in the different channels, as shown in Figure 1.8 [29]. The observed values match the Standard Model predictions within measurement uncertainty [29]. ggF and VBF production modes were observed, while evidence was found for VH and ttH production modes. Similarly, couplings to vector bosons were observed and initial measurements provided evidence for Higgs decay into fermions.

Another important aspect of the Higgs boson, as predicted by the Standard Model, is its spin-CP property. By using the correlations between different angular and mass-related observables in the diboson decays, both collaborations established the preference for the 0^+ hypothesis over any other alternate spin-CP hypothesis [30], matching the theoretical prediction.

Properties of the Higgs boson were further probed by measuring the differential production cross-sections. Within the statistical and systematic uncertainty, all observed measurements are compatible with the SM predictions [31, 32]. Furthermore, the width of the Higgs boson was observed to be compatible with the SM prediction, as an upper limit of 22.7 MeV at 95% CL_s was obtained by using the off-shell Higgs boson coupling [33].

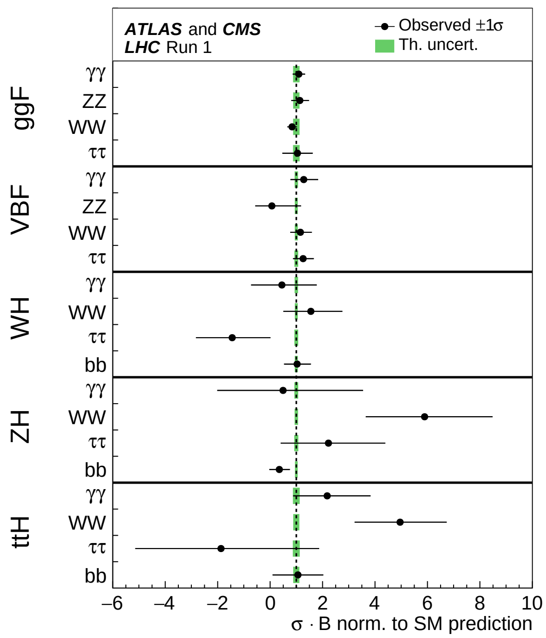

(a) Production cross-sections for various decay channels

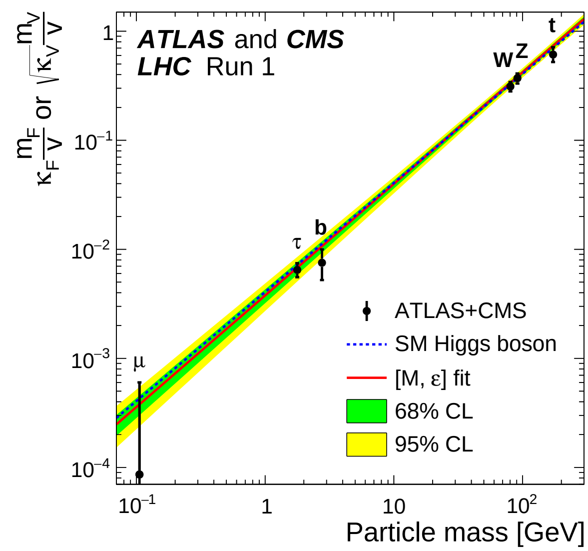

(b) Measured Higgs boson couplings

Figure 1.8: The measured production cross-section in various decay channels (a) and Higgs boson coupling to other Standard Model particles (b) [29].

Chapter 2

The LHC and the ATLAS detector

2.1 The Large Hadron Collider

The LHC is a superconducting accelerator and collider installed in a 27 km underground tunnel at CERN. It is designed to accelerate bunches of protons and heavy-ions to a center of mass energy of 14 TeV and 5.52 TeV per nucleon respectively at a peak instantaneous luminosity of 10^{34} cm^{-2}s^{-1} [34, 35]. At four points along the ring, the LHC collides two oppositely rotating particle beams and each interaction point accommodates a main experiment: ATLAS, ALICE, CMS or LHCb. ATLAS and CMS are two general purpose detectors, designed to investigate a wide variety of physical phenomenon. ALICE focuses on investigating QCD using heavy ion collisions and LHCb is optimized for physics measurements with hadrons containing a b-quark.

The LHC is the final step of the accelerator chain at CERN, shown in Figure 2.1, that increases the energy of particles to their final values [34]. Protons start in LINAC 2 where their energy is increased to 50 MeV. They are then transported to the Proton Synchrotron (PS) Booster and then to the PS which results in an energy of 25 GeV. These protons are then injected into the Super Proton Synchrotron (SPS) which accelerates them to 450 GeV. The beams are then injected into the LHC in a series of bunches with approximately 1.15×10^{11} protons each. Each beam can contain about 2808 bunches which are arranged with either 25 ns or 50 ns spacing.

Once the particle bunches are transported to the LHC, a radio-frequency (RF) system is used to increase the beam energy. This RF system consists of sixteen 400 MHz single-cell Niobium sputtered copper cavities [34], which are designed to create a superconducting inner layer when operated at 1.9 K. Four of these cavities are housed inside a cryomodule and two are used per beam. Figure 2.2 shows the schematic of the LHC cryomodules. Cavities, operating at their nominal gradient of 5.5 $^{\mathrm{MV}}/_{\mathrm{m}}$, provide an energy increase of 0.5 MeV per beam turn [34]. The cryomodule also contains other auxiliary devices to ensure proper operation of the cavities. These include a 'tuner' to correct for changes in cavity resonance frequency caused by external factors such as variations in helium pressure and include a 'Higher Order Modes (HOM) coupler' to dampen the higher order resonances excited by beam wakefields [34].

Due to the space limitations and LHC being a particle-particle accelerator, it uses a "two-in-one" design, where two pipes with counter rotating beams share the same mechanical structure and cryostat, as illustrated in Figure 2.3 [34]. For each beam pipe, a set of dipole magnets guides the proton beam along the circular tunnel [36]. These dipole magnets are made of niobium-titanium (NbTi) cables, which

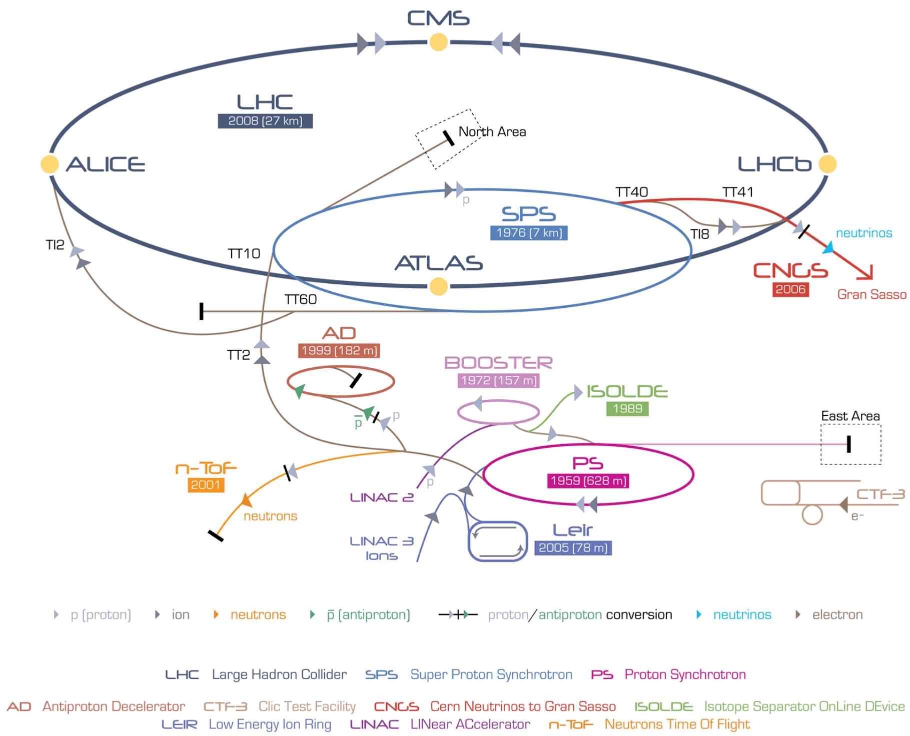

Figure 2.1: The accelerator complex at CERN.

become superconducting at temperatures below 10 K. With an electric current of over 11000 A, these coils generate a bending magnetic field of 8.33 T. At the LHC, this bending power ultimately limits the highest possible achievable beam energy. The LHC uses 1232 of these dipoles magnets.

The LHC also contains many quadrupole and higher multipole magnets to ensure stable beam orbit [36]. Pairs of quadrupole magnets focus and defocus beam in perpendicular directions to prevent an increase in the transverse size of the beam, while the higher multipole magnets correct for small orbit imperfections, such as those arising due to chromatic aberrations. A series of insertion magnets are also placed around the interaction points. These consist of a triplet of quadrupole magnets, which squeeze the beam to allow for a higher probability of proton-proton collision at the interaction point. The two counter-rotating beams share the same beam pipe between these insertion magnets.

The number of expected events (N_s) for a given process in a particle-particle collision is given by:

$$N_s = \int L \, dt \times \sigma = \mathcal{L} \times \sigma, \tag{2.1}$$

where σ is a process dependent cross-section, L is the instantaneous luminosity and $\mathcal{L}$ is the total time-integrated luminosity. For many of the physics processes probed at the LHC, such as the Higgs boson, the production cross-section is small. As such, one of the main LHC design criteria is to maximize the total luminosity delivered to the experiments.

The instantaneous luminosity at a collider is given by:

$$L = \frac{N_b^2 n_b f_{rev} \gamma F}{4\pi \epsilon_n \beta^*}, \tag{2.2}$$

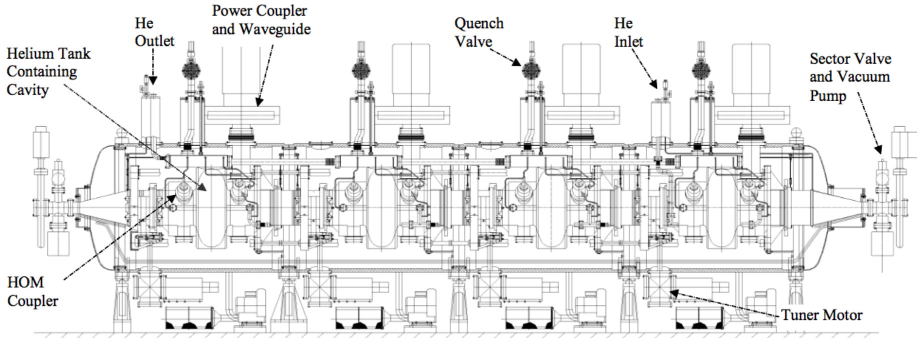

Figure 2.2: Schematic of the LHC accelerator cryomodule.

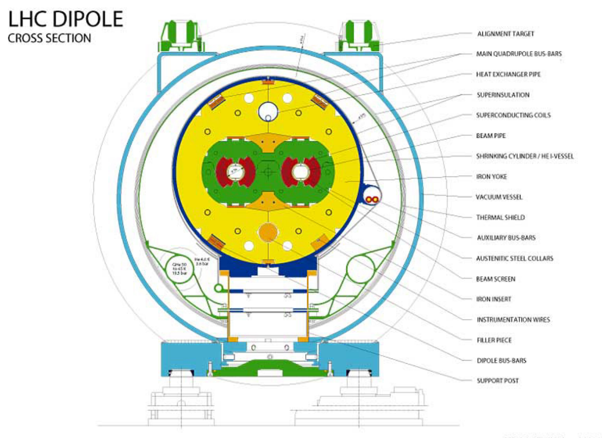

Figure 2.3: Diagram showing the cross-section of an LHC dipole magnet with its components including the coils and the vacuum vessel.

where N_b is the number of protons in a bunch, n_b is number of bunches per beam, f_{rev} is the revolution frequency and γ is the Lorentz factor. F is a geometric factor, which takes into account the reduction in luminosity due to a non-zero crossing angle at the collision point. ϵ_n is the beam emittance and characterizes the momentum spread of the particles in a bunch. β^* is the β-function at the collision points and is proportional to the transverse size of the beam.

Since the start of its operation, the LHC has steadily improved its performance and delivered a larger luminosity to the experiments. The evolution of the LHC operational parameters is summarized in Table 2.1 and the integrated luminosity delivered to the ATLAS experiment is shown in Figure 2.4. During Run 1, which occurred between 2010 and 2012, the LHC operated at a total center of mass energy of $7-8$ TeV and 28.3 fb^{-1} of data was delivered to the ATLAS experiment. After the first long shutdown, the accelerator underwent significant upgrades to improve the operational safety and reliability. In the first 2 years of Run 2, the LHC operated at $\sqrt{s} = 13$ TeV and surpassed many of its design parameters. A total integrated luminosity of 42.6 fb^{-1} was delivered to the ATLAS experiment during this time period. For the full Run 2 dataset, the LHC delivered a total luminosity of 156 fb^{-1}.

Table 2.1: Design and operational parameters for the LHC [37].

	Design	2010	2011	2012	2015	2016	2017	2018
Beam Energy (TeV)	7.0	3.5	3.5	4	6.5	6.5	6.5	6.5
Protons/bunch (10^{11} p)	1.15	1.0	1.3	1.5	1.1	1.1	1.15	1.15
Number of bunches	2808	368	1380	1380	2244	2208	2556	2556
Beam Emittance (μm)	3.75	2.6	2.4	2.4	3.5	2.6	2.2	2.0
β^* (m)	0.55	2.0-3.5	1.0-1.5	0.6	0.8	0.4	0.3	0.3
Peak Luminosity (10^{34}cm^{-2}s^{-}1)	1	0.021	0.35	0.77	0.51	1.38	2.05	2.01
Total Integrated Luminosity (fb^{-1})		0.048	5.5	22.8	4.1	38.5	50	66

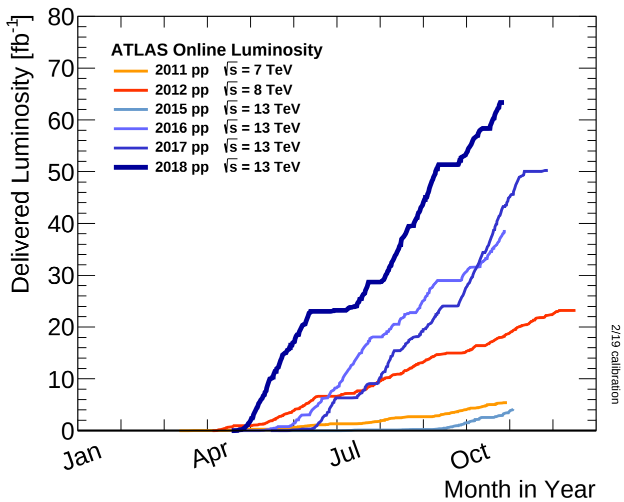

Figure 2.4: Total integrated luminosity delivered to the ATLAS detector between 2010-2018 [38].

2.2 The ATLAS Detector

ATLAS (A Toroidal LHC ApparatuS) [39] is a general purpose detector built around one of the LHC's interaction points. It is 44 m long, 25 m high, weighs over 7,000 tonnes and covers almost the entire 4π solid angle. Figure 2.5 shows a schematic of the ATLAS detector while Figure 2.6 shows a cross-sectional view with simulated particles and their interactions within the detector. The various sub-detectors are layered cylindrically to provide uniform coverage. From the centre to the outside, these are:

- The *Inner Detector* which measures tracks of charged particles and provides momentum and vertex measurements. It also aids in electron identification.
- The *Electromagnetic and Hadronic Calorimeters* which absorb electrons, photons and hadrons and measure their energy.
- As muons escape the calorimeters, the *Muon Spectrometer* provides additional measurements that can be used to independently reconstruct muons.

A system of toroidal and solenoid magnets provides magnetic fields of 4 T and 2 T respectively. These bend the trajectory of charged particles and allow their momentum to be measured. Since the interaction rate at LHC design luminosity is approximately 1 GHz and data recording is limited to $\sim$ 1 kHz, a

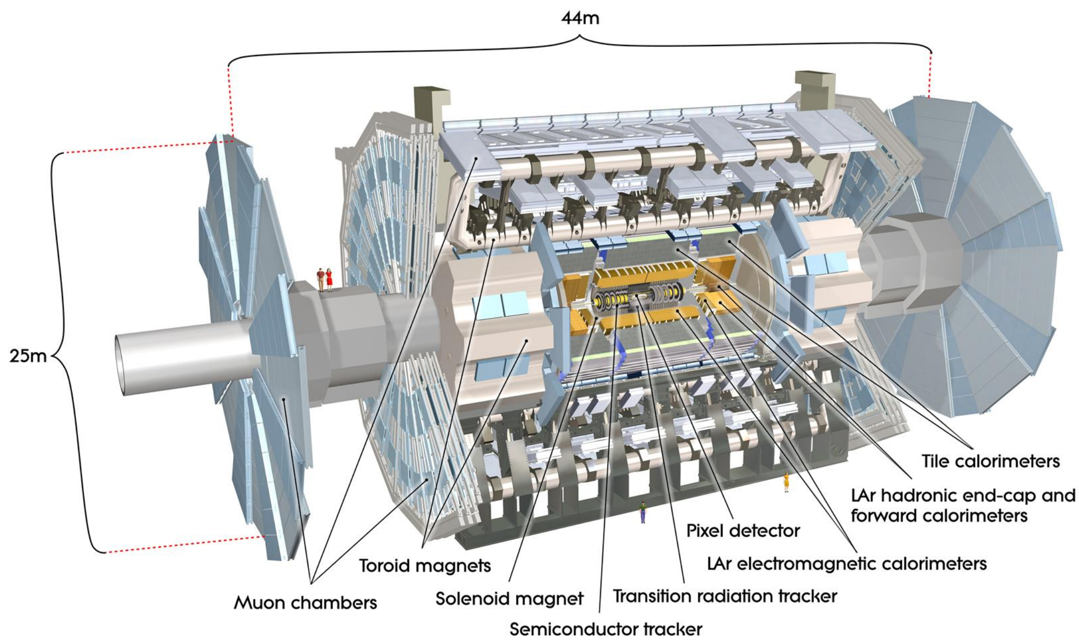

Figure 2.5: Cut away view of the ATLAS detector with its various subsystems labelled.

trigger system is used to reject events by a factor of $\sim 10^7$. To maximize the physics reach of ATLAS, this system is designed to accept events with decay signatures from rare and exotic particles.

ATLAS uses a right-handed coordinate system. The origin is placed at the nominal beam interaction point, which also corresponds to the centre of the detector. The z-axis is oriented along the beam pipe and the x-y plane is orthogonal to it. The x-axis points towards the centre of the LHC ring and the y-axis points upward. In polar coordinates, the azimuthal angle ϕ is defined around the beam pipe. The pseudo-rapidity η is defined as $\eta = -\ln[\tan(\theta/2)]$ where θ is the polar angle.

2.2.1 Inner Detector

Due to the large number of particles created in a single event and the required momentum resolution, vertexing and identification requirements, the Inner Detector (ID) employs three different technologies to measure the path of a charged particle in the $|\eta| < 2.5$ region [39, 40]. The pixel detector and the semiconductor tracker use silicon pixels and strips, while the transition radiation tracker uses straw tubes to track particles and provides identification using transition radiation. Figure 2.7 shows a view of the ID.

Installed during the long shutdown between 2013 and 2015, the Insertable B-Layer (IBL) is the closest tracking detector. It is only 33mm away from the interaction point [41]. It uses reverse-biased doped silicon pixels to measure the passage of a charged particle. When the charged particles interact with the semiconductor, electron-hole pairs are created and a subsequent collection of these pairs creates the required electrical signal. The central part of the IBL uses conventional 2D pixel silicon sensors, each with a size of 50×250 μm^2 in $R - \phi$ and thickness of 200 μm. To improve the radiation hardness and reduce the required bias voltage, 3D pixel sensors are employed close to the edges of the detector. In

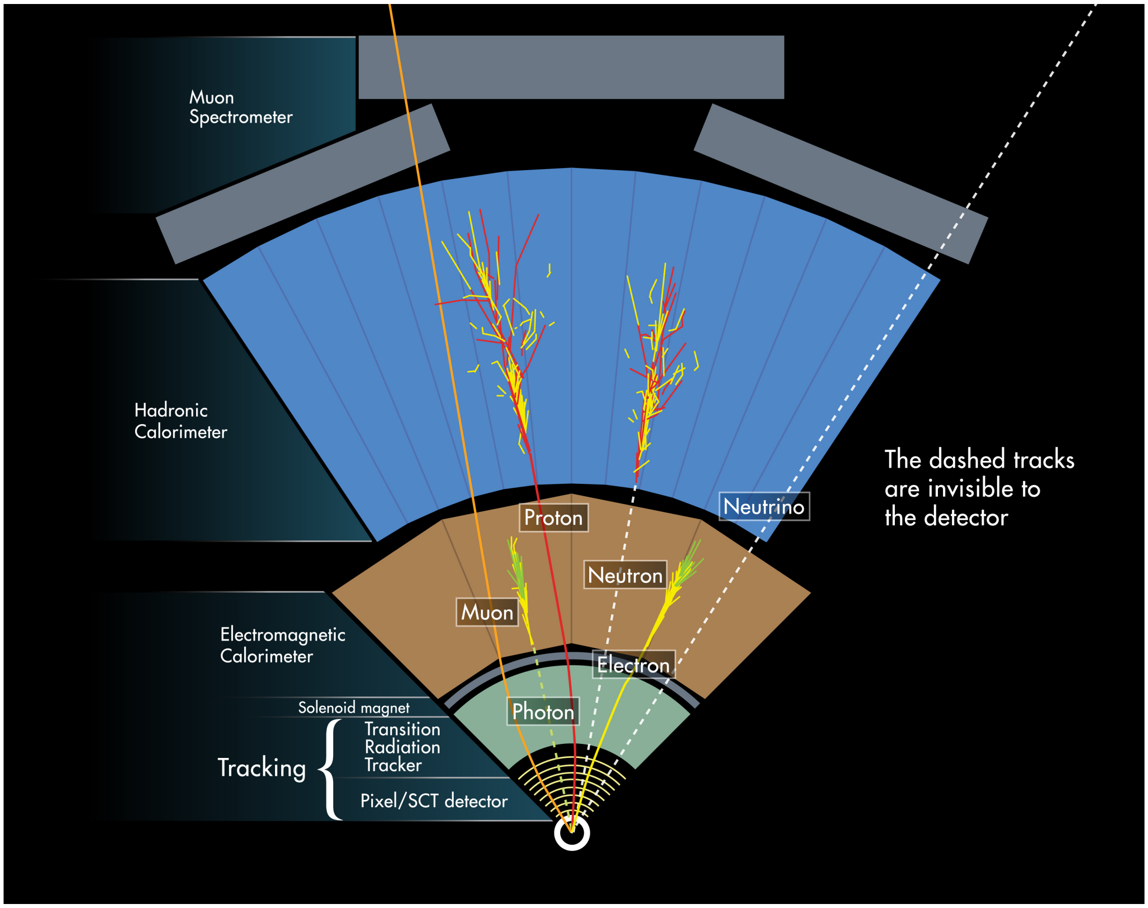

Figure 2.6: Cutaway view of ATLAS. Simulated particles and their interactions within the detector are overlaid.

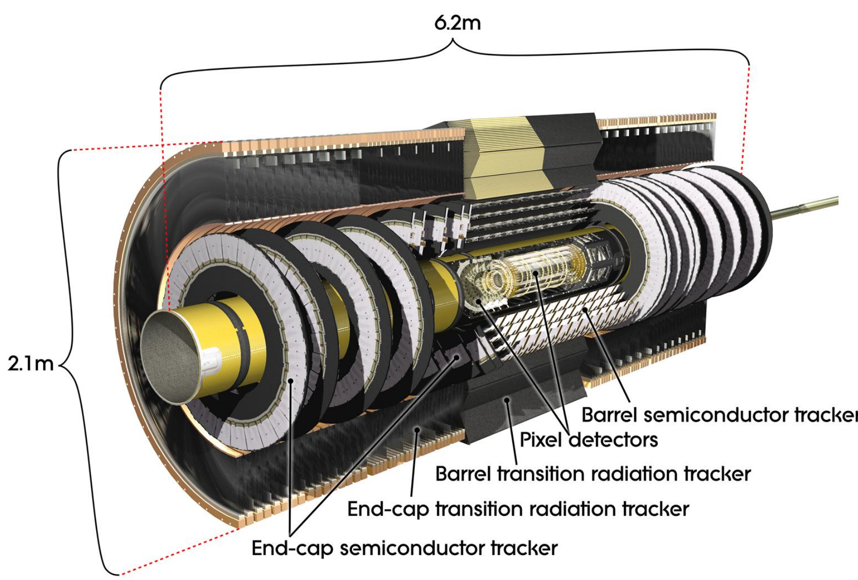

Figure 2.7: Perspective view of the ATLAS Inner Detector.

contrast to the planar electrode design of 2D sensors, the electrodes are etched into the silicon bulk for the 3D sensors. IBL provides tracking coverage up to $|\eta| < 3$.

The pixel detector is second closest to the interaction point and provides measurements of charged particles using high granularity pixel sensors. In total, it uses 80.4 million pixel sensors, each with a size of 50×400 μm^2 in $R-\phi$. These are arranged in 3 concentric cylinders in the central barrel region and in 3 rings for each end-cap region. The barrel (ring) region has an intrinsic accuracy of 10 μm in $R-\phi$ and 115 μm in z (R). The pixel detector provides tracking up to $|\eta| < 2.5$ and a charged particle, on average, leaves 3 hits.

The semiconductor tracker (SCT) uses small angle stereo silicon strips [42] to provide a practical method to accurately track particles. Two strip detectors are stacked together with a 40 mrad offset and the long sensor axis is placed along the beam direction. This stereo configuration provides a constraint in the longitudinal (radial) position of the particle in the barrel (end-cap) regions and leads to an intrinsic accuracy of 17×580 μm in $R-\phi \times z$ direction in the barrel (R direction in the end-cap). The 6.3 million SCT sensors are arranged in 4 layers in the barrel region and in 9 rings in each end-cap region. A particle typically leaves 8 hits in the SCT region.

The transition radiation tracker (TRT) provides approximately 36 hits per track in the $|\eta| < 2.0$ region. It uses 2 mm straws with a 32 μm tungsten wire strung at the center of each straw. The straw is filled with a xenon-carbon dioxide-oxygen gas mixture and the wire is held at -1500 V with respect to the straw. When a charged particle traverses the straw, it ionizes the gas. The electrons cause a further avalanche of ionization and drift toward the wire where they are collected. Due to the long lever-arm, TRT measurements contribute significantly to the track momentum measurement.

To discriminate between electrons and charged hadrons, the TRT tubes are surrounded with polypropylene and polyethylene radiation fibres. When a particle crosses the interface between materials with different indices of refraction, it radiates photons, which is referred to as transition radiation. The amount of energy emitted through this process is dependent on the particle's relativistic factor. As such, for a given energy, electrons produce more transition radiation when compared to other hadrons. This allows the TRT detector to provide electron identification up to ~ 150 GeV.

2.2.2 Calorimeter

The ATLAS calorimetry system consists of two major components, covering the $|\eta| < 4.9$ region: the electromagnetic calorimeter (ECal) and the hadronic calorimeter (HCal). The ECal is designed to measure the energy of particles that predominately interact electromagnetically, such as electrons and photons. Jets leave a significant energy deposit in the ECal, but they escape it and are contained and measured within the HCal. Figure 2.8 shows a cutaway view of the calorimeters.

The ECal is a liquid argon-lead sampling calorimeter. When an electron or photon passes through the lead absorber material, it creates a shower of particles through $\gamma \to e^+e^-$ conversions and the $e^\pm \to \gamma e^\pm$ bremsstrahlung process. The active liquid argon layer 'samples' these showers through ionization and provides a measurement for the energy of the incoming particle. The ECal is divided into a barrel region ($|\eta| < 1.475$) and two end-cap components ($1.375 < |\eta| < 3.2$). These are approximately 22 radiation lengths (X_o) in depth to contain most of the EM shower. Electrons lose are left with $^1/_e$ of their energy due to bremsstrahlung or photons have a probability of approximately 54% to undergo conversion with one radiation length.

An important aspect of the ECal is its accordion shaped geometry, as shown in Figure 2.9. This

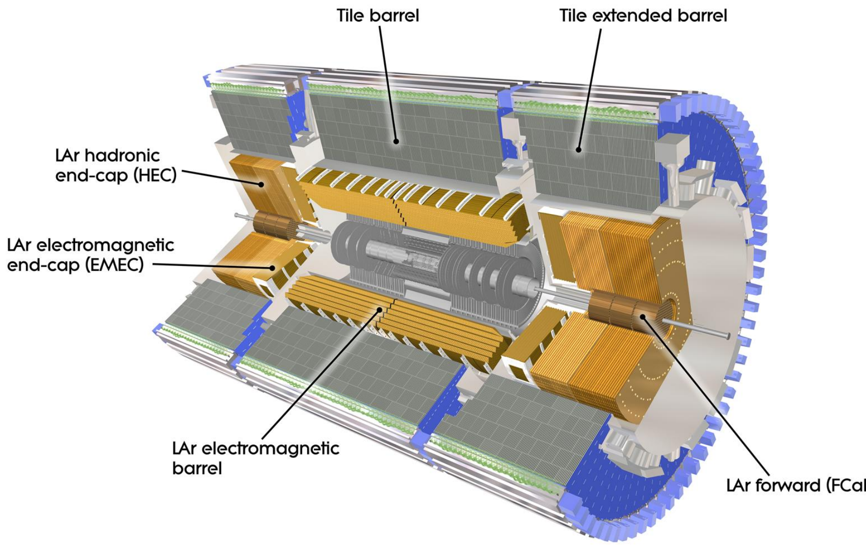

Figure 2.8: Cut away view of the ATLAS calorimeter system.

provides a constant coverage in azimuthal angle without any cracks. The first layer of this geometry, with the finest granularity, aids in photon identification. The second layer, with $\Delta\eta \times \Delta\phi = 0.025 \times 0.025$ cells, is designed to contain most of the deposited energy. The third layer provides an extra measurement before the particles enter the HCal.

The HCal uses multiple different types of calorimeters, depending on the expected radiation levels. In the barrel region ($|\eta| < 1$) and the extended barrel region ($0.8 < |\eta| < 1.7$), a tile calorimeter is used. Using a similar principle as the ECal, it employs steel absorbers and scintillating tiles as the active material. It is approximately 11 interaction lengths thick, which reduces the hadronic particles escaping to the muon spectrometer ('punch-through'). In the end-cap region ($1.7 < |\eta| < 3.2$), a liquid argon with copper absorber calorimeter is used. Finally, in the forward region ($3.2 < |\eta| < 4.9$), another liquid argon calorimeter is used. It relies on three layers of absorbers: 1 layer of copper absorber and 2 layers of tungsten absorber. The copper absorber provides uniform coverage and prevents LAr from boiling by efficiently transferring the heat generated due to the high interaction rate. The tungsten absorber restricts the transverse and longitudinal expansion of hadronic showers, allowing them to be contained within the detector. The forward calorimeter is enclosed by an non-instrumented brass plug that reduces the hadronic shower from escaping to the muon spectrometer.

2.2.3 Muon Spectrometer

The muon spectrometer (MS) is designed to provide an independent measurement for muons with p_{T} approximately greater than 1 GeV. These muons are minimum ionizing particles and escape the ID and the calorimeters. It can measure muon momenta accurately down to 3 GeV. For high p_{T} (≈ 3 TeV) muons, the MS has a resolution of $\approx 10\%$ and provides excellent charge identification. The MS also contains a series of dedicated chambers for fast triggering.

The monitored drift tubes (MDT) and cathode strip chambers (CSC) are two technologies used in

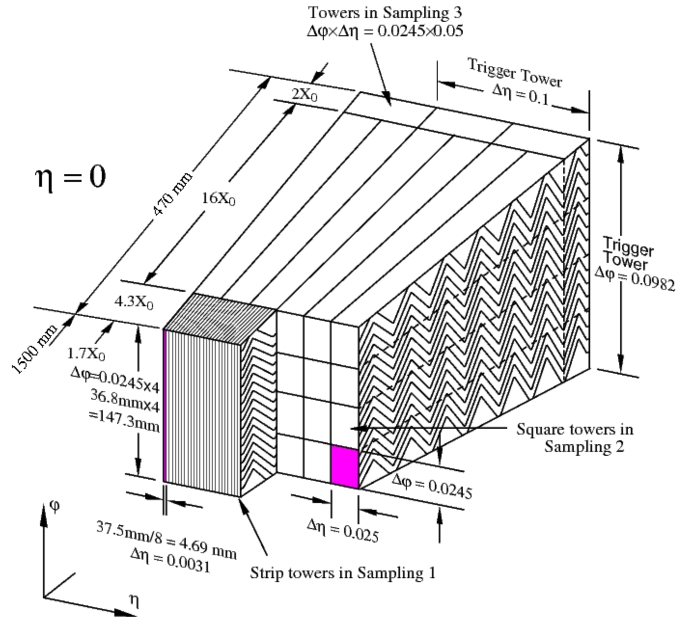

Figure 2.9: Accordion shaped geometry of the ECal.

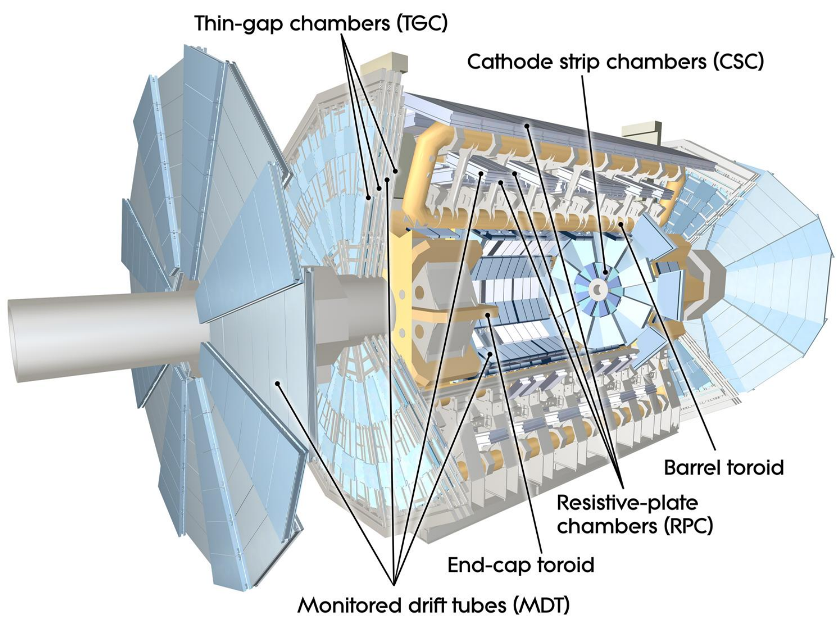

Figure 2.10: The ATLAS muon spectrometer.

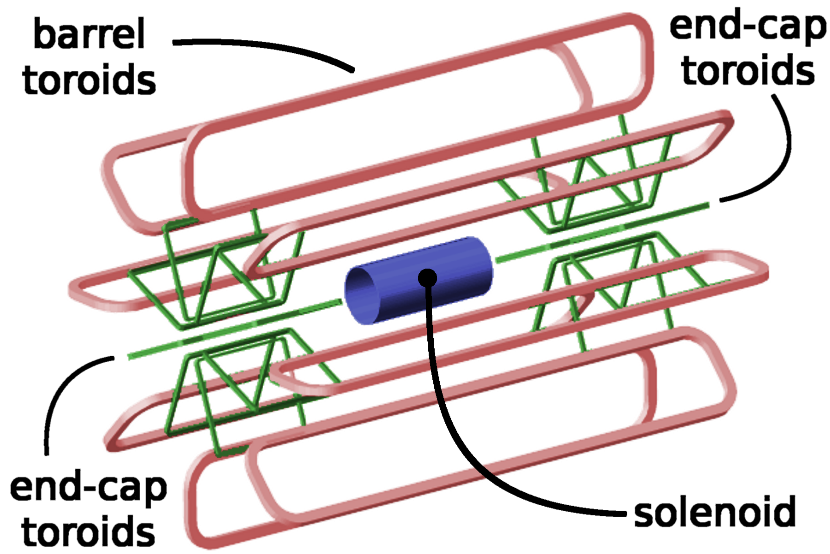

Figure 2.11: The ATLAS magnet system.

the MS for precision tracking. Similar to the TRT, the MDTs use aluminum drift tubes with a tungsten wire at the centre and are filled with an argon-carbon dioxide gas mixture. Three layers of MDTs are used to provide tracking in the $|\eta| < 2$ region. The MDTs are consistently monitored through a laser system to ensure a combined resolution of 50 μm for the tracks. The CSCs are multi-wire proportional chambers designed to cope with the high interaction rates in the forward region ($2 < |\eta| < 2.7$). The ionized gas created by the passage of a muon is collected using the anode wires and also the particle induces a charge in the cathode strips. This combined measurement in orthogonal directions allows for a 60 μm resolution in the track position.

To allow for triggering in the event crossing time space, the muon triggering chambers are designed for fast response. Resistive Plate Chambers (RPCs) are used in the barrel region and are located on both sides of a MDT station. Each RPC consists of two bakelite sheets separated by a narrow gas region filled with tetrafluoroethane gas. An electric field is applied for collection of ionized gas. On the other hand, Thin Gap Chambers (TGCs) are used in the end-cap regions and are very similar to CSCs in design. These triggering chambers also provide a measurement of the muon track coordinate in the direction orthogonal to the one determined by the precision chambers.

2.2.4 Magnet System

The ATLAS magnet system consists of 4 separate systems, as shown in Figure 2.11. The magnetic field inside the inner detector is provided by a solenoid magnet. The 2 T magnetic field is aligned along the beam and bends charged particles in the ϕ direction. The barrel and two end-cap toroids create a field between 0.5 T to 5 T which bends charged particles in the η directions. The large volume covered by the toroid magnets results in a better lever arm for momentum measurement in the MS detector.

The solenoid and toroid magnets are made of niobium-titanium (NbTi) cables, which become superconducting when cooled to 6.5 K. To reduce the material thickness and the subsequent energy loss before the calorimeters, the solenoid magnet is designed to be 0.66 X_o and is housed in the same cryostat

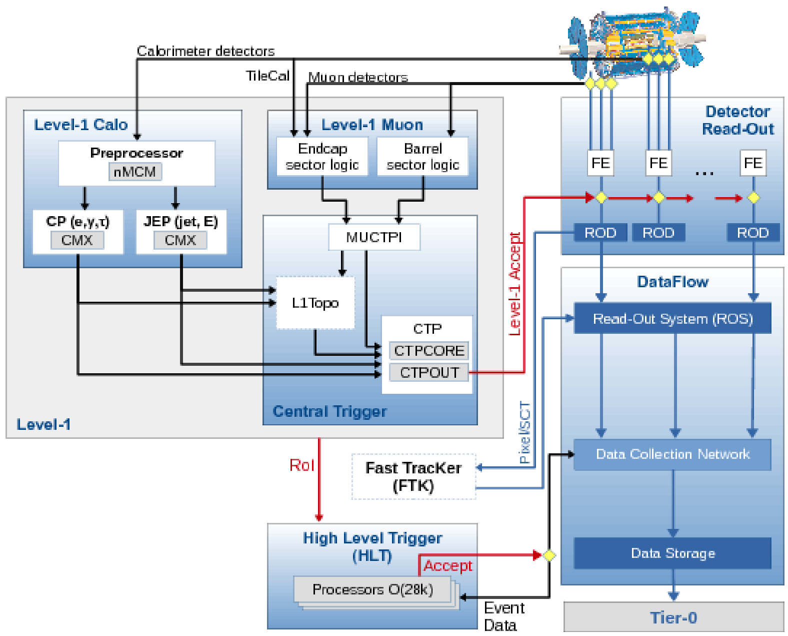

Figure 2.12: The ATLAS trigger system.

as the electromagnetic calorimeter. Similarly, the toroid magnets are designed using the air-core system, which allows muons to pass through the MS detector without interacting with the superconducting coils.

2.2.5 Trigger System

The trigger system is one of the most important parts of the ATLAS data acquisition system. While the collision occurs at a rate of 40 MHz, bandwidth considerations limit the readout to only $\sim$ 1kHz. The trigger system applies a series of criteria to select and reduce the number of events for which the information is saved for later analysis. The criteria are designed to be sensitive to interesting physics processes and reject events from background processes, such as low-energy QCD interactions of protons.

The ATLAS trigger system used for Run 2 consists of two levels of event selection [43], which are shown in Figure 2.12. The first level, called as Level 1 (L1), is a hardware based trigger system. It is designed to identify events for the second level in 2.5 μs, which reduces the rate to 100 kHz. Due to limited time available for generating an accept signal, the L1 system uses information only from the calorimeter and muon spectrometer systems. It can identify events with large p_{T} leptons, energetic jets or photons or with large missing energy.

Once accepted by the L1 system, the events are buffered and passed to a software-based high level trigger (HLT) system. It has access to fine-granularity calorimeter information and tracking measurements from the inner detector. This allows the HLT to reconstruct particles in the event and apply more stringent selection criteria. The average processing time for a given event is highly dependent on the trigger menu and the average pileup [43]. If accepted by the HLT system, the detector information for the respective event is read out and saved to disk for offline analysis.

Chapter 3

Coupling measurement in the $H \to ZZ^* \to 4\ell$ channel with 36.1 fb^{-1}

3.1 Overview

One of the main motivations for introducing spontaneous symmetry breaking through the Higgs mechanism is to allow for mass terms in the Standard Model Lagrangian for bosons and fermions while preserving the imposed gauge symmetry. As shown in Chapter 1, a consequence of this methodology is that the couplings to other particles are fixed once the Higgs boson mass is specified. As a result, the production cross-sections and decay branching ratios are uniquely predicted as a function of the mass.

The relationship between the different properties of the Higgs boson provides a portal to probe for the consistency of the Standard Model. Experimentally, the Higgs boson mass can be measured with minimal theoretical assumptions [28]. Similarly, different production methods and final states have unique experimental signatures, which allows us to directly measure their production cross-section and decay branching fraction. [29]. These mass and cross-sections measurements can be subsequently combined to probe the coupling of the Higgs boson to other particles.

Contributions from any Beyond the Standard Model (BSM) processes will modify the effective coupling between the Higgs boson and other particles. As such, any observed deviations from the SM prediction of the inclusive production cross-sections would indicate the presence of such processes. Moreover, by measuring the differential production cross-sections, the process through which BSM physics could contribute can be disentangled. This motivates the use of the Simplified Template Cross-Section (STXS) framework [44] as described in Section 3.2.1.

The couplings and STXS measurements provide sensitivity to a large variety of potential BSM effects. A few such examples are listed as follows:

- The presence of a heavy BSM particle with a colour charge which can couple to both gluons and the Higgs boson will create an effective Higgs-gluon interaction at low energy [45]. As shown in Figure 3.1(a), this will modify both the inclusive ggF cross-section and its differential production cross-section at high Higgs boson transverse momentum, where the presence of such a particle will contribute more.

- Any deviation of the Higgs boson to charm quark coupling will modify the ggF cross-section [46].

As light-quarks contribute more to the production cross-section at low energies, this BSM effect is more pronounced at low Higgs boson transverse momentum as shown in Figure 3.1(b). Furthermore, cross-section measurements at transverse momentum close to half the Higgs boson mass can distinguish between deviations to Higgs boson-charm quark coupling and Higgs boson-bottom quark coupling. This is due to down-type quarks contributing with an opposite sign with respect to the up-quarks in the ggF amplitude.

- Modifications to the Higgs boson and vector boson coupling will change the VBF cross-section and the Higgs boson decay fractions [47]. A simultaneous measurement of all production modes in a single final state can probe for such deviations.
- The presence of a heavy BSM particle with no colour charge which can couple to vector bosons and the Higgs boson will create an enchantment in the VH cross-section [48]. This enchantment will be larger at higher transverse momentum of the Higgs boson.
- Modification to the CP structure of the Higgs boson will change all production cross-sections. The relative deviation from the SM prediction between the ggF and ttH [49], and VBF and VH [50] cross-section can disentangle if the CP structure is different for the Higgs boson-fermion and Higgs boson-vector boson interactions respectively.

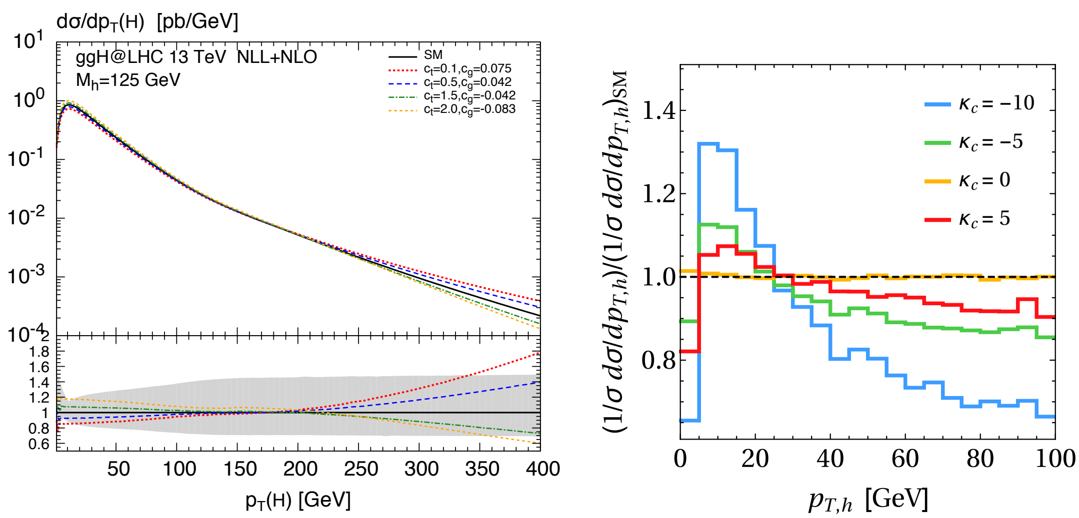

(a) Heavy BSM particle with a colour charge [45].

(b) Modification to the Higgs boson-charm quark coupling [46].

Figure 3.1: Modification to the ggF Higgs boson transverse momentum production cross-section due to presence of potential BSM effects.

The $H \to ZZ^* \to 4\ell$ (H4l) decay channel, with ℓ being a muon or electron, provides one such portal to probe for SM consistency and for BSM processes. This final state is fully reconstructible, can be precisely measured, and SM background processes leading to the same final state are rare. Despite the small branching ratio for this decay, the signal to background ratio is expected to be greater than 2 [51, 52]. This allows the H4l channel to have good sensitivity to measure Higgs boson couplings.

Initial measurements of the Higgs boson couplings were carried out in this channel using the Run 1 dataset [24]. Due to the limited statistics, only combined measurements of ggF $+ttH$ and VBF $+VH$

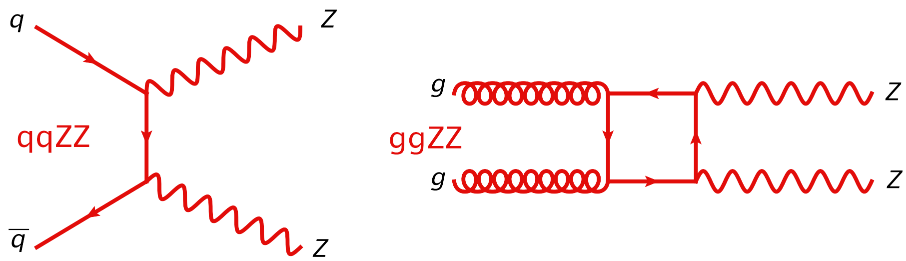

Figure 3.2: Leading order Feynman diagrams for continuum ZZ^* production at LHC. Quark-initiated production ($qqZZ$) is approximately 10 times larger than gluon-initiated ($ggZZ$) production.

were performed. The signal strength, defined as the measured production cross-section divided by the SM predicted value, for ggF $+ttH$ was found to be $1.7^{+0.5}_{-0.4}$, while the signal strength for VBF $+VH$ was found to be $0.3^{+1.6}_{-0.9}$. No significant deviation from the SM prediction was observed.

In 2015, the LHC started Run 2 of data collection. The aim was to provide the experiments with a dataset at $\sqrt{s} = 13$ TeV which was approximately 5 times larger than the Run 1 dataset. Coupled with the increase in cross-section due to the higher centre of mass energy, this greatly increases the statistics available for precision measurements. Therefore, the Higgs coupling can be probed with increased precision and in finer phase space regions using the collected Run 2 dataset [51].

3.2 Analysis Strategy

To measure Higgs boson couplings in the $H \to ZZ^* \to 4\ell$ channel, events consistent with this decay channel are selected from the collected dataset. As the Higgs and the Z boson decay before interacting with any part of the detector, only the final state leptons are detected. Due to ATLAS's ability to detect and reconstruct electrons and muons with high precision, only final states with these particles are considered for this analysis. Tau leptons have comparatively worse energy resolution and larger systematic uncertainties, which limits their impact on the final results [24] and are not considered in this analysis.

The presence of 4 leptons in the final state serves as a powerful discriminant to select events consistent with a Higgs boson decay. This is due to the fact that very few physics processes in proton-proton collisions lead to events with a large multiplicity of leptons. The largest background for this analysis is the continuum $(Z^{(*)}/\gamma^*)(Z^{(*)}/\gamma^*)$ production, referred to as ZZ^* hereafter. Leading order Feynman diagrams are shown in Figure 3.2. There are also small but non-negligible background contributions from $Z+$jets and $t\bar{t}$ production with two prompt leptons. The additional charged lepton candidates in these processes arise from decays of hadrons, in-flight decays of pions or kaons, photon conversions or misidentification of hadron jets. $t\bar{t}+V$ and tri-boson continuum production have a small contribution in the VH-like and ttH-like production phase space.

Additional selection criteria are designed and applied to improve the signal to background ratio in the analysis. The presence of the two Z bosons decaying from a single scalar particle introduces correlations between the detected leptons. These are used to reduce the impact and contributions of other processes which have uncorrelated Z bosons. Moreover, additional leptons found in $Z+$jets and $t\bar{t}$ processes have unique experimental signatures. Specifically, leptons have displaced vertices with respect to the hard-scatter vertex and have a shower of nearby hadrons around it. This is used to distinguish and limit contributions from these processes.

Once $H \to ZZ^* \to 4\ell$ candidates have been selected, they are further classified into different exclusive categories to target the Higgs production modes. Each production mode leads to a specific event topology, which serves as a method to tag the reconstructed event as coming from one of the given production processes. Within these categories, discriminating observables can be introduced to further improve sensitivity. For this analysis, these observables are combined into a single discriminant using dedicated boosted decision trees (BDTs) [53].

Using these classified events, measurements of the production cross-sections are performed. Results using both cross-section and signal strength modifier as parameters of interest are extracted. The former has the advantage that many theoretical uncertainties affecting the SM prediction are factorized out. The measured cross-section for a production mode X ($\sigma^X_{\text{measured}}$) is defined as:

$$\sigma^X_{\text{measured}} = \frac{N^X_{measured}}{\mathcal{A} \cdot \epsilon \cdot \mathcal{L}}, \tag{3.1}$$

where $N^X_{measured}$ is the measured number of events for the X_{th} production mode in the observed data, $\mathcal{A}$ and ϵ are the theoretical acceptance and detector reconstruction efficiency, respectively, calculated using simulations, and $\mathcal{L}$ is the luminosity of the dataset. Similarly, the signal strength modifier, μ_X is defined as:

$$\mu_X = \frac{N^X_{measured}}{N^X_{expected}} = \frac{N^X_{measured}}{\mathcal{A} \cdot \epsilon \cdot \mathcal{L} \cdot \sigma^X_{expected}} = \frac{\sigma^X_{measured}}{\sigma^X_{expected}}, \tag{3.2}$$

where $\sigma^X_{expected}$ is the predicted cross-section of the X_{th} production mode.

These measurements are also extended using the Simplified Template Cross-Section (STXS) framework [44]. Within this framework, cross-section measurements are carried out in small regions or 'bins' of phase space for production mode. The phase space bin definition used in this analysis are described in Section 3.2.1. For this framework, the measured cross-section for bin i for production mode X ($\sigma^{X,i}_{\text{measured}}$) is defined as:

$$\sigma^{X,i}_{\text{measured}} = \frac{N^{X,i}_{measured}}{\mathcal{A}^i \cdot \epsilon^i \cdot \mathcal{L}}, \tag{3.3}$$

where $N^{X,i}_{measured}$ is the measured number of events and $\mathcal{A}^i$ and ϵ^i are the theoretical acceptance and detector efficiency, respectively, for the given phase-space region.

The results are then interpreted to provide constraints on the Higgs boson coupling. This is achieved using the κ-framework [44]. Multiplicative modifiers are introduced for every Higgs boson coupling in the SM Lagrangian and their impact on the leading order cross-section is propagated through. Cross-section measurements are subsequently used to constrain these multiplicative modifiers.

As the κ-framework does not capture all possible deviations that BSM physics might create, additional interpretations of the results are carried out by placing limits on the Wilson coefficients of an Effective Field Theory (EFT) [44].

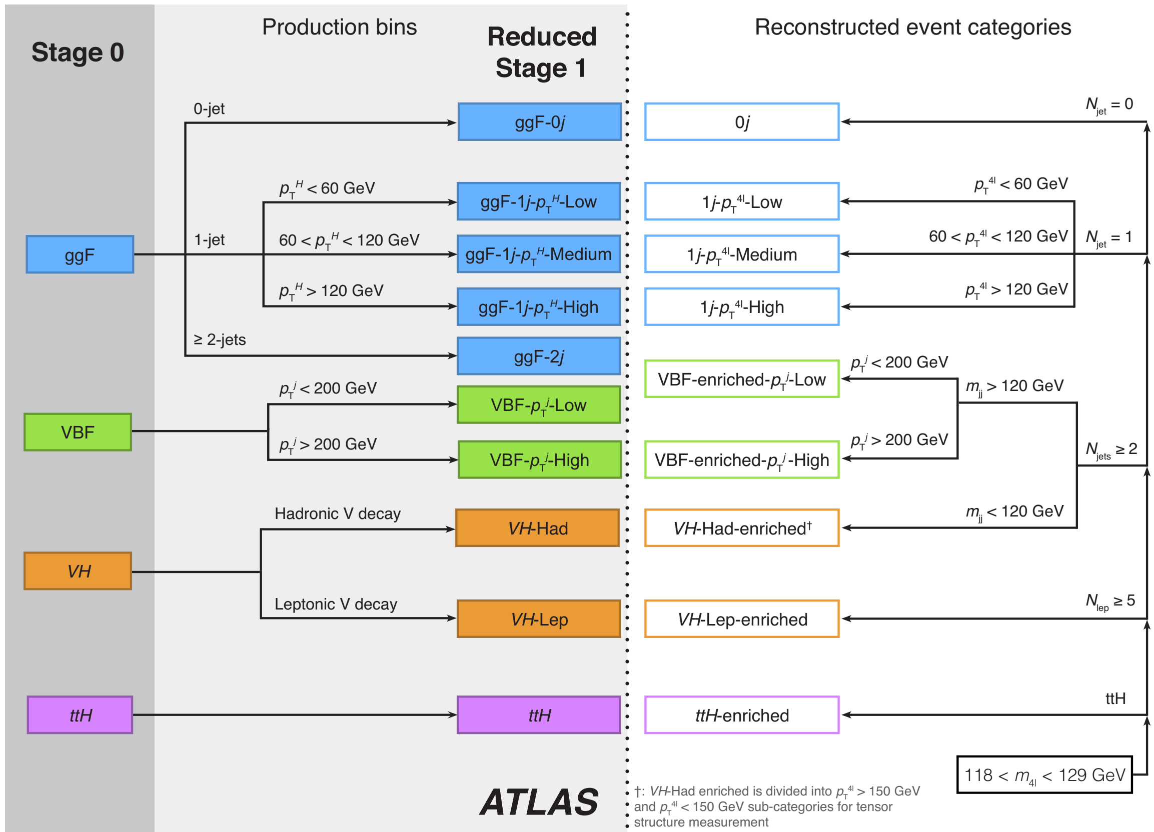

Figure 3.3: The phase-space regions (production bins) for the measurement of the Higgs boson production cross sections defined for two different stages and the corresponding reconstructed event categories.

3.2.1 Simplified Template Cross-Section Framework

The Simplified Template Cross-Section Framework [44] is an extension of the Higgs boson coupling measurements performed at the end of LHC Run 1 [54–56]. Within this framework, the cross-section measurements are performed in several dedicated mutually exclusive regions of the phase space based on the production process. This framework effectively measures the differential cross-section with irregular bin definitions for a production mode. These differential bins, or regions, are referred to as 'production bins' hereafter. The bins are designed to minimize the dependency of the results on theoretical assumptions, maximize experimental sensitivity and isolate the impact of any BSM physics. As such, STXS bins are defined in stages with varying levels of granularity. The two sets of bin definitions used for this analysis are shown in Figure 3.3 (shaded area).

In 'Stage 0' of the STXS framework, the production bins are defined to match the major production modes: gluon–gluon fusion (ggF), vector boson fusion (VBF) and associated production with vector bosons (VH, where $V = W$ or Z) or top quark pairs (ttH). Due to similar acceptance and limited sensitivity, bbH and tH processes are merged with the ggF and the ttH bin definitions, respectively. As opposed to the Stage-0 production bins described in Ref. [44], the VH events with a hadronically decaying vector boson V are included in the VH production bin rather than in the ggF or VBF bins. The definition also limits the Higgs boson to a rapidity of $|y_H| < 2.5$. Higgs bosons produced at larger rapidities almost always decay into stable particles that are outside the detector acceptance. The inclusivity of this definition is designed to have a small statistical uncertainty, but it is affected by theoretical modelling uncertainties.

A more exclusive and granular set ('Stage 1') of STXS bins is defined in Ref. [44]. This set of definitions greatly limits the impact of theoretical uncertainties and probes the phase space with the largest sensitivity to BSM physics. However, it is intended to be used with the combination of results from all measurable Higgs boson decay channels with the full Run 2 LHC dataset. As such, all Stage 1 bins cannot be measured within the $H \to ZZ^* \to 4\ell$ channel with the available dataset. Therefore, a reduced version ('Reduced Stage 1') [51], which matches the sensitivity of this analysis, is defined.

This reduced version is optimized using a 'tick-tock' methodology. This method starts with the Stage 0 bins, reconstructed categories defined in Ref. [52] and the statistical method described in Section 3.8.2. For the tick part of the cycle, the inclusive signal is split into production bins which follow the Stage 1 template. This splitting is continued until the expected statistical error on the measured cross-section for the split production bins exceeds 100%. A specific example of this is the VBF bin being split into two bins with the leading jet p_{T} below and above 200 GeV, with the lower p_{T} bin being a sum of five Stage 1 VBF bins. Afterwards, for the tock part of the cycle, the reconstructed categories are optimized by creating new sub-categories or introducing new machine learning observables to reduce the expected error. For this example, the VBF-enriched reconstructed category is split into two bins with the p_{T} of the reconstructed leading jet below and above 200 GeV. After the optimization, if the expected statistical error is reduced below 100%, the production binning split is accepted. This cycle is repeated until no more production bin splits are accepted. In cases where multiple competing splittings are possible, the ones that target processes with smaller predicted cross-sections are prioritized. For bins targeting BSM signatures, the upper limit on the statistical error is relaxed.

For Reduced Stage 1 (RS1), the bins are defined based on the number of jets in the final state, transverse momentum of the leading jet (p_{T}^{j1}), transverse momentum of the Higgs boson (p_{T}^{H}) and decay of the associated bosons. All particles used for the categorization are defined at particle level. Particle-level jets are built from all stable particles (all particles with $c\tau > 10$ mm) including neutrinos, photons and leptons from hadron decays or those produced in the shower. All Higgs boson decay products, as well as the leptons and neutrinos from the decays of the associated V bosons, are not included in the particle-level jets, while the decay products from hadronically decaying associated V bosons are included. The anti-k_t jet reconstruction algorithm [57, 58] with a radius parameter $R = 0.4$ is used and jets are required to have $p_{\mathrm{T}} > 30$ GeV.

In the RS1 scheme, the Stage 0 ggF bin is divided into categories with zero, one and at least two jets in the final state. The one jet bin is further divided into three bins with p_{T}^{H} less than 60 GeV, between 60 GeV and 120 GeV, and greater than 120 GeV. These bins are correspondingly denoted as ggF-0j, ggF-1j-p_{T}^{H}-Low, ggF-1j-p_{T}^{H}-Med, ggF-1j-p_{T}^{H}-High and ggF-2j. The splitting according to jets and p_{T}^{H} is designed to probe the QCD structure of the SM, while the highest p_{T}^{H} bin is sensitive to potential BSM contributions.

The VBF bin is split into two bins with p_{T}^{j1} below and above 200 GeV (VBF-p_{T}^{j}-Low and VBF-p_{T}^{j}-High, respectively). The first bin is expected to be dominated by SM production while the latter one is sensitive to potential BSM contribution. For VH production, hadronically (VH-Had) and leptonically (VH-Lep) decaying vector bosons are considered as separate bins. Due to its limited sensitivity, ttH is not split further in this scheme.

Figure 3.3 also summarizes the corresponding reconstructed categories that target each production bin. Details of these categories are outlined in Section 3.5.

3.2.2 Interpretation in the κ framework

The couplings measurements are interpreted within a leading-order-motivated κ-framework [59, 60]. A set of coupling modifiers $\vec{\kappa}$ is introduced to parametrize possible deviations from the SM predictions of the Higgs boson couplings to SM bosons and fermions. The framework assumes that the data originate from a single CP-even Higgs boson state and the tensor coupling structure of the SM for its interactions. Only the coupling strengths are allowed to be modified by the BSM physics. The Higgs boson width is assumed to be small enough that the narrow-width approximation is valid. This allows the Higgs boson production and the decay to be factorized: $\sigma \cdot BR\ (i \to H \to f) = \sigma_i(\vec{\kappa}) \cdot \Gamma_f(\vec{\kappa})/\Gamma_H(\vec{\kappa})$ where σ_i is the production cross section via the initial state i, BR and Γ_f are the branching ratio and partial decay width for the decay into the final state f, respectively, and Γ_H is the total width of the Higgs boson. For a Higgs boson production or decay process via a given coupling j, a coupling-strength modifier κ_j is defined as $\kappa_j^2 = \sigma_j/\sigma_j^{\text{SM}}$ or $\kappa_j^2 = \Gamma_j/\Gamma_j^{\text{SM}}$.

3.2.3 Interpretation in the Effective Field Theory framework

In order to study potential contributions from BSM physics, an effective field theory approach [20] is taken in this analysis. Within this approach, higher order operators with modifiable coupling parameters are included with the SM Lagrangian. The additional operators modify both the predicted cross-section and distribution of various observables. Fitting the observed data as a function of these couplings parameters allows us to infer potential contributions from different operators.

While these higher-order operators are not renormalizable, these offer a novel way to probe potential contributions from new physics. Most BSM QFT models with new heavy particles will map to a subset of all potential higher order operators in the low-energy limit. As such, a suitable eigenbasis of these operators provides a relatively model-independent method to probe a large class of BSM theories.

For this analysis, the Higgs characterization model [61] is used. This model only includes operators constructed out of physical fields of order 6 that modify the Higgs boson interaction. It is defined as,

$$\begin{aligned}
\mathcal{L}_0^V = \Bigg\{ & \kappa_{\text{SM}} \left[\frac{1}{2} g_{HZZ} Z_\mu Z^\mu + g_{HWW} W_\mu^+ W^{-\mu} \right] \\
& - \frac{1}{4} \left[\kappa_{Hgg} g_{Hgg} G_{\mu\nu}^a G^{a,\mu\nu} + \tan\alpha \kappa_{Agg} g_{Agg} G_{\mu\nu}^a \tilde{G}^{a,\mu\nu} \right] \\
& - \frac{1}{4} \frac{1}{\Lambda} \left[\kappa_{HZZ} Z_{\mu\nu} Z^{\mu\nu} + \tan\alpha \kappa_{AZZ} Z_{\mu\nu} \tilde{Z}^{\mu\nu} \right] \\
& - \frac{1}{2} \frac{1}{\Lambda} \left[\kappa_{HWW} W_{\mu\nu}^+ W^{-\mu\nu} + \tan\alpha \kappa_{AWW} W_{\mu\nu}^+ \tilde{W}^{-\mu\nu} \right] \Bigg\} \mathcal{X}_0.
\end{aligned} \tag{3.4}$$

Additional terms in the Lagrangian involving direct Higgs boson coupling to fermions are not considered since the current analysis is not sensitive to effects of these operators. The model assumes that there are no new BSM particles below a energy scale Λ, which is set to 1 TeV for this analysis. This choice is driven by the fact that direct searches for new heavy particles have typically excluded mass ranges up to this scale.

The notation used mostly follows Ref. [61], where the spin 0 boson state is described by $\mathcal{X}_0$. The difference is that the dimensionless coupling parameters κ are redefined by dividing them by $\cos\alpha$, where α is the mixing angle between the 0^+ and 0^- CP states. This implies CP-violation for $\alpha \neq 0$ and $\alpha \neq \pi$.

For this measurement, only the operator terms with coupling parameters κ_{HVV}, κ_{AVV} and κ_{Agg} are considered. These terms describe the CP-even (scalar) and CP-odd (pseudo-scalar) BSM interaction with vector bosons and the CP-odd BSM interaction with gluons, respectively. The BSM couplings are assumed to be the same for W and Z bosons (i.e. $\kappa_{HWW} = \kappa_{HZZ} \equiv \kappa_{HVV}$ and $\kappa_{AWW} = \kappa_{AZZ} \equiv \kappa_{AVV}$). The value of α is arbitrarily set to $\pi/4$ such that the CP-odd couplings can be more simply denoted by $\kappa_{AVV}\ \tan\alpha \Rightarrow \kappa_{AVV}$ and $\kappa_{Agg}\ \tan\alpha\ \Rightarrow \kappa_{Agg}$.

In this model, SM Higgs boson predictions are obtained by setting $\kappa_{\rm SM} = 1$ and $\kappa_{Hgg} = 1$ with the values of the BSM couplings being zero.

3.3 Data and Monte Carlo Samples

3.3.1 Data Samples

The data collected during the first half of Run 2, running from 2015 to 2016, are used for this analysis. During this period, the LHC delivered 42.7 fb^{-1} of data, of which ATLAS collected 39.5 fb^{-1}. This yields an overall collection efficiency of 92%. Data quality requirements, such as requiring stable beam conditions and requiring all ATLAS sub-detectors be fully operational, are further applied. This yields 36.1 fb^{-1} of data available for this analysis. The relatively large part of the collected dataset is not used, as the toroidal magnet was not operational for a few data collection runs.

In addition to hard-scatter events, multiple other proton-proton interactions occur in a single bunch-crossing, which is referred to as pileup. The average pileup interactions per bunch crossing is 22.9 and Figure 3.4 shows the luminosity averaged pileup interactions per event for this dataset [38].

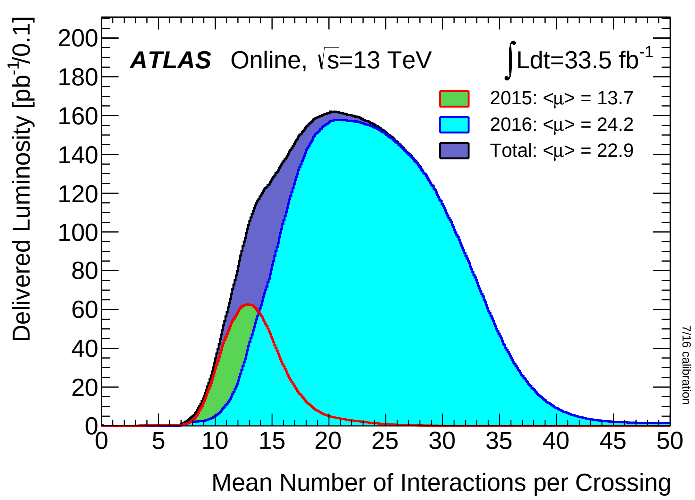

Figure 3.4: The luminosity-weighted distribution of the mean number of interactions per crossing for the combined 13 TeV data collected during 2015 and 2016 runs [38].

3.3.2 Monte Carlo Samples

Monte Carlo simulation of different processes is extensively used for optimizing the event selection, estimating contributions from background, training the BDTs, and modelling the signal response. A brief description of these samples is presented below.

The production of the SM Higgs boson via the ggF, VBF and VH (including $gg \to ZH$) production mechanisms is modelled with the POWHEG-BOX v2 Monte Carlo (MC) event generator [62, 63] interfaced to EvtGen [64]. The PDF4LHC next-to-leading-order (NLO) set of parton distribution functions (PDF) is used [65] for the central prediction. The gluon–fusion Higgs boson production is accurate to next-to-next-to-leading order (NNLO) for the strong coupling. This is achieved using the POWHEG method for merging the NLO Higgs + jet cross section with the parton shower, and the MiNLO method [66] to simultaneously achieve NLO accuracy for inclusive Higgs boson production. A reweighting procedure, using the Higgs boson rapidity distribution, is also applied using the HNNLO program [67, 68].

The matrix elements of the VBF and VH production mechanisms are calculated up to NLO in QCD. For VH production, the MiNLO method is used to merge 0- and 1-jet events [69]. The $gg \to ZH$ contribution is modelled at leading order (LO) in QCD.

The production of a Higgs boson in association with a top (bottom) quark pair is simulated at NLO with MadGraph5_aMC@NLO [70, 71] v2.2.3 (v2.3.3), using the CT10nlo PDF set [72] for ttH production and the NNPDF23 PDF set [73] for bbH production.

For the ggF, VBF, VH and bbH production mechanisms, the PYTHIA 8 [74] generator is used for the $H \to ZZ^* \to 4\ell$ decay as well as for parton showering and simulation of multiple partonic interactions. The AZNLO tune is employed [75]. For the ttH production mechanism, the Herwig++ [76] generator is used with the UEEE5 tune [77]. All signal samples are simulated for the Higgs boson assuming a mass $m_H = 125.00$ GeV. Wherever relevant, the signal mass distribution is shifted to the reference value of 125.09 GeV, to match the experimentally measured Higgs Boson mass from the Run 1 ATLAS and CMS mass combination [27, 28].

The Higgs boson production cross sections and decay branching ratios, as well as their uncertainties, are taken from Ref. [44]. The ggF production is calculated with next-to-next-to-next-to-leading order (N^3LO) accuracy in QCD and has NLO electroweak (EW) corrections applied. For VBF production, full NLO QCD and EW calculations are used with approximate NNLO QCD corrections. The VH production is calculated at NNLO in QCD and NLO EW corrections are applied. The ttH and bbH processes are calculated to NLO accuracy in QCD. The branching ratio for the $H \to ZZ^* \to 4\ell$ decay with $m_H = 125.09$ GeV is predicted to be 0.0125% [78] in the SM using PROPHECY4F [79, 80], which includes the complete NLO QCD and EW corrections, and the interference effects between identical final-state fermions. Table 1.4 summarizes the production cross sections and branching ratios for the $H \to ZZ^* \to 4\ell$ decay for $m_H = 125.09$ GeV.

Additional ggF, VBF and VH signal samples with different values of the BSM couplings κ_{Agg}, κ_{HVV} and κ_{AVV} are generated with MadGraph5_aMC@NLO and used for parameterizing the cross-section as a function of the κ modifier to the Higgs boson coupling. The ggF simulation includes samples at NLO QCD accuracy for zero, one and two additional partons merged with the FxFx merging scheme [70, 81], while the VBF and VH simulations are accurate to LO in α_s. Equivalent VBF and VH processes are also generated at NLO QCD accuracy and used to estimate the relative uncertainties of higher-order QCD effects as a function of the BSM coupling parameters.

The ZZ^* continuum background from quark–antiquark annihilation is modelled using SHERPA 2.2.2 [82–84], which provides a matrix element calculation accurate to NLO in α_s for 0-, and 1-jet final states and LO accuracy for 2- and 3-jet final states. The jet merging is performed with the SHERPA parton shower [85] using the ME+PS@NLO prescription [86]. The NLO EW corrections are applied as a function of the invariant mass of the ZZ^* system m_{ZZ^*} [87, 88].

The gluon-induced ZZ^* production is modelled by GG2VV [89] at LO in QCD. The higher-order QCD effects for the $gg \to ZZ^*$ continuum production have been calculated for massless quark loops [90–92] in the heavy top-quark approximation [93], including the $gg \to H^* \to ZZ$ processes [94, 95]. The simulated LO samples are scaled by the k-factor of 1.7 ± 1.0, defined as the ratio of the higher-order and the leading-order cross section predictions.

The WZ background is modelled using POWHEG-BOX v2 interfaced to PYTHIA 8 and EVT-GEN v1.2.0 [64] for improved simulation of the bottom and charm hadron decays. The triboson backgrounds ZZZ, WZZ, and WWZ with four or more prompt leptons are modelled using SHERPA 2.1.1.

The simulation of the $t\bar{t}Z$ events with both top quarks decaying semi-leptonically and the Z boson decaying leptonically is performed with MADGRAPH interfaced to PYTHIA 8 and the total cross section is normalized to the prediction which includes the two dominant terms at both LO and NLO in a mixed perturbative expansion in the QCD and EW couplings [96].

The modelling of events containing a Z boson with associated jets is performed using the SHERPA 2.2.2 generator. Matrix elements are calculated for up to two partons at NLO and four partons at LO using the COMIX [83] and OPENLOOPS [84] generators and merged with the SHERPA parton shower [85] using the ME+PS@NLO prescription [86]. The NNPDF3.0 NNLO PDF set is used in conjunction with dedicated parton shower model parameter tuning developed by the SHERPA authors. Simulated samples are normalized to the data-driven estimate described in Section 3.6.

The $t\bar{t}$ background is modelled using POWHEG-BOX v2 interfaced to PYTHIA 6 [97] for parton showering, hadronization, and the underlying event and to EVTGEN for properties of the bottom and charm hadron decays.

Generated events are processed through the ATLAS detector simulation [98] within the GEANT4 framework [99] and reconstructed the same way as the data. Additional pp interactions in the same and nearby bunch crossings (pileup) are included in the simulation. The simulation samples are re-weighted to reproduce the observed distribution of the mean number of interactions per bunch crossing in the data.

Validation and Higher Order Corrections for $qq \to ZZ^*$ Process

As mentioned in Section 3.3.2, higher order k-factors are applied to $qq \to ZZ^*$ processes to match the best available predictions. This has the benefit of improving the predicted yields and modelling of different observed variables. Extensive validation of the k-factors and the simulation of these processes is carried out by comparing predictions from other generators. For the $H \to ZZ^* \to 4\ell$ analysis, only the region close to the reconstructed Higgs boson mass is needed. However, this region has significant contributions from the interference between the single resonant Z production and the high mass double on-shell Z production. Moreover, sizable contributions also arise from the mis-reconstruction of high mass events with the Z decaying into τ leptons, which subsequently decay into electrons or muons. As such, the validation for the k-factors and the simulation of these events is carried out in the entire mass region.

For this comparison, the fiducial phase space defined for the ATLAS Higgs ZZ analysis [52, 100] is used. The selection criteria are summarized in Table 3.1. This fiducial space is sufficiently inclusive to

Table 3.1: Fiducial phase space definition for generator comparison of $ZZ^* \to 4\ell$ final states. The primary Z boson (Z_1) is defined to be the same-flavour opposite-charge lepton pair with invariant mass $m(\ell^+, \ell^-)$ closest to the Z PDG mass $m_Z = 91.1876$ GeV. The secondary Z boson (Z_2) is a remaining same-flavour opposite-charge leptons pair with $m(\ell^+, \ell^-)$ next-closest to m_Z.

Lepton Selection	
Electrons	$E_\text{T} > 7$ GeV, $\lvert\eta\rvert < 2.47$
Muons	$p_\text{T} > 6$ GeV, $\lvert\eta\rvert < 2.7$
Lepton p_T requirement	$p_\text{T}^3 > 10$ GeV, $p_\text{T}^2 > 15$ GeV, $p_\text{T}^1 > 20$ GeV
Lepton separation	$\Delta R(\ell, \ell) > 0.1$ for same flavour $\Delta R(\ell, \ell') > 0.2$ for different flavour

Event Selection		
J/Ψ veto	no same-flavour opposite-charge lepton pair with $m(\ell^+, \ell^-) < 5$ GeV	
$m(Z_1)$ requirement	$50 \text{ GeV} < m(Z_1) < 106$ GeV	
Sliding mass selection	$m(4\ell) < 140$ GeV	$12 \text{ GeV} < m(Z_2) < 115$ GeV
	$140 \text{ GeV} < m(4\ell) < 190$ GeV	$12 + \left(\frac{m(4\ell)}{\text{GeV}} - 140\right) \cdot 0.76 < \frac{m(Z_2)}{\text{GeV}} < 115$
	$m(4\ell) > 190$ GeV	$50 \text{ GeV} < m(Z_2) < 115$ GeV

include off-shell Z decays.

The baseline generator for the $qq \to ZZ^* \to 4\ell$ process is SHERPA [101]. SHERPA is a parton shower Monte Carlo generator, which can simulate hard scatter events and match them to a parton shower. NLO+PS matching is employed for different jet multiplicities which are then merged into an inclusive sample using the MEPS@NLO approach. For NLO matrix elements (ME), virtual QCD corrections are provided by the OpenLoops library. This allows the $qq \to ZZ^* \to 4\ell$ process to be simulated up to NLO accuracy for 0- and 1-jet events, and LO accuracy for 2- and 3-jet final states. The setup used for simulation is provided by the SHERPA authors and includes a tuning based on NNPDF3.0 NNLO PDF.

POWHEG-BOX [62] is used for comparison for this process. It provides a general framework for calculating processes to NLO accuracy in QCD and interfacing them to parton showering code using the POWHEG method. Hence, this generator simulates $qqZZ$ to NLO accuracy. The final state includes all interference effects from $Z/\gamma*$ and off-shell singly resonant amplitudes. PYTHIA 8 with the AZNLO [102] tune and the CTEQ6L1 [103] PDF is used for the showering. The EVTGEN [64] program is employed to ensure the proper decay of heavy quarks. The factorization and renormalization scale are dynamically set to the mass of the diboson system.

Predictions from each generator without any modification are compared as the initial baseline. Figure 3.5 shows a comparison for different variables. As the four-lepton invariant mass system is not sensitive to higher order (HO) QCD effects, good agreement is observed. In mass ranges where interference effects from $Z/\gamma*$ and off-shell singly resonant amplitudes are large, differences up to 10% are observed. An overall normalization difference is attributed to QCD corrections which increase the predicted cross-section and are partially included in SHERPA. As expected, observables sensitive to QCD effects, such as the transverse momentum of the four-lepton system or the ϕ distance between the two Z bosons, show differences at the tail-end of the respective distributions. Differences in the number of jets are due to SHERPA modelling higher jet multiplicity at matrix-element level rather than through using a parton shower.

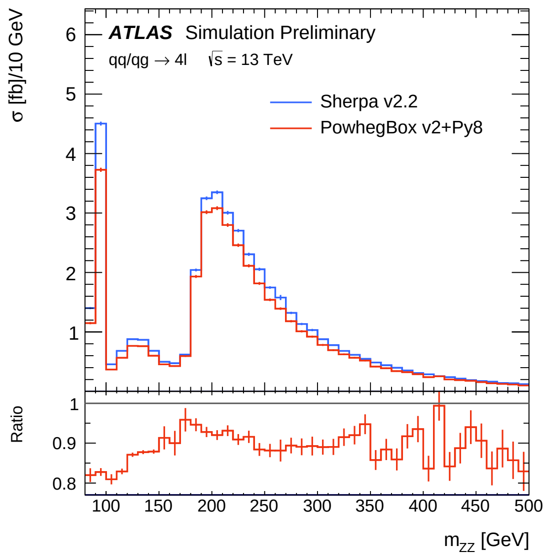

(a) Four-lepton invariant mass

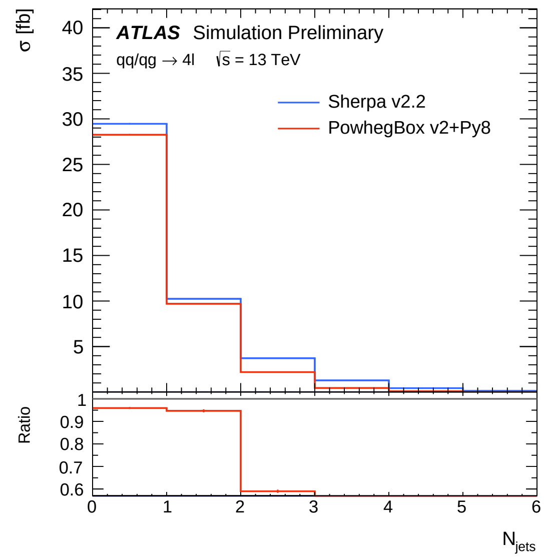

(b) Jet multiplicity

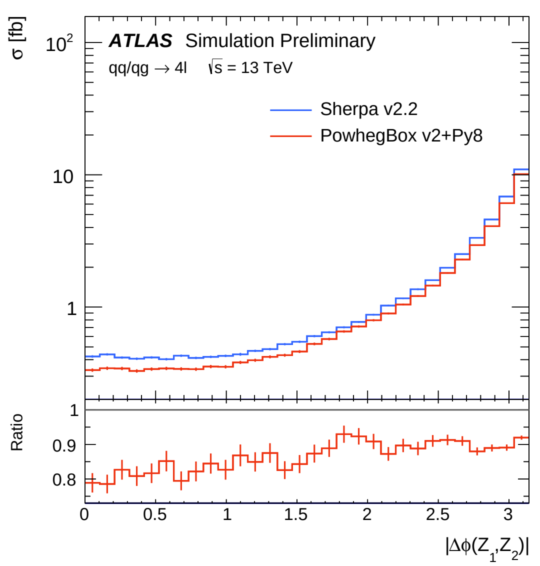

(c) ϕ distance between the two Z bosons

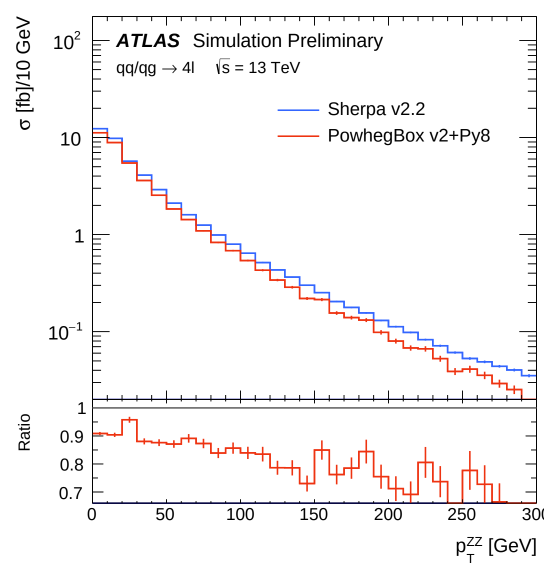

(d) Transverse momentum of the four-lepton system

Figure 3.5: Comparison of shapes normalized to the samples' cross section as predicted by POWHEG-BOX and SHERPA. The ratio is taken with respect to the SHERPA prediction. Distributions comparing a) four-lepton invariant mass, b) jet multiplicity, c) ϕ distance between the two Z bosons and d) transverse momentum of the four-lepton system are shown.

In addition to QCD effects, HO electroweak corrections can significantly affect the generator prediction. Example Feynman diagrams leading to these corrections for the $qqZZ$ process are shown in Figure 3.6. Recent calculations [87, 88] have provided k-factors individually for same-flavour and different-flavour final states. Figure 3.7 compares the baseline Sherpa prediction with those including these HO effects. The k-factors are calculated as a function of $m(4\ell)$ and special care is taken to match the electroweak scheme used in Sherpa and the calculation. Additionally, as final state radiation is already modelled by the showering algorithm, the k-factors calculation specifically excludes these contributions to avoid double counting.

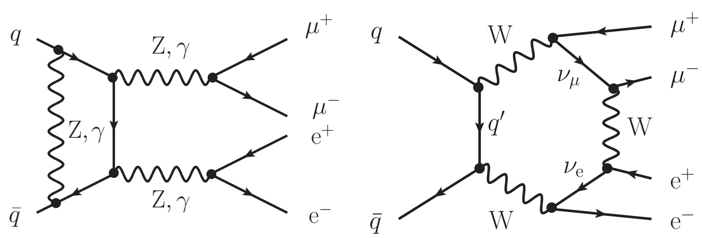

Figure 3.6: Feynman diagrams for higher order electroweak correction to the $qqZZ$ process. Adapted from [87, 88].

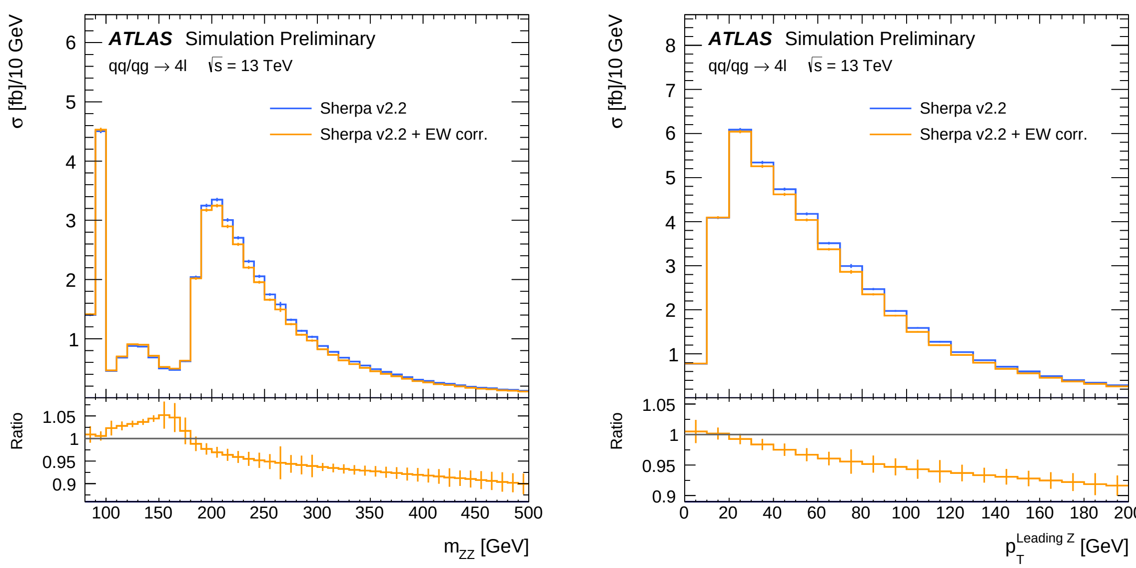

(a) Four-lepton invariant mass

(b) Transverse momentum of the leading Z bosons

Figure 3.7: Comparison of the default Sherpa prediction and that with higher order electroweak effects taken into account. The reweighting is based on per final state k-factors calculated for the four lepton invariant mass [87, 88]. Distributions comparing a) four-lepton invariant mass and b) transverse momentum of the leading Z bosons are shown.

A full comparison of differential cross section as predicted by Sherpa and POWHEG-BOX is shown in Figure 3.8. Both generator predictions are corrected for HO electroweak effects. Additionally, predictions from POWHEG-BOX are reweighted to improve the prediction accuracy from NLO to approximately NNLO QCD accuracy [104], allowing it to match SHERPA accuracy for up to two jets. These corrections are based on k-factors calculated in an inclusive setup but differential in the four-lepton invariant mass. With these corrections, the predictions from the two generators show better agreement, with the inclusive cross-section matching almost exactly. Although much smaller, variables sensitive to QCD effects still show differences at the tail-ends of the respective distributions.

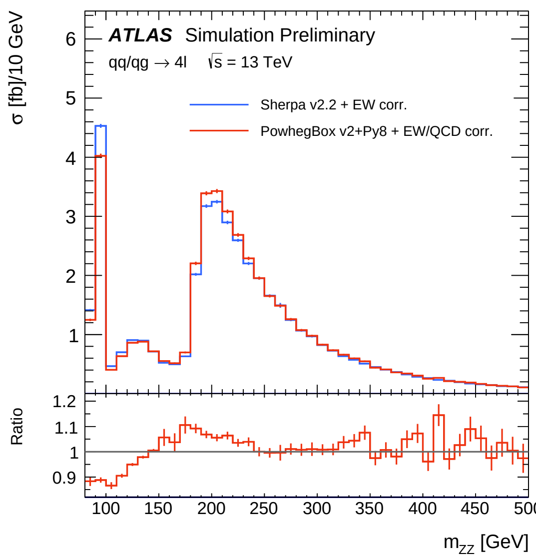

(a) Four-lepton invariant mass

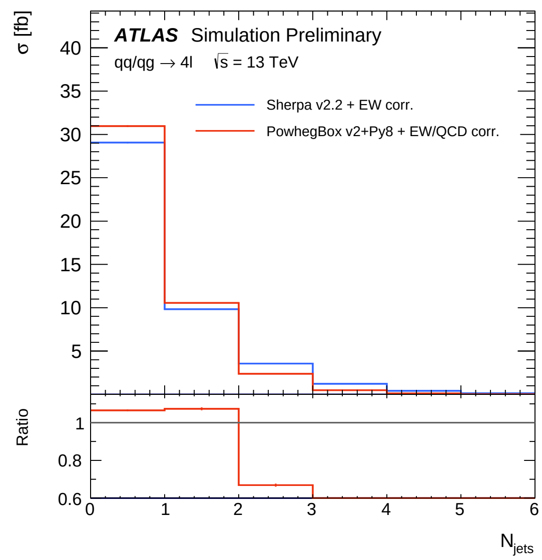

(b) Jet multiplicity

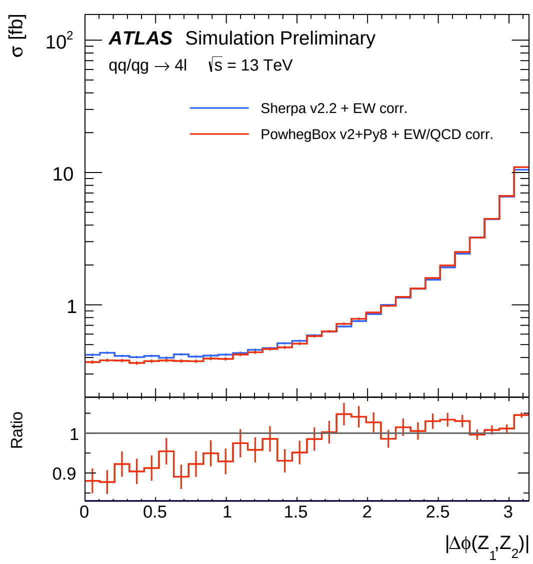

(c) ϕ distance between the two Z bosons

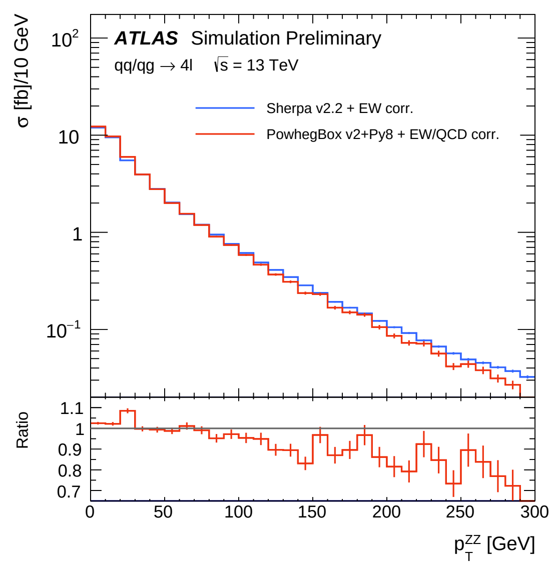

(d) Transverse momentum of the four-lepton system

Figure 3.8: Differential cross section predictions of SHERPA and POWHEG-BOX. Both generator predictions are corrected for higher-order electroweak effects and additional QCD effects are included for POWHEG-BOX. The ratio is taken with respect to the SHERPA prediction. Distributions comparing a) four-lepton invariant mass, b) jet multiplicity, c) ϕ distance between the two Z bosons and d) transverse momentum of the four-lepton system are shown.

Validation and Higher Order Corrections for $gg \to ZZ^*$ Process

The $gg \to ZZ^*$ process is a part of the NNLO QCD corrections to the diboson production in a proton-proton collision. However, due to the purely gluonic initial state, these calculations are computed separately and added to other NNLO predictions. Depending on the four lepton invariant mass range, the $ggZZ$ process is dominated by the continuum ZZ^* production or the s-channel resonant production mediated by the Higgs boson. Feynman diagrams for these processes are shown in Figure 3.2 and Figure 1.4 respectively. The two processes interfere and have large effects in the high four lepton invariant mass region.

For this analysis, the different parts of $gg \to ZZ^*$ production are modelled separately. As stated in Section 3.3.2, the resonant production forms part of the Higgs boson signal predictions. The continuum production is simulated using the GG2VV [89] program. For validation of the continuum production, the fiducial phase space defined in Table 3.1 is used [101].

The GG2VV [89] program calculates the matrix elements for this process at LO. The CT10 PDF set is used and the factorization and renormalization scale are dynamically set to the mass of the diboson system. Subsequently, the events are showered using PYTHIA 8 with the A14 tune and the NNPDF2.3 LO PDF set. The EVTGEN generator is employed to ensure the proper decay of heavy quarks.

For comparison, MCFM with the CT10 NNLO PDF set and SHERPA with the CT10 NLO PDF set are also used to generate this process. For both generators, matrix elements are calculated at LO with the factorization and renormalization scales dynamically set to half of the mass of the diboson system. SHERPA predictions are further scaled by 0.91 to account for the G_μ electroweak scheme. By default, SHERPA uses boson masses and $\alpha_{\text{QED}}\,(m_Z)$ and calculates the remaining parameters from using LO relations. However, using the G_μ electroweak scheme introduces differences to $\alpha_{\text{QED}}\,(m_Z)$ or leads to deviations from the PDG value for other electroweak parameters. SHERPA partially includes NLO QCD effects as it models one additional parton at matrix element level.

Recent calculations [105] also allow this process to be modelled at NLO accuracy but the predictions are limited to the $2e2\mu$ final state. The qg initiated diagrams involving two loops are omitted due to the unavailability of current methods to calculate them. The impact of this is expected to be small as it is suppressed by the gluonic-quark luminosity ratio. Despite these, this setup is also used for validation of the baseline $ggZZ$ simulation. An initial version of this process is implemented in POWHEG-BOX. Events generated through this process are showered using PYTHIA 8 with the A14 tune and the NNPDF2.3 LO PDF set. The EVTGEN [64] program is employed to ensure the proper decay of heavy quarks. The factorization and renormalization scales are dynamically set to the mass of the diboson system.

A large enhancement in the predicted cross-section is expected for the $gg \to ZZ^*$ continuum production when HO QCD effects are included. NLO corrections have been calculated for massless quark loops [90–92] and in the heavy top-quark approximation [93], including the $gg \to H^* \to ZZ$ processes [94, 95]. A complete calculation using all quark masses is currently not available. Based on these results, a k-factor of 1.7 with a conservative 60% systematic uncertainty is applied to all LO predictions. Despite including some HO corrections, this k-factor is also applied to the SHERPA prediction. However, it is expected that at higher diboson invariant masses SHERPA will approach full NLO calculations and include top quark mass effects.

Figure 3.9 and Figure 3.10 shows the comparison of predictions from GG2VV, MCFM and SHERPA and partial NLO QCD results using the POWHEG-BOX test version. The agreement between different

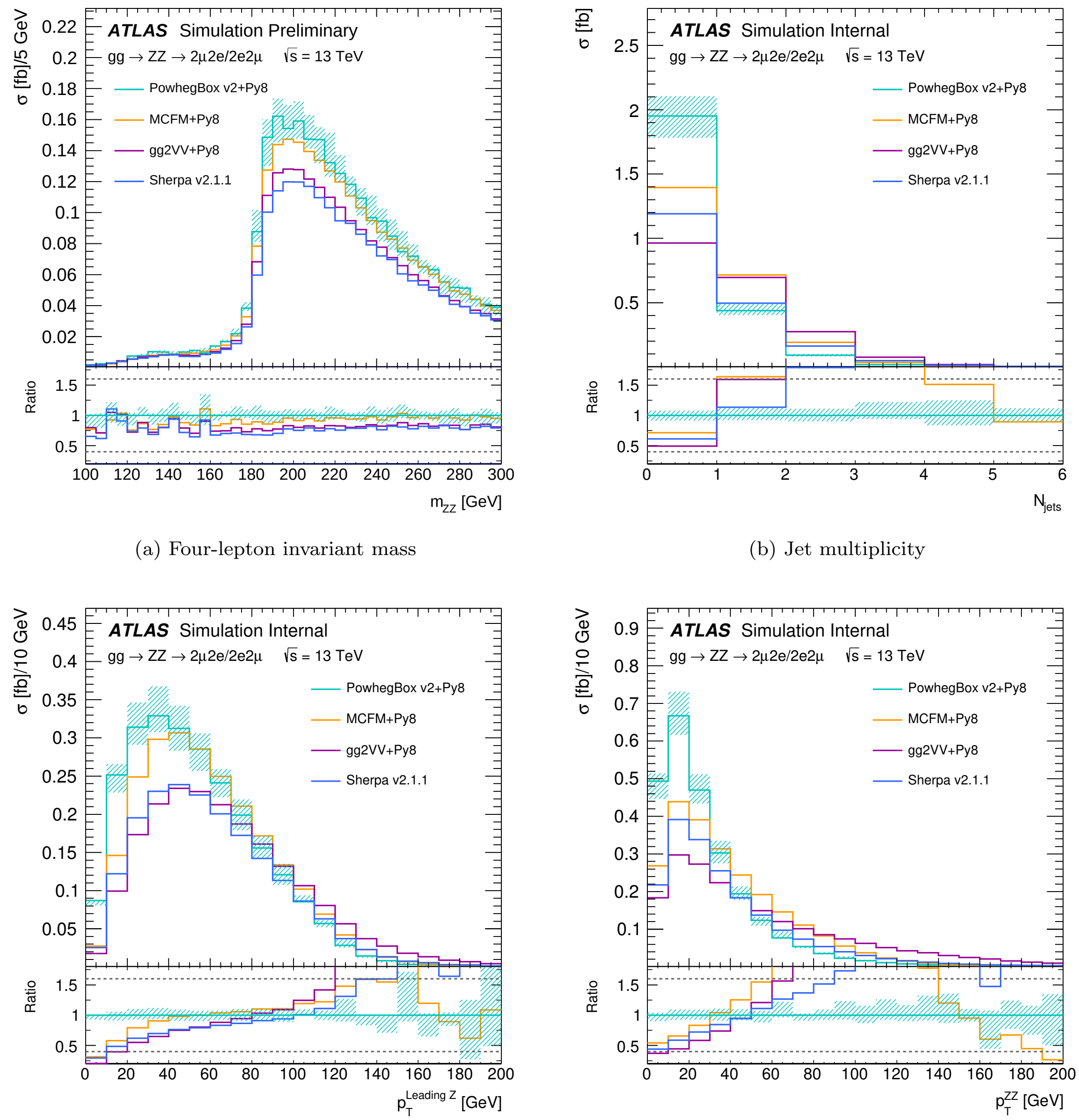

(a) Four-lepton invariant mass

(b) Jet multiplicity

(c) Transverse momentum of the leading Z boson

(d) Transverse momentum of the four-lepton system

Figure 3.9: Differential cross section predictions for the low mass region for the continuum $gg \to ZZ^*$ system in the $2e2\mu$ final state. GG2VV, MCFM and SHERPA and partial NLO QCD results using the POWHEG-BOX test version are compared. The shaded band indicates the NLO QCD scale uncertainty. The ratio is taken with respect to the POWHEG-BOX predictions. In the ratio plots, the dashed lines indicate the 60% systematic uncertainty on the applied k-factor. Distributions comparing a) four-lepton invariant mass, b) jet multiplicity, c) transverse momentum of the leading Z boson and d) transverse momentum of the four-lepton system are shown.

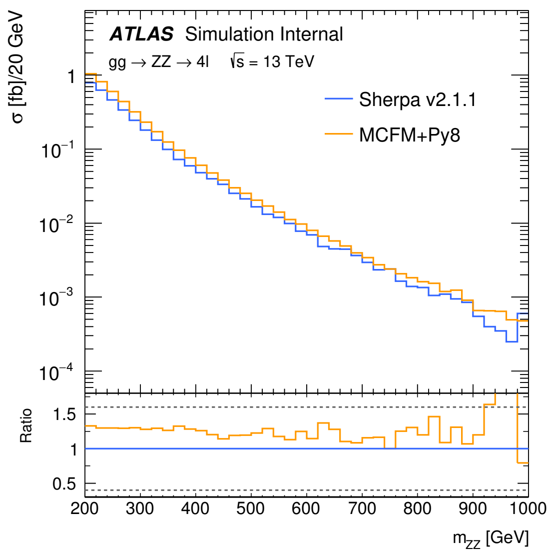

(a) Four-lepton invariant mass

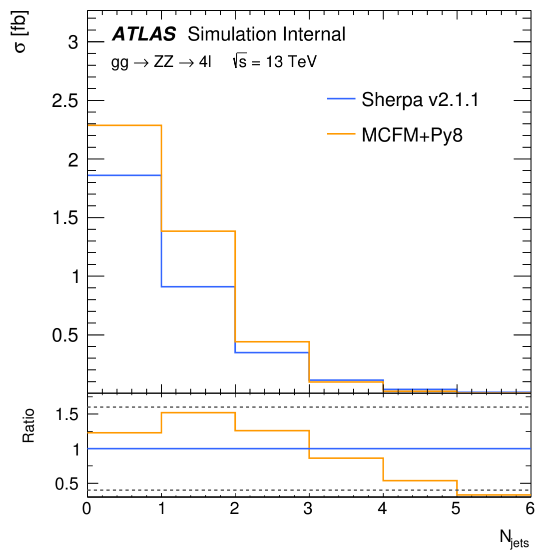

(b) Jet multiplicity

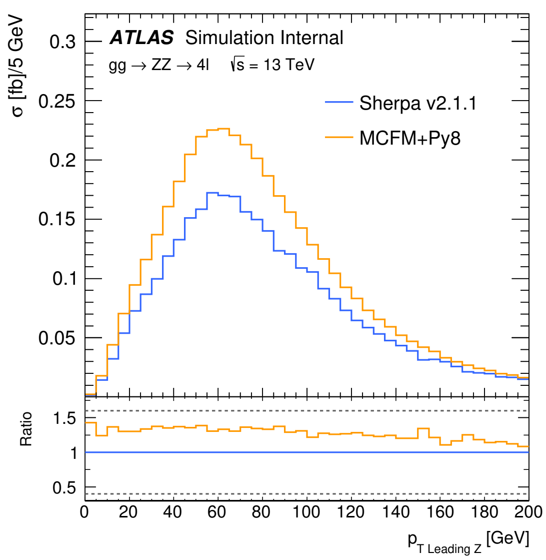

(c) Transverse momentum of the leading Z boson

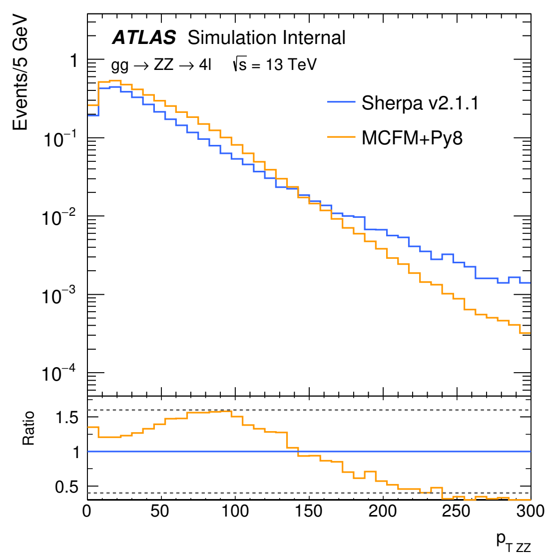

(d) Transverse momentum of the four-lepton system

Figure 3.10: Differential cross section predictions for the high mass region for the continuum $gg \to ZZ^*$ system in the $2e2\mu$ final state. MCFM and Sherpa generators are compared. The ratio is taken with respect to the Sherpa predictions. In the ratio plots, the dashed lines indicate the 60% systematic uncertainty on the applied k-factor. Distributions comparing a) four-lepton invariant mass, b) jet multiplicity, c) transverse momentum of the leading Z boson and d) transverse momentum of the four-lepton system are shown.

generators is within the conservative 60% uncertainty for the four lepton invariant mass distribution. Higgs interference and top quark mass events are relevant at diboson masses above 340 GeV and, therefore, are not included for the low mass comparisons. A mild slope dependency on m_{ZZ} is observed between SHERPA and MCFM in the high mass region as the description by SHERPA is expected to be more accurate. Other quantities like the transverse momentum of the leading Z boson or the ZZ^* system show significant deviations. In the low-mass region, differences with respect to POWHEG-BOX are attributed to missing contributions from the gq initial state. While suppressed by the quark-gluon luminosity ratio, variables sensitive to the number of jets show large variations due to missing interference effects for events with fewer jets and missing contributions to higher jet count final states. In both mass regions, differences with respect to SHERPA are attributed to it modelling the first parton at ME level.

These differences in the predictions between the generators motivates the use of data driven techniques to estimate this background. However, with the limited statistics in the sidebands for the 36.1 fb^{-1}analysis, it is not possible to develop such methods. As such, the conservative 60% systematic uncertainty is incorporated in the analysis. With a larger dataset and estimation of these backgrounds through data driven methods, it is expected that this uncertainty will not be required.

3.4 Event Selection

This section summarizes event triggering criteria, reconstruction, identification and selection of Higgs boson candidates for the $H \to ZZ^* \to 4\ell$ coupling analysis.

3.4.1 Trigger Requirements

Events collected by the ATLAS detector using single, di- and tri-lepton triggers are used in this analysis [43]. For the lowest-p_{T} single muon (electron) triggers, the p_{T} threshold ranges from 20 to 26 GeV (24 to 26 GeV) and varying isolation requirements are applied. As the instantaneous luminosity delivered by the LHC varies during the data-taking collection period, this range of p_{T} threshold is used to ensure the trigger bandwidth is within acceptable limits. To complement the lowest-p_{T} triggers, other single lepton triggers with higher thresholds but with looser or no isolation requirements are also used. Since events with multiple leptons are relatively rare, the p_{T} requirements on di- and tri-lepton triggers are comparatively lower, down to 6 GeV for the tri-muon trigger.

The combination of this set of triggers allows for high efficiency across the varying data collection and across the Higgs boson production phase space. The typical efficiencies for the different final states are approximately 0.99 ($4e$), 0.98 (4μ), 0.99 ($2e2\mu$) and 0.96 ($2\mu 2e$). The trigger efficiency as a function of the Higgs p_{T} for the full 2015 + 2016 dataset is shown Figure 3.11.

3.4.2 Particle Reconstruction and Identification

Once the event is triggered and saved to disk, a variety of algorithms are used to reconstruct and identify the leptons and jets, which are described below.

Electron

The electron reconstruction algorithm [106, 107] exploits the fact that electrons interact with the ID and then are subsequently absorbed in the ECal. As such, a sliding window of 3×5 in units of 0.025×0.025

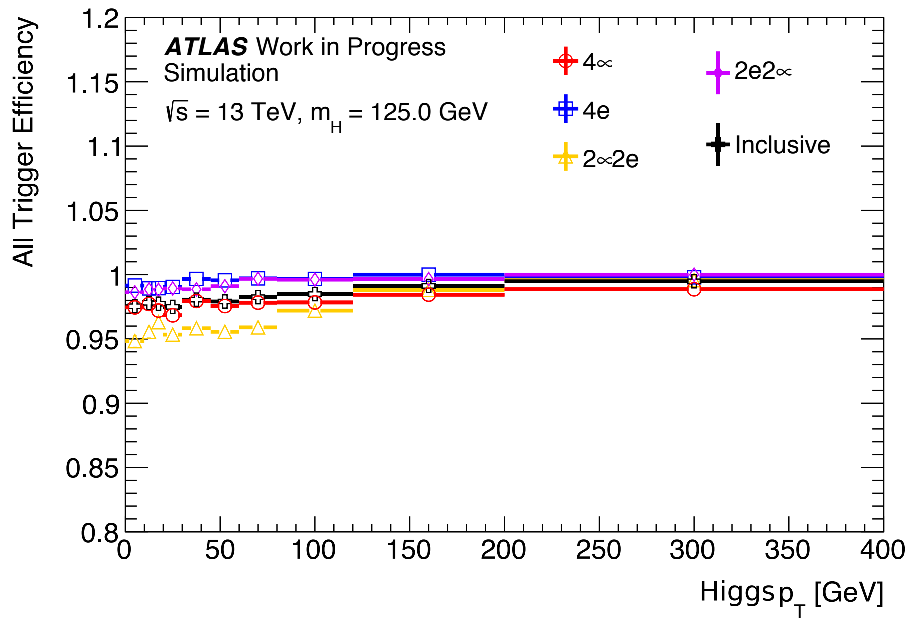

Figure 3.11: Trigger efficiency in the combined final state and in each of the four final states as a function of the Higgs boson p_{T}. Efficiencies are stable within 2% over the range of the variable, except for the $2\mu2e$ channel which shows variations up to 5%. The variation for this channel is due to the electron triggers for which the efficiency improves as p_{T} increases.

in $\eta \times \phi$ space is used to search for "seed" towers in the ECal. A clustering algorithm then sums up the nearby energy deposits around each seed tower. Tracks reconstructed in the ID [108], using the pion or electron hypothesis, are extrapolated to the ECal and matched to the EM cluster barycenter. If successfully matched, the electron cluster is then re-formed using 3×7 (5×5) longitudinal towers in the barrel (endcaps) region and the track is re-fitted using the Gaussian Sum Filter. This improves the reconstruction efficiency for electrons which undergo significant energy loss due to bremsstrahlung.

To distinguish between prompt electrons and other objects such as hadronic jets being reconstructed as electrons, a set of selection criteria based on the expected distribution of different variables is used [107]. A simple cut on the presence of IBL hits or, if no such hit is expected, a B-layer hit and total number of track hits is applied. For $|\eta| < 2.47$, variables describing the longitudinal and transverse shapes of the electromagnetic showers and track-cluster matching are combined into a likelihood discriminant. A $|\eta|$ and E_{T} dependent cut on the likelihood score is tuned to match and define a target signal efficiency working point. The $H \to ZZ^* \to 4\ell$ analysis uses the *Loose* working point, which corresponds to a 95% signal efficiency.

Electron candidates are calibrated to account for the energy loss in the detector [109].

Muon

Muon reconstruction [110] occurs independently in the ID and MS and their information is subsequently combined to create final muon candidates. Tracks in the ID are reconstructed using the standard ATLAS algorithm [108]. For each MS chamber, track segments are found through a straight line fit to the Hough transformed [111] MDT hit information. Trigger chambers provide tracking information orthogonal to the bending plane. For CSC chambers, a combinatorial search in the $\eta \times \phi$ plane is used. Afterwards, MS track candidates are constructed by combining the segments in different layers in a combinatorial search. Selection criteria based on hit multiplicity, fit quality and relative positions and angles are applied. At least two segments are required to build a track, except in the barrel–endcap transition region where a single high-quality segment can be used. Finally, the hits associated with segments in the track are used in a global χ^2 fit. A track candidate is accepted if the χ^2 of the fit satisfies certain selection criteria.

Afterwards, a combination of the ID, Calorimeter and MS information is performed [110]. Depending on the information available, this combination leads to 4 muon types. *Combined* (CB) muons are constructed through a global fit of ID and MS tracks. Most muons are reconstructed using an outside-in pattern recognition procedure, in which MS tracks are extrapolated towards the ID. This is also complemented by an inside-out procedure. *Segment-tagged* (ST) muons are ID tracks which match only to a MS segment. This algorithm is used to improve the reconstruction efficiency for low-p_{T} muons. *Calorimeter-tagged* (CT) muons are an ID track matched to a calorimeter deposit consistent with a minimum-ionizing particle. This algorithm is used to recover acceptance in the $|\eta| < 0.1$ region, where the MS is not instrumented. Finally, *Extrapolated* (ME) muons recover acceptance in the $2.5 < |\eta| < 2.7$ region where the ID coverage is limited. These muons are "MS track" which are consistent with originating from the interaction point.

The $H \to ZZ^* \to 4\ell$ analysis uses the *Loose* working point for muons. This includes all muon types with selection criteria applied to remove misreconstructed particles, such as pions or kaons decaying in-flight. These criteria consist of requiring CB muons to have ≥ 3 hits in at least two MDT layers. A loose selection on the compatibility between ID and MS momentum measurements is applied to reduce the contamination due to hadrons misidentified as muons. CT and ST muons are restricted to the $|\eta| < 0.1$ region.

Muons in data are not calibrated; rather, the MC is smeared to match the measured momentum scale and resolution [110].

Jet and B-tagging

Showers of hadrons, created during the hadronization of a coloured particle, are absorbed in the calorimeters and reconstructed as jets in the ATLAS detector. This is accomplished by using the anti-kt algorithm with a radius parameter $R = 0.4$, using positive-energy topological clusters (topoclusters) [112] of calorimeter cell energies as inputs. The three-dimensional topoclusters are built from topologically connected calorimeter cells, which are calibrated to the electromagnetic energy scale and corrected for contributions from in-time and out-of-time pileup. Due to the complex energy response of the calorimeters, an extensive calibration procedure is used to correct the hadronic energy scale and resolution [113].

For jets, the main backgrounds are pile-up jets, beam-induced jets, cosmic-ray showers and coherent calorimeter noise. To reduce jets arising from pile-up, jets with $p_{\text{T}} < 60$ GeV and $|\eta| < 2.4$ are required to pass a jet-vertex-tagger (JVT) selection [114]. JVT is a 2-dimensional likelihood method that uses the corrected jet-vertex fraction [114] and the ratio of the scalar p_{T} sum of the tracks associated to a primary vertex to the jet p_{T} in order to discriminate against pile-up jets. Jets that pass JVT, or are outside of its phase space, are then required to fulfill the *Loose* set of quality criteria to reject the beam-induced background: if any jet fails those criteria, the event is rejected [115].

To classify jets as originating from a b-hadron, a multivariate discriminant is applied to each jet [116]. This discriminant combines complementary information from stand-alone algorithms designed to provide this classification. These are based on information from the impact parameter, secondary vertex and reconstruction of b-hadron decay using tracks within a jet. The cut on the multivariate discriminant is chosen to allow for a 70% efficiency in $t\bar{t}$ events for correctly tagging a jet as originating from a b-hadron.

3.4.3 $H \to ZZ^* \to 4\ell$ Event Selection

Lepton and Jet Selection

Once reconstructed, further selection cuts are applied to leptons and jets to ensure they are within the fiducial phase space and well-measured by the ATLAS detector.

Electrons are required to have $E_{\mathrm{T}} > 7$ GeV, $|\eta| < 2.47$ and to pass the *Loose* Likelihood requirement. All muons, except calorimeter-tagged muons, must pass the *Loose* selection and have $p_{\mathrm{T}} > 5$ GeV. This p_{T} requirement is comparatively lower than the 6 GeV requirement used in the Run 1 publication [24]. As shown in Figure 3.12, approximately 19% of events have the lowest lepton p_{T} below this threshold. As such, lowering this requirement increases the acceptance of the 4μ final state by 7% [51]. Calorimeter-tagged muons are required to pass the *Loose* selection and have $p_{\mathrm{T}} > 15$ GeV.

As both the Higgs and Z boson decay without travelling a measurable distance, additional cuts are required to ensure leptons originate from the primary vertex. The lepton tracks are required to have $|z_0 \cdot \sin(\theta)| < 0.5$ mm, where $z_0 \cdot \sin(\theta)$ is the distance from the primary vertex along the proton beam pipe to the reconstructed track vertex. To reduce the cosmic ray background, an additional cut of $|d_0| < 1$ mm is applied to muons. d_0 is the transverse distance from the primary vertex to the reconstructed track vertex.

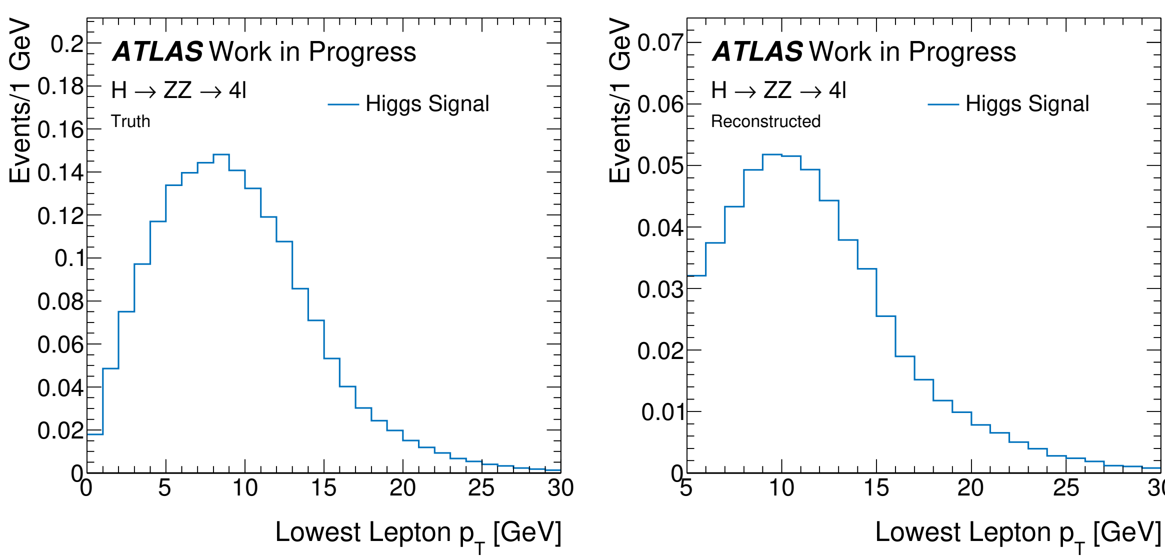

(a) Truth lowest lepton p_{T}

(b) Reconstructed lowest lepton p_{T}

Figure 3.12: (a) True and (b) reconstructed p_{T} distribution of the lowest lepton in the $H \to ZZ^* \to 4\ell$ decay. Approximately 19% of 4μ events have a lepton with true $p_{\mathrm{T}} < 5$ GeV. Lowering the p_{T} requirement on the reconstructed measured p_{T} from 6 GeV to 5 GeV increases the acceptance of the 4μ final state by 7% [51].

Jets are required to have $p_{\mathrm{T}} >$ 30 GeV and $|\eta| < 4.5$. Compared to the Run 1 analysis [24], the p_{T} threshold in the central barrel region, $|\eta| < 2.5$, has been increased from $p_{\mathrm{T}} >$ 25 GeV. This is done to reduce contamination from pileup jets that have a comparatively higher production rate due to the instantaneous luminosity conditions of the Run 2 LHC.

If lepton or jet candidates are reconstructed using the same detector information, ambiguities are resolved with preference given to objects with a lower mis-identification rate within the given fiducial region. If an electron and muon share the same ID track, the muon is rejected if it is calorimeter-tagged; otherwise the electron is rejected. Low p_{T} electrons have calorimeter deposits that are consistent with originating from a minimum ionizing particle and thus are typically reconstructed as calorimeter-tagged muons. High-p_{T} muons, bending in the magnetic field, can emit a final state radiation photon which can be reconstructed as a fake electron. Despite the leptons originating from hadron decays, reconstructed jets geometrically overlapping in a cone of radius R = 0.2 with electrons or muons are removed. This allows for a higher acceptance for Higgs boson candidates.

4-Lepton Selection

Collision vertices are reconstructed from ID tracks with transverse momentum $p_{\mathrm{T}} > 400$ MeV. The vertex with the highest $\sum p_{\mathrm{T}}^2$ is selected as the primary vertex. Events are required to have at least one collision vertex with at least three associated tracks. Additional criteria are applied to ensure that all ATLAS sub-detectors were fully-functional when the event was recorded.

After selection of single leptons, 'dilepton' pairs of same-flavour opposite sign leptons are constructed to ensure that they are consistent with a Z boson decay. Dilepton pairs are combined to form a 'quadruplet'. The same-flavour opposite sign lepton pair with the invariant mass m_{12} (m_{34}) closest (second closest) to the Z boson mass in each quadruplet is referred to as the leading (subleading) lepton pair. Based on the lepton flavour, each quadruplet is classified into one of the following decay channels: 4μ, $2e2\mu$, $2\mu2e$ and $4e$, with the first two leptons always representing the leading lepton pair. For an event, multiple quadruplets are accepted at this stage. However, in each sub-channel, the quadruplets are required to have the same leading lepton pair with the invariant mass closest to the Z boson mass. Additionally, at most one calorimeter-tagged or extrapolated muon per quadruplet is allowed.

The three highest p_{T} leptons are required to have a transverse momentum greater than 20 GeV, 15 GeV and 10 GeV respectively. The leading lepton pair must satisfy 50 GeV $< m_{12} <$ 106 GeV. The subleading lepton pair is required to have a mass $m_{\mathrm{min}} < m_{34} <$ 115 GeV, where m_{min} is 12 GeV for the four-lepton invariant mass $m_{4\ell}$ below 140 GeV, rising linearly to 50 GeV at $m_{4\ell} =$ 190 GeV and then remaining at 50 GeV for all higher $m_{4\ell}$ values.

To suppress J/ψ background events, alternative opposite-charge lepton pairings within a quadruplet are required to have a mass above 5 GeV. All leptons within a quadruplet are required to be angularly separated and satisfy $\Delta R = \sqrt{(\Delta y)^2 + (\Delta\phi)^2} > 0.1$ (0.2) for same-flavour (different-flavour) lepton pairs.

Isolation, Transverse Impact Parameter Significance and 4ℓ Vertex Cut

Due to their large production cross-section, backgrounds arising from $Z+$jets and $t\bar{t}$ have a significant contribution in this analysis. These backgrounds are typically referred to as reducible backgrounds. Within these topologies, prompt leptons are produced from leptonic decays of the Z boson or the W boson in the $t \to Wb$ chain. Mis-identified leptons arise from either leptonic decay of hadrons or incorrectly reconstructed jets originating from light quark decay. These are typically referred to as 'fake leptons'. As

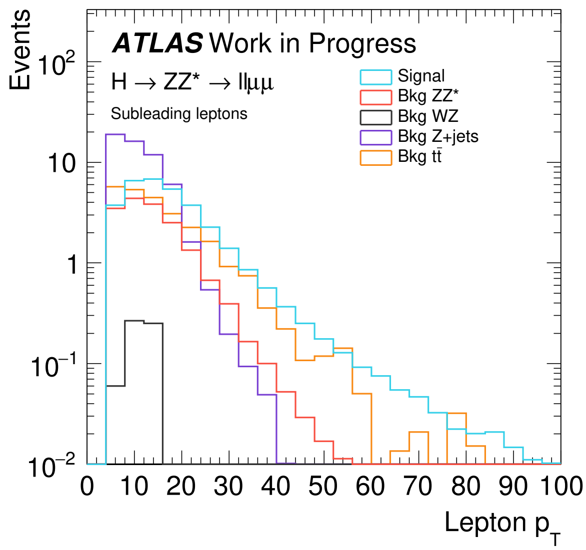

(a) $\ell\ell\mu\mu$

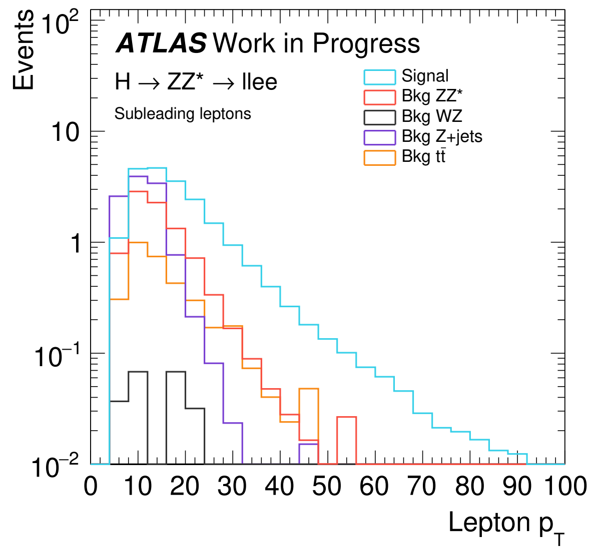

(b) $\ell\ell ee$

Figure 3.13: The $p_{\rm T}$ of subleading leptons for various process contributing to the analysis for (a) $\ell\ell\mu\mu$ and (b) $\ell\ell ee$ final states. Fake leptons arising in $Z+$jets and $t\bar{t}$ typically have a lower $p_{\rm T}$ lepton compared to the Higgs boson signal or ZZ^*. Event yields are normalized to 36.1 fb^{-1} .

shown in Figure 3.13, fake leptons typically have a lower $p_{\rm T}$ when compared to the subleading leptons originating from Higgs boson or ZZ^* decay.

Fake leptons have a unique experimental signature that is used to suppress contribution from these backgrounds. Leptons from heavy flavour quark decays have a displaced vertex. A distribution of the transverse impact parameter significance is shown in Figure 3.14. This parameter is defined as $|d_0|/\sigma(d_0)$, where d_0 is the transverse distance from the primary vertex to the reconstructed lepton vertex and $\sigma(d_0)$ is the associated measurement error. As fake leptons typically have higher values for $|d_0|/\sigma(d_0)$, quadruplets containing electrons (muons) with a d_0 significance above 5 (3) are rejected.

Fake leptons typically have a concentration of other particles around them, which can leave a signature in the ID and calorimeters. As such, each muon (electron) is required to have a track and calorimeter isolation less than 15% (15%) and 30% (20%) of the lepton $p_{\rm T}$ respectively. Track isolation is defined as the scalar sum of the $p_{\rm T}$ of the tracks lying within a cone of $\Delta R = 0.3$ (0.2) around the muon (electron), while calorimeter isolation is the sum of the cluster transverse energies, $E_{\rm T}$, in a cone of $\Delta R = 0.2$ around the muon (electron). Calorimeter isolation is corrected for contributions from pileup, underlying event and energy leakage due to the fixed sliding window used for electron reconstruction. Distributions of these variables are shown in Figure 3.15.

To offset the relatively larger increase in reducible background from lowering the muon $p_{\rm T}$ cut, a new vertex requirement is imposed on the quadruplets. Specifically, a χ^2 fit is performed to measure the compatibility of the 4 leptons to originate from the same vertex. For 4μ events, the reduced χ^2 value is required to be less than 6, while for all other sub-channels, quadruplets with reduced χ^2 values greater than 9 are rejected.

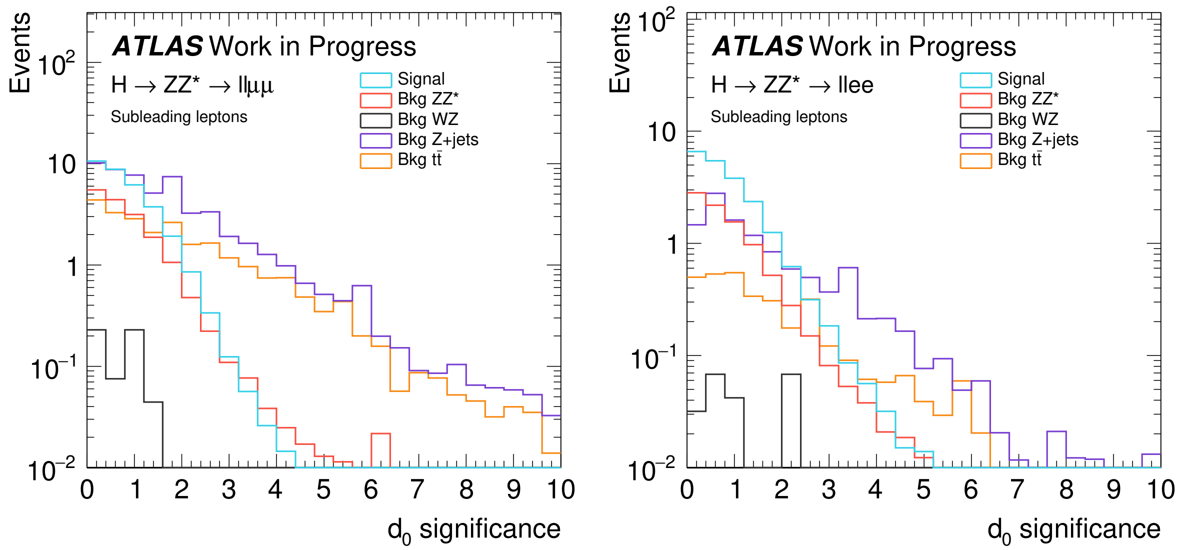

(a) $\ell\ell\mu\mu$

(b) $\ell\ell ee$

Figure 3.14: Transverse impact parameter significance ($|d_0|/\sigma(d_0)$) subleading leptons for various processes contributing to the analysis for (a) $\ell\ell\mu\mu$ and (b) $\ell\ell ee$ final states respectively. Event yields are normalized to 36.1 fb^{-1} .

Final Quadruplet Selection

In $> 99\%$ of events, only one candidate quadruplet passes all the selection criteria and it is designated as the Higgs Boson candidate. However, in cases where there are ≥ 5 leptons, multiple quadruplets per event may pass all selection cuts. For the ggF and VBF production modes, this happens for less than 0.1% of events. However for WH, ZH and ttH production modes, this occurs approximately for 18%, 11% and 32% of all events respectively. In Run 1 publications [24], a single quadruplet from the sub-channel with highest efficiency was chosen as the Higgs boson candidate. However, this led to a large mis-pairing rate where leptons not originating from Higgs boson decays were selected. In turn, this caused approximately 35%, 78% and 43% of WH, ZH and ttH events simulated with $m_H = 125$ GeV with an extra lepton to fall outside of the $115 < m_{4\ell} < 130$ GeV range.

To improve this mis-pairing, a matrix element (ME) based selection criterion is used. For all quadruplets passing the selection, the matrix element for the Higgs boson decay is computed at LO using the MadGraph5_aMC@NLO [70] generator. The quadruplet with the largest matrix element value is selected as the final Higgs boson candidate. This criterion reduces the mis-pairing by a factor of 2.

The number of expected events and the relative efficiency of each selection criterion, as evaluated for the gluon-fusion production mode, are presented in Table 3.2.

3.4.4 FSR Recovery and Z Mass Constraint

To improve four-lepton mass reconstruction, a dedicated method was developed [24] to account for final-state radiation (FSR) photons in Z boson decays. Due to topological differences, separate criteria are

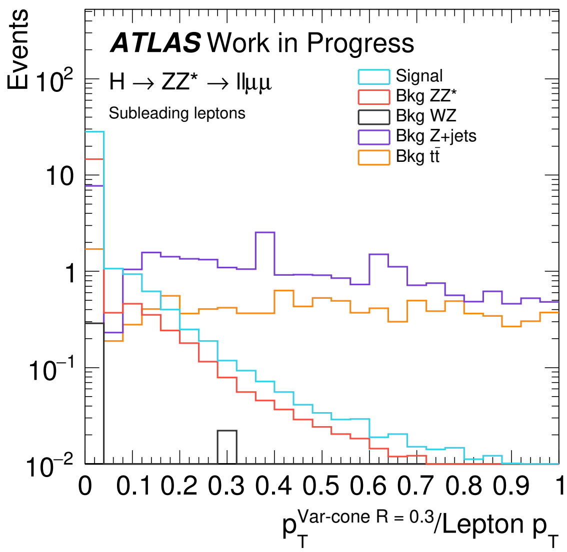

(a) Relative Track Isolation

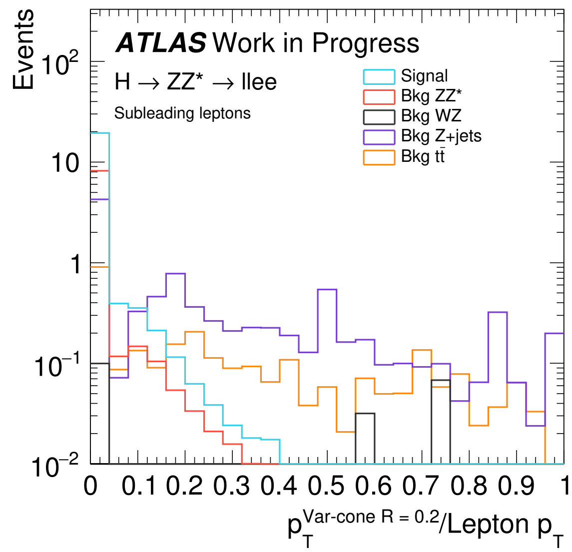

(b) Relative Track Isolation

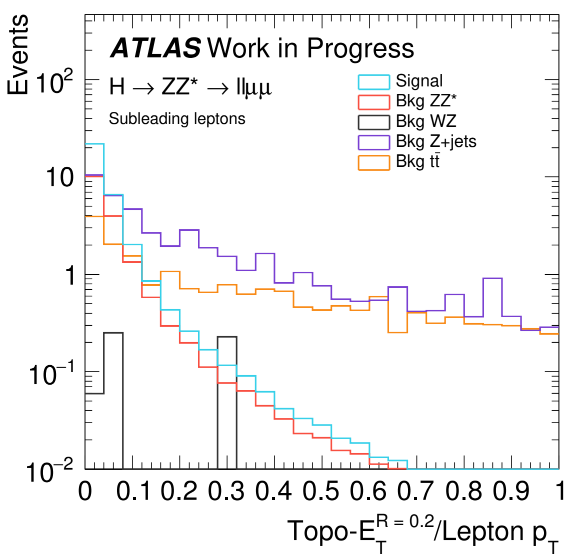

(c) Relative Calorimeter Isolation

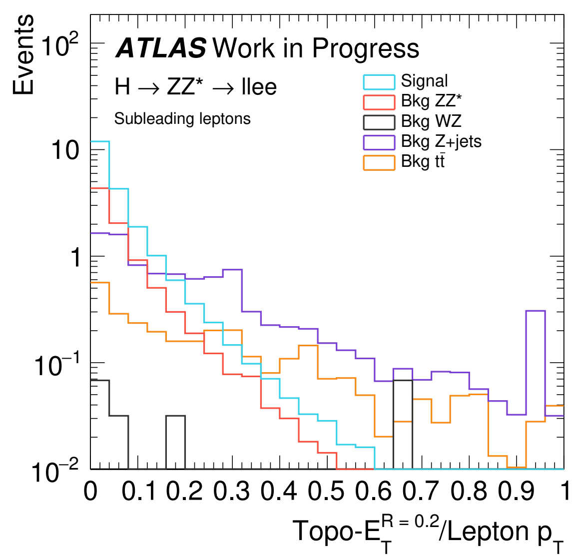

(d) Relative Calorimeter Isolation

Figure 3.15: Relative track and calorimeter isolation of subleading leptons for various processes contributing to the analysis for (a, c) $\ell\ell\mu\mu$ and (b, d) $\ell\ell ee$ final states respectively. Event yields are normalized to 36.1 fb^{-1} .

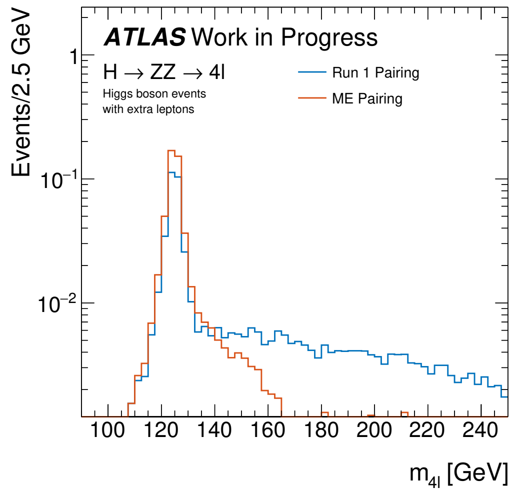

Figure 3.16: Comparison of the four-lepton invariant mass, $m_{4\ell}$, of WH, ZH and ttH events with an extra lepton in the final state with quadruplet selection based on the expected efficiency or matrix-element.

Table 3.2: Number of expected events and the relative efficiency (rel. eff.) of each selection criteria for the gluon-fusion production mode for each sub-channel. The 4ℓ-vertex cut is not included but has close to 100% efficiency. Yields are normalized to 36.1 fb^{-1} . Note that from the m_{Z_1} selection all quadruplets passing each selection are counted. At the 'Single quadruplet' stage, a single candidate is chosen based on the matrix-element based pairing.

	4μ		$2e2\mu$		$2\mu 2e$		$4e$	
	N_{pass}	rel. eff.	N_{pass}	rel. eff.	N_{pass}	rel. eff.	N_{pass}	rel. eff.
Preselection	204.32	1.00	204.32	1.00	204.32	1.00	204.32	1.00
Trigger	184.27	0.90	184.27	0.90	184.27	0.90	184.27	0.90
$\geq$4 leptons	29.75	0.15	38.90	0.22	38.90	0.22	15.38	0.08
SF-OS pairing	29.62	1.00	22.05	0.57	16.35	0.42	15.02	0.98
Lepton p_{T} cuts	27.95	0.94	20.96	0.95	15.73	0.96	14.50	0.97
m_{Z_1} cut	37.47	1.34	18.17	0.87	13.98	0.89	19.19	1.32
m_{Z_2} cut	34.75	0.93	16.61	0.91	12.80	0.92	17.85	0.93
ΔR and J/ψ	33.95	0.98	15.95	0.96	12.29	0.96	17.62	0.99
Isolation	28.04	0.83	13.26	0.83	9.94	0.81	14.53	0.82
d_0 signif.	27.48	0.98	13.06	0.98	9.84	0.99	14.44	0.99
Single quadruplet	18.25	0.66	13.00	1.00	9.81	1.00	9.73	0.67

used for collinear and noncollinear FSR photons. Collinear photons are characterized by $\Delta R(\ell, \gamma) < 0.15$ and, by design, are taken into account during the reconstruction of electrons. For muons, collinear photons are required to have $E_{\text{T}} > 1.5$ GeV and have the fraction of the total energy deposited in the front sampling layer of the calorimeter greater than 0.1. Noncollinear FSR photons can be associated to either muons or electrons and are required to have $E_{\text{T}} > 10$ GeV, pass the isolation criteria and satisfy the "tight" photon identification criteria. Only the highest-E_{T} FSR is kept for a given event. From MC simulation, approximately 7% of events will have a FSR photon. Figure 3.17 shows the improvement in $m_{4\ell}$ resolution for events with FSR photons.

To further improve the reconstructed $m_{4\ell}$ resolution, a Z-mass-constrained kinematic fit is used [24,

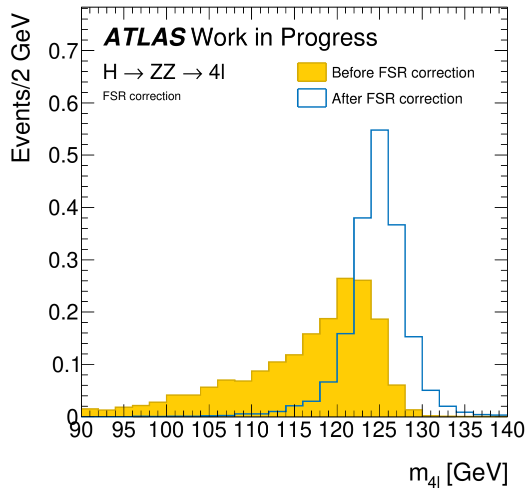

Figure 3.17: Impact on $m_{4\ell}$ for simulated Higgs boson events with m_H = 125 GeV and a final-state radiation (FSR) photon correction.

51]. This method exploits the fact that the leading lepton pair predominately is produced from the decay of an on-shell Z boson. A likelihood fit, using a Breit–Wigner Z line shape and a momentum response function for the expected resolution of each lepton, is used to better measure the p_{T} of the leptons and the reconstructed m_{12}. Overall, this improves the $m_{4\ell}$ resolution by about 15%.

3.5 Event Categorization and Boosted Decision Trees

3.5.1 Categorization of Higgs Boson Candidates

To gain sensitivity to production modes and STXS production bins, each Higgs boson candidate is classified into exclusive categories based on the additional jets and leptons present in the final state. Figure 3.3 summarizes the reconstructed categories definition used for this analysis [51]. To reduce contributions from ZZ^* and other background processes, only Higgs boson candidates with $118 < m_{4\ell} < 129$ GeV are considered. The reconstructed categories are designed to target production modes with smaller cross-sections first, to allow for a high signal-to-background ratio within these categories.

Events satisfying the selection and mass window criteria are first classified into a ttH-enriched region. This region is defined by requiring at least four jets, or one lepton with $p_{\mathrm{T}} > 12$ GeV with at least two jets. Additionally, at least one jet is required to be b-tagged. The additional lepton is required to satisfy the same isolation, impact parameter and angular separation requirements as the leptons in the quadruplet. Events failing the jet requirement but containing additional leptons are then classified into the VH-Lep-enriched category. This region is enriched in events originating from VH production with the associated vector boson decaying leptonically.

Events failing the above criteria are classified based on the jet multiplicity. VBF and VH production processes typically lead to event topologies with greater than or equal to 2 jets. To enhance contributions from VH production with the associated vector boson decaying hadronically, events with at least 2 jets and the invariant mass, m_{jj}, of the two leading jets less than 120 GeV are classified into the VH-Had-enriched category. Events with $m_{jj} > 120$ GeV are further classified into two regions. This classification is based on the VBF STXS bin definitions and depends on the p_T of the leading reconstructed jet (p_T^{j1}). As such, events with $m_{jj} > 120$ GeV and $p_T^{j1} < 200$ GeV are classified into the VBF-enriched-p_T^j-Low category, while events with $p_T^{j1} > 200$ GeV are placed into the VBF-enriched-p_T^j-High category.

Events with exactly zero or one jet are expected to be dominated by the ggF production mode. Events with one jet are split into three categories with the four-lepton transverse momentum $p_T^{4\ell}$ smaller than 60 GeV ($1j$-$p_T^{4\ell}$-Low), between 60 and 120 GeV ($1j$-$p_T^{4\ell}$-Med), and larger than 120 GeV ($1j$-$p_T^{4\ell}$-High). This follows the STXS bin definitions for ggF. Events with zero jets are classified into the $0j$ category.

The expected number of events in each category for all Stage 0 bins is shown in Table 3.3. Contributions from ggF and bbH are shown separately but have similar contributions in each category. The signal composition for the reduced Stage 1 bins is shown in Figure 3.18, while the signal acceptance in each category for the STXS bins is summarized in Figure 3.19 and Figure 3.20. The signal acceptance is obtained by taking the ratio of the expected number of signal events satisfying the event selection criteria in each reconstructed event category to the total number of expected events in each production bin. This is calculated using the predicted cross-section in the bin and the luminosity of the data. Except for ggF-$2j$, the contributions from the STXS bins are predominately concentrated in the reconstructed categories for which they are designed. Despite the small misclassification rate, when coupled to the relatively large cross-section, many reconstructed categories have large expected yields from other 'off-diagonal' production bins.

Table 3.3: The expected number of SM Higgs boson events with a mass $m_H = 125.09$ GeV in the mass range $118 < m_{4\ell} < 129$ GeV for an integrated luminosity of 36.1 fb^{-1} and $\sqrt{s} = 13$ TeV in each reconstructed event category, shown separately for each Stage-0 production bin. The ggF and bbH contributions are shown separately but both contribute to the same (ggF) production bin. Statistical and systematic uncertainties are added in quadrature. The systematic uncertainties included in this analysis are detailed in Section 3.7.

Reconstructed event category	SM Higgs boson production mode ggF	VBF	VH	ttH	bbH
$0j$	25.9 ± 2.5	0.29 ± 0.09	0.253 ± 0.025	0.00025 ± 0.00019	0.29 ± 0.14
$1j$-$p_T^{4\ell}$-Low	8.0 ± 1.1	0.514 ± 0.034	0.230 ± 0.018	0.0007 ± 0.0005	0.09 ± 0.05
$1j$-$p_T^{4\ell}$-Med	4.5 ± 0.7	0.64 ± 0.09	0.227 ± 0.019	0.0010 ± 0.0005	0.026 ± 0.013
$1j$-$p_T^{4\ell}$-High	1.10 ± 0.24	0.27 ± 0.04	0.095 ± 0.007	0.00080 ± 0.00024	0.0036 ± 0.0018
VBF-enriched-p_T^j-Low	3.9 ± 0.8	2.03 ± 0.19	0.285 ± 0.024	0.065 ± 0.009	0.045 ± 0.023
VBF-enriched-p_T^j-High	0.33 ± 0.09	0.185 ± 0.024	0.050 ± 0.004	0.0159 ± 0.0027	0.00058 ± 0.00029
VH-Had-enriched	2.72 ± 0.51	0.217 ± 0.016	0.58 ± 0.02	0.031 ± 0.004	0.025 ± 0.013
VH-Lep-enriched	0.0129 ± 0.0018	0.00310 ± 0.00021	0.263 ± 0.018	0.038 ± 0.005	0.0009 ± 0.0005
ttH-enriched	0.050 ± 0.016	0.010 ± 0.006	0.0196 ± 0.0031	0.301 ± 0.032	0.0064 ± 0.0035
Total	47 ± 4	4.16 ± 0.23	2.00 ± 0.11	0.45 ± 0.05	0.49 ± 0.24

3.5.2 Discriminating observables

To further increase the sensitivity of the measurements of the productions bins, Boosted Decision Trees (BDTs) [53] based discriminants are introduced in the reconstructed categories. BDTs are binary classification trees which are trained to achieve the goal of labelling an event as signal-like or background-like by having output nodes with a high purity of the given event type. This is accomplished by basing a left/right decision for each node on the value of a given variable at each node. This splits the phase space

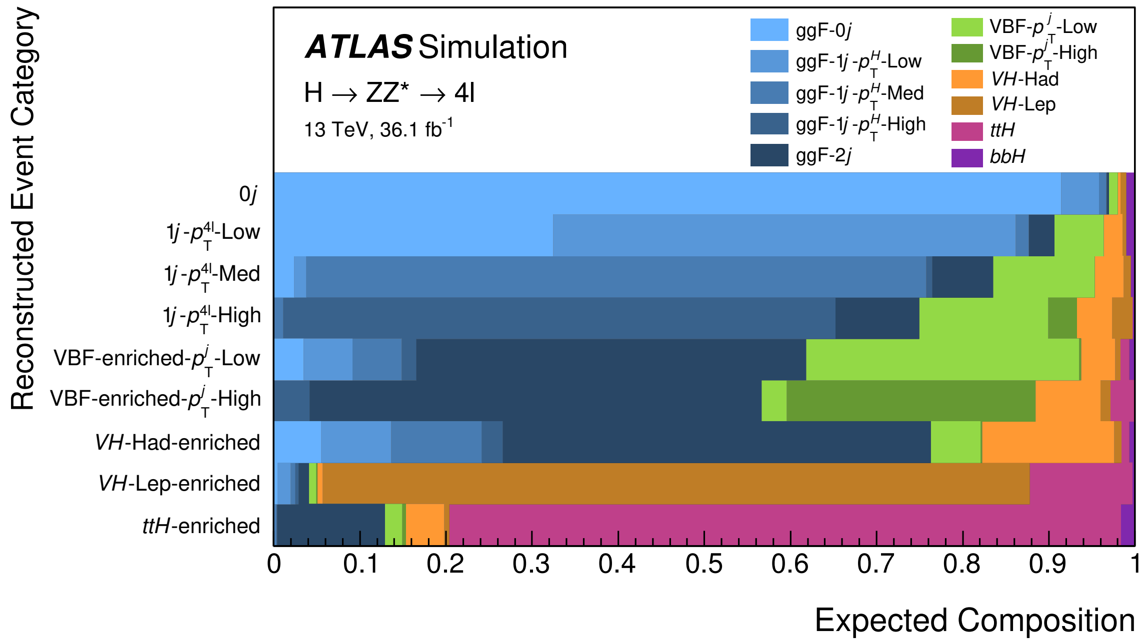

Figure 3.18: Signal composition in terms of the reduced Stage-1 production bins in each reconstructed event category. The ggF and bbH contributions are shown separately but both contribute to the same (ggF) production bin.

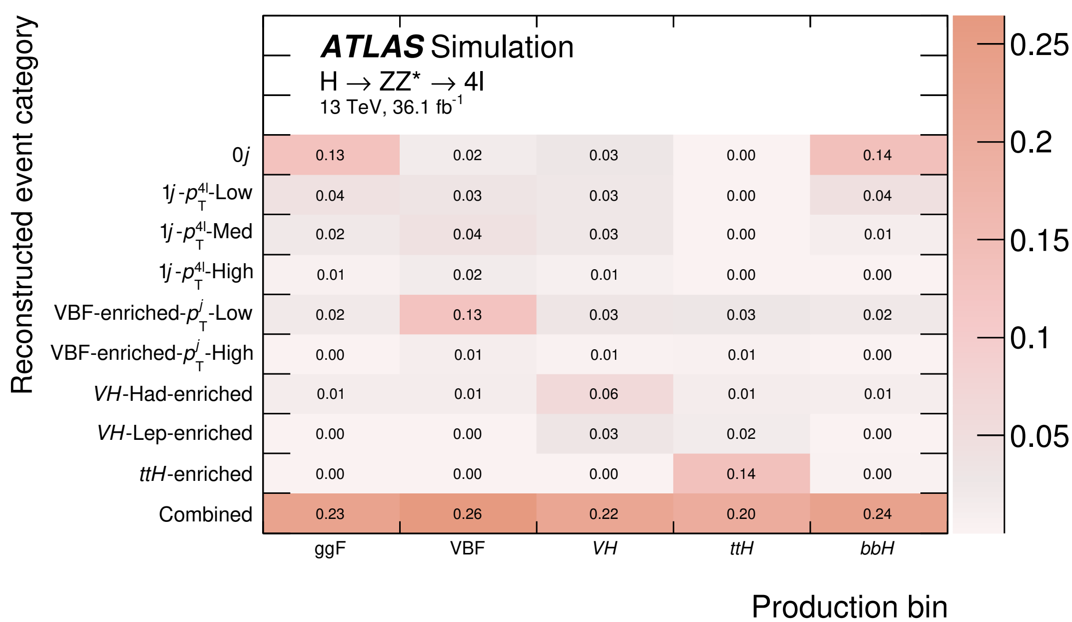

Figure 3.19: Signal acceptance obtained as the ratio of the number of simulated signal events satisfying the event selection criteria in each reconstructed event category to the total number of events generated in the phase space specified by a given Stage-0 production bin.

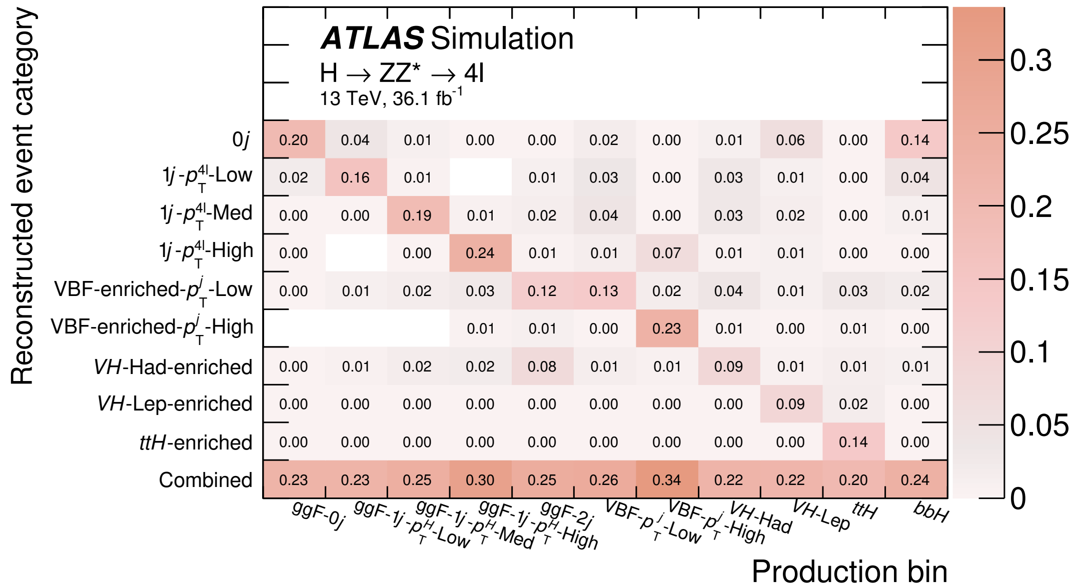

Figure 3.20: Signal acceptance obtained as the ratio of the number of simulated signal events satisfying the event selection criteria in each reconstructed event category to the total number of events generated in the phase space specified by a given reduced Stage-1 production bin.

spanned by the input variables into rectangular hyper-cubiods, each with a signal-like or background-like label. Typically, a 'forest' of these decision trees is trained using a boosting technique [53], with the final discriminating observable being a weighted average of results from the individual decision trees.

In this measurement, the BDTs are trained to either discriminate between the ZZ continuum background and the Higgs boson signal or discriminate between different production modes. The training is performed using simulated MC samples and it is assumed that the distributions of the input variables follow SM predictions. In the following section, a detailed description of the BDT discriminant in the VH-Had-enriched reconstructed category is presented. Only a general overview of the other observables is provided.

VH-Had-enriched BDT discriminant

At leading order, for the VH production with the associated vector boson decaying hadronically, the final state consists of 4 leptons and 2 jets. With higher order corrections or pileup contributions, additional jets may be found in the final state. However, the two leading jets with the highest p_{T} predominantly arise from the vector boson decay. On the other hand, for ggF and background processes, jets arise from QCD emissions, have a lower p_{T} spectrum and have a largely uncorrelated angular distribution. The VBF process contributes within this reconstructed category, with the jets typically found in higher η regions.

Given this, the kinematics and topology of the jets can be summarized into a few discriminating variables and are used in the BDT training. Specifically these variables include:

- Invariant mass of the two leading jets (m_{jj})

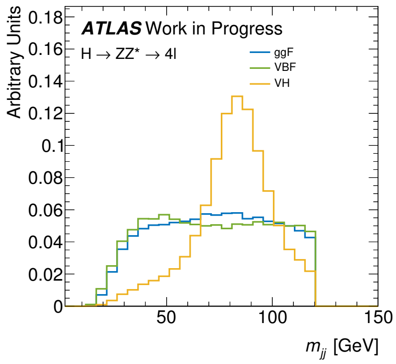

(a) m_{jj}

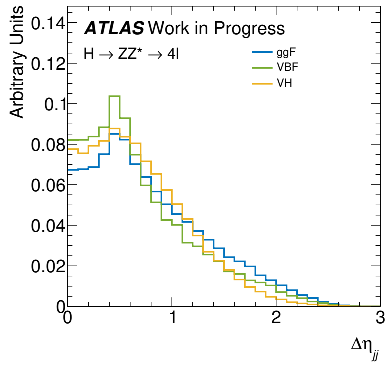

(b) $\Delta\eta_{jj}$

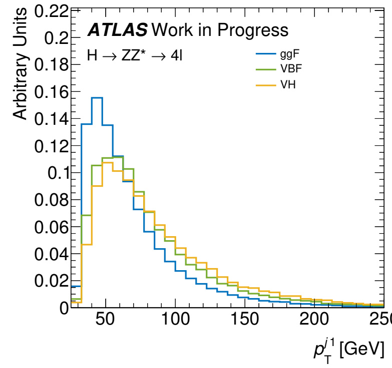

(c) p_{T}^{j1}

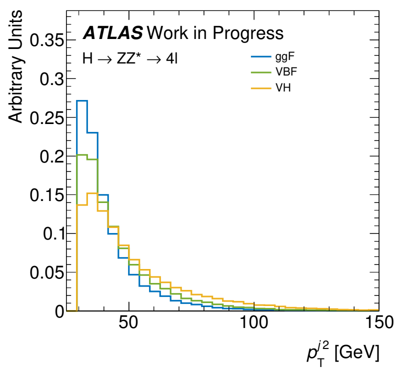

(d) p_{T}^{j2}

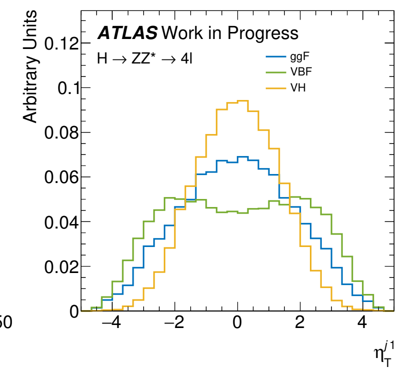

(e) η_{j1}

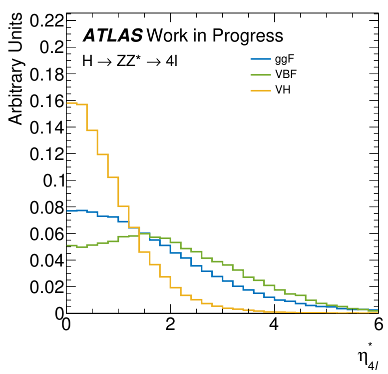

(f) $\eta^*_{4\ell}$

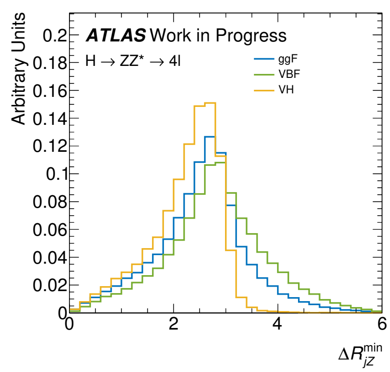

(g) $\Delta R_{jZ}^{\mathrm{min}}$

Figure 3.21: The input variables used for training the BDT observable ($\mathrm{BDT}_{VH\text{-Had}}$) in the VH-Had-enriched category. See text for details on the input variables. All distributions are normalized to unity.

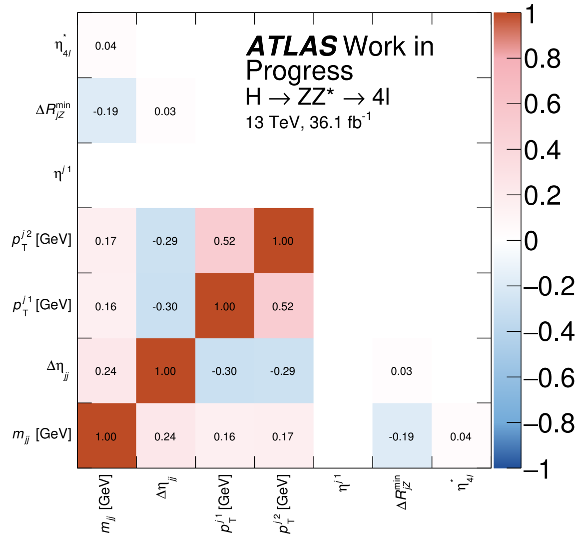

(a) Signal: VH

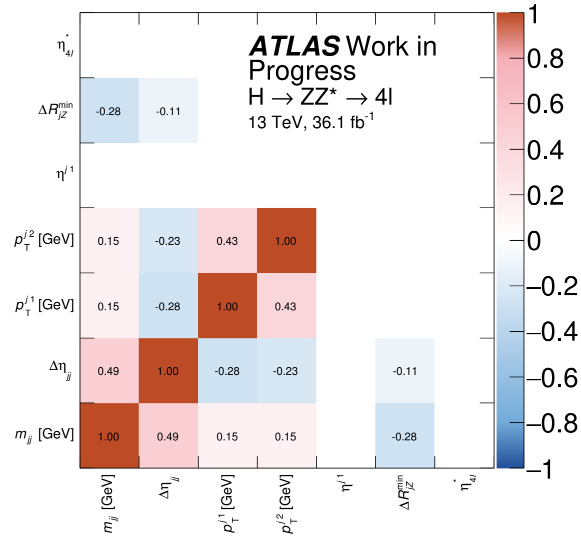

(b) Background: ggF + VBF

Figure 3.22: Linear correlation between the input variables used for training the BDT$_{VH\text{-Had}}$.

- Pseudorapidity separation of the two leading jets ($\Delta\eta_{jj}$)
- Transverse momentum of the leading and subleading jets (p_{T}^{j1} and p_{T}^{j2})
- Pseudorapidity of the leading jet (η_{j1})
- Difference between the pseudorapidity of the four-lepton system and the average pseudorapidity of the two leading jets ($\eta^*_{4\ell} = \eta_{4l} - \langle \eta_{j1}, \eta_{j2} \rangle$)
- Minimum angular separation between the reconstructed lepton pairs and the two leading jets ($\Delta R^{\mathrm{min}}_{jZ}$)

Plots comparing the distributions of these variables are shown in Figure 3.21. $\eta^*_{4\ell}$ and $\Delta R^{\mathrm{min}}_{jZ}$ are typically used to probe VBF-like production, but as seen from the plots these variables provide discrimination for VH production as well. Correlations between the variables reduce the impact they have in the final observables and are shown in Figure 3.22.

For training the BDT, the VH process is labelled as signal, while ggF and VBF are considered as background processes. The final resulting distribution of the BDT score (BDT$_{VH\text{-Had}}$) is plotted in Figure 3.23, showing a clear separation between the different production modes. To check for over-training, only half of the simulated events are used in the training and the remaining half are used for validation. Comparing the distribution of the BDT$_{VH\text{-Had}}$ for the test and training samples shows no signs of over-training.

Compared to using no discriminating variables within the VH-Had-enriched category, BDT$_{VH\text{-Had}}$ improves the expected statistical error on the VH cross-section measurement by approximately 25%. Similarly, the BDT offers a 10% improvement over just using m_{jj} as the observable. A significant percentage of this improvement (6%) is due to the inclusion of jet kinematics as input variables in the training. $\eta^*_{4\ell}$ and $\Delta R^{\mathrm{min}}_{jZ}$ offer modest improvements of about 2% each. These impacts are calculated using the statistical method described in Section 3.8.2.

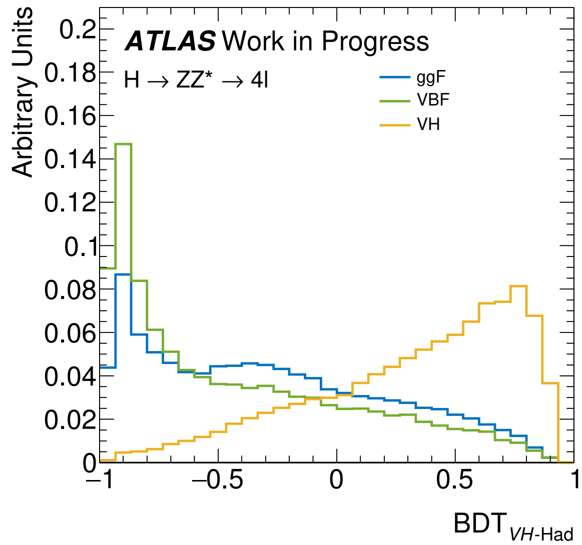

(a) BDT$_{VH\text{-Had}}$

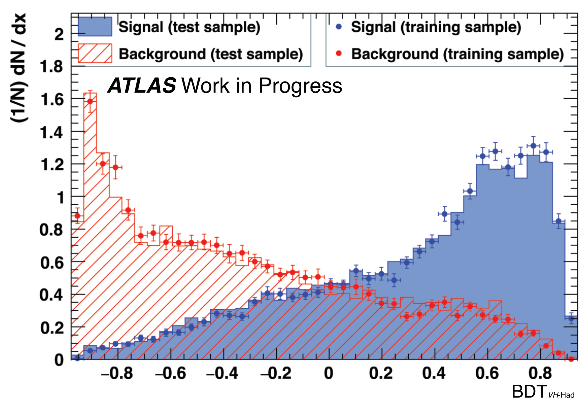

(b) Over-training check

Figure 3.23: Resulting distribution (a) for BDT score (BDT$_{VH\text{-Had}}$) for signal and background process in the VH-Had-enriched category. The test and training samples are super-imposed (b), showing no sign of over-training.

Discriminants in other categories

Table 3.4: The BDT discriminants and their corresponding input variables used for the measurement of cross-sections per production bin. The jets are denoted by "j". See the text for variable definitions. The expected yield is used in categories with no listed BDT discriminant. Information about VH-Had-enriched is provided again to ensure consistency.

Reconstructed event category	BDT discriminants	Target Signal	Target Background	Input Variables
$0j$	$\mathrm{BDT_{ggF}}$	ggF	ZZ^*	$p_{\mathrm{T}}^{4\ell}$, $\eta_{4\ell}$, D_{ZZ^*}
$1j$-$p_{\mathrm{T}}^{4\ell}$-Low	$\mathrm{BDT}_{\mathrm{VBF}}^{1j\text{-}p_{\mathrm{T}}^{4\ell}\text{-Low}}$	VBF	ggF	p_{T}^{j}, η_j, $\Delta R(j,4\ell)$
$1j$-$p_{\mathrm{T}}^{4\ell}$-Med	$\mathrm{BDT}_{\mathrm{VBF}}^{1j\text{-}p_{\mathrm{T}}^{4\ell}\text{-Med}}$	VBF	ggF	p_{T}^{j}, η_j, $\Delta R(j,4\ell)$
$1j$-$p_{\mathrm{T}}^{4\ell}$-High	-	-	-	-
VBF-enriched-p_{T}^{j}-Low	$\mathrm{BDT_{VBF}}$	VBF	ggF	m_{jj}, $\Delta\eta_{jj}$, p_{T}^{j1}, p_{T}^{j2}, $\eta_{4\ell}^{*}$, $\Delta R_{jZ}^{\mathrm{min}}$, $(p_{\mathrm{T}}^{4\ell jj})_{\mathrm{constrained}}$
VBF-enriched-p_{T}^{j}-High	-	-	-	-
VH-Had-enriched	$\mathrm{BDT}_{VH\text{-Had}}$	VH	ggF + VBF	m_{jj}, $\Delta\eta_{jj}$, p_{T}^{j1}, p_{T}^{j2}, $\eta_{4\ell}^{*}$, $\Delta R_{jZ}^{\mathrm{min}}$, η_{j1}
VH-Lep-enriched	-	-	-	-
ttH-enriched	-	-	-	-

In other reconstructed categories, BDT discriminants are used to target different processes. In the $0j$ category, the BDT is trained to separate the ggF process from the continuum ZZ^* background. This BDT was originally designed for the Run 1 mass measurement [24] and relies on the four-lepton transverse momentum ($p_{\mathrm{T}}^{4\ell}$) and rapidity ($\eta_{4\ell}$) as well as on the kinematic discriminant D_{ZZ^*}. This kinematic discriminant is defined as the difference between the logarithms of the signal and background matrix elements squared. These matrix elements are calculated using the same procedure as outlined in Section 3.4.3.

In the two 1-jet categories, namely $1j$-$p_{\mathrm{T}}^{4\ell}$-Low and $1j$-$p_{\mathrm{T}}^{4\ell}$-Med, the BDT discriminant is used to target the VBF process to improve sensitivity to it. The input variables used for this BDT include the jet transverse momentum (p_{T}^{j}), rapidity (η_j) and angular separation between the jet and the four-lepton system ($\Delta R(j,4\ell)$).

The BDT used in the VBF-enriched-p_{T}^{j}-Low category relies on similar variables as the $\mathrm{BDT}_{VH\text{-Had}}$, with η_{j1} being replaced with $(p_{\mathrm{T}}^{4\ell jj})_{\mathrm{constrained}}$. This variable is the constrained transverse momentum of the Higgs–dijet system and is defined as $(p_{\mathrm{T}}^{4\ell jj})_{\mathrm{constrained}} = p_{\mathrm{T}}^{4\ell jj}$ (50 GeV) for $p_{\mathrm{T}}^{4\ell jj} > 50$ GeV ($p_{\mathrm{T}}^{4\ell jj} < 50$ GeV). The transverse momentum $p_{\mathrm{T}}^{4\ell jj}$ of the Higgs–dijet system is limited to > 50 GeV to reduce the impact of theoretical uncertainties.

A summary of the BDT used in this analysis is provided in Table 3.4 and the expected distributions are shown in Figure 3.24. Compared to using no discriminants, the inclusion of BDT discriminants improves the expected statistical uncertainties on the ggF, VBF and VH Stage-0 production bins cross-section measurement by 15%, 35% and 25% respectively.

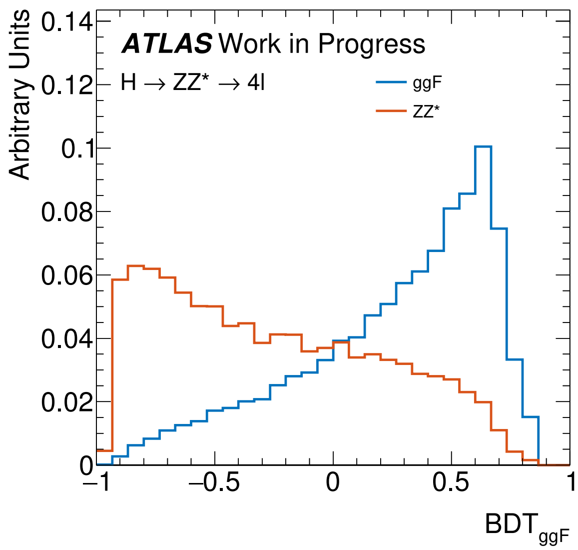

(a) $0j$ category

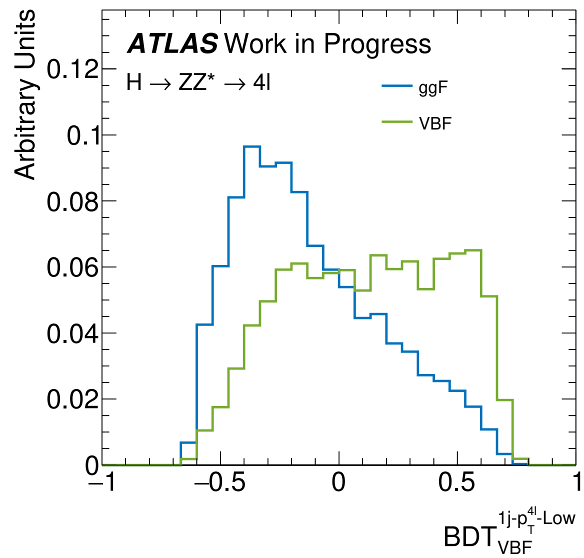

(b) $1j$-$p_{\mathrm{T}}^{4\ell}$-Low category

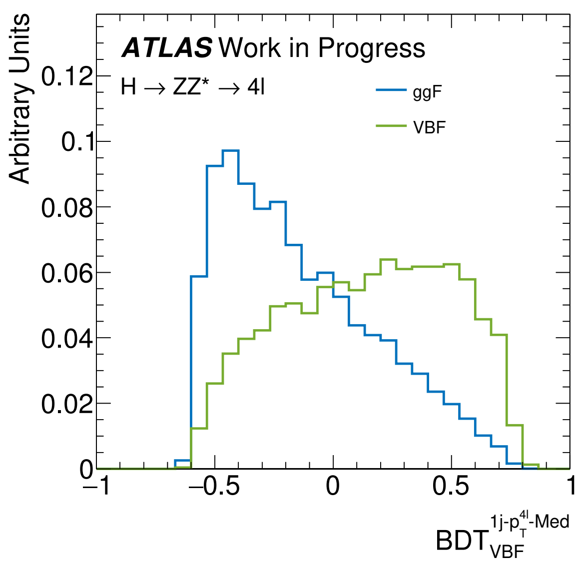

(c) $1j$-$p_{\mathrm{T}}^{4\ell}$-Med category

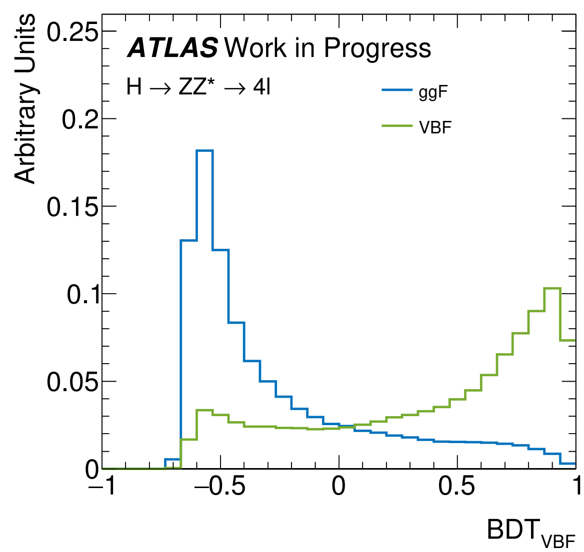

(d) VBF-enriched-p_{T}^{j}-Low category

Figure 3.24: BDT discriminants used in various categories. All distributions are normalized to unity.

3.6 Background Estimation

3.6.1 Non-resonant ZZ^*, $t\bar{t}+V$ and tri-boson

The main source of background in this analysis originates from the continuum ZZ^* process. Moreover, in VH- and ttH-like phase space, $t\bar{t}+V$ and tri-boson (VVV) processes also have a measurable contribution. Due to their large jet/lepton multiplicity and small cross-section, these processes have negligible contributions in categories with fewer than 2 jets.

Since there are 4 prompt leptons in the final state, ZZ^*, $t\bar{t}+V$ and tri-boson processes can be reliably estimated from MC simulation and are normalized to the best available predicted cross-sections as described in Section 3.3.2. The estimated yields of each process in the reconstructed categories are presented in Table 3.5. MC simulation is also used to predict the BDT response.

Table 3.5: The expected number of background events in the mass range $118 < m_{4\ell} < 129$ GeV in each reconstructed event category for a luminosity of 36.1 fb^{-1} at $\sqrt{s} = 13$ TeV. Statistical and systematic uncertainties are added in quadrature. The systematic uncertainties are detailed in Section 3.7.

Reconstructed event category	ZZ^* background	$t\bar{t}+V+VVV$ backgrounds
$0j$	13.7 ± 1.0	0.02 ± 0.01
$1j$-$p_{\mathrm{T}}^{4\ell}$-Low	3.1 ± 0.4	0.01 ± 0.01
$1j$-$p_{\mathrm{T}}^{4\ell}$-Med	0.88 ± 0.12	0.03 ± 0.02
$1j$-$p_{\mathrm{T}}^{4\ell}$-High	0.139 ± 0.022	0.004 ± 0.002
VBF-enriched-p_{T}^{j}-Low	1.08 ± 0.32	0.13 ± 0.03
VBF-enriched-p_{T}^{j}-High	0.093 ± 0.032	0.016 ± 0.004
VH-Had-enriched	0.66 ± 0.17	0.048 ± 0.015
VH-Lep-enriched	0.049 ± 0.008	0.014 ± 0.002
ttH-enriched	0.014 ± 0.006	0.04 ± 0.02
Total	19.7 ± 1.5	0.3 ± 0.1

To validate the MC prediction, the expected event yields and BDT shape are compared to the observed data in a 'side-band' region. This region is defined by applying all event and category definition requirements, but selecting candidates that satisfy $m_{4\ell} < 115$ GeV or $130 < m_{4\ell} < 170$ GeV. This mass range requirement suppresses contributions from the on-shell Higgs decay, while ensuring the kinematic phase space available to the background processes is similar to the signal region. Table 3.6 and Figure 3.25 compare the expected and observed yield and distributions respectively. The largest discrepancies are observed in categories with low expected yields, but are consistent with statistical fluctuations. Overall, the MC simulations model well the background processes at the statistical precision of the data.

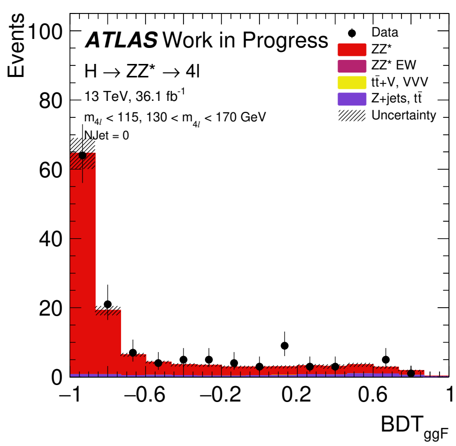

(a) $0j$ category

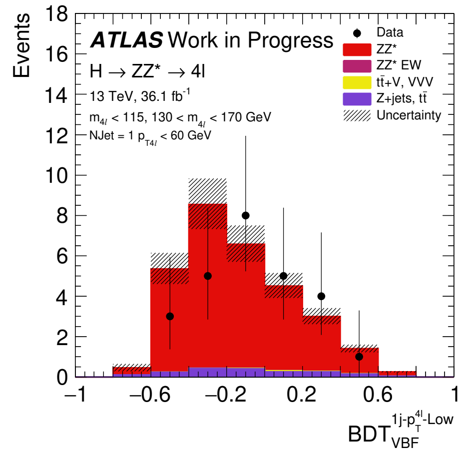

(b) $1j$-$p_{\mathrm{T}}^{4\ell}$-Low category

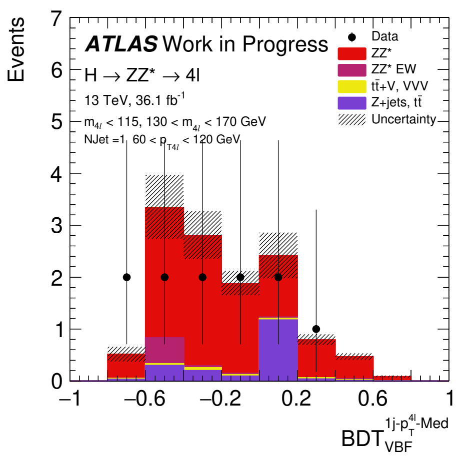

(c) $1j$-$p_{\mathrm{T}}^{4\ell}$-Med category

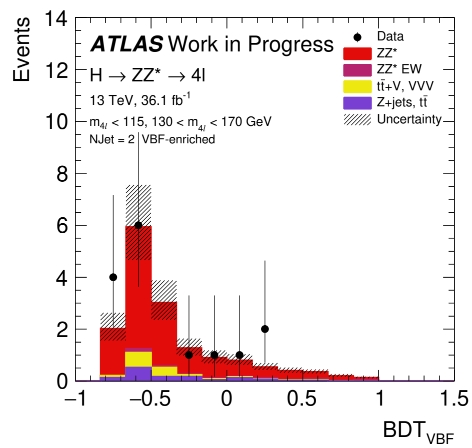

(d) VBF-enriched-p_{T}^{j}-Low category

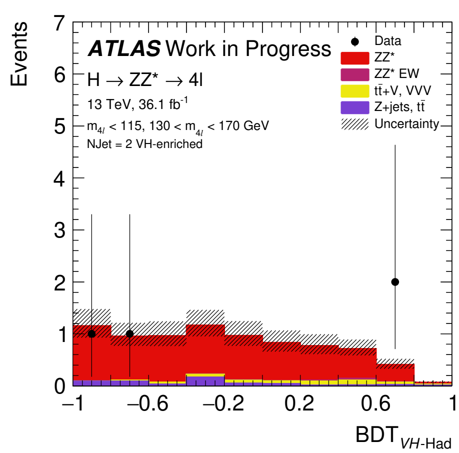

(e) VH-Had-enriched category

Figure 3.25: BDT discriminant distributions of selected candidates in the experimental categories for events satisfying $m_{4\ell} < 115$ GeV or $130 < m_{4\ell} < 170$ GeV. The expected yields are normalized to a luminosity of 36.1 fb^{-1} at $\sqrt{s} = 13$ TeV. The ZZ^* process is split into production via vector boson scattering (ZZ^* EW) and via quark-antiquark and gluon-induced (ZZ^*). The estimation of contributions from $Z+$jets, $t\bar{t}$ processes is described in Section 3.6.2. The error bars represent 68.3% central confidence interval statistical uncertainty. The systematic uncertainty on the prediction is shown by the dashed band.

Table 3.6: Expected and observed yields in the experimental categories for event satisfying $m_{4\ell} < 115$ GeV or $130 < m_{4\ell} < 170$ GeV. The expected yields are normalized to a luminosity of 36.1 fb^{-1} at $\sqrt{s} = 13$ TeV. Statistical and systematic uncertainties are added in quadrature with the systematic uncertainties being defined in Section 3.7. The estimation of contributions from $Z+$jets, $t\bar{t}$ processes is described in Section 3.6.2.

Reconstructed event category	ZZ^*	$Z+$jets, $t\bar{t}$, $t\bar{t}+V$,VVV	Total Expected	Observed
$0j$	116 ± 8	7.5 ± 1.0	124 ± 8	134
$1j$-$p_{\mathrm{T}}^{4\ell}$-Low	28 ± 4	1.95 ± 0.26	30 ± 4	26
$1j$-$p_{\mathrm{T}}^{4\ell}$-Med	10.2 ± 1.2	1.52 ± 0.19	11.8 ± 1.3	11
$1j$-$p_{\mathrm{T}}^{4\ell}$-High	1.84 ± 0.28	0.26 ± 0.12	2.10 ± 0.31	4
VBF-enriched-p_{T}^{j}-Low	11.7 ± 3.4	2.38 ± 0.25	14.1 ± 3.4	13
VBF-enriched-p_{T}^{j}-High	1.2 ± 0.4	0.245 ± 0.027	1.4 ± 0.4	2
VH-Had-enriched	7.0 ± 1.8	1.10 ± 0.15	8.1 ± 1.8	4
VH-Lep-enriched	0.25 ± 0.04	0.099 ± 0.015	0.35 ± 0.04	2
ttH-enriched	0.17 ± 0.07	0.6 ± 0.5	0.8 ± 0.5	3
Total	177 ± 14	15.5 ± 1.9	192 ± 14	199

3.6.2 Reducible background

As detailed in Section 3.4, contributions from $Z+$jets and $t\bar{t}$ processes arise mainly from the mis-identification of jets or leptons originating from the decay of hadrons. While the lepton identification, isolation and transverse impact parameter requirements are designed to keep the mis-identification rate low, the comparatively large cross-sections of $Z+$jets and $t\bar{t}$ processes allow them to have a non-negligible contribution in the analysis.

The contributions from these processes are estimated from dedicated control regions (CRs) separately for events with different flavours of the subleading lepton pair. These final states are labelled as $\ell\ell+\mu\mu$ or $\ell\ell+ee$, where $\ell\ell$ denotes the leading and $\mu\mu$ or ee the subleading lepton pair respectively. The estimation is performed first in an inclusive region without any mass requirements. Afterwards, these estimations are split into different categories and the BDT shape is computed.

$\ell\ell+\mu\mu$ estimation in the inclusive region

The reducible background in the $\ell\ell+\mu\mu$ final state is estimated separately for each process ($Z+$jets and $t\bar{t}$), with the $Z+$jets process further sub-divided into a heavy-flavour (HF) and a light-flavour (LF) component. In the Z+HF topology, the subleading muons originate from b- or c-quark decay, while the Z+LF process consists of pion or kaon decays.

For estimating the $t\bar{t}$ and the Z+HF processes, the mass distribution of the leading lepton pair (m_{12}) is simultaneously fit in two CRs. The CRs are defined by following the event selection criteria as described in Section 3.4, with the changes described as follow. For the "Inverted d_0" CR, the transverse impact parameter requirement is inverted for at least one lepton in the subleading pair, while no isolation requirements are applied to the subleading pair. This CR is enhanced in heavy quark decays as they are characterized by a large d_0 significance. In the "e$\mu+\mu\mu$" CR, an opposite-charge different-flavour leading dilepton is required, while isolation, d_0 significance and charge requirements are not applied for the subleading pair. This creates a CR that is highly pure in the $t\bar{t}$ process. The vertex requirement is also not applied to either control region.

The results of the fit are shown in Figure 3.26. The distributions for the different processes are parametrized by fitting the distribution obtained from MC simulations which are then held constant in the fit to data. Afterwards, the Z+LF component is estimated from an "Inverted isolation" CR. This CR is formed by inverting the isolation requirement on at least one lepton in the subleading pair and not applying the vertex cut. The Z+HF and $t\bar{t}$ contributions in this CR are subtracted using MC simulation that is scaled with the same factor as that obtained by comparing MC and the results from the simultaneous fit.

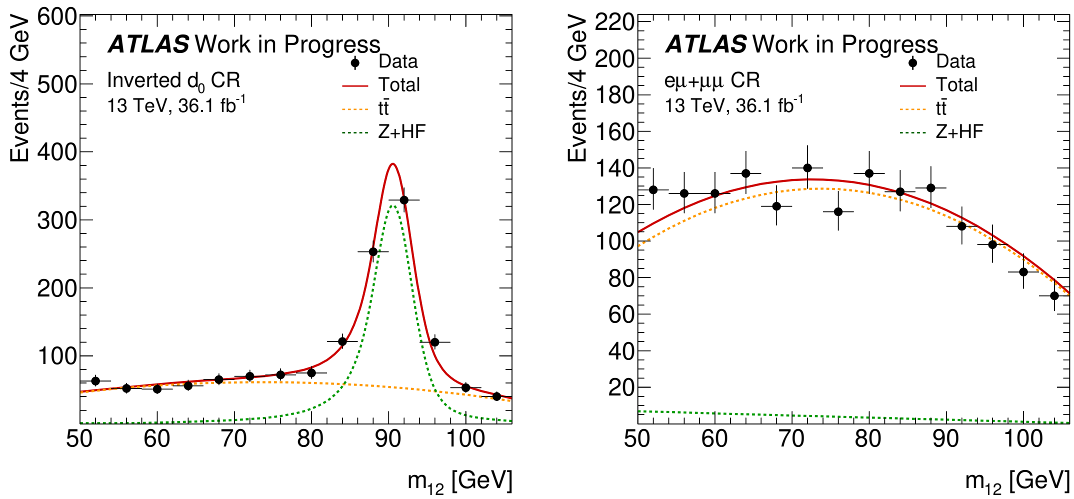

(a) Inverted d_0 CR

(b) e$\mu + \mu\mu$ CR

Figure 3.26: Distributions of m_{12} for data in two control regions for estimating for the $\ell\ell + \mu\mu$ background. The data are fit simultaneously in (a) the Inverted d_0 and (b) the e$\mu + \mu\mu$ CRs, with the result of the fit shown with the continuous line. The dashed lines correspond to the Z+HF and $t\bar{t}$ components of the fit.

The estimates are extrapolated into the SR using MC-based factors, which encode the efficiency of the subleading leptons to pass the necessary cuts to extrapolate from the CR to the signal region. These factors are cross-checked in a 3-lepton $Z + \mu$ CR with differences between data and MC assigned as systematic errors. The estimated yields in the SR without any mass cuts are presented in Table 3.7. To validate these results, the estimates are extrapolated to a "Relaxed Isolation-d_0" CR where no isolation, d_0 significance requirements for the subleading leptons or vertex requirements are applied. As seen in Figure 3.27, good closure is observed in this CR.

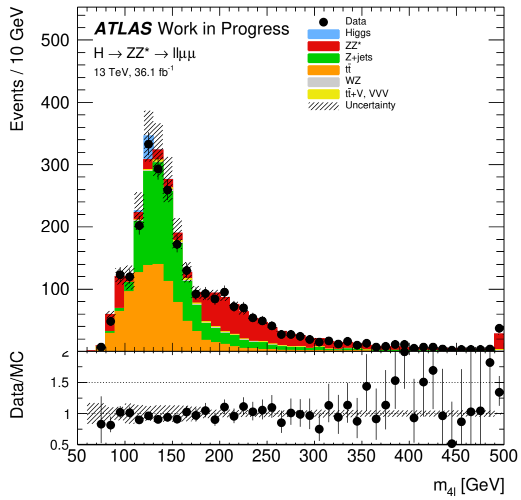

(a) $m_{4\ell}$

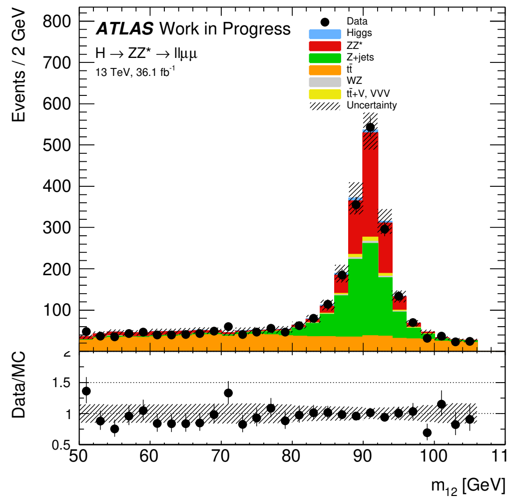

(b) m_{12}

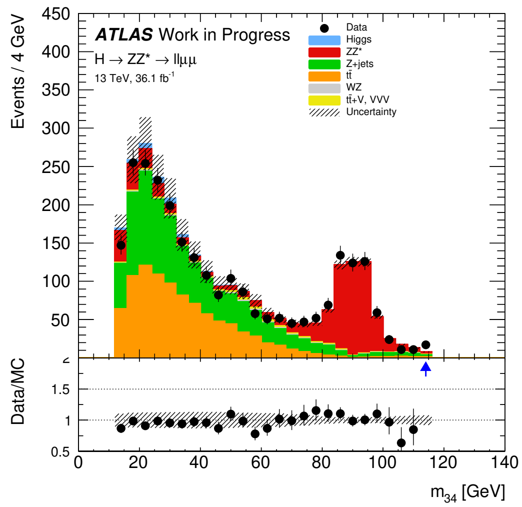

(c) m_{34}

Figure 3.27: The $m_{4\ell}$, m_{12} and m_{34} distributions for the $\ell\ell + \mu\mu$ final state in the Relaxed Isolation-d_0 CR. The last bin contains the integral of the overflow. The systematic uncertainty on the prediction is shown by the dashed band. The arrows in the ratio panel indicate data points outside the plotted range.

Table 3.7: Data fit results for the Z+HF, $t\bar{t}$ and Z+LF processes shown together with the per-event efficiencies from MC simulation. The data fit results are extrapolated to the common relaxed isolation-d_0 CR. The final estimates in the signal region are also shown with their statistical and systematic uncertainties.

$\ell\ell + \mu\mu$			
type	data fit	extrapolation factor [x10^{-2}]	SR yield
Z+jets (HF)	928 ± 50	0.75 ± 0.09	$6.96 \pm 0.37 \pm 1.19$
$t\bar{t}$	934 ± 23	0.25 ± 0.03	$2.33 \pm 0.06 \pm 0.44$
Z+jets (LF)	0 ± 16	3.0 ± 0.40	$0 \pm 0.49 \pm 0.25$

$\ell\ell + ee$ estimation in the inclusive region

The reducible background in the $\ell\ell + ee$ final state is estimated by measuring the contributions from the originating source rather than the underlying process. The fake electron can originate from heavy flavour decay (q), which is estimated using MC, or can arise from misidentified jets faking an electron (f) or electrons from photon conversions (γ). The latter two are estimated using a template fit in the $3\ell + X$ CR.

The $3\ell + X$ CR is defined by following the event selection criteria as described in Section 3.4 but by relaxing the identification, isolation and d_0 significance requirements on the lowest-p_{T} electron in the quadruplet. This lepton, denoted as X, has the highest probability of being a fake electron. To suppress background from ZZ^*, only same sign subleading pairs are selected. Contributions from f and γ are separately estimated by fitting the number of track hits ($n_{InnerPix}$) in the innermost or next-to-innermost pixel layer for the associated track. A hit in the next-to-innermost pixel layer is used when the electron falls in a region that is either not instrumented with an IBL module or the IBL module is not operating. Backgrounds originating from the γ's are typically expected to leave a hit in the layer where the conversion process took place.

The results of the fit are shown in Figure 3.28. The templates for the different processes are obtained from data from a 3-lepton $Z + X$ CR, where the requirements on the third lepton match the relaxed lepton definition in the $3\ell + X$ CR.

The estimates are extrapolated into the SR using transfer factors, which are also obtained from the exclusive subsets of the $Z + X$ CR that are enriched in f and γ respectively. This is accomplished by comparing data and MC in this CR, and iteratively correcting the MC based transfer factor. The iteration is performed as significant cross contamination of f and γ are found. The estimated yields in the SR without any mass cuts are presented in Table 3.8. To validate these results, the estimates are extrapolated to the Relaxed Isolation-d_0 CR. As seen in Figure 3.29, good agreement is observed in this CR.

Estimation in reconstructed categories

To estimate the fraction of the inclusive yield contribution in different reconstructed categories, different approaches are taken for each subleading final state. The $\ell\ell + ee$ estimates are obtained by performing the above mentioned data-driven approach in each separate category, which are created by sub-dividing the $3\ell + X$ CR using the criteria defined in Section 3.5.

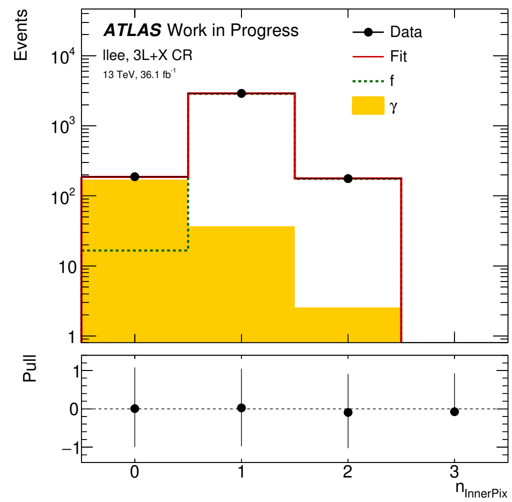

(a)

Figure 3.28: Distributions of $n_{InnerPix}$ for data in the $3\ell + X$ control region for estimating for the $\ell\ell + ee$ background.

Table 3.8: Fit results for yields in the 3ℓ+X CR with statistical errors, shown together with the Z+HF contamination and the efficiency used to extrapolate the yields to the SR. The SR yields for the f and γ components are quoted with statistical uncertainty from the data fits and systematic uncertainty of the efficiency and the fit. For the q component that is not fitted in the data, the SR yield is taken directly from MC simulation (with the $t\bar{t}$ component weighted to match the data using the scaling derived for $\ell\ell + \mu\mu$) and is quoted with its total uncertainty.

$4e$+$2\mu 2e$				
type	data fit	ZZ^*+HF	efficiency [%]	SR yield
f	3075 ± 56	280 ± 6	0.20 ± 0.04	$5.68 \pm 0.36 \pm 1.19$
γ	208 ± 17	19.4 ± 0.5	0.71 ± 0.14	$1.34 \pm 0.35 \pm 0.27$
q	(MC-based estimation)			6.34 ± 1.93

For the $\ell\ell + \mu\mu$ final state, the fractions are obtained from MC simulation. The validity of the fractions are checked by comparing the results in the Relaxed Isolation-d_0 CR. It is found that MC fractions are well modelled within the statistical uncertainty of the data.

To include the impact of the mass window in the SR definition, the $m_{4\ell}$ distribution of $Z+$jets and $t\bar{t}$ for $\ell\ell + \mu\mu$ and f and γ for $\ell\ell + ee$ are smoothed in each category using the kernel density estimation method [117]. These distributions are then integrated to obtain the fraction of events falling within the mass range. The smoothed $m_{4\ell}$ distributions for the inclusive region are shown in Figure 3.30.

The final yield estimates for the reducible background in the reconstructed categories are presented in Table 3.9 with the associated systematic uncertainty. The uncertainty on the inclusive background estimates due to the data/MC difference in the selection efficiencies related to the lepton ID, isolation and impact parameter significance criteria and the relatively small statistical uncertainty from the fit is treated as a correlated error across each category. Finally, there is an additional uncorrelated uncertainty that is due to the statistical precision of the MC samples used to derive the fraction of inclusive estimates

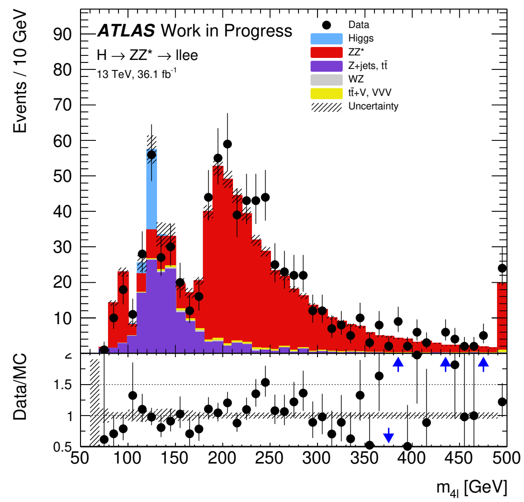

(a) $m_{4\ell}$

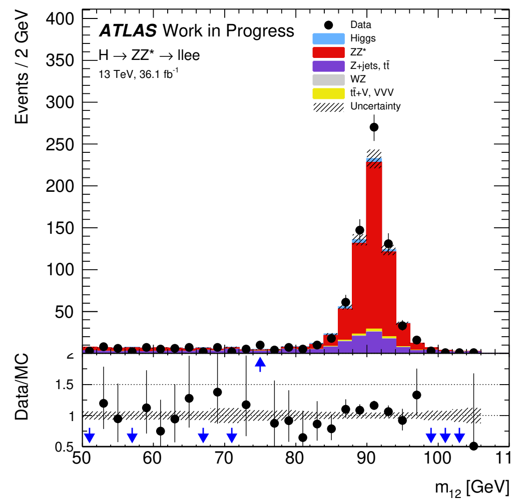

(b) m_{12}

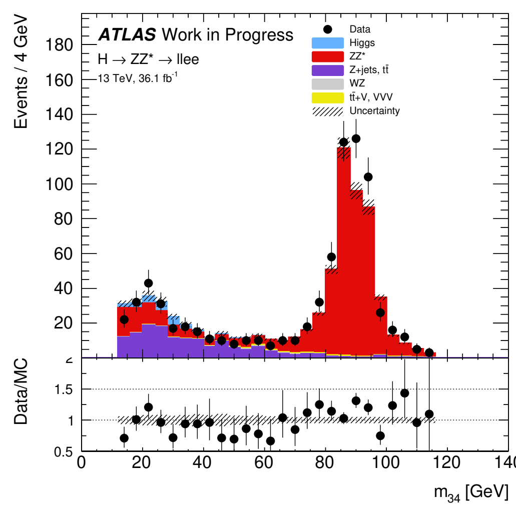

(c) m_{34}

Figure 3.29: The $m_{4\ell}$, m_{12} and m_{34} distributions for the $\ell\ell + ee$ final state in the Relaxed Isolation-d_0 CR. The last bin contains the integral of the overflow. The systematic uncertainty on the prediction is shown by the dashed band. The arrows in the ratio panel indicate data points outside the plotted range.

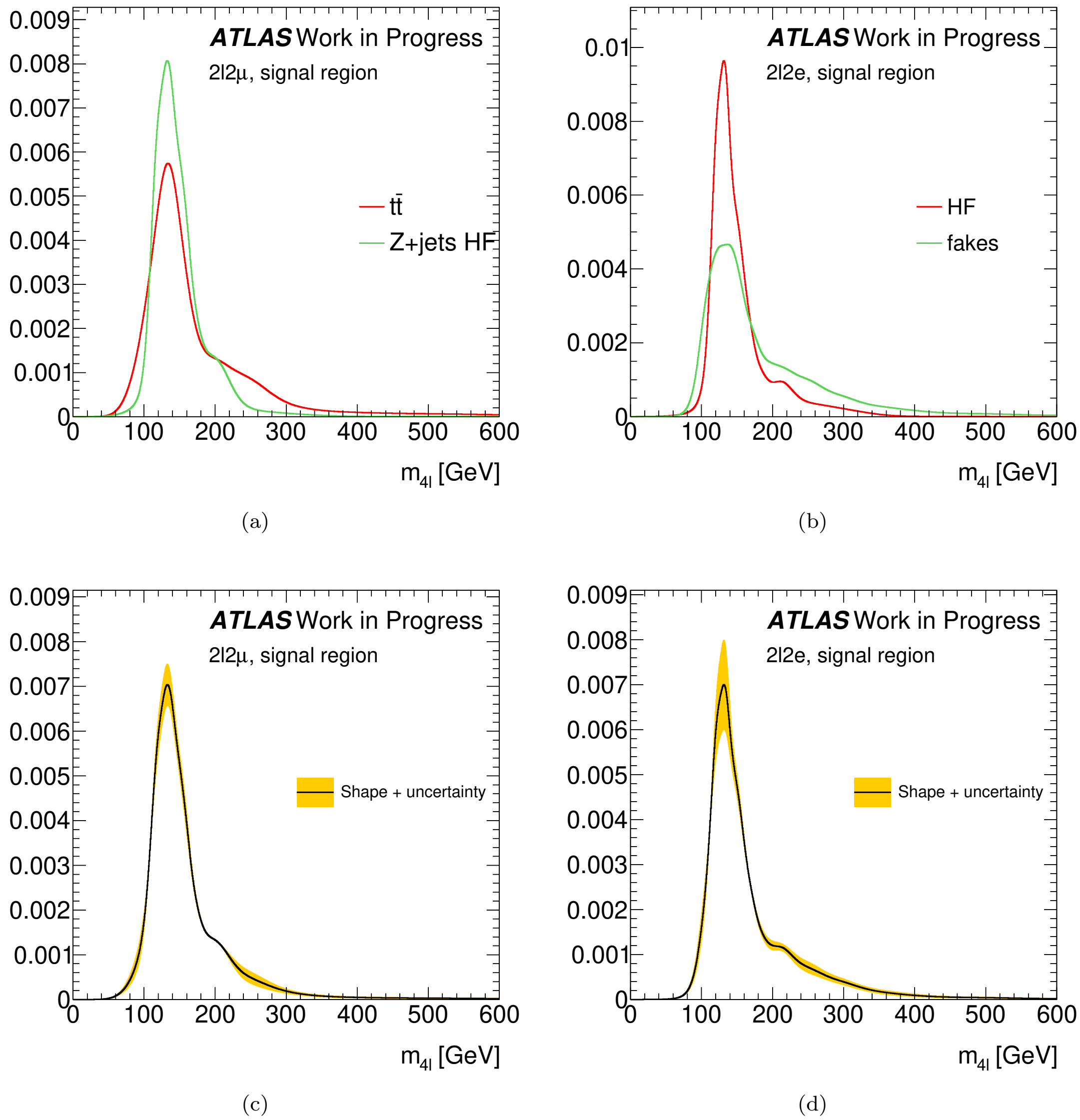

Figure 3.30: The smoothed $m_{4\ell}$ distributions for each $\ell\ell + \mu\mu$ and $\ell\ell + ee$ background process shown respectively in (a) and (b). The combined results with the associated uncertainty band are shown in (c) and (d). The uncertainty is obtained by varying the relative contributions within their fit uncertainty.

Table 3.9: Estimates of reducible background yields in each reconstructed event category in the signal region for 36.1 fb^{-1} at $\sqrt{s} = 13$ TeV, together with the associated correlated and uncorrelated systematic uncertainties. The total error in each category is composed of the combined statistical and systematic uncertainty of the inclusive background estimate, as well as an additional statistical uncertainty in the fraction of the reducible background in each category. The uncertainty due to the inclusive background estimate is considered as correlated (penultimate column), while the statistical uncertainty due to the event categorization (last column) is uncorrelated across the reconstructed event categories. The large statistical uncertainty in the VH-Lep-enriched category is due to limited statistics in the MC simulation.

Reconstructed		Reducible background		Uncertainty	
event category	$\ell\ell+\mu\mu$	$\ell\ell+ee$	Total	Corr.	Uncorr.
$0j$	0.96 ± 0.21	1.25 ± 0.23	2.21 ± 0.33	$\pm 13\%$	$\pm 7\%$
$1j$-$p_T^{4\ell}$-Low	0.21 ± 0.05	0.30 ± 0.06	0.52 ± 0.08	$\pm 13\%$	$\pm 10\%$
$1j$-$p_T^{4\ell}$-Med	0.19 ± 0.12	0.16 ± 0.04	0.35 ± 0.13	$\pm 13\%$	$\pm 40\%$
$1j$-$p_T^{4\ell}$-High	0.0049 ± 0.0025	0.036 ± 0.008	0.041 ± 0.009	$\pm 13\%$	$\pm 18\%$
VBF-enriched-p_T^j-Low	0.14 ± 0.04	0.128 ± 0.025	0.27 ± 0.05	$\pm 13\%$	$\pm 15\%$
VBF-enriched-p_T^j-High	0.019 ± 0.010	0.018 ± 0.004	0.037 ± 0.009	$\pm 13\%$	$\pm 28\%$
VH-Had-enriched	0.060 ± 0.017	0.078 ± 0.015	0.139 ± 0.025	$\pm 13\%$	$\pm 14\%$
VH-Lep-enriched	0.003 ± 0.004	0.0005 ± 0.0008	0.0031 ± 0.0031	$\pm 13\%$	$\pm 100\%$
ttH-enriched	0.009 ± 0.004	0.022 ± 0.005	0.031 ± 0.007	$\pm 13\%$	$\pm 22\%$

falling in each category.

The BDT discriminant shapes for the reducible background are obtained from MC simulation. The contribution of each process is rescaled to match the data-driven estimate. The shapes are shown in Figure 3.31. To increase the statistical precision, the isolation requirements are relaxed and the $m_{4\ell}$ range is extended. The mass window requirement is relaxed in the $0j$ category to $115 < m_{4\ell} < 130$ GeV and to $110 < m_{4\ell} < 200$ GeV for all other categories. These looser selection criteria have been checked and found to show minimal impact on the shape of the BDT distributions within the expected sensitivity of the analysis. The statistical precision of the MC samples and the uncertainty in the relative fractions of the different processes are taken into account as a systematic uncertainty.

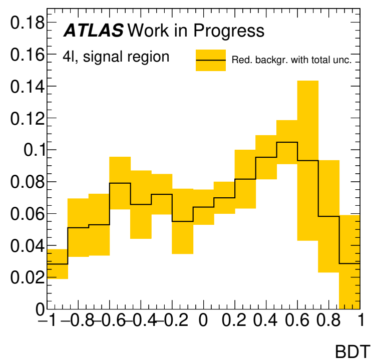

(a) $0j$

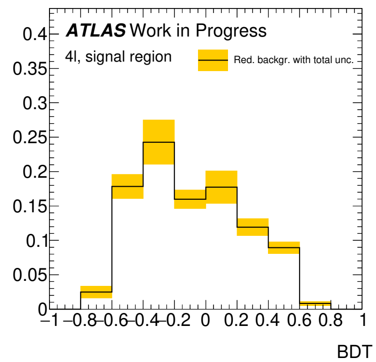

(b) $1j$-$p_{\mathrm{T}}^{4\ell}$-Low

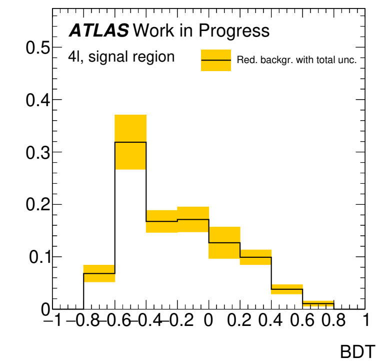

(c) $1j$-$p_{\mathrm{T}}^{4\ell}$-Med

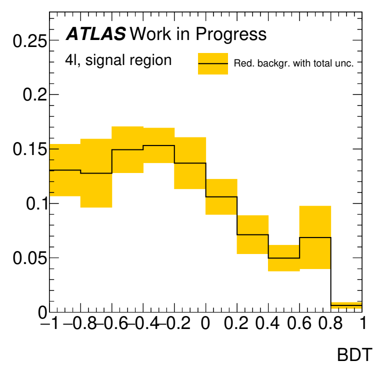

(d) VH-Had-enriched

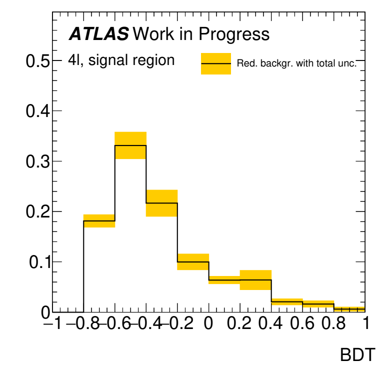

(e) VBF-enriched-p_{T}^{j}-Low

Figure 3.31: The BDT discriminant shape for reducible background. The uncertainty band is obtained by taking into account the statistical precision of the MC sample and by varying the fraction of different processes.

3.7 Systematic Uncertainty

For this analysis, different sources of uncertainties are expected to contribute to the cross-section measurement of the production modes. The main and the largest source expected in this analysis comes from the limited dataset, and this uncertainty is labelled as statistical. It is estimated using the procedure outlined in Section 3.8.2. All other sources are labelled as systematic uncertainties.

Systematic uncertainties are further divided into two categories. Experimental systematic uncertainties originate from the analysis choices related to the detector such as calibration of energy scale, correcting object reconstruction in MC simulation to match data, luminosity measurement or estimating background processes through data-driven methods such as described in Section 3.6.2. On the other hand, theoretical uncertainties originate from the choices made when modelling the signal and background processes using MC simulation.

When measuring the cross-sections (Equation 3.1) or signal strength modifiers (Equation 3.2) uncertainties affect the acceptance, detector efficiency and BDT discriminant distributions. These also affect the background estimates, which in turn influence the extracted yield and the measured cross-sections. Furthermore, for signal strength modifiers, the error on the predicted signal cross-section needs to be taken into account, while for cross-section measurements these uncertainties have no impact. This allows cross-sections measurements to have smaller systematics uncertainties and be more ‘model-independent’.

The dominant sources of uncertainties are outlined in the following sections. The impact of these uncertainties on the cross-section measurements in different production bins is summarized in Table 3.10 and for the signal strength modifiers in Table 3.11. The impact, defined as the percent increase in the total error when the given uncertainty is added to the fit model, is calculated using the statistical method described in Section 3.8.2. Due to statistical correlations between the fit parameters, the impacts are typically different than the derived uncertainties. As described previously, the theoretical uncertainties have a smaller impact for cross-section measurements. A description of the experimental and theoretical systematic uncertainties is provided below.

3.7.1 Experimental Uncertainty

The uncertainty on the integrated luminosity is 3.2%. It is derived following the Van der Meer methodology as described in Ref. [118]. The preliminary calibration of the luminosity scale using x–y beam-separation scans was performed in August 2015 and May 2016.

The presence of pile-up interaction affects the reconstruction, energy calibration and identification of different physics objects and needs to be modelled accurately in simulations. The uncertainty is derived by varying the average number of pile-up events in the simulation. This is to cover the uncertainty in the ratio of the predicted to measured inelastic cross sections [119]. The impact on the measured cross-section is about 2%.

In addition to corrections to the lepton energy/momentum scale and resolution, the MC simulation is corrected to match the measured selection efficiencies for lepton reconstruction, identification and isolation criteria [109, 110, 120]. Typical uncertainties in the predicted yield due to the reconstruction and identification efficiency scale factors are in the range 0.5–1.0% for muons and 1.0–1.3% for electrons. The uncertainties in the expected yields coming from the muon and electron isolation efficiencies are also taken into account, with the typical size being 2%. The uncertainties in the electron and muon energy scale and resolution are small and have a negligible impact on the measurements.

Table 3.10: Impact of the dominant systematic uncertainties (in percent) on the measured inclusive, the Stage 0 and Reduced Stage 1 production mode cross sections $\sigma \cdot B(H \to ZZ^*)$. Signal theory uncertainties include only acceptance effects and no uncertainty in predicted cross sections. Similar sources of systematic uncertainties are grouped together - Luminosity (Lumi.), electron/muon reconstruction and identification efficiencies and pile-up modelling (e, μ, pile-up), jet energy scale/resolution and b-tagging efficiencies (Jets, flav. tag.), change in the acceptance and BDT shape due to experimental uncertainty in the Higgs mass (Higgs mass), uncertainties on reducible background (Red. bkg.), theoretical uncertainties on ZZ^* background, and theoretical uncertainties on the signal due to parton density function (PDF), QCD scale (QCD) and showering algorithm (Shower).

	Experimental uncertainties [%]					Theory uncertainties [%]			
Production bin	Lumi	e, μ, pile-up	Jets, flav. tag.	Higgs mass	Red. bkg.	ZZ^* bkg.	Signal theory PDF	Signal theory QCD scale	Signal theory Shower
Inclusive cross section									
$\sigma \cdot B(H \to ZZ^*)$	4.1	3.1	0.7	0.8	0.9	1.9	0.3	0.8	1.2
Stage-0 production bin cross sections									
ggF	4.3	3.4	1.1	1.2	1.1	1.8	0.5	1.8	1.4
VBF	2.6	2.7	10.0	1.3	0.9	2.2	1.6	10.8	5.3
VH	3.0	2.7	10.6	1.6	1.7	5.9	2.1	11.9	3.7
ttH	3.6	2.9	19.4	< 0.1	2.4	1.9	3.3	7.9	2.1
Reduced Stage-1 production bin cross sections									
ggF-0j	4.4	4.1	5.1	2.0	1.2	1.7	0.3	0.5	1.0
ggF-1j-p_T^H-Low	4.2	3.8	17.8	1.1	1.4	5.0	0.2	0.8	2.8
ggF-1j-p_T^H-Med	3.7	4.4	6.2	< 0.1	3.6	2.0	0.2	0.8	6.3
ggF-1j-p_T^H-High	3.5	2.7	8.8	< 0.1	1.0	1.0	< 0.1	1.5	6.8
ggF-2j	4.2	4.0	17.6	< 0.1	1.5	8.2	0.1	2.9	6.2
VBF-p_T^j-Low	2.9	2.4	5.0	< 0.1	0.5	1.6	0.3	4.0	5.6
VBF-p_T^j-High	3.2	6.7	16.8	< 0.1	6.7	4.1	2.0	25.6	9.5
VH-Had	3.1	4.1	10.0	< 0.1	1.3	1.0	< 0.1	5.2	5.0
VH-Lep	3.4	4.6	2.6	< 0.1	2.5	2.1	0.3	1.1	0.8
ttH	3.6	3.3	5.0	< 0.1	2.4	1.2	3.3	7.1	2.0

Table 3.11: Impact of the dominant systematic uncertainties (in percent) on the measured inclusive, the Stage 0 and Reduced Stage 1 production mode signal strength modifiers. Signal theory uncertainties include both acceptance effects and the uncertainty in predicted cross sections. Similar sources of systematic uncertainties are grouped together - Luminosity (Lumi.), electron/muon reconstruction and identification efficiencies and pile-up modelling (e, μ, pile-up), jet energy scale/resolution and b-tagging efficiencies (Jets, flav. tag.), change in the acceptance and BDT shape due to experimental uncertainty in the Higgs mass (Higgs mass), uncertainties on reducible background (Red. bkg.), theoretical uncertainties on ZZ^* background, and theoretical uncertainties on the signal due to parton density function (PDF), QCD scale (QCD) and showering algorithm (Shower).

Production bin	Experimental uncertainties [%]					Theory uncertainties [%]			
	Lumi	e, μ, pile-up	Jets, flav. tag	Higgs mass	Red. bkg.	ZZ^* bkg.	Signal theory PDF	Signal theory QCD scale	Signal theory Shower
Inclusive cross section									
μ	4.1	3.1	0.6	0.8	0.9	1.9	2.4	5.1	1.1
Stage-0 production bin cross sections									
ggF	4.3	3.4	1.2	1.2	1.1	1.8	2.8	5.2	1.4
VBF	2.6	2.7	9.9	1.3	0.9	2.2	2.2	11.6	5.3
VH	3.0	2.7	10.5	1.6	1.7	5.8	3.1	14.1	3.7
ttH	3.6	2.9	19.4	< 0.1	2.4	1.9	3.3	8.3	2.1
Reduced Stage-1 production bin cross sections									
ggF-0j	4.4	4.1	5.3	2.0	1.2	1.7	2.8	6.0	1.0
ggF-1j-p_{T}^{H}-Low	4.2	3.8	18.5	1.1	1.4	5.0	4.0	13.8	3.0
ggF-1j-p_{T}^{H}-Med	3.7	4.4	6.5	< 0.1	3.6	2.0	3.6	13.9	6.3
ggF-1j-p_{T}^{H}-High	3.5	2.8	9.4	< 0.1	1.0	1.0	3.4	20.5	6.5
ggF-2j	4.2	4.1	18.2	< 0.1	1.5	8.2	3.4	19.7	5.8
VBF-p_{T}^{j}-Low	2.9	2.4	5.4	< 0.1	0.5	1.6	1.0	4.6	5.8
VBF-p_{T}^{j}-High	3.2	6.6	17.4	< 0.1	6.7	4.1	3.0	26.5	9.6
VH-Had	3.1	4.1	10.5	< 0.1	1.3	1.0	1.7	8.3	9.6
VH-Lep	3.4	4.6	2.7	< 0.1	2.5	2.1	1.1	6.4	0.8
ttH	3.6	3.3	5.2	< 0.1	2.4	1.2	3.3	7.6	2.0

The uncertainties in the jet energy scale and resolution are in the range of 3–7% and 2–4%, respectively [121, 122] and have an impact on migrating the predicted yields between different reconstructed categories. Given the analysis categories, the impacts of these uncertainties are more relevant for the VBF, *VH* and *ttH* production modes cross-section measurements (10–20%) and for all the reduced Stage-1 cross-section measurements, including the ggF process split into the different *n-jet* exclusive production bins (5–20%). These are negligible for the inclusive and the ggF (Stage-0) cross-section measurements.

Similar to lepton identification, the efficiency in simulation for the *b*-tagging algorithm is corrected by using observed $t\bar{t}$ events. The uncertainties associated with this are at the level of a few percent over most of the jet p_{T} range [123]. This uncertainty is only relevant in the *ttH*-enriched category, with its expected impact being approximately 5% in the *ttH* cross-section measurement.

The impact of the precision of the measured Higgs boson mass, $m_H = 125.09 \pm 0.24$ GeV [28], on the signal acceptance due to the signal region mass window requirement is negligible. A small dependency of the $\mathrm{BDT}_{\mathrm{ggF}}$ shape on m_H is observed for the signal (below 2% in the highest BDT bins) and is included in the fit model. This uncertainty, obtained by comparing the $\mathrm{BDT}_{\mathrm{ggF}}$ shape obtained from simulation with different Higgs boson masses, affects the measurement of ggF production, as well as the measurements in other production bins with large ggF contamination.

3.7.2 Theoretical uncertainties

The theoretical modelling of the signal and background processes is affected by uncertainties from QCD scale variations, modelling of parton showers and multiple-particle interactions, and PDF uncertainties. These are typically estimated by the MC simulation generator internally reweighing each event with an alternative PDF, QCD or shower parameter choice, or using alternative generators, or reweighing events based on theoretical studies and truth particle level information.

The impact of the theory systematic uncertainties on the signal depends on the kind of measurement that is performed. For the signal strength measurements and the EFT analysis, each source of theory uncertainty affects both the fiducial acceptance and the predicted SM cross section. For the cross-section measurements, only effects on the acceptance within the STXS production bin need to be considered. Moreover, the two different granularities of the STXS scheme will have different effect due to theoretical uncertainties. For example, uncertainties changing the number of jets for the ggF process will have an impact on the Stage 0 measurement, as event topologies with different jet multiplicities have different acceptance and reconstruction efficiencies. However, for the Reduced Stage 1 measurement, as the ggF STXS bins are split first according to the jet multiplicity, the impact of this systematic will mostly cancel out.

One of the dominant sources of theoretical uncertainty is the prediction of the ggF process in different jet categories. To estimate the QCD scale variation and migration effects on the ggF cross sections, the approach described in Ref. [44] is used, which exploits the latest predictions for the inclusive jet cross sections and the exclusive jet bin fractions. In particular, the uncertainty from the choice of the factorization and renormalization scales, the choice of resummation scales, and the migrations between the 0-jet and 1-jet phase-space bins or between the 1-jet and $\geq$ 2-jet bins are considered as uncorrelated variations. The impact of QCD scale variations on the Higgs boson p_{T} distribution is also taken into account as an additional uncorrelated uncertainty. The uncertainty in the Higgs boson p_{T} at higher order, originating from the assumption about masses in the heavy-quark loop, is taken into account by comparing the p_{T} distribution predictions to finite-mass calculations. An additional uncertainty in the acceptance of the ggF process in VBF topologies due to missing higher orders in QCD in the calculation is estimated by varying the resummation and factorization scales using fixed-order calculations implemented in the MCFM generator [124]. The effects of these uncertainties are propagated by matching the event topology as generated at the matrix element level and scaling the MC simulated weight by the associated uncertainty [125]. The variation on acceptance typically ranges from 3–25%, with higher uncertainties associated with events with high jet multiplicity.

For the other production modes, the QCD scale uncertainties are obtained by varying the resummation and factorization scale choice during the ME generation by factors of two. These are propagated through the internal reweighing scheme in the POWHEG-BOX v2 generator [62, 63]. The largest relative difference between the prediction with a given configuration and the nominal configuration is chosen to define the uncertainty in each experimental category. QCD scale uncertainties are treated as uncorrelated among the different production modes. For the VBF process, the uncertainty on the predicted acceptance is below 1%, while for VH process, the uncertainty is approximately 5%.

The uncertainties in the acceptances due to the modelling of parton showers and multiple-parton interactions are estimated by varying the values used for the AZNLO tune eigenvectors [75] and by comparing the acceptance computed using the parton showering algorithm from the PYTHIA 8 generator with the HERWIG7 generator for the ggF, VBF and VH processes. The HERWIG++ generator is compared with the PYTHIA 8 generator for the ttH process. The uncertainty due to each AZNLO tune variation is taken as correlated among the different production modes while the difference between the parton showering algorithms is treated as an uncorrelated uncertainty. The AZNLO tune variations have a small impact on the measurement, but the choice of parton showering algorithm can have up to a 15% variation in the predicted acceptance for the VBF and VH processes.

Compared to the statistical precision, uncertainties due to the modelling of the ggF production in association with b-quarks have a negligible affect in the ttH production bin and are not taken into account for the final result.

The impact of the PDF uncertainties is estimated with the eigenvector variations of the PDF4LHC_NLO_30 Hessian set. These are propagated as a variation on the MC weight as computed by the internal POWHEG-BOX v2 generator reweighing scheme. The modification of the predictions for each eigenvector variation, which is approximately 0.5–1.5%, is added as a separate source of uncertainty in the fit model. The same procedure is applied for the ggF, VBF and VH processes, enabling correlations in the uncertainty to be taken into account in the fit model.

For signal strength measurements, an additional uncertainty (2.2%) related to the $H \rightarrow ZZ^*$ branching ratio [79, 80] is included in the measurement.

The same procedure is used to estimate the impact of the sources of theoretical uncertainties described above on the shape of BDT discriminants. In addition, for VBF Higgs production, the changes in the $\Delta\eta_{jj}$ distribution as predicted at NNLO accuracy compared to NLO in QCD [126] are considered and shown to have a negligible effect on the BDT distributions. For ggF production, a further cross-check is performed by comparing the $\mathrm{BDT}_{\mathrm{VBF}}^{1j\text{-}p_{\mathrm{T}}^{4\ell}\text{-Low}}$, $\mathrm{BDT}_{\mathrm{VBF}}^{1j\text{-}p_{\mathrm{T}}^{4\ell}\text{-Med}}$, $\mathrm{BDT}_{\mathrm{VBF}}$ and $\mathrm{BDT}_{VH\text{-Had}}$ shapes in the corresponding categories as predicted by POWHEG and MADGRAPH5_AMC@NLO with the FxFx merging scheme. The BDT shapes from the two generators agree within the statistical uncertainties and, therefore, no additional shape uncertainty is included.

The dominant theoretical uncertainty in the expected ZZ^* background yield is obtained by varying the factorization and renormalization QCD scales by factors of two. The configuration with the largest difference with respect to the nominal configuration is chosen to define the uncertainty in each experimental category. This uncertainty is about 4% for the inclusive event yield and is as large as 30% for the categories where additional jets are required. The impact of the QCD scale uncertainty on the BDT discriminant shapes is approximately 1–2%.

The PDF uncertainty on the ZZ^* event yield in each category and on the BDT distributions, obtained using the MC replicas of the NNPDF3.0 PDF set, is found to be approximately 1–2%.

The impact of the parton shower modelling uncertainty on the ZZ^* event yield is estimated to be approximately 1–5%, with the largest value reached in the categories where the presence of one or more jets is required.

3.8 Results and interpretation

3.8.1 Observed Data

The expected and observed four-lepton invariant mass distribution of the selected Higgs boson candidates after the event selection, FSR recovery and applying the Z mass constraint is shown in Figure 3.32 for the inclusive category and for each final state in Figure 3.33. The corresponding expected and observed number of events are shown in Table 3.12 separately for each of the four decay channels. The predicted event yields are in reasonable agreement with the data.

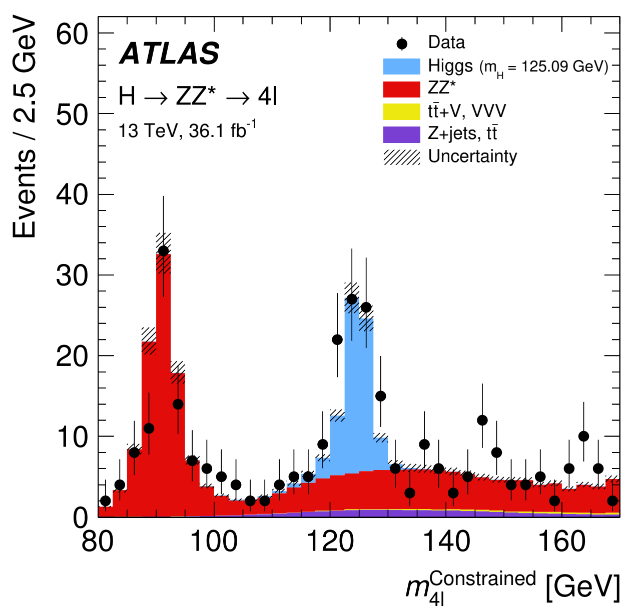

Figure 3.32: The expected and observed four-lepton invariant mass distribution for the selected Higgs boson candidates with a constrained Z boson mass, shown for an integrated luminosity of 36.1 fb^{-1} and at $\sqrt{s} = 13$ TeV assuming the SM Higgs boson signal with a mass $m_H = 125.09$ GeV. The error bars represent the 68.3% central confidence interval statistical uncertainty. The systematic uncertainty on the prediction is shown by the dashed band.

The observed and expected distributions of the jet multiplicity, the dijet invariant mass, as well as the leading jet and the four-lepton transverse momenta, which are used for the categorization of reconstructed events, are shown in Figure 3.34 for different stages of the event categorization. As shown

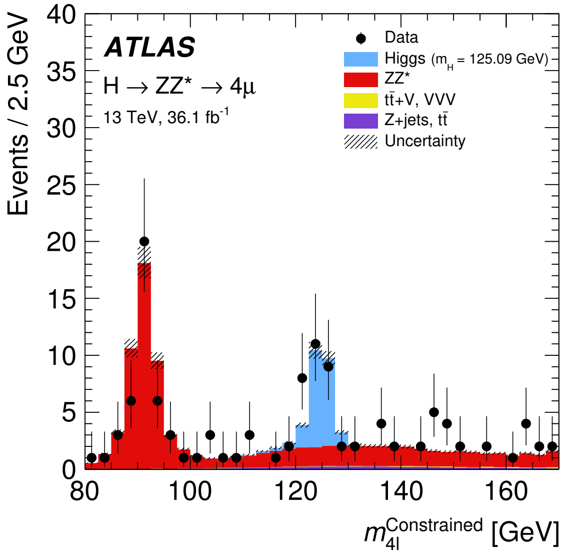

(a) 4μ

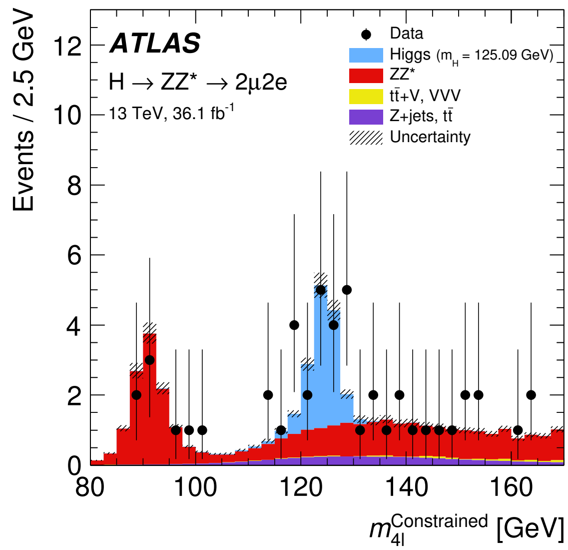

(b) $2\mu 2e$

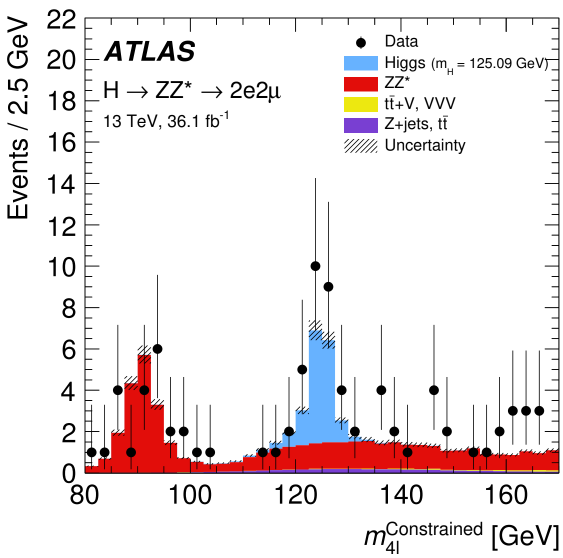

(c) $2e2\mu$

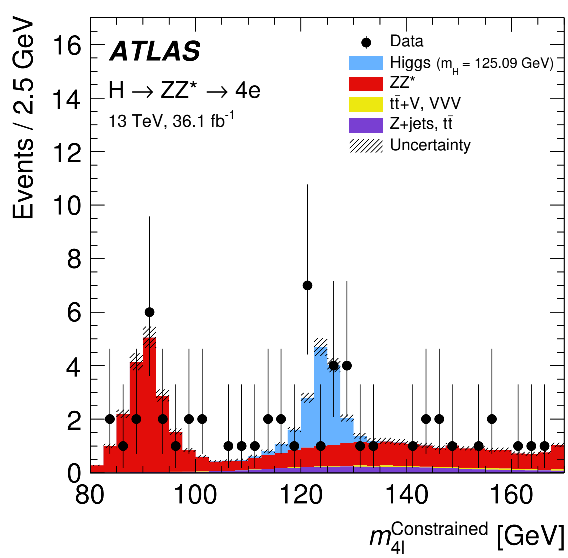

(d) 44

Figure 3.33: The observed and expected four-lepton invariant mass distribution for the selected Higgs boson candidates with a constrained Z boson mass, shown for an integrated luminosity of 36.1 fb^{-1} at $\sqrt{s} = 13$ TeV for the different channels of the analysis: (a) 4μ, (b) $2\mu 2e$, (c) $2e2\mu$ and (d) $4e$. The error bars represent the 68.3% central confidence interval statistical uncertainty. The systematic uncertainty on the prediction is shown by the dashed band.

Table 3.12: The expected and observed numbers of signal and background events in the four-lepton decay channels for an integrated luminosity of 36.1 fb^{-1} and at $\sqrt{\text{s}} = 13$ TeV, assuming the SM Higgs boson signal with a mass $m_H = 125.09$ GeV. The second column shows the expected number of signal events for the full mass range while the subsequent columns correspond to the mass range of $118 < m_{4\ell} < 129$ GeV. In addition to the ZZ^* background, the contribution of other backgrounds is shown, comprising of the data-driven estimate from Table 3.9 and the simulation-based estimate of contributions from rare triboson and $t\bar{t}V$ processes. Statistical and systematic uncertainties are added in quadrature.

Decay channel	Signal (full mass range)	Signal	ZZ^* background	Other backgrounds	Total expected	Observed
4μ	21.0 ± 1.7	19.7 ± 1.6	7.5 ± 0.6	1.00 ± 0.21	28.1 ± 1.7	32
$2e2\mu$	15.0 ± 1.2	13.5 ± 1.0	5.4 ± 0.4	0.78 ± 0.17	19.7 ± 1.1	30
$2\mu 2e$	11.4 ± 1.1	10.4 ± 1.0	3.57 ± 0.35	1.09 ± 0.19	15.1 ± 1.0	18
$4e$	11.3 ± 1.1	9.9 ± 1.0	3.35 ± 0.32	1.01 ± 0.17	14.3 ± 1.0	15
Total	59 ± 5	54 ± 4	19.7 ± 1.5	3.9 ± 0.5	77 ± 4	95

in Figures 3.34(c) and 3.34(d), there is an excess of events observed in the sample with ≥ 2 jets (shown as a dijet invariant mass distribution) and also in the subset with $m_{jj} > 120$ GeV (shown as the jet p_{T} distribution) in comparison to the expectations. All other distributions are in good agreement with the data. The expected numbers of signal and background events in each reconstructed event category[1] are shown in Table 3.13 together with the corresponding observed number of events. The expected event yields are in reasonable agreement with the observed ones. The largest differences are observed in the two VBF-enriched categories. This difference is consistent with an upward statistical fluctuation.

The expected and observed distributions of the BDT discriminants are shown in Figure 3.35. A small excess is observed at larger values of the VBF-enriched-p_{T}^{j}-Low, while all other distributions are in good agreement with the data.

[1] The VH-enriched category is split into two sub-categories with p_{T}^{4l} below and above 150 GeV for the tensor structure measurement.

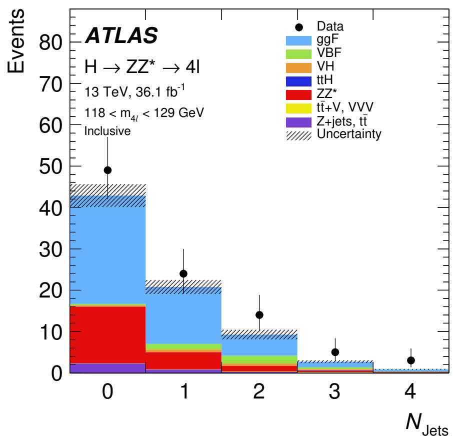

(a)

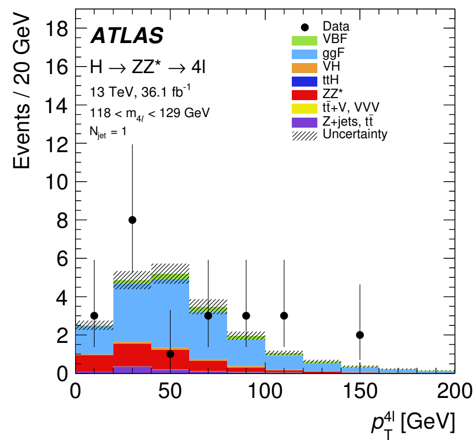

(b)

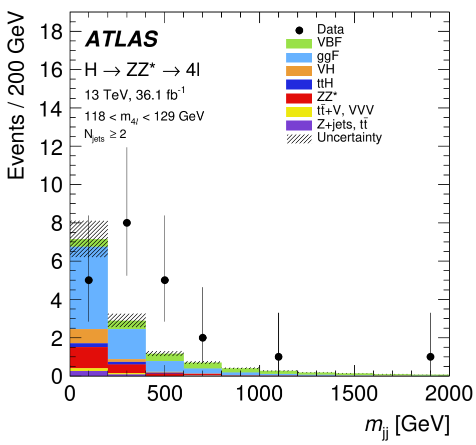

(c)

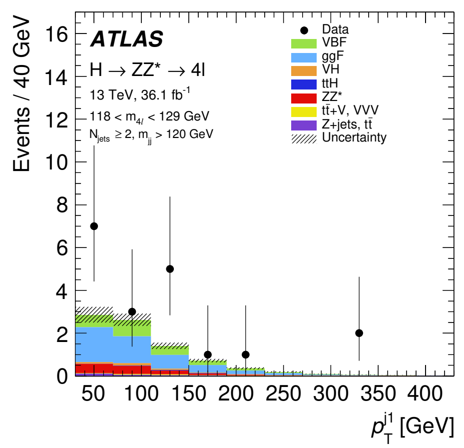

(d)

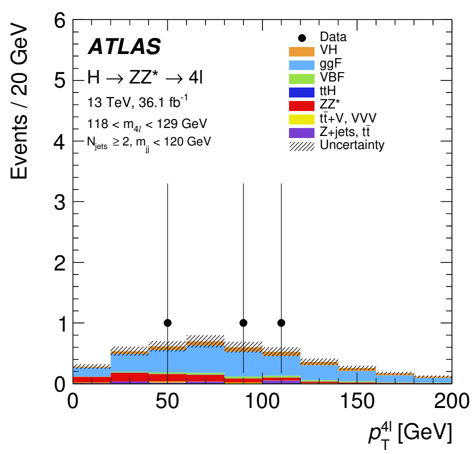

(e)

Figure 3.34: The observed and expected distributions of (a) N_{jet} after the inclusive selection, (b) p_{T}^{4l} in the 1-jet categories, (c) m_{jj} in the 2-jet categories, (d) p_{T}^{j1} in the VBF-enriched categories and (e) p_{T}^{4l} in the VH-Had-enriched categories for an integrated luminosity of 36.1 fb^{-1} collected at $\sqrt{\text{s}} = 13$ TeV assuming the SM Higgs boson signal with a mass $m_H = 125.09$ GeV. The systematic uncertainty on the prediction is shown by the dashed band.

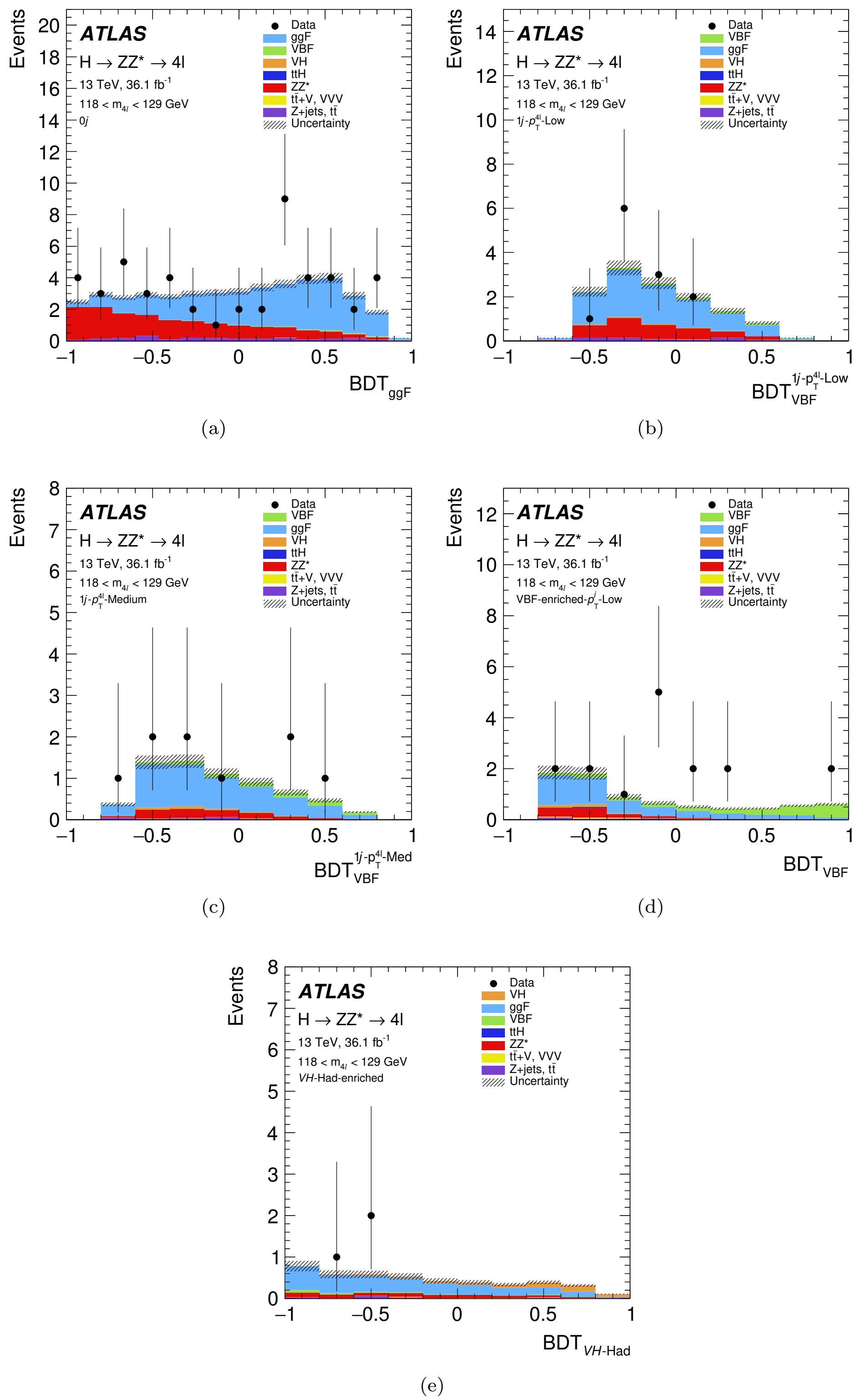

Figure 3.35: The observed and expected BDT output distributions in the (a) $0j$, (b) $1j$-$p_{\mathrm{T}}^{4\ell}$-Low, (c) $1j$-$p_{\mathrm{T}}^{4\ell}$-Med, (d) VBF-enriched-p_{T}^{j}-Low and (e) VH-Had-enriched categories for an integrated luminosity of 36.1 fb^{-1} and at $\sqrt{s} = 13$ TeV assuming the SM Higgs boson signal with a mass $m_H = 125.09$ GeV.

Table 3.13: The expected and observed numbers of signal and background events in the mass range $118 < m_{4\ell} < 129$ GeV for an integrated luminosity of 36.1 fb^{-1} and at $\sqrt{s} = 13$ TeV in each reconstructed event category (including the splitting of the VH-enriched category for the tensor structure measurement), assuming the SM Higgs boson signal with a mass $m_H = 125.09$ GeV. In addition to the ZZ^* background, the contribution of other backgrounds is shown, comprising the data-driven estimate from Table 3.9 and the simulation-based estimate of contributions from rare triboson and $t\bar{t}V$ processes. Statistical and systematic uncertainties are added in quadrature.

Reconstructed event category	Signal	ZZ^* background	Other backgrounds	Total expected	Observed
$0j$	26.8 ± 2.5	13.7 ± 1.0	2.23 ± 0.31	42.7 ± 2.7	49
$1j$-$p_{\mathrm{T}}^{4\ell}$-Low	8.8 ± 1.1	3.1 ± 0.4	0.53 ± 0.07	12.5 ± 1.2	12
$1j$-$p_{\mathrm{T}}^{4\ell}$-Med	5.4 ± 0.7	0.88 ± 0.12	0.38 ± 0.05	6.7 ± 0.7	9
$1j$-$p_{\mathrm{T}}^{4\ell}$-High	1.47 ± 0.24	0.139 ± 0.022	0.045 ± 0.007	1.65 ± 0.24	3
VBF-enriched-p_{T}^{j}-Low	6.3 ± 0.8	1.08 ± 0.32	0.40 ± 0.04	7.7 ± 0.9	16
VBF-enriched-p_{T}^{j}-High	0.58 ± 0.10	0.093 ± 0.032	0.054 ± 0.006	0.72 ± 0.10	3
VH-Had-enriched-$p_{\mathrm{T}}^{4\ell}$-Low	2.9 ± 0.5	0.63 ± 0.16	0.169 ± 0.021	3.7 ± 0.5	3
VH-Had-enriched-$p_{\mathrm{T}}^{4\ell}$-High	0.64 ± 0.09	0.029 ± 0.008	0.0182 ± 0.0022	0.69 ± 0.09	0
VH-Lep-enriched	0.318 ± 0.019	0.049 ± 0.008	0.0137 ± 0.0019	0.380 ± 0.020	0
ttH-enriched	0.39 ± 0.04	0.014 ± 0.006	0.07 ± 0.04	0.47 ± 0.05	0
Total	54 ± 4	19.7 ± 1.5	3.9 ± 0.5	77 ± 4	95

3.8.2 Measurement of production mode cross sections

Statistical method

In order to measure the Higgs boson production cross section times branching ratio for $H \to ZZ^*$ decay for each Stage-0 or reduced Stage-1 production bins, a fit to the data is performed. The likelihood function $\mathcal{L}(\vec{\sigma}, \vec{\theta})$ depends on the Higgs boson production cross section $\vec{\sigma} = \{\sigma_1, \sigma_2, \ldots, \sigma_N\}$ for each production bin and the nuisance parameters $\vec{\theta}$ accounting for the systematic uncertainties. The likelihood function is defined as a product of conditional probabilities P over binned distributions of the discriminating observables in each reconstructed event category j as defined in Section 3.5,

$$\mathcal{L}(\vec{\sigma}, \vec{\theta}) = \prod_{j}^{N_{\text{categories}}} \prod_{i}^{N_{\text{bins}}} P\left(N_{i,j} \mid L \cdot \vec{\sigma} \cdot \vec{A}_{i,j}(\vec{\theta}) \; + B_{i,j}(\vec{\theta})\right) \times \prod_{m}^{N_{\text{nuisance}}} \mathcal{C}_m(\vec{\theta}) \, ,$$

with Poisson distributions P corresponding to the observed $N_{i,j}$ events in each bin i of the discriminating observable given the expectations for the background, $B_{i,j}(\vec{\theta})$, and for the signal, $S_{i,j}(\vec{\theta}) = L \cdot \vec{\sigma} \cdot \vec{A}_{i,j}(\vec{\theta})$, where L is the integrated luminosity and $\vec{A}_{i,j}(\vec{\theta})$ the signal acceptance in each production bin. The signal acceptances are defined in Section 3.5. Both signal acceptance and the number of background events are a function of nuisance parameters. The nuisance parameters linearly interpolate the expectations within the uncertainties outlined in Section 3.7. The nuisance parameters are constrained by adding Gaussian constraints, represented by the functions $\mathcal{C}_m(\vec{\theta})$, to the likelihood function. The cross sections are treated as independent parameters for each production bin and correlated among the different categories.

The test statistic used to compare the probabilities of different hypotheses is the ratio of profile likelihoods [127],

$$q = -2 \ln \frac{\mathcal{L}(\vec{\sigma}, \hat{\hat{\vec{\theta}}}(\vec{\sigma}))}{\mathcal{L}(\hat{\vec{\sigma}}, \hat{\vec{\theta}})} = -2 \ln \lambda(\vec{\sigma}) \ ,$$

where $\vec{\sigma}$ represents the subset of cross section(s) considered as parameter(s) of interest in the fit. The likelihood is maximized with respect to all remaining cross sections and nuisance parameters. In the denominator, the likelihood is maximized with respect to all other cross sections and nuisance parameters as well as the parameters of interest(s), which are fixed to tested values in the numerator. The parameter of interest σ in each production bin is alternatively replaced by $\mu \cdot \sigma_{\mathrm{SM}}(\vec{\theta})$, allowing for an interpretation in terms of the signal strength μ relative to the SM prediction $\sigma_{\mathrm{SM}}(\vec{\theta})$.

The best fit value for a given parameter of interest for the observed data can be found by minimizing the test statistics with respect to the parameter. The test statistic can also be used to derive confidence level (CL) intervals. In the asymptotic regime, the 68% (95%) or 1σ (2σ) CL can be constructed by finding all values of the parameters for which the test statistics satisfies $|q| < 1(4)$.

The addition of nuisance parameters and their corresponding uncertainties has the effect of increasing the CL interval. The impact of a nuisance parameter or a group of nuisance parameters can subsequently be measured by holding them to their best fit value, constructing the CL intervals and calculating the quadrature difference with respect to the nominal interval. Similarly, the statistical uncertainty can be defined by constructing the interval with all nuisance parameters held to their best fit value.

Measured results

Assuming that the relative signal fractions in each production bin are given by the predictions for the SM Higgs boson, the inclusive production cross section is measured to be

$$\sigma \cdot B \equiv \sigma \cdot B(H \to ZZ^*) \ = \ 1.73^{+0.24}_{-0.23}(\mathrm{stat.})^{+0.10}_{-0.08}(\mathrm{exp.}) \pm 0.04(\mathrm{th.}) \ \mathrm{pb} \ = \ 1.73^{+0.26}_{-0.24} \ \mathrm{pb}$$

in the rapidity range $|y_H| < 2.5$. This is compared to the SM prediction of

$$(\sigma \cdot B)_{\mathrm{SM}} \ \equiv \ (\sigma \cdot B(H \to ZZ^*))_{\mathrm{SM}} \ = 1.34 \pm 0.09 \ \mathrm{pb}.$$

The data are also interpreted in terms of the global signal strength, yielding

$$\mu = 1.28^{+0.18}_{-0.17}(\mathrm{stat.})^{+0.08}_{-0.06}(\mathrm{exp.})^{+0.08}_{-0.06}(\mathrm{th.}) = 1.28^{+0.21}_{-0.19}.$$

The measured uncertainty is split into three components: the statistical uncertainty (stat.), the uncertainty due to 'experimental' systematic uncertainties (exp.) and the uncertainty due to 'theoretical' systematic uncertainties (th.). The measured cross section and signal strength agree with the SM prediction at the level of 1.7σ and 1.6σ, respectively.

The test statistic or likelihood scans for the $\sigma \cdot B$ and μ parameter of interest are shown in Figure 3.36. The dominant systematic uncertainty for the cross-section measurement is the experimental uncertainty on the integrated luminosity and lepton efficiency measurements. The signal strength measurement is also equally affected by the theoretical uncertainty of the ggF signal yield due to QCD scale variations. This theory uncertainty in the predicted signal yield cancels out when expressing the results in terms of the ratio of the observed to expected cross section times the branching ratio $(\sigma \cdot B)/(\sigma \cdot B)_{\mathrm{SM}} = 1.29^{+0.20}_{-0.18}$, with no uncertainty assigned to the denominator.

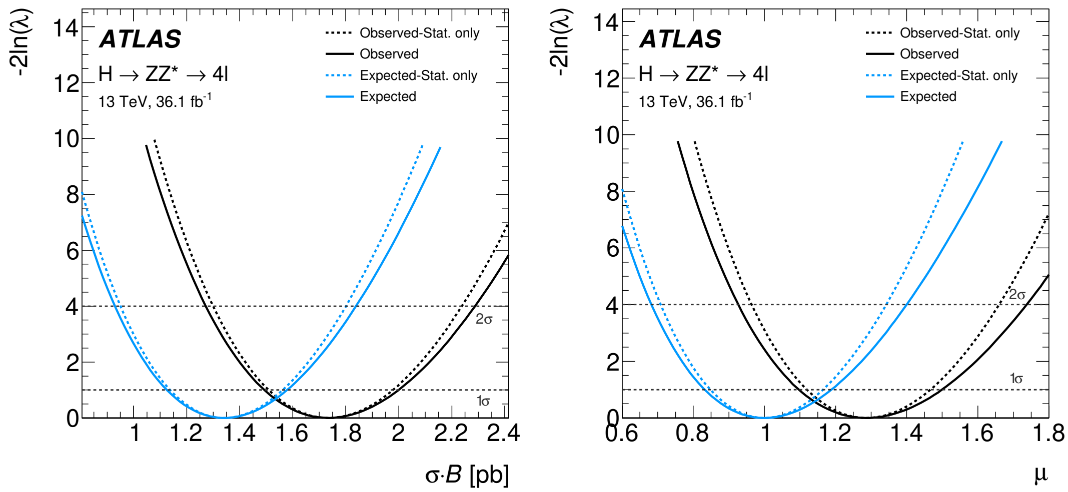

(a) $\sigma \cdot B(H \to ZZ^*)$ (b) μ

Figure 3.36: The profile likelihood as a function of (a) $\sigma \cdot B(H \to ZZ^*)$ and (b) the inclusive signal strength μ; the scans are shown both with (solid line) and without (dashed line) systematic uncertainties.

The SM expected cross section, the observed values of $\sigma \cdot B(H \to ZZ^*)$ and their ratio for the inclusive production and in each Stage-0 and reduced Stage-1 production bin are shown in Table 3.14. The corresponding values are summarized in Figure 3.37. In the ratio calculation, uncertainties on the SM expectation are not taken into account.

All measured Stage-0 and reduced Stage-1 ggF results agree with the predictions for the SM Higgs boson within 1σ. Somewhat worse agreement is obtained for the VBF bins due to the observed excess of events in the two VBF-enriched reconstructed event categories. The largest deviation of 2.2σ is observed for the Stage-0 VBF production bin. Due to the limited number of events in the VH- and ttH-enriched categories, only upper limits are set on the cross sections and signal strengths for these production modes. The limits are based on the CL_s prescription [128] and derived using pseudo-experiments. The VH and ttH parameters of interest are constrained to positive values to avoid predictions of negative event yields in the VH-Lep-enriched and ttH-enriched categories and to provide a stable fit configuration. It was found that the impact of this constraint on the final fit results is negligible.

The correlation matrices for Stage-0 and reduced Stage-1 parameters of interest is shown in Figure 3.38. For parameters of interest, such as those related to VH and ttH production modes, where only upper limits are derived, correlations with other parameters are not calculated. Due to similar event topology and limited discriminating variables, ggF-$2j$ and reduced Stage 1 VBF-like cross-sections have a high correlation.

The dominant contribution to the measurement uncertainty in the Stage-0 ggF production bin originates from the same sources as in the inclusive measurement. In the remaining three Stage-0 production bins, similar sources of uncertainty are relevant for both the cross section and the signal strength measurements: the jet energy scale or resolution uncertainties in all production bins and, additionally, jet bin migrations for the VBF and VH processes. For the reduced Stage-1 bins, the dominant cross-section uncertainties are the integrated luminosity and lepton efficiency measurements

Table 3.14: The SM expected cross section $(\sigma \cdot B)_{\text{SM}}$, the observed values of $\sigma \cdot B(H \to ZZ^*)$, and their ratio $(\sigma \cdot B)/(\sigma \cdot B)_{\text{SM}}$ for the inclusive production and in each Stage-0 and reduced Stage-1 production bin for an integrated luminosity of 36.1 fb^{-1} and at $\sqrt{s} = 13$ TeV. The bbH contribution is considered as a part of the ggF production bins. The upper limits correspond to the 95% CL obtained with pseudo-experiments using the CL_s method. The uncertainties are given as (stat.)+(exp.)+(th.) for Stage 0 and as (stat.)+(syst.) for reduced Stage 1.

Production bin	Cross section $(\sigma \cdot B)$ [pb]		$(\sigma \cdot B)/(\sigma \cdot B)_{\text{SM}}$
	SM expected	Observed	Observed
Inclusive production, $\lvert y_H \rvert < 2.5$			
	1.34 ± 0.09	$1.73^{+0.24+0.10}_{-0.23-0.08} \pm 0.04$	$1.29^{+0.18+0.07}_{-0.17-0.06} \pm 0.03$
Stage-0 production bins, $\lvert y_H \rvert < 2.5$			
ggF	1.18 ± 0.08	$1.31^{+0.26+0.09}_{-0.24-0.07} \pm 0.05$	$1.11^{+0.22+0.07}_{-0.20-0.06} \pm 0.04$
VBF	0.0928 ± 0.0028	$0.37^{+0.15}_{-0.13} \pm 0.03 \pm 0.03$	$4.0^{+1.7}_{-1.4} \pm 0.3 \pm 0.3$
VH	$0.053^{+0.003}_{-0.005}$	< 0.20	< 3.7
ttH	$0.0154^{+0.0011}_{-0.0016}$	< 0.12	< 7.5
Reduced Stage-1 production bins, $\lvert y_H \rvert < 2.5$			
ggF-$0j$	0.73 ± 0.05	$0.88^{+0.22+0.09}_{-0.20-0.07}$	$1.22^{+0.30+0.13}_{-0.27-0.09}$
ggF-$1j$-p_{T}^{H}-Low	0.174 ± 0.025	$0.08^{+0.15+0.04}_{-0.12-0.06}$	$0.5^{+0.8+0.3}_{-0.7-0.4}$
ggF-$1j$-p_{T}^{H}-Med	0.120 ± 0.018	$0.16^{+0.11+0.03}_{-0.09-0.01}$	$1.3^{+0.9}_{-0.7} \pm 0.2$
ggF-$1j$-p_{T}^{H}-High	0.024 ± 0.005	$0.03^{+0.05}_{-0.04} \pm 0.01$	$1.2^{+2.3}_{-1.7} \pm 0.3$
ggF-$2j$	0.137 ± 0.029	$0.20^{+0.16}_{-0.14} \pm 0.03$	$1.4^{+1.2}_{-1.0} \pm 0.2$
VBF-p_{T}^{j}-Low	0.0886 ± 0.0027	$0.26^{+0.18+0.03}_{-0.14-0.02}$	$3.0^{+2.0+0.4}_{-1.6-0.2}$
VBF-p_{T}^{j}-High	$0.0042^{+0.0004}_{-0.0002}$	$0.06^{+0.05}_{-0.04} \pm 0.01$	$13^{+12}_{-8} \pm 1$
VH-Had	$0.0362^{+0.0019}_{-0.0033}$	< 0.20	< 5.6
VH-Lep	$0.0166^{+0.0008}_{-0.0014}$	< 0.16	< 9.3
ttH	$0.0154^{+0.0011}_{-0.0016}$	< 0.11	< 7.1

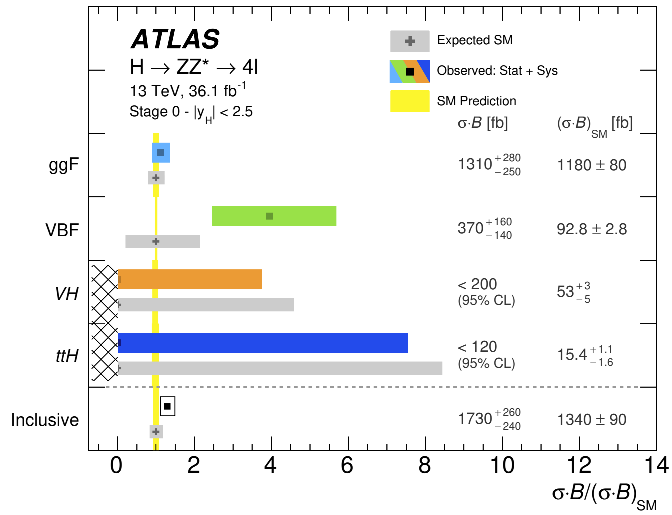

(a) Stage 0

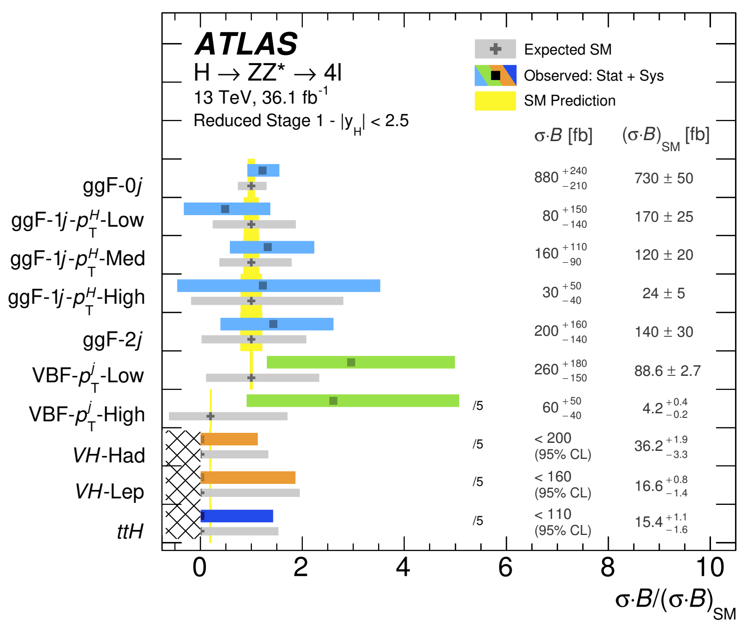

(b) Reduced Stage 1

Figure 3.37: The observed and expected SM values of the cross-section ratios $\sigma \cdot B$ normalized by the SM expectation $(\sigma \cdot B)_{\text{SM}}$ for the inclusive production and in the (a) Stage-0 and (b) reduced Stage-1 production bins for an integrated luminosity of 36.1 fb^{-1} at $\sqrt{s} = 13$ TeV. Different colours for the observed results indicate different Higgs boson production modes. The hatched area indicates that the VH and ttH parameters of interest are constrained to positive values. For visualization purposes, the VBF-p_{T}^{j}-High value and the limits for the three reduced Stage-1 production bins VH-Had, VH-Lep and ttH are divided by a factor of five when shown normalized to $(\sigma \cdot B)_{\text{SM}}$. The yellow vertical band represents the theory uncertainty in the signal prediction, while the horizontal grey bands represent the expected measurement uncertainty.

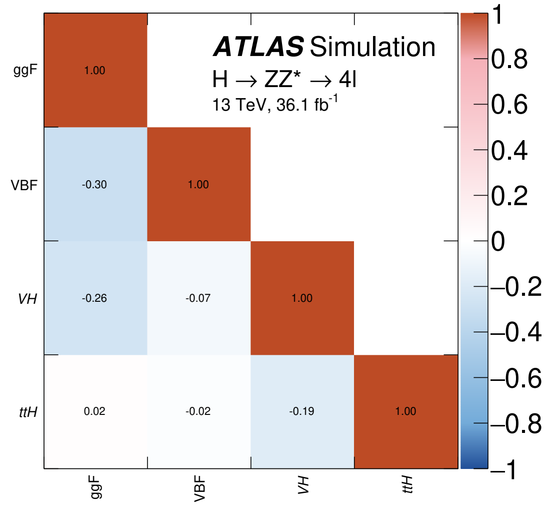

(a) Stage 0, expected

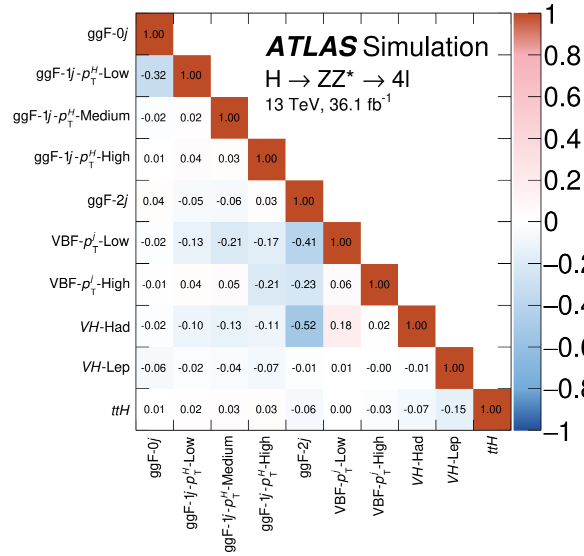

(b) Reduced Stage 1, expected

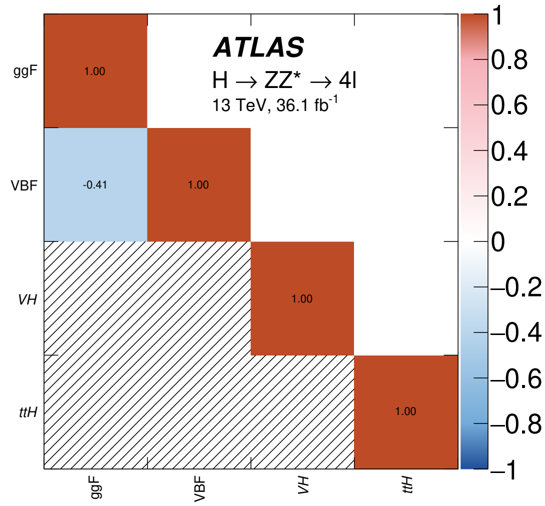

(c) Stage 0, observed

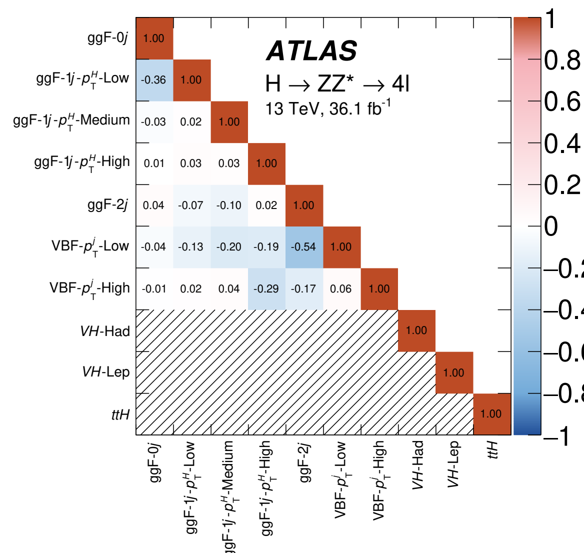

(d) Reduced Stage 1, observed

Figure 3.38: Correlation matrix for the different parameters of interest when fitting the expected MC dataset for (a) Stage-0 and (b) reduced Stage-1 signal strength parameters and when fitting the data for (c) Stage-0 and (d) reduced Stage-1. For parameters of interest where only upper limits are derived, correlations with other parameters are not calculated.

for the ggF-0j and VH-Lep bins and the jet energy scale or resolution for all other categories. The VBF-p_{T}^{j}-Low bin is additionally affected by parton shower uncertainties. The uncertainty due to the finite top quark mass and the uncertainty in the Higgs boson transverse momentum prediction have a dominant impact on the VBF-p_{T}^{j}-High bin. The signal strength measurement of the reduced Stage-1 ggF processes is also strongly affected by the theory uncertainties from event migrations between different jet multiplicity and Higgs boson transverse momentum bins, while parton shower and QCD scale uncertainties affect the remaining reduced Stage-1 production bins.

Figure 3.39(a) shows the likelihood contours in the ($\sigma_{\mathrm{ggF}} \cdot B$, $\sigma_{\mathrm{VBF}} \cdot B$) plane. The VH and ttH cross section parameters are left free in the fit, i.e. they are not treated as parameters of interest. The compatibility with respect to the Standard Model expectation is at the level of 2.3σ, due to the discrepancies observed in the VBF-related distributions in Figures 3.34 and 3.35.

The cross-section results by production mode (Stage 0) can also be interpreted in the κ framework [44, 59]. One benchmark scenario allows two different Higgs boson coupling strength modifiers to fermions and bosons, reflecting the different structure of the interactions of the SM Higgs sector with gauge bosons and fermions. The universal coupling-strength scale factors κ_F for all fermions and κ_V for all vector bosons are defined as $\kappa_V = \kappa_W = \kappa_Z$ and $\kappa_F = \kappa_t = \kappa_b = \kappa_c = \kappa_\tau = \kappa_\mu = \kappa_g$. The observed likelihood contours in the $\kappa_V - \kappa_F$ plane are shown in Figure 3.39(b) (only the quadrant $\kappa_F > 0$ and $\kappa_V > 0$ is shown since this channel is not sensitive to the relative sign of the two coupling modifiers). The compatibility with the Standard Model expectation is at the level of 1.4σ. Better agreement is observed here compared to the likelihood contours for the cross sections, since the lower observed yield in the VH categories compared with SM expectations compensates for the observed excess in the VBF categories. The long tear-drop shape is observed as κ_F is inversely proportional to the VBF cross-section and the measured value of $\sigma_{\mathrm{VBF}} \cdot B$ is consistent with zero within approximately 2σ.

3.8.3 Tensor structure of Higgs boson couplings to vector bosons

In order to probe the tensor structure of the Higgs boson couplings to vector bosons using the EFT approach, a likelihood function is constructed similar to that described in Section 3.8.2. The cross-section parameters of interest and the signal acceptance are parameterized as a function of the BSM couplings.

The coupling parameter κ_{Agg} is measured assuming that all other BSM couplings are equal to zero. The coupling parameters κ_{HVV} and κ_{AVV} are probed both simultaneously and one at a time assuming that all other BSM couplings vanish. If not stated otherwise, the SM couplings κ_{SM} and κ_{Hgg} described in Section 3.2.3 are fixed to the SM value of one. The BSM changes in the Higgs sector are assumed not to affect the SM background processes.

Figure 3.40 shows the observed negative log-likelihood as a function of one BSM coupling at a time, together with the expectation for the SM Higgs boson. The corresponding exclusion limits at a 95% CL, the best-fit values and the compatibility with respect to the SM are summarized in Table 3.15. Due to the larger number of events observed compared with expectation in the reconstructed VBF-enriched event categories, the best-fit values for the coupling parameters κ_{Agg}, κ_{HVV} and κ_{AVV} differ from zero and deviate from the SM expectation at the level of 1.8σ, 2.3σ and 1.4σ, respectively. If the coupling parameter κ_{SM} of the SM interaction is left free in the fit, the expected limits on the BSM HVV and AVV couplings decrease by up to 10%. The observed deviation from the SM hypothesis decreases to below 2σ (1σ) for the BSM HVV (AVV) coupling, since the observed excess of events is at least partially absorbed by a 20% increase of the SM coupling parameter κ_{SM}. The best-fit κ_{HVV} and κ_{AVV} values

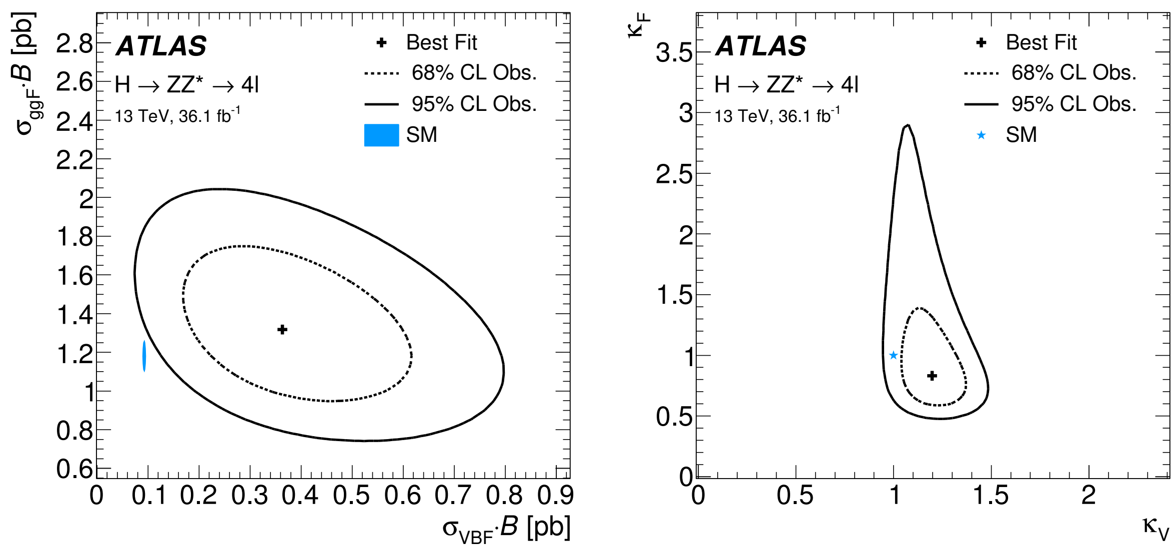

(a) $\sigma_{\mathrm{ggF}} \cdot B$ vs $\sigma_{\mathrm{VBF}} \cdot B$

(b) κ_V vs κ_F

Figure 3.39: (a) Likelihood contours at 68% CL (dashed line) and 95% CL (solid line) in the ($\sigma_{\mathrm{ggF}} \cdot B$, $\sigma_{\mathrm{VBF}} \cdot B$) plane and (b) likelihood contours in the κ_V–κ_F plane. The best fits to the data (solid cross) and the SM predictions are also indicated. In (a), the SM prediction is shown together with its theory uncertainty (filled blue elipse), while in (b) only the central value of the SM prediction (solid blue star) is shown.

decrease correspondingly.

The CP-even and CP-odd BSM couplings to heavy vector bosons are also probed simultaneously in a two-dimensional contour analysis of the negative log-likelihood. The results are shown in Figure 3.41 and summarized in Table 3.16.

The best-fit value of $\hat{\kappa}_{HVV}$ obtained from the two-dimensional scan is similar to the one obtained in the one-dimensional scan. The value of $\hat{\kappa}_{AVV}$ from the two-dimensional scan is closer to the SM expectation than the corresponding value from the one-dimensional scan. The result obtained is compatible with the SM prediction within 2σ.

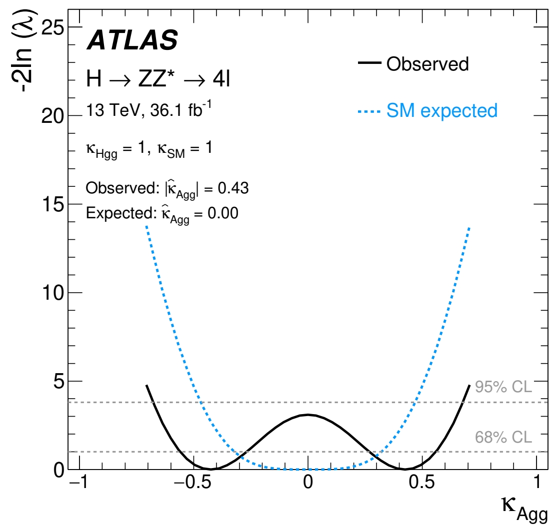

(a) κ_{Agg}

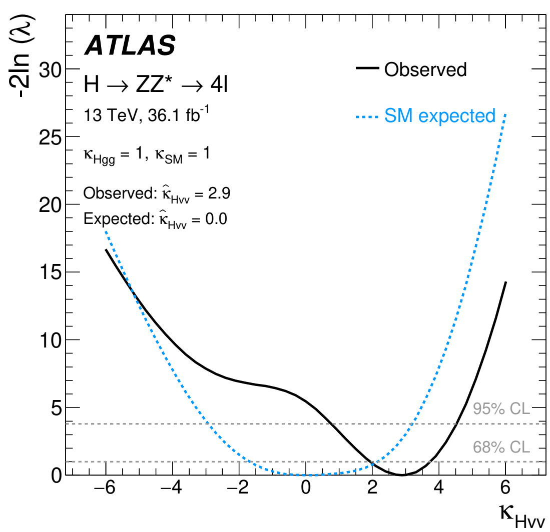

(b) κ_{HVV}

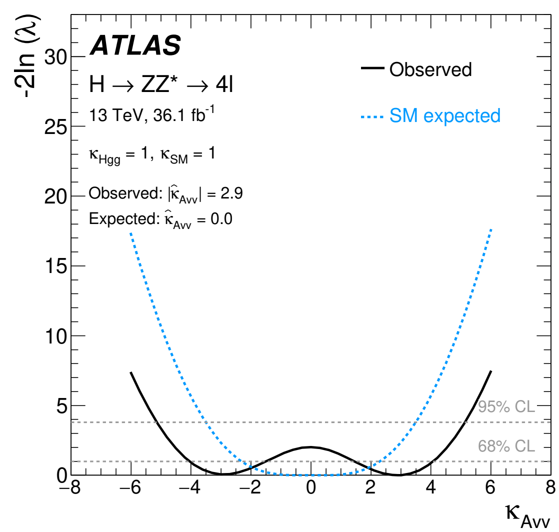

(c) κ_{AVV}

Figure 3.40: Observed (solid black line) and SM expected (dashed blue line) negative log-likelihood scans for (a) κ_{Agg}, (b) κ_{HVV} and (c) κ_{AVV} coupling parameters using 36.1 fb^{-1} of data at $\sqrt{s} = 13$ TeV. The horizontal lines indicate the value of the profile likelihood ratio corresponding to the 68% and 95% CL intervals for the parameter of interest, assuming the asymptotic χ^2 distribution of the test statistic. As the analysis is not sensitive to the sign of the CP-Odd operators, the κ_{Agg} and κ_{AVV} results have two degenerate minima.

Table 3.15: Expected and observed confidence intervals at 95% CL on the κ_{Agg}, κ_{HVV} and κ_{AVV} coupling parameters, their best-fit values and corresponding compatibility with the SM expectation, as obtained from the negative log-likelihood scans performed with 36.1 fb^{-1} of data at $\sqrt{s} = 13$ TeV. The coupling κ_{Hgg} is fixed to the SM value of one in the fit, while the coupling κ_{SM} is either fixed to the SM value of one or left as a free parameter of the fit.

BSM coupling κ_{BSM}	Fit configuration	Expected conf. inter.	Observed conf. inter.	Best-fit $\hat{\kappa}_{\text{BSM}}$	Best-fit $\hat{\kappa}_{\text{SM}}$	Deviation from SM
κ_{Agg}	$(\kappa_{Hgg} = 1, \kappa_{\text{SM}} = 1)$	$[-0.47, 0.47]$	$[-0.68, 0.68]$	± 0.43	-	1.8σ
κ_{HVV}	$(\kappa_{Hgg} = 1, \kappa_{\text{SM}} = 1)$	$[-2.9, 3.2]$	$[0.8, 4.5]$	2.9	-	2.3σ
κ_{HVV}	$(\kappa_{Hgg} = 1, \kappa_{\text{SM}}$ free$)$	$[-3.1, 4.0]$	$[-0.6, 4.2]$	2.2	1.2	1.7σ
κ_{AVV}	$(\kappa_{Hgg} = 1, \kappa_{\text{SM}} = 1)$	$[-3.5, 3.5]$	$[-5.2, 5.2]$	± 2.9	-	1.4σ
κ_{AVV}	$(\kappa_{Hgg} = 1, \kappa_{\text{SM}}$ free$)$	$[-4.0, 4.0]$	$[-4.4, 4.4]$	± 1.5	1.2	0.5σ

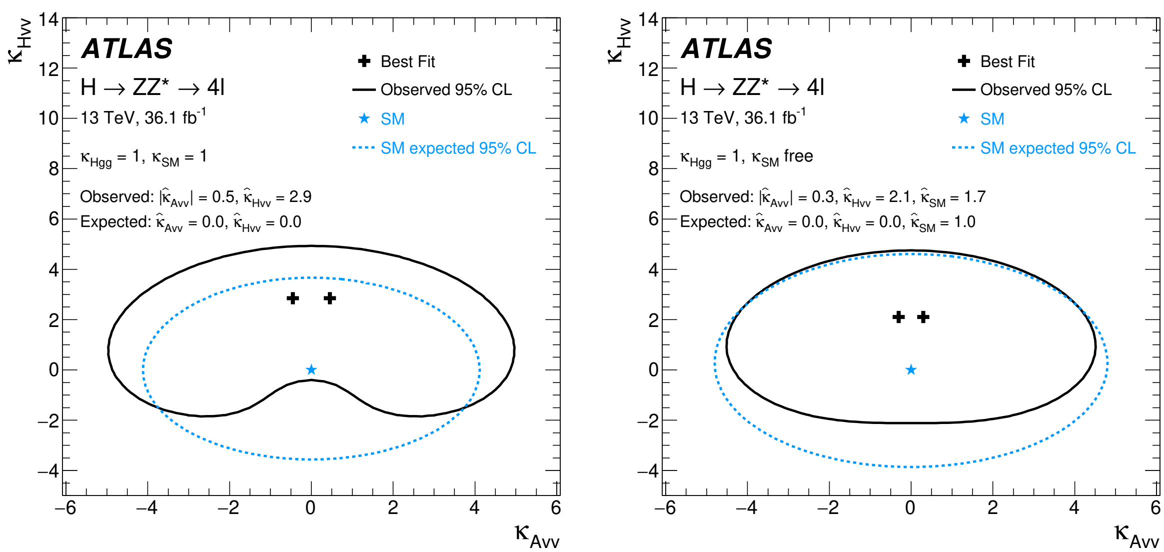

(a) (b)

Figure 3.41: Observed (black) and SM expected (blue) contours of the two-dimensional negative log-likelihood at 95% CL for the κ_{HVV} and κ_{AVV} coupling parameters with 36.1 fb^{-1} of data at $\sqrt{s} = 13$ TeV. The coupling κ_{Hgg} is fixed to the SM value of one in the fit. The coupling κ_{SM} is (a) fixed to the SM value of one or (b) left as a free parameter of the fit (b).

Table 3.16: The best-fit coupling values and corresponding deviation from the SM expectation, as obtained from the two-dimensional $\kappa_{HVV} - \kappa_{AVV}$ negative log-likelihood scans performed with 36.1 fb^{-1} of data at $\sqrt{s} = 13$ TeV.

Fit configuration	Best-fit $\hat{\kappa}_{HVV}$	Best-fit $\hat{\kappa}_{AVV}$	Best-fit $\hat{\kappa}_{\text{SM}}$	Deviation from SM
$\kappa_{Hgg} = 1, \kappa_{\text{SM}} = 1$	2.9	± 0.5	-	1.9σ
$\kappa_{Hgg} = 1, \kappa_{\text{SM}}$ free	2.1	± 0.3	1.7	1.2σ

Chapter 4

Coupling measurement in the $H \to ZZ^* \to 4\ell$ channel with 140 fb^{-1}

4.1 Overview

During Run 2, the ATLAS detector collected a proton-proton collision dataset with an integrated luminosity of 140 fb^{-1}. This large dataset makes it possible to probe the Higgs boson sector with increased precision. This allows us to test the validity of the SM and look for potential BSM physics in finer regions of the phase space.

The $H \to ZZ^* \to 4\ell$ coupling analysis, as described in Chapter 3, was updated with this larger dataset. Building upon the strategy and experiences of analyzing the 36.1 fb^{-1} dataset, multiple improvements were designed and implemented for the 140 fb^{-1} analysis. Preliminary results were presented in Ref. [129] for the 80 fb^{-1} dataset and in Ref. [130, 131] for the 140 fb^{-1} dataset.

The $H \to ZZ^* \to 4\ell$ coupling analysis with the full Run 2 dataset with all improvements is presented below, with a focus on the improvements with respect to the 36.1 fb^{-1} analysis.

4.2 Analysis Strategy

For the analysis with the full Run 2 dataset, the overall analysis strategy remains unchanged from that presented in Section 3.2. Data events with a 4 lepton final state, which are consistent with a Higgs boson decay, are selected. Specific criteria are imposed to reduce the contribution from the background processes. These events are further classified into reconstructed categories to improve the coupling measurement of the Higgs boson. The reconstructed categories and the simplified template production bins are optimized to match the sensitivity of the full dataset.

To reduce the dependency on simulation and theoretical modelling, all major backgrounds in this analysis, the continuum ZZ^*, the gauge boson production in association with top quarks, and the $Z+\text{jets}/t\bar{t}$ production with two prompt leptons, are estimated using a data-driven method. It is possible to perform these additional measurements with the larger available statistics. This ultimately improves the final coupling measurement by reducing the associated theoretical uncertainties.

In each reconstructed category, neural network (NN) based discriminants are introduced in place of the BDTs described in Section 3.5. NNs allow the use of particle level kinematic information for classifying events and further improve the signal to background ratio. This reduces the measurement statistical error.

The experimental and theoretical methods are updated to use the most precise calibrations and cross-section predictions, which have recently been made available. These have lower associated uncertainties and reduce the total error on the final measurements.

For a more general and unified approach, the effective field theory interpretation is performed using the Standard Model Effective Field Theory (SMEFT) formalism [47] in the Warsaw basis [132]. This allows for an easier comparison of the BSM physics sensitivity that different Higgs boson analyses have, and it allows for an easier global statistical combination of analyses probing different processes and the SM phase space.

Unlike the 36.1 fb^{-1} analysis, the Higgs boson mass is assumed to be 125 GeV to simplify theoretical comparisons.

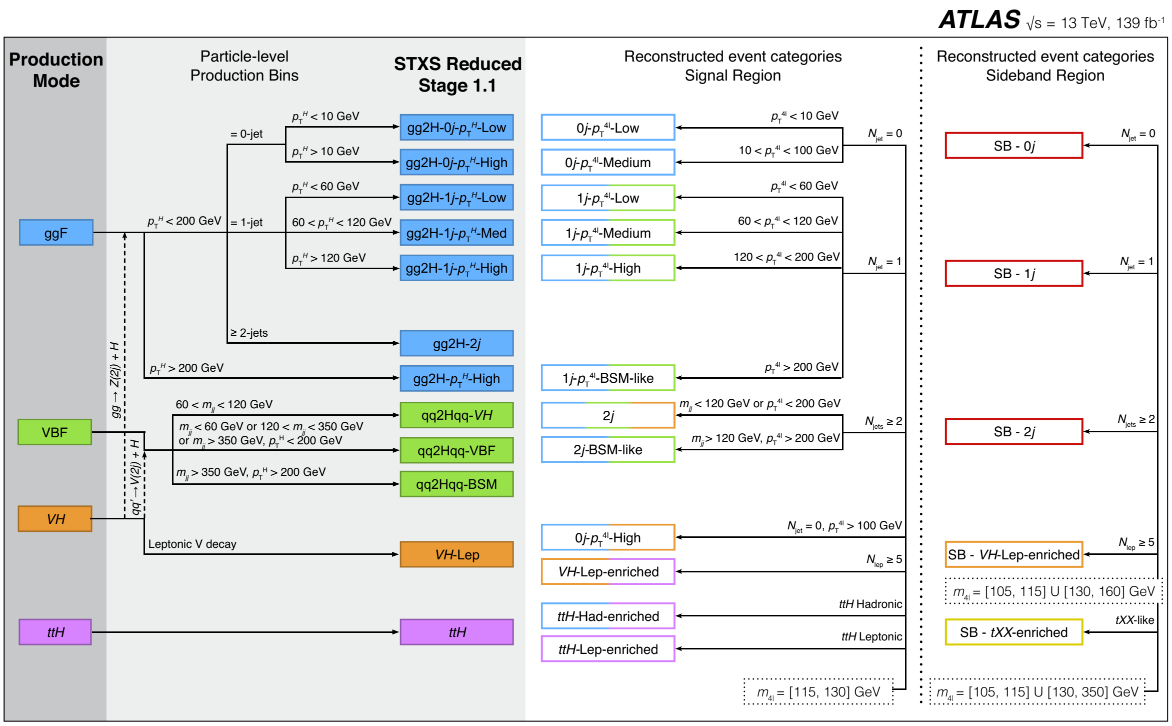

Figure 4.1: Two sets (Production Mode Stage and Reduced Stage 1.1) of exclusive phase-space regions (production bins) defined at particle level for the measurement of the Higgs boson production cross sections (left panel). The corresponding reconstructed event categories for signal (middle panel) and sidebands (right panel). The description of the production bins is given in Section 4.2.1, while the reconstructed signal region and sideband event categories are described in Section 4.5 and Section 4.6, respectively. The bbH (tH) contribution is included in the ggF (ttH) production bins.

4.2.1 Simplified Template Cross-Section Framework

The Simplified Template Cross-Section Framework [44], as described in Section 3.2.1, is used to measure the Higgs boson coupling in different phase space bins. Following the strategy of the 36.1 fb^{-1} analysis, two different granularities of the production bins are introduced. Each granularity has a different level of dependency on theoretical assumptions, a different level of experimental sensitivity and a different ability to isolate the impact from any BSM physics. The two different schemes are shown in Figure 4.1 (shaded area).

The first set of production bins (Production Mode Stage or Stage 0) is simply defined according to the Higgs boson production modes: ggF, VBF, VH, and ttH. The bbH (tH) and ggF (ttH) production modes have similar acceptances and their contributions are considered together in the analysis. Their relative ratio is fixed to according to the SM predictions. In contrast to the Stage-0 production bins described in Ref. [44], the VH events with a hadronically decaying vector boson V are included in the VH production bin rather than in the ggF or VBF bins.

The second set of production bins (Reduced Stage 1.1) is more exclusive compared to the first one. Starting from the production bins of a more granular Stage 1.1 set [44, 133], the 'tick-tock' methodology is used to optimize this merging scheme. The bins are defined based on the multiplicity of particle-level jets, the Higgs boson transverse momentum, p_{T}^{H}, and the invariant mass, m_{jj}, of the two jets with the highest transverse momentum.

Events from the ggF and the $gg \to ZH$ production modes with a hadronically decaying Z boson are split into seven common production bins. Six bins have a transverse momentum below 200 GeV, while the seventh bin with p_{T}^{H} above 200 GeV (gg2H-p_{T}^{H}-High) is sensitive to contributions from BSM physics. For p_{T}^{H} below 200 GeV, further splits are made according to the jet multiplicity and p_{T}^{H}. Events with no additional jets are split into two bins with p_{T}^{H} below and above 10 GeV. These bins provide sensitivity to light-quark to Higgs coupling through loop diagrams. Events with one jet are split into three bins with p_{T}^{H} below 60 GeV, between 60 GeV and 120 GeV, and above 120 GeV. These bins probe radiative QCD corrections at different energy scales. Finally, Higgs boson events with two or more jets are combined into one bin. The bins are respectively denoted by gg2H-0j-p_{T}^{H}-Low, gg2H-0j-p_{T}^{H}-High, gg2H-1j-p_{T}^{H}-Low, gg2H-1j-p_{T}^{H}-Med, gg2H-1j-p_{T}^{H}-High and gg2H-2j.

As described in Ref. [133], the VBF and VH production modes, with a hadronically decaying associated V boson, represent different contributions to the same physical process. Therefore, these are considered together for further splitting. Three bins are defined: one bin, sensitive to BSM contributions (qq2Hqq-BSM), with p_{T}^{H} above 200 GeV and m_{jj} above 350 GeV; one bin (qq2Hqq-VH) with m_{jj} between 60 GeV and 120 GeV to target the VH-like production mode; and one bin (qq2Hqq-VBF) with the Higgs boson not satisfying the previously mentioned criteria to ensure sensitivity to the VBF-like process.

The VH process with the associated V boson decaying leptonically is considered separately (VH-Lep). The leptonic decay includes the decays into τ leptons and into neutrino pairs. The ttH production bin remains the same as for the Production Mode Stage scheme.

Compared to the Reduced Stage 1 scheme defined in Section 3.2.1 for the 36.1 fb^{-1} analysis, this scheme is more granular and probes finer regions of the Higgs boson phase space. Theoretically indistinguishable processes are considered together, which allows interference effects to be taken into account. For example, the interference between the VBF and VH production modes is negligible in the SM. However, numerous BSM models predict interference effects of up to 20% in their respective cross-sections. This potential interference is taken into account when measuring the 3 bins for the qq2Hqq production mode. Similarly the interference between the ggF and the $gg \to ZH$ production modes is taken into account when measuring gg2H bins.

4.2.2 Effective Field Theory

In order to probe the tensor structure of the Higgs boson coupling, the measured simplified template cross sections are interpreted using an effective field theory (EFT) framework. In this approach, the BSM interactions are introduced via additional higher-dimensional operators, O_i^d, of dimension d. These supplement the SM Lagrangian, $\mathcal{L}_{\mathrm{SM}}$:

$$\mathcal{L}_{EFT} = \mathcal{L}_{SM} + \sum_{i=1}^{n_d} \frac{C_i^{(d)}}{\Lambda^{(d-4)}} \mathcal{O}_i^{(d)} \quad \text{for } d > 4. \tag{4.1}$$

The Wilson coefficients, or the $C_i^{(d)}$ parameters, specify the strength of these new interactions, and the Λ parameter is the scale of new physics. Only dimension-six operators are considered, as dimension-five and dimension-seven operators violate lepton and baryon number conservation. The impact of higher-dimension operators is suppressed by additional factors of Λ. In the low energy regime, only the ratio $c_i = C_i^{(d=6)}/\Lambda^2$ is accessible.

The operators and the associated Wilson coefficients are defined within the Standard Model Effective Field Theory (SMEFT) formalism [47] in the Warsaw basis [132]. The measurements in the $H \to ZZ^* \to 4\ell$ channel do not provide the sensitivity to constrain the full set of these coefficients. To reduce the number of relevant parameters, a minimal flavour violating scenario is assumed and only operators affecting the Higgs boson at tree level are considered. Due to their limited sensitivity, operators associated with only the double Higgs boson production and those affecting the Higgs boson couplings to down-type quarks and leptons are neglected. The impact of these operators on the total Higgs boson decay width is also neglected.

Table 4.1: Summary of EFT operators in the SMEFT formalism that are probed in the $H \to ZZ^* \to 4\ell$ channel. The corresponding tensor structure in terms of the SM fields from Ref. [47] is shown together with the associated Wilson coefficients, affected production vertices and the impact on the $H \to ZZ^*$ decay vertex.

CP-even			CP-odd			Impact on	
Operator	Structure	Coeff.	Operator	Structure	Coeff.	production	decay
$\mathcal{O}_{HG}$	$HH^\dagger G^A_{\mu\nu} G^{\mu\nu A}$	c_{HG}	$\mathcal{O}_{H\widetilde{G}}$	$HH^\dagger \widetilde{G}^A_{\mu\nu} G^{\mu\nu A}$	$c_{H\widetilde{G}}$	ggF	Yes
$\mathcal{O}_{uH}$	$HH^\dagger \bar{q}_p u_r \tilde{H}$	c_{uH}	$\mathcal{O}_{\tilde{u}H}$	$HH^\dagger \bar{q}_p u_r \tilde{H}$	$c_{\tilde{u}H}$	ttH	-
$\mathcal{O}_{HW}$	$HH^\dagger W^l_{\mu\nu} W^{\mu\nu l}$	c_{HW}	$\mathcal{O}_{H\widetilde{W}}$	$HH^\dagger \widetilde{W}^l_{\mu\nu} W^{\mu\nu l}$	$c_{H\widetilde{W}}$	VBF, VH	Yes
$\mathcal{O}_{HB}$	$HH^\dagger B_{\mu\nu} B^{\mu\nu}$	c_{HB}	$\mathcal{O}_{H\widetilde{B}}$	$HH^\dagger \widetilde{B}_{\mu\nu} B^{\mu\nu}$	$c_{H\widetilde{B}}$	VBF, VH	Yes
$\mathcal{O}_{HWB}$	$HH^\dagger \tau^l W^l_{\mu\nu} B^{\mu\nu}$	c_{HWB}	$\mathcal{O}_{H\widetilde{W}B}$	$HH^\dagger \tau^l \widetilde{W}^l_{\mu\nu} B^{\mu\nu}$	$c_{H\widetilde{W}B}$	VBF, VH	Yes

The remaining ten operators (see Table 4.1) consist of five CP-even and five CP-odd operators. The CP-even operators describing interactions between the Higgs boson and gluons and the top-Yukawa interactions are associated to the Wilson coefficients c_{HG} and c_{uH} from Ref. [47], respectively. Similarly, the CP-even Higgs boson interactions with vector bosons are related to the c_{HW}, c_{HB}, and c_{HWB} parameters. These affect the VBF and VH production modes and the Higgs boson decay to Z bosons. The Wilson coefficients for the corresponding CP-odd operators are $c_{H\widetilde{G}}$, $c_{\tilde{u}H}$, $c_{H\widetilde{W}}$, $c_{H\widetilde{B}}$ and $c_{H\widetilde{W}B}$.

The constraints on the Wilson coefficients can be derived by comparing the expected simplified template cross sections to the measured results. Using the procedure outlined in Ref. [134], the expected signal production cross sections, the branching ratio and the signal acceptances are parametrized in terms of the Wilson coefficients. The criteria used to select four-lepton candidates introduces an additional dependency of the signal acceptance on the EFT parameters. This analysis is one of the first Higgs boson measurements to incorporate this effect into the measured results.

4.3 Data and Monte Carlo Samples

4.3.1 Data Samples

The data collected during the full Run 2, which occurred from 2015 to 2018, are used for this analysis. During this period, the LHC delivered 156 fb^{-1} of data, of which ATLAS collected 147 fb^{-1}. Data quality requirements, such as requiring stable beam conditions and requiring all ATLAS sub-detectors be fully operational, are further applied. This yields 140 fb^{-1} of data available for this analysis [135]. The average number of pileup interactions per bunch crossing is 33.7 and Figure 4.2 shows the luminosity averaged pileup interactions per event for this dataset [135].

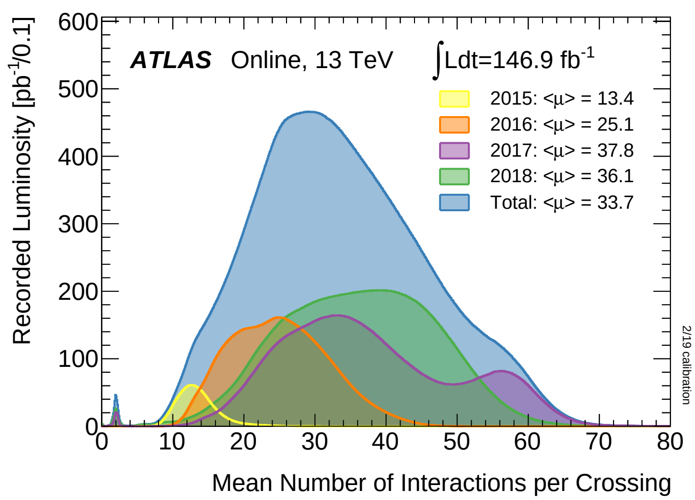

Figure 4.2: The luminosity-weighted distribution of the mean number of interactions per crossing for the combined 13 TeV data collected during Run 2 [135].

4.3.2 Monte Carlo Samples

The Monte Carlo simulations used for this analysis remain largely unchanged from those described in Section 3.3.2.

For all signal processes, the POWHEG-BOX v2 Monte Carlo (MC) event generator [62, 63] interfaced to EvtGen [64] is used for the matrix element generation. In comparison to the previous analysis, this setup calculates the ttH production matrix elements to up to NLO in QCD. Higgs boson production in association with a single top quark (tH+X where X is either jb or W, defined in the following as tH) is simulated at NLO with MadGraph5_aMC@NLO v2.6.0 using the NNPDF30 PDF set [73].

For the ggF, VH and bbH production mechanisms, the same setup of the PYTHIA 8 [74] generator is used for the $H \to ZZ^* \to 4\ell$ decay as well as for parton showering and simulation of multiple partonic interactions. The ttH and single top quark production processes are updated to use this generator. For the VBF process, PYTHIA 8 with an updated scheme for dipole showering is used [136–138]. This scheme uses an improved description of colour-flow and dipole emission between colour connected initial and final state particles.

For additional cross checks, the ggF production process was also generated with aMC@NLO with the FxFx merging scheme [70, 81]. This simulation is accurate at NLO QCD accuracy for zero, one and two additional partons.

For the study of the tensor structure of Higgs boson couplings within an effective field theory approach, several simulations with different values of EFT parameters are calculated at LO in QCD separately for each production mode using the MadGraph5_aMC@NLO program and the NNPDF23lo PDF set. The BSM signal is defined by the SMEFTsim_A_U35_MwScheme_UFO_v2.1 model [139, 140]. The light quarks and leptons are assumed to be massless. The events are showered with PYTHIA 8 using the CKKW-L matching scheme [74].

The quark-antiquark ZZ^* continuum background is modelled as before using Sherpa v2.2.2 [82–84]. The gluon-induced ZZ^* production is modelled using Sherpa 2.2.2 [82–84] at LO in QCD for 0-, and 1-jet final states. This is in contrast to previously being modelled only at LO in QCD. The higher-order QCD effects for the $gg \to ZZ^*$ continuum production have been calculated for massless quark loops [90–92] and in the heavy top-quark approximation [93], including the $gg \to H^* \to ZZ$ process [94, 95]. The $gg \to ZZ$ simulation is scaled by the K-factor of 1.7±1.0, defined as the ratio of the higher-order and the leading-order cross section predictions. The production of ZZ^* via vector boson scattering is simulated with the Sherpa v2.2.2 [141] generator. The LO-accurate matrix elements are matched to a parton shower using the MEPS@LO prescription. For all ZZ^* processes modelled using Sherpa, the NNPDF3.0nnlo PDF set [73] is used, along with the dedicated set of tuned parton-shower parameters developed by the Sherpa authors.

For additional checks, the quark–antiquark initiated ZZ^* continuum background is also modelled using POWHEG-BOX v2 and MadGraph5_aMC@NLO. For the former, matrix elements are generated at NLO accuracy in QCD and effects of singly resonant amplitudes and interference effects due to Z/γ^* are included. For the latter, the simulation is accurate at NLO QCD accuracy for zero and one additional partons merged with the FxFx merging scheme. For both, the PYTHIA 8 generator is used for modelling the parton shower.

The simulation of $t\bar{t}Z$ events, with both top quarks decaying semi-leptonically and the Z boson decaying leptonically, is updated to use MadGraph5_aMC@NLO interfaced to PYTHIA 8. The total cross section is normalized to the prediction which includes the two dominant terms at both the LO and the NLO in a mixed perturbative expansion in the QCD and EW couplings [96]. For modelling comparisons, Sherpa 2.2.1 was used to simulate $t\bar{t} + Z$ events at LO. The smaller tWZ, $t\bar{t}W^+W^-$, $t\bar{t}W^{\pm}Z$, $t\bar{t}Z\gamma$, $t\bar{t}ZZ$, $t\bar{t}t$, $t\bar{t}t\bar{t}$ and tZ background processes are simulated with MadGraph5_aMC@NLO interfaced to PYTHIA 8. These processes are jointly referred to as the tXX process.

The $t\bar{t}$ background is updated to be modelled using POWHEG-BOX v2 interfaced to PYTHIA 8 for parton showering, hadronisation, and the underlying event, and to EvtGen v1.2.0 for heavy flavoured hadron decays. For this sample, the A14 parameter set [142, 143] is used.

4.4 Event Selection

For this analysis, the event triggering criteria and reconstruction, identification and selection of Higgs boson candidates closely matches that described in Section 3.4. The differences are presented in the following sections.

4.4.1 Particle Reconstruction and Identification

For reconstruction of electrons and jets, new algorithms described in the following sections are used. These new algorithms improve the energy or momentum resolution, which ultimately leads to a better signal to background discrimination. For tagging jets as originating from a b-hadron, a new continuous tagging approach is used. Rather that being restricted to a binary decision at a particular tagging efficiency, the new algorithm provides tagging information at various efficiencies which can be used simultaneously.

For muon reconstruction and identification, the algorithms and criteria described in Section 3.4 are used.

Electrons

Electron candidates are reconstructed from energy clusters in the electromagnetic calorimeter that are matched to ID tracks [144, 145]. As before, a Gaussian-sum filter algorithm [146] is used to compensate for radiative energy losses in the ID for the track reconstruction. In contrast to the sliding window algorithm, a dynamical topological cell clustering-based algorithm is used to improve the energy resolution [144]. Topological cells, which closely match the spatial pattern of energy loss in the calorimeter, are combined using an algorithm that merges near-by localized energy deposits. This improves the energy resolution in cases where Bremsstrahlung photons are emitted. This new reconstruction algorithm leads to a 3%–5% improvement in the 4-lepton mass resolution.

Jet and B-tagging

Jets are now reconstructed using a particle flow algorithm [147]. This uses noise-suppressed positive-energy topological clusters [148] in the calorimeter and tracks that are matched to the hard-scatter primary vertex. The particle flow algorithm uses the energy-momentum information from the object with the better expected resolution: track information at low p_{T} and calorimeter information at high p_{T}. Any overlap between track and calorimeter information is removed to prevent double counting when clustering is performed. The anti-k_t algorithm, with a radius parameter $R = 0.4$, is used for clustering. Compared to jets constructed using only the topological clusters, the transverse momentum resolution improves by 10% for jets with p_{T} approximately equal to 30 GeVand matches above 100 GeV.

Jets with $|\eta| < 2.5$ containing b-hadrons are identified using the MV2c10 b-tagging algorithm [149, 150]. The 60%, 70%, 77% and 85% efficiency working points are combined into a single pseudo-continuous b-tagging discriminant which is assigned to each jet. This combined discriminant is calibrated using $t\bar{t}$ events and allows reconstructed categories to be defined using multiple working points.

4.4.2 $H \to ZZ^* \to 4\ell$ Event Selection

The selection of candidate events closely follows the criteria from Section 3.4.3. The differences are outlined below.

4-Lepton Selection

To simplify the definition of the fiducial phase space, all leptons within a quadruplet are required to be angularly separated and satisfy $\Delta R = \sqrt{(\Delta y)^2 + (\Delta\phi)^2} > 0.1$ for all lepton pairs. Previously, the threshold for different-flavour lepton pairs was $\Delta R > 0.2$.

Isolation Criteria

To benefit from the improved reconstruction techniques and to mitigate the loss in the signal selection efficiency due to increased pileup per event, new algorithms and criteria for isolation were implemented and optimized.

As outlined in Section 3.4, the background contributions from the Z+jets and $t\bar{t}$ processes are suppressed by imposing track-based and calorimeter-based isolation criteria on each lepton [110, 144]. For the track-based isolation, a scalar sum is made of the p_{T} of the tracks with $p_{\mathrm{T}} > 500$ MeV. These either come from the primary vertex or have $|z_0 \sin\theta| < 3$ mm if not associated with any vertex and lie within a cone of $\Delta R = 0.3$ around the muon or electron. For leptons with $p_{\mathrm{T}} \geq 33$ GeV, this cone size falls linearly with p_{T} to a minimum cone size of 0.2 at $p_{\mathrm{T}} = 50$ GeV. This reduces the probability of tracks from pileup events affecting the track isolation. For the calorimeter isolation, the scalar sum is made of the E_T of positive-energy topological clusters which are not associated with a charged track in a cone of $\Delta R = 0.2$ around the muon or electron. The calorimeter-based isolation sum is corrected for electron shower leakage, pile-up and underlying-event contributions. Both isolation sums are corrected for track and topocluster contributions from the remaining three leptons.

The sum of the track isolation and 40% of the calorimeter isolation is required to be less than 16% of the lepton p_{T}. The pileup dependence of this isolation selection is improved [51, 129, 151] by the exclusion of tracks associated with a vertex other than the primary vertex and by the removal of topoclusters associated to tracks. The signal efficiency of the isolation criteria is greater than 80%, improving the efficiency by 5% with respect to the previous analysis for the same level of background rejection.

4.4.3 FSR Recovery and Z Mass Constraint

As the electron reconstruction was improved to better account for final state radiation (FSR), the additional analysis specific criteria for FSR recovery have been re-optimized.

Collinear (non-collinear) FSR candidates are defined as candidates with $\Delta R <$ ($>$) 0.15 to the nearest lepton in the quadruplet. Collinear FSR candidates are considered only for muons from the leading lepton pair, while non-collinear FSR candidates are considered for both muons and electrons from the leading and sub-leading Z bosons.

Collinear FSR candidates are selected from reconstructed photon candidates and from electron candidates which share an ID track with the muon. Further criteria are applied on each candidate based on the following discriminants: the fraction, f_1, of candidate's energy in the front of the EM calorimeter to reduce backgrounds from muon ionization, the angular distance, $\Delta R_{\mathrm{cluster},\mu}$, between the candidate's EM cluster and the muon, and the candidate p_{T} which must be at least 1 GeV. For all selected electron candidates and for photon candidates with $p_T < 3.5$ GeV, a requirement of $f_1 > 0.2$ and $\Delta R_{\text{cluster},\mu} < 0.08$ is imposed. The collinear photon candidates with $p_T > 3.5$ GeV are selected if $f_1 > 0.1$ and $\Delta R_{\text{cluster},\ell} < 0.15$. Non-collinear FSR candidates are selected only from reconstructed isolated photons passing the "tight" likelihood criteria [152, 153] and satisfying $p_T > 10$ GeV and $\Delta R_{\text{cluster},\ell} > 0.15$.

Only one FSR candidate is included in the quadruplet with preference given to collinear FSR and to the candidate with the highest p_T. The FSR candidate is added to the lepton pair if the invariant mass of the lepton pair is between 66 GeV and 89 GeV and if the invariant mass of the lepton pair and the photon is below 100 GeV. Approximately 3% of reconstructed Higgs candidates have a FSR candidate and their impact on the expected invariant mass distribution is shown in Figure 4.3.

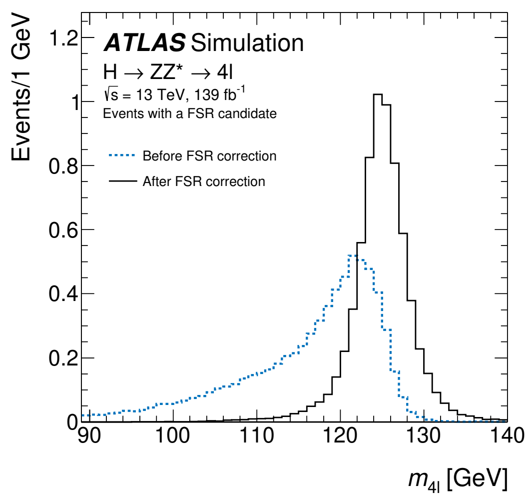

Figure 4.3: Impact on the expected invariant mass distribution of the selected Higgs boson candidates due to accounting for final-state radiation (FSR). Only candidates with a FSR photon are plotted.

The Z mass constraint, as described in Figure 3.4, was used previously to improve the 4-lepton mass resolution. However, this technique requires the assumption that the Higgs boson decay is well described by the SM. To limit the impact of this assumption, the Z mass constraint is not applied. As the 4-lepton mass is only used to define the mass window for the signal region, this change creates a negligible loss in sensitivity.

The 4-lepton candidates within a mass window of 115 GeV $< m_{4\ell} <$ 130 GeV are selected as Higgs boson candidates and define the signal region. The side-band regions consist of events failing this requirement but are within a larger mass window. This region is used to estimate the leading backgrounds as described in Section 4.6.

4.5 Event Categorization and Neural Networks

4.5.1 Event Categorization

Similar to Section 3.5, to gain sensitivity to production modes and STXS production bins, each Higgs boson candidate is classified into exclusive categories. Figure 4.1 summarizes the definition for these categories. The reconstructed categories are designed to target production modes with smaller cross-sections, to allow for high signal-to-background ratio within these categories. The Run 2 dataset also allows different decay modes of the Higgs boson production processes to be individually targeted to further improve the overall sensitivity.

For signal events, the classification is performed in the order shown in the middle-right panel of Figure 4.1 and as described below. First, events are classified as enriched in the ttH process and are split according to the decay mode of the two W bosons from the top quark decays. The continuous b-tagging score is used to iteratively select ttH-like events with a high expected signal to background ratio.

For semi- and di-leptonic decays (ttH-Lep-enriched), at least one additional lepton with $p_{\mathrm{T}} > 12$ GeV[1] together with at least two b-tagged jets (with 85% b-tagging efficiency), or at least five jets with at least one b-tagged jet (with 85% b-tagging efficiency), or at least two jets with at least one b-tagged jet (with 60% b-tagging efficiency) is required. Despite the low expected number of events, 98% of events in this category are expected to originate from the semi- and di-leptonic decays of the ttH process.

For the fully hadronic decay (ttH-Had-enriched), there must be either at least five jets with at least two b-tagged jets (with 85% b-tagging efficiency), or at least four jets with at least one b-tagged jet (with 60% b-tagging efficiency). This category has relatively large contributions from the ggF and tXX production processes.

Events with additional lepton(s) but not satisfying the above jet requirements define the category of events which are enriched in VH production followed by leptonic vector boson decay (VH-Lep-enriched). The requirement of at least an additional lepton creates a category where 80% of events are expected to originate from the VH or ttH process.

The remaining events are classified according to their reconstructed jet multiplicity into categories with no jets, exactly one jet or at least two jets. Events with at least two reconstructed jets are divided into two categories: one is a BSM-like category ($2j$-BSM-like) and the other ($2j$) contains the bulk of events with significant contributions from the VBF and VH production modes. The $2j$-BSM-like category requires the invariant mass, m_{jj}, of the two leading jets to be larger than 120 GeV and the four-lepton transverse momentum, $p_{\mathrm{T}}^{4\ell}$, to be larger than 200 GeV. The remaining events are classified in the $2j$ category.

Events with zero or one jet in the final state are expected to be dominated by the ggF process. Following the particle-level definition of production bins from Section 4.2.1, the 1-jet category is further split into four categories with $p_{\mathrm{T}}^{4\ell}$ smaller than 60 GeV ($1j$-$p_{\mathrm{T}}^{4\ell}$-Low), between 60 and 120 GeV ($1j$-$p_{\mathrm{T}}^{4\ell}$-Med), between 120 and 200 GeV ($1j$-$p_{\mathrm{T}}^{4\ell}$-High), and larger than 200 GeV ($1j$-$p_{\mathrm{T}}^{4\ell}$-BSM-Like).

The largest number of ggF events and the highest ggF purity are expected in the zero-jet category. The zero-jet category is split into three categories with $p_{\mathrm{T}}^{4\ell}$ smaller than 10 GeV ($0j$-$p_{\mathrm{T}}^{4\ell}$-Low), between 10 and 100 GeV ($0j$-$p_{\mathrm{T}}^{4\ell}$-Med) and above 100 GeV ($0j$-$p_{\mathrm{T}}^{4\ell}$-High). The first two categories follow the production bin splitting, and the last category improves the discrimination between the VH ($V \to \ell\nu/\nu\nu$) and ggF processes.

As illustrated in Figure 4.1, there is a dedicated reconstructed event category for each production bin except for gg2H-$2j$, qq2Hqq-VH and qq2Hqq-VBF. These production bins are largely measured from the 2-jet reconstruction category and to a lesser extent from the 1-jet categories using multi-variate discriminants (see Section 4.5.2). The gg2H-p_{T}^{H}-High production bin is simultaneously measured in all reconstructed event categories with high transverse momentum of the four-lepton system. This is

[1]The additional lepton is a lepton candidate as defined in Section 4.4. It is also required to satisfy the same isolation, impact parameter and angular separation requirements as the leptons in the quadruplet as outlined in Section 4.4.

independent of the reconstructed jet multiplicity.

The right-hand panel of Figure 4.1 shows the background event classification. For estimating the tXX process from the mass side band, a tXX-enriched sideband category (SB-tXX-enriched) is defined. This includes events with at least two jets in which at least one is tagged as a b-jet with 60% efficiency and $E_{\mathrm{T}}^{\mathrm{miss}} > 100$ GeV in the mass range of 105-115 GeV or 130-350 GeV. This region is dominated by ttZ (87%) and has small contributions from: ttt, $tttt$, tWZ, ttW, $ttWW$, $ttWZ$, $ttZ\gamma$, $ttZZ$, and tZ. The tXX process is expected to have the largest contribution in ttH-like categories. The large mass range for this category, larger than that for the non-resonant ZZ^* as discussed next, allows for an improved statistical precision on the estimate of this background. This mass range also limits the uncertainty associated with modelling these processes with two on-shell top quarks.

For measuring the non-resonant ZZ^* production, events not passing the criteria for the SB-tXX-enriched category are split in the $m_{4\ell}$ mass range of 105-115 GeV or 130-160 GeV according to the number of reconstructed jets: exactly zero jets (SB-$0j$), exactly one jet (SB-$1j$) or at least 2 jets (SB-$2j$). This mass range limits contributions from the single resonant process and from the on-shell ZZ^* process. Similarly, events in the same mass range with an extra reconstructed lepton separately form the SB-VH-Lep-enriched category. This is enriched with Higgs boson candidates that fall outside the signal region mass window and contain leptons from the associated V and top quark leptonic decays. With a VH purity of about 20%, this category improves the expected sensitivity for VH-Lep by 5%.

The expected number of signal events is shown in Table 4.2 for each production mode and separately for each reconstructed event category. The ggF and bbH contributions are shown separately in order to compare their relative contributions, but both belong in the same (ggF) production bin. The highest bbH event yield is expected in the $0j$ categories, as the jets tend to have a high pseudo-rapidity when compared to those from the ttH process, thus escaping the detector acceptance.

The signal composition in terms of the reduced Stage-1.1 production bins is shown in Figure 4.4. The signal acceptance in each category for the STXS bins is summarized in Figure 4.5 and Figure 4.6.

4.5.2 Neural Network discriminating observables

In order to increase the sensitivity of the cross section measurement in the production bins, multivariate discriminants using neural networks (NNs) are introduced in many of the reconstructed signal event categories as observables in the statistical fit. This is similar to the BDTs used in Section 3.5, but NNs train more efficiently and effectively with basic kinematic information of the physics objects, such as the p_{T} of leptons and jets. NNs can use inputs with variable length, which allows different event topologies originating from the same production mode to be discriminated coherently. For example, VBF production with two or three final state jets can be classified simultaneously with NNs.

The NN architecture and training procedure are defined using Keras with TensorFlow [154]. These are optimized for improving sensitivity while preventing over-training. These networks are trained using several discriminating observables on simulated SM Higgs boson signal and/or non-Higgs background events. Due to the low expected signal events, only the observed yield is used as the discriminant in the $0j$-$p_{\mathrm{T}}^{4\ell}$-High, $1j$-$p_{\mathrm{T}}^{4\ell}$-BSM-Like and ttH-Lep-enriched categories.

Two types of neural networks are used: feed-forward or multilayer perceptons (MLP) and recurrent NNs (rNNs) [154–156]. Each NN combines two rNNs, one for the variables related to the four leptons in the quadruplet and one for variables related to jets, and an MLP with additional variables related to the event. The jet rNN accepts inputs from up to three jets. The MLP and two rNNs components

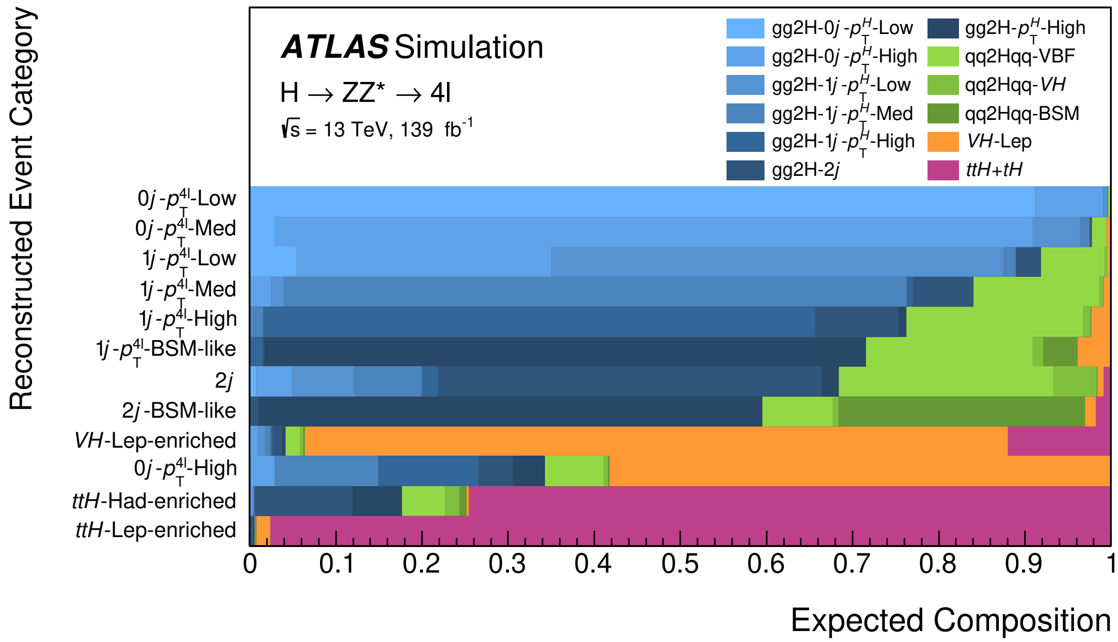

Figure 4.4: Standard Model signal composition in terms of the reduced Stage-1.1 production bins in each reconstructed event category. The bbH contributions are included in the ggF production bins.

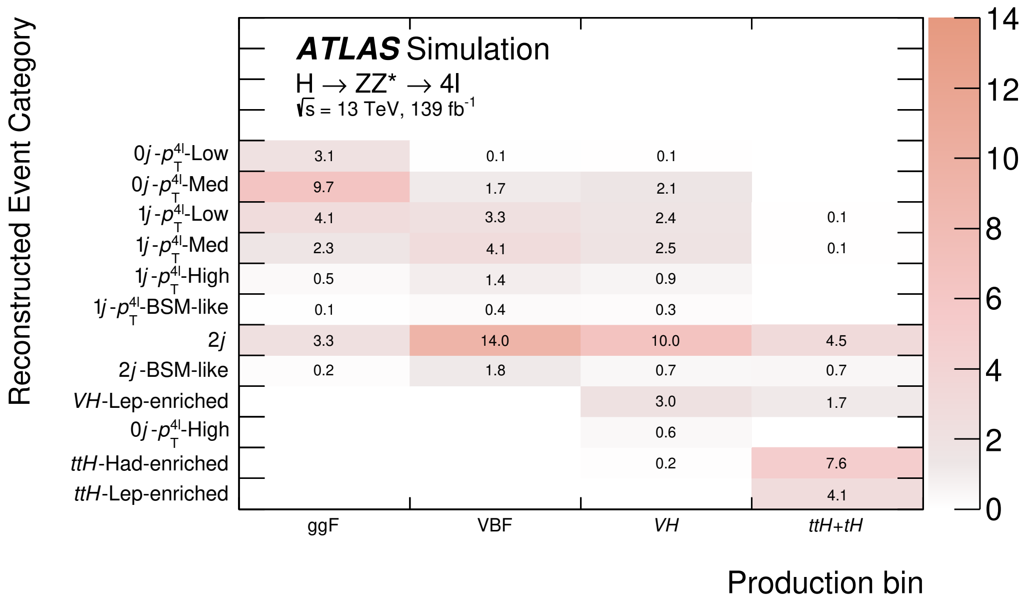

Figure 4.5: Signal acceptance times efficiency in percentage for Stage-0 production bins. This is obtained by taking the ratio of the number of simulated signal events satisfying the event selection criteria in each reconstructed event category to the total number of events generated in the phase space specified by a given production bin.

Table 4.2: The expected number of SM Higgs boson events with $m_H = 125$ GeV at an integrated luminosity of 140 fb^{-1} and $\sqrt{s} = 13$ TeV in each reconstructed event signal ($115 < m_{4\ell} < 130$ GeV) and sideband ($m_{4\ell}$ in 105-115 GeV or 130-160 GeV for ZZ^*, 130-350 GeV for tXX) category, shown separately for each production bin of the Production Mode Stage. The ggF and bbH yields are shown separately but both contribute to the same (ggF) production bin, and ZH and WH are reported separately but are merged together for the final result. Statistical and systematic uncertainties, including those for theory, are added in quadrature. Contributions that are below 0.2% of the total signal in each reconstructed category are not shown and are replaced by "–".

Reconstructed	SM Higgs boson production mode					
event category	ggF	VBF	WH	ZH	ttH + tH	bbH
Signal	$115 < m_{4\ell} < 130$ GeV					
$0j$-$p_T^{4\ell}$-Low	23.9 ± 3.5	0.073 ± 0.006	0.0173 ± 0.0031	0.0131 ± 0.0023	–	0.17 ± 0.09
$0j$-$p_T^{4\ell}$-Med	74 ± 8	1.03 ± 0.15	0.37 ± 0.05	0.40 ± 0.05	–	0.8 ± 0.4
$0j$-$p_T^{4\ell}$-High	0.109 ± 0.026	0.0157 ± 0.0024	0.056 ± 0.005	0.173 ± 0.016	0.00065 ± 0.00023	–
$1j$-$p_T^{4\ell}$-Low	31 ± 4	1.99 ± 0.11	0.52 ± 0.05	0.35 ± 0.04	–	0.41 ± 0.21
$1j$-$p_T^{4\ell}$-Med	17.3 ± 2.8	2.50 ± 0.18	0.52 ± 0.06	0.40 ± 0.04	0.0078 ± 0.0013	0.09 ± 0.04
$1j$-$p_T^{4\ell}$-High	3.6 ± 0.8	0.84 ± 0.07	0.158 ± 0.015	0.166 ± 0.016	0.0044 ± 0.0006	0.011 ± 0.006
$1j$-$p_T^{4\ell}$-BSM-Like	0.87 ± 0.23	0.246 ± 0.020	0.060 ± 0.007	0.054 ± 0.006	0.00156 ± 0.00032	0.0009 ± 0.0005
$2j$	25 ± 5	8.5 ± 0.6	1.94 ± 0.15	1.69 ± 0.13	0.46 ± 0.04	0.30 ± 0.15
$2j$-BSM-like	1.9 ± 0.6	1.08 ± 0.05	0.120 ± 0.016	0.122 ± 0.016	0.075 ± 0.007	0.0021 ± 0.0010
VH-Lep-enriched	0.050 ± 0.011	0.019 ± 0.004	0.80 ± 0.07	0.245 ± 0.021	0.166 ± 0.013	0.0027 ± 0.0014
ttH-Had-enriched	0.15 ± 0.16	0.021 ± 0.004	0.020 ± 0.005	0.055 ± 0.013	0.75 ± 0.07	0.020 ± 0.011
ttH-Lep-enriched	0.0019 ± 0.0022	0.00019 ± 0.00008	0.0046 ± 0.0026	0.0032 ± 0.0018	0.41 ± 0.04	–
Sideband	$105 < m_{4\ell} < 115$ GeV or $130 < m_{4\ell} < 160$ GeV					
SB-$0j$	4.2 ± 0.5	0.050 ± 0.010	0.096 ± 0.011	0.042 ± 0.005	–	0.044 ± 0.022
SB-$1j$	2.37 ± 0.29	0.241 ± 0.024	0.100 ± 0.013	0.063 ± 0.008	0.0049 ± 0.0009	0.023 ± 0.012
SB-$2j$	1.25 ± 0.26	0.43 ± 0.05	0.119 ± 0.014	0.103 ± 0.012	0.109 ± 0.010	0.016 ± 0.008
SB-VH-Lep-enriched	0.015 ± 0.005	0.0029 ± 0.0011	0.084 ± 0.008	0.104 ± 0.010	0.065 ± 0.006	0.0013 ± 0.0007
	$105 < m_{4\ell} < 115$ GeV or $130 < m_{4\ell} < 350$ GeV					
SB-ttV-enriched	0.001 ± 0.010	0.00012 ± 0.00009	0.0006 ± 0.0004	0.0008 ± 0.0004	0.068 ± 0.008	–
Total	186 ± 14	17.0 ± 0.8	5.0 ± 0.4	3.97 ± 0.29	2.13 ± 0.18	1.9 ± 1.0

are chained into another MLP to complete the NN, which is configured to output the probability for an event to come from the given process. A schematic of the general NN architecture is shown in Figure 4.7. The NNs are used in each reconstructed event category to discriminate between two or three processes, e.g. ggF, VBF and ZZ background in the $1j$-$p_T^{4\ell}$-Low category. The variables used for training the NN for each category along with the processes being separated are summarized in Table 4.3.

The variables, which have not been previously described are as follows. The kinematic discriminant D_{ZZ^*} [24], is defined as the difference between the logarithms of the signal decay and background matrix elements squared and it is used to distinguish ggF from the non-resonant ZZ^* background. Three angles [157] are used for further distinguishing these processes: the cosine of the leading Z boson production angle, θ^*, in the four-lepton rest frame, the cosine of θ_1 which is defined as the angle between the negatively charged lepton of the leading Z in the leading Z rest frame and the direction of flight of the leading Z in the four-leptons rest frame, and the angle, ϕ_{ZZ}, between two Z decay planes in the four lepton rest frame. The angular separation of the leading jet from the 4ℓ system, $\Delta R_{4\ell j}$, is used to distinguish VBF or ttH from ggF. For categories with two or more jets, the kinematic variables of the two leading jets are used: the invariant mass, m_{jj}, the transverse momentum of the 4ℓ and the 2 jets system, $p_T^{4\ell jj}$, and the Zeppenfeld variable, $\eta_{ZZ}^{\mathrm{Zepp}}$, as defined in [158]. The number of reconstructed jets,

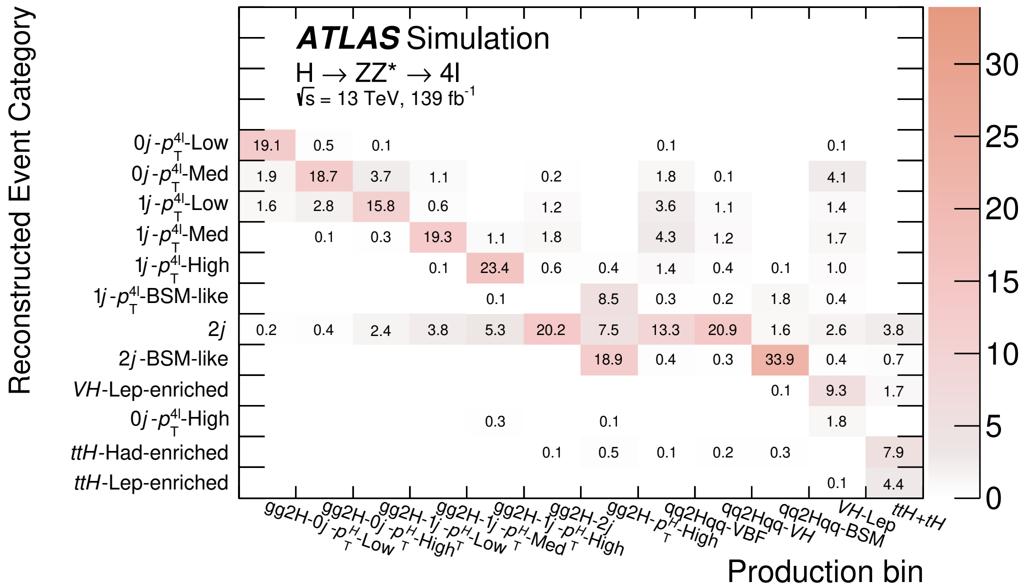

Figure 4.6: Signal acceptance times efficiency in percentage for reduced stage 1.1 production bins. This is obtained by taking the ratio of the number of simulated signal events satisfying the event selection criteria in each reconstructed event category to the total number of events generated in the phase space specified by a given production bin.

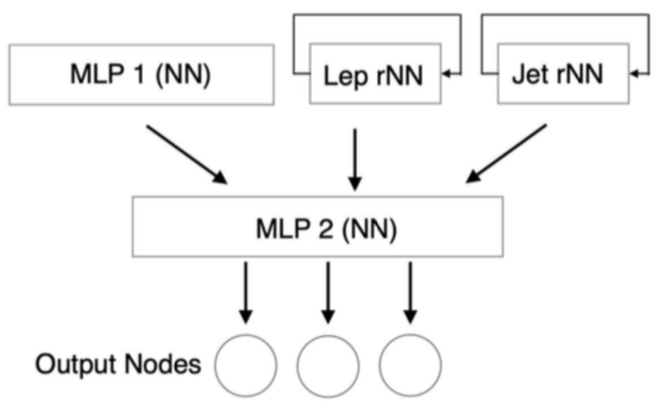

Figure 4.7: A schematic of the general NN architecture used for training and classifying different production modes.

N_{jets}, number of b-tagged jets at 70% tagging efficiency, $N_{\text{b-jets,70\%}}$, and the scalar sum of the p_{T} of all reconstructed jets, H_{T}, are used to identify the ttH process.

Depending on the category and the number of processes being targeted, the NN has two or three output nodes. The value computed at each node represents the probability for the event to originate from the given process. For example, in the 0-jet category, two probabilities are evaluated, NN_{ggF} and NN_{ZZ}. As these two values are a linear transformation of each other, only one output, NN_{ggF}, is used as a discriminant in the fit model. In categories with three targeted processes, only two output probabilities

Table 4.3: The input variables used to train the MLP, and the two rNNs for the four leptons and the (up to three) jets. For each category, the processes which are classified by a NN, their corresponding variables and the observable used in each category are shown. For example, there are eight variables for the Lepton rNN being trained if p_{T}^{ℓ} and η_ℓ are listed. Leptons and jets are denoted by "ℓ" and "j". See the text for variable definitions.

Category	Processes	MLP	Lepton rNN	Jet rNN	Observable
$0j$-$p_{\mathrm{T}}^{4\ell}$-Low $0j$-$p_{\mathrm{T}}^{4\ell}$-Med	ggF, ZZ^*	p_{T}^{H}, D_{ZZ^*}, m_{12}, m_{34}, $\lvert\cos\theta^*\rvert$, $\cos\theta_1$, ϕ_{ZZ}	p_{T}^{ℓ}, η_ℓ	-	$\mathrm{NN}_{\mathrm{ggF}}$
$1j$-$p_{\mathrm{T}}^{4\ell}$-Low	ggF, VBF, ZZ^*	p_{T}^{H}, p_{T}^{j1}, η_j, $\Delta R_{4\ell j}$, D_{ZZ^*}	p_{T}^{ℓ}, η_ℓ	-	$\mathrm{NN}_{\mathrm{VBF}}$ for $\mathrm{NN}_{ZZ} < 0.25$ NN_{ZZ} for $\mathrm{NN}_{ZZ} > 0.25$
$1j$-$p_{\mathrm{T}}^{4\ell}$-Med	ggF, VBF, ZZ^*	p_{T}^{H}, p_{T}^{j1}, η_j, $E_{\mathrm{T}}^{\mathrm{miss}}$, $\Delta R_{4\ell j}$, D_{ZZ^*}, $\eta_{4\ell}$	p_{T}^{ℓ}, η_ℓ	-	$\mathrm{NN}_{\mathrm{VBF}}$ for $\mathrm{NN}_{ZZ} < 0.25$ NN_{ZZ} for $\mathrm{NN}_{ZZ} > 0.25$
$1j$-$p_{\mathrm{T}}^{4\ell}$-High	ggF, VBF	p_{T}^{H}, p_{T}^{j1}, η_j, $E_{\mathrm{T}}^{\mathrm{miss}}$, $\Delta R_{4\ell j}$, $\eta_{4\ell}$	p_{T}^{ℓ}, η_ℓ	-	$\mathrm{NN}_{\mathrm{VBF}}$
$2j$	ggF, VBF, VH	m_{jj}, $p_{\mathrm{T}}^{4\ell jj}$	p_{T}^{ℓ}, η_ℓ	p_{T}^{j1}, η_j	$\mathrm{NN}_{\mathrm{VBF}}$ for $\mathrm{NN}_{VH} < 0.2$ NN_{VH} for $\mathrm{NN}_{VH} > 0.2$
$2j$-BSM-like	ggF, VBF	$\eta_{ZZ}^{\mathrm{Zepp}}$, $p_{\mathrm{T}}^{4\ell jj}$	p_{T}^{ℓ}, η_ℓ	p_{T}^{j1}, η_j	$\mathrm{NN}_{\mathrm{VBF}}$
VH-Lep-enriched	VH, ttH	N_{jets}, $N_{\text{b-jets,70\%}}$, $E_{\mathrm{T}}^{\mathrm{miss}}$, H_{T}	p_{T}^{ℓ}	-	NN_{ttH}
ttH-Had-enriched	ggF, ttH, tXX	p_{T}^{H}, m_{jj}, $\Delta R_{4\ell j}$, $N_{\text{b-jets,70\%}}$,	p_{T}^{ℓ}, η_ℓ	p_{T}^{j1}, η_j	NN_{ttH} for $\mathrm{NN}_{tXX} < 0.4$ NN_{tXX} for $\mathrm{NN}_{tXX} > 0.4$

are independent. To incorporate these into the fit model, the events in this category are divided into two sub-categories and one of two output probabilities is used in each sub-category. For example, in the 1-jet categories, $\mathrm{NN}_{\mathrm{VBF}}$ and NN_{ZZ} are used. The sub-categories are defined by requiring NN_{ZZ} to be smaller or larger than 0.25. In these two regions, the $\mathrm{NN}_{\mathrm{VBF}}$ and NN_{ZZ} probabilities are used respectively as the discriminant in the fit model. The sub-category definitions and observables used in all reconstructed event categories are summarized in Table 4.3.

The improvement due to the introduction of NN based discriminants when compared to BDT based discriminants on the expected statistical error for the measurement of Stage 0 and Reduced Stage 1 cross-sections is shown in Table 4.4.

Table 4.4: Percentage improvement on the expected upper and lower statistical error on Stage 0 and Reduced Stage 1 cross-section measurement.

Production Bin	Lower Error	Upper Error
	Stage 0	
ggF	4.8%	4.6%
VBF	7.7%	6.6%
VH	5.5%	3.9%
ttH	1.1%	3.9%
	Reduced Stage 1	
ggF-0j	3.0%	0.3%
ggF-1j-p_{T}^{H}-Low	6.5%	5.6%
ggF-1j-p_{T}^{H}-Med	1.5%	1.2%
ggF-1j-p_{T}^{H}-High	4.2%	1.9%
ggF-2j	14.1%	13.3%
VBF-p_{T}^{j}-Low	8.3%	6.7%
VBF-p_{T}^{j}-High	60.0%	23.6%
VH-Had	14.3%	10.9%
VH-Lep	7.5%	1.7%
ttH	1.1%	4.3%

4.6 Background Estimation

4.6.1 Non-resonant ZZ^*, $t\bar{t}+V$ and tri-boson

Continuum background from ZZ^* production via $q\bar{q}$ annihilation, gluon–gluon fusion and vector boson scattering can result in four prompt leptons in the final state, and constitutes the largest background in most categories. For previous analyses [51, 129, 151], simulation was exclusively used to estimate both the shape and the normalization. It was found that while the observed distributions matched the predictions, theoretical simulations underestimated the observed yields by 10%–20%. To improve upon this and best utilize the larger dataset, the normalization for ZZ^* is estimated using a data-driven technique for this analysis. This leads to a reduction in the total uncertainty by removing both the theoretical and the luminosity uncertainty from impacting the normalization. Similarly, dedicated measurements of $t\bar{t}+Z$ [159, 160] have shown large theoretical mis-modelling. As such, the normalization for $t\bar{t}+Z$ and other rare top background is also estimated from data.

As outlined in Section 4.5, to estimate the normalization, sideband categories in the mass region 105–115 GeV and 130–160 GeV are defined according to the jet multiplicity (SB-0j, SB-1j, SB-2j). Normalization of the ZZ^* background is simultaneously fit with a common normalization factor for signal region and sideband categories with the same jet multiplicity. For example, the ZZ^* background is scaled by the common factor for the 2j, 2j-BSM-like and SB-2j categories. The full correlation scheme is outlined in Table 4.5. The shape templates for NN discriminants and the expected fraction of events in each reconstructed event category are obtained from simulation. Good agreement is found between data and simulation for the shape of the NN observable in the dedicated phase space region constructed for validation. Due to limited sensitivity and low expected yield, the normalization of ZZ^* in the ttH-like categories is estimated from simulation.

The estimation of the ZZ^* process in jet multiplicity bins removes one of the leading theoretical uncertainties [101]. However, the additional degrees of freedom introduced in the fit limit the improvement of this change to 1%–2%. It is expected that as more data are collected, the expected improvement of this method will become higher.

Table 4.5: Correlation scheme for estimating the major backgrounds. Signal categories in rows marked with "X" are fitted simultaneously with the sideband categories in columns.

Category Factor	SB-$0j$	SB-$1j$	SB-$2j$	SB-tXX-enriched
$0j$-$p_{\mathrm{T}}^{4\ell}$-Low	X			
$0j$-$p_{\mathrm{T}}^{4\ell}$-Med	X			
$0j$-$p_{\mathrm{T}}^{4\ell}$-High	X			
$1j$-$p_{\mathrm{T}}^{4\ell}$-Low		X		
$1j$-$p_{\mathrm{T}}^{4\ell}$-Med		X		
$1j$-$p_{\mathrm{T}}^{4\ell}$-High		X		
$1j$-$p_{\mathrm{T}}^{4\ell}$-BSM-Like		X		
$2j$			X	
$2j$-BSM-like			X	
VH-Lep-enriched	X			
ttH-Had-enriched				X
ttH-Lep-enriched				X

Similarly, backgrounds affecting ttH-like categories are estimated simultaneously from an enriched sample selected in a dedicated side band region (SB-tXX-enriched), with the mass cut extended up to 350 GeV to improve the statistical precision of the estimate. The normalization of the tXX process is simultaneously fit across ttH-Lep-enriched, ttH-Had-enriched and SB-tXX-enriched categories. Due to limited sensitivity, the normalization of this process in all other categories is estimated from simulation.

Due to their limited expected contribution, the VVV process is estimated and cross-checked for all categories using the simulated samples.

4.6.2 Reducible background

For estimating contributions from background originating from $Z+$jets and $t\bar{t}$ processes in the $\ell\ell + ee$ channels, the method outlined in Section 3.6.2 is used.

For the $\ell\ell + \mu\mu$ final states, the overall methodology remains the same as before. Two additional control regions are introduced in the simultaneous fit to improve the statistical error: a control region constructed by following the main event selection criteria but by inverting the isolation requirements for at least one lepton in the sub-leading lepton pair, and a $\ell\ell + \mu^{\pm}\mu^{\pm}$ control region with relaxed impact-parameter and isolation requirements and a same-sign requirement on the subleading lepton pair. Rather than using MC simulation to estimate the fraction of background in each category, the simultaneous fit is performed in each category.

For both $\ell\ell + ee$ and $\ell\ell + \mu\mu$ channels, a data-driven approach is used for estimating the shape of the NN observable in each category. The observed data distributions in the $3\ell + X$ and the Relaxed Isolation-d_0 control region are extrapolated to the signal region. Data-driven transfer factors, as described in Section 3.6.2, are used, while fractions of each process in the different bins are estimated from MC simulation.

4.7 Systematic Uncertainty

The strategy outlined in Section 3.7 is used for this analysis as well, with the changes outlined below. The impact of systematic uncertainties on the cross-section measurements in different production bins is summarized in Table 4.6.

Table 4.6: The impact of the dominant systematic uncertainties (in percent) on the cross sections in production bins of the Production Mode Stage and the reduced Stage 1.1. Similar sources of systematic uncertainties are grouped together - Luminosity (Lumi.), electron/muon reconstruction and identification efficiencies and pile-up modelling (e, μ, pile-up), jet energy scale/resolution and b-tagging efficiencies (Jets, flav. tagging), uncertainties on reducible background (reducible backg.), theoretical uncertainties on ZZ^* background and tXX background, and theoretical uncertainties on the signal due to parton density function (PDF), QCD scale (QCD) and showering algorithm (Shower). The uncertainties are rounded to the nearest 0.5%, except for the luminosity uncertainty that is measured to be 1.7% and increases for the VH signal processes due to the simulation-based normalisation of the VVV background.

Measurement	Experimental uncertainties [%]				Theory uncertainties [%]				
					Background		Signal		
	Lumi.	e, μ, pile-up	Jets, flav. tagging	Reducible backg.	ZZ^*	tXX	PDF	QCD	Shower
Inclusive cross section									
	1.7	2.5	0.5	< 0.5	1	< 0.5	< 0.5	1	2
Production mode cross sections									
ggF	1.7	2.5	1	< 0.5	1.5	< 0.5	0.5	1	2
VBF	1.7	2	4	< 0.5	1.5	< 0.5	1	5	7
VH	1.9	2	4	1	6	< 0.5	2	13.5	7.5
ttH	1.7	2	6	< 0.5	1	0.5	0.5	12.5	4
Stage 1.1 production bin cross sections									
gg2H-0j-p_T^H-Low	1.7	3	1.5	0.5	6.5	< 0.5	< 0.5	1	1.5
gg2H-0j-p_T^H-High	1.7	3	5	< 0.5	3	< 0.5	< 0.5	0.5	5.5
gg2H-1j-p_T^H-Low	1.7	2.5	12	0.5	7	< 0.5	< 0.5	1	6
gg2H-1j-p_T^H-Med	1.7	3	7.5	< 0.5	1	< 0.5	< 0.5	1.5	5.6
gg2H-1j-p_T^H-High	1.7	3.0	11	0.5	2	< 0.5	< 0.5	2	7.5
gg2H-2j	1.7	2.5	16.5	1	12.5	0.5	< 0.5	2.5	10.5
gg2H-p_T^H-High	1.7	1.5	3	0.5	3.5	< 0.5	< 0.5	2	3.5
qq2Hqq-VH	1.8	4	17	1	4	1	0.5	5.5	8
qq2Hqq-VBF	1.7	2	3.5	< 0.5	5	< 0.5	< 0.5	6	10.5
qq2Hqq-BSM	1.7	2	4	< 0.5	2.5	< 0.5	< 0.5	3	8
VH-Lep	1.8	2.5	2	1	2	0.5	< 0.5	1.5	3
ttH	1.7	2.5	5	0.5	1	0.5	< 0.5	11	3

4.8 Experimental Uncertainty

With the use of better reconstruction algorithms and calibration methods, experimental systematic uncertainties are reduced compared to the 36.1 fb^{-1} analysis.

The uncertainty on the total luminosity is reduced to 1.7%, which significantly improves the sensitivity of the inclusive and Stage 0 ggF measurements. The impact of uncertainties related to electron, muon

[109, 110, 120] and jet [121, 122] calibration and efficiencies are reduced by a factor of two.

4.8.1 Theoretical uncertainties

As new STXS bins are added to the overall scheme, new theoretical uncertainties describing the migration between bins are added to the theoretical uncertainty scheme. Specifically, for ggF, new p_{T}^{H} bins in the 0-jet topology are added. To define a migration uncertainty due to the boundary at $p_{\mathrm{T}}^{H} = 10$ GeV, the renormalization and factorization scales used in the NNLOPS ggF simulation (see Section 3.3.2) were varied by factor of 2. Additionally, the scale associated with the NNLOPS reweighing was also varied by a factor of 2. The effect of these variations is shown in Figure 4.8. The configuration with the largest variation is chosen to define the uncertainty, which leads to an impact of 11.2% and -3.6% in the lower and upper p_{T}^{H} bins respectively.

For the ggF process, to account for higher order corrections to p_{T}^{Hjj}, which is used as a NN input variable, the uncertainty is derived by comparing the predicted distribution obtained using POWHEG NNLOPS and MADGRAPH5_AMC@NLO with the FxFx merging scheme. The former simulation models this variable at LO precision, while the latter models it at NLO. As shown in Figure 4.9, the variation for this distribution is 50%. However, the impact of this systematic uncertainty on the measured cross-section is below 2%.

For the VBF production mode, the QCD scale uncertainty is parameterized using the scheme outlined in Ref. [125]. The migration effects due to the selection criteria on the number of jets, transverse momentum of the Higgs boson, transverse momentum of the Higgs boson plus leading dijet systems and the invariant mass of the two leading jets are computed by varying the renormalization and factorization scales by a factor of two. The uncertainties are cross-checked with fixed-order calculations. Similarly, for the VH production mode with the associated V decaying leptonically, the scale variations are parameterized as migration effects due to the selection criteria on the number of jets and the transverse momentum of the associated boson [161].

For the ZZ^* background, as the normalization is computed using a data-driven approach, only the impact of PDF, QCD scales and the showering algorithm choice on the relative fraction of events for simultaneously estimated categories are considered. Additional uncertainties on the gluon and the vector boson initiated ZZ^* process are taken into account by changing the relative composition of the three processes according to the theoretical uncertainty on the predicted cross sections. The difference in the relative fraction of events in each category as predicted by the SHERPA, POWHEG and MADGRAPH5_AMC@NLO generators is taken as an additional uncorrelated uncertainty. The combined impact of these uncertainties ranges from about 2% in ggF to about 5% in VH.

For the tXX processes, uncertainties due to PDF and QCD scales variations are considered on the relative fraction of events present in the ttH-enriched categories and in the SB-tXX-enriched control region and on the NN discriminant shape. Differences between MADGRAPH5_AMC@NLO and SHERPA are considered as an additional systematic uncertainty. The impact on the ttH cross-section is about 0.5%. For all other categories where this process is estimated from simulation, the effect of these uncertainties on the SM cross-section and acceptance is also considered.

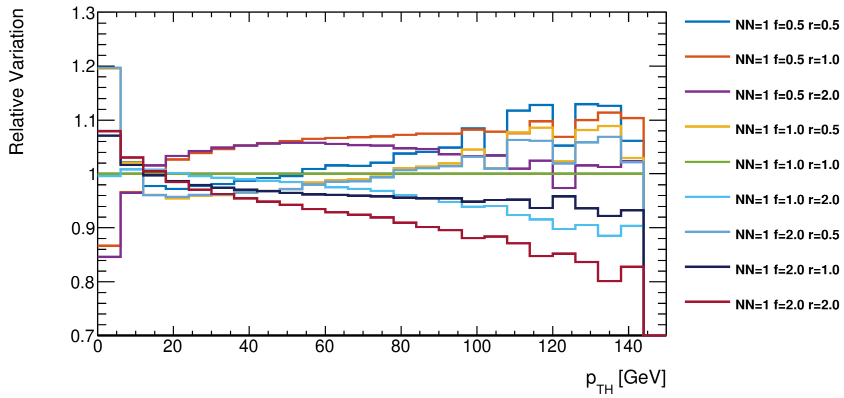

(a) NNLOPS Scale = Nominal

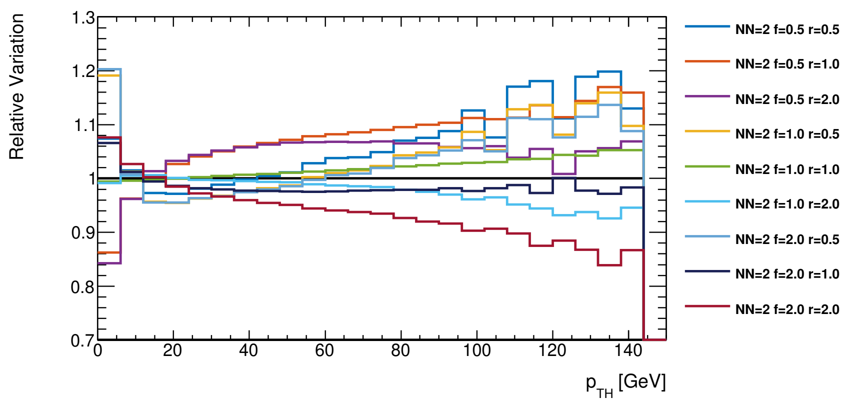

(b) NNLOPS Scale = 2×Nominal

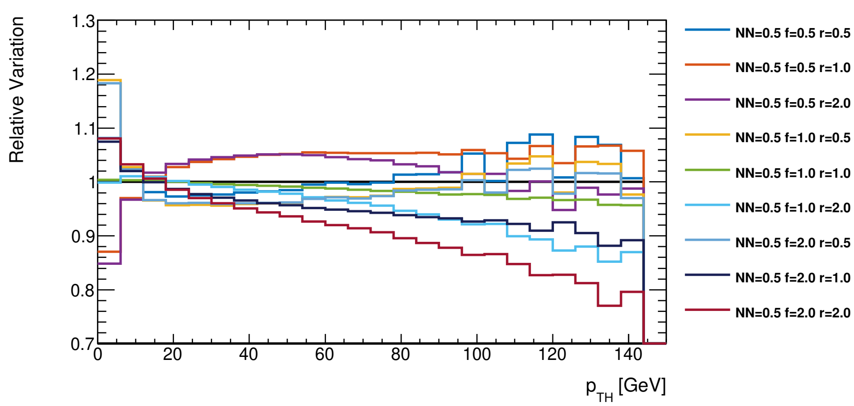

(c) NNLOPS Scale = 0.5×Nominal

Figure 4.8: The relative variation in the p_{T}^{H} distribution in the 0-jet topology, when varying the NNLOPS (NN) reweighing scale, the factorization (f) and renormalization (r) scale. The configuration with the largest variation is used to define the overall migration uncertainty.

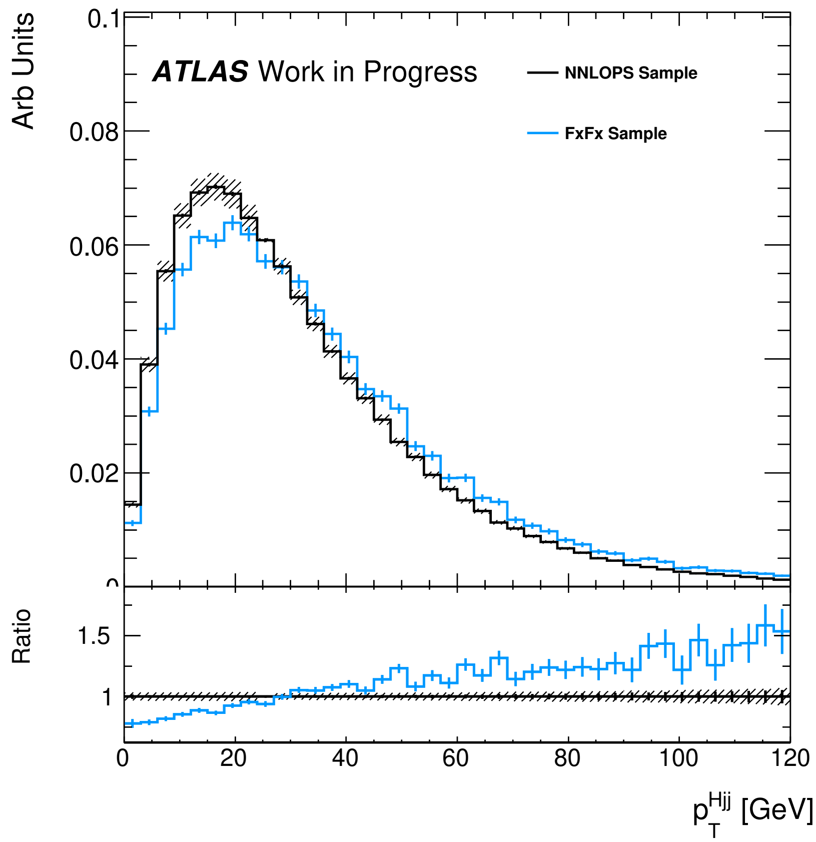

Figure 4.9: The variation in the distribution for the p_{T}^{Hjj} variable as obtained from Powheg NNLOPS and MadGraph5_aMC@NLO with the FxFx merging scheme. The former models this variable at LO, while the latter models this at NLO. The difference between the two is used to define the theoretical uncertainty associated with this variable.

4.9 Results and interpretation

4.9.1 Observed Data

The expected and observed four-lepton invariant mass distribution of the Higgs boson candidates after the event selection is shown in Figure 4.10. The figure compares the observed distribution to the post-fit expected distributions where the normalization is scaled to match the fitted results. This is contrast to prefit distributions, where the expected distribution are normalized to theoretical expectations.

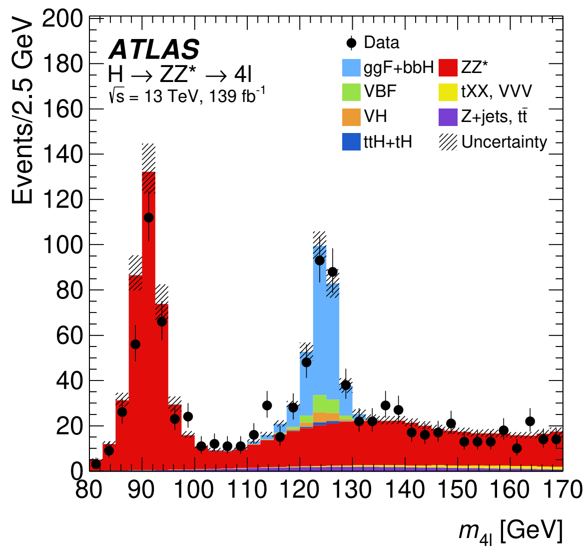

Figure 4.10: The expected and observed (post-fit) four-lepton invariant mass distribution for the selected Higgs boson candidates, shown for an integrated luminosity of 140 fb^{-1} and at $\sqrt{s} = 13$ TeV. The SM Higgs boson signal is assumed to have a mass of $m_H = 125$ GeV. The uncertainty in the prediction is shown by the hatched band, calculated as described in Section 4.7, and includes the theoretical uncertainties on the SM cross section for the signal and the background processes.

The observed and expected distributions of the jet multiplicity, the dijet invariant mass, and the four-lepton transverse momenta, which are used for the categorization of reconstructed events, are shown in Figure 4.11.

The expected numbers of signal and background events in each reconstructed event category are shown in Table 4.7 together with the corresponding observed number of events. The expected event yields are in good agreement with the observed ones. The expected and observed post-fit distributions of the NN discriminants are shown in Figure 4.12 and in Figure 4.13. In addition, Figure 4.13(g) and Figure 4.13(h) show the expected and observed yields in the categories where no NN discriminant is used and in the mass sidebands used to constrain ZZ^* and tXX background respectively. All distributions are in good agreement with the data.

Using the methodology outlined in Section 3.8.2, the statistical interpretation of the results and compatibility with the SM is discussed in the following sections. The results have similar sensitivity for the ggF bins, better sensitivity for VBF and VH bins and slightly worse sensitivity for the ttH bins when compared to the results presented in Ref. [162]. The improved sensitivity is attributed to the extensive use of the NNs, while the worse sensitivity is attributed to the different criteria for STXS bin

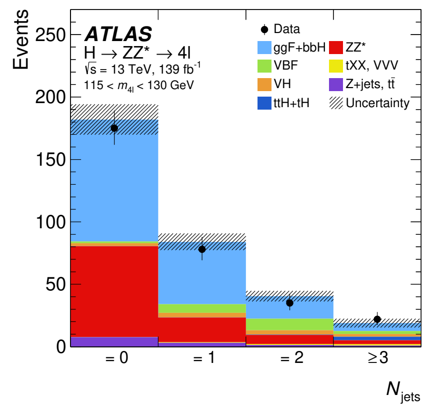

(a) N_{jets}

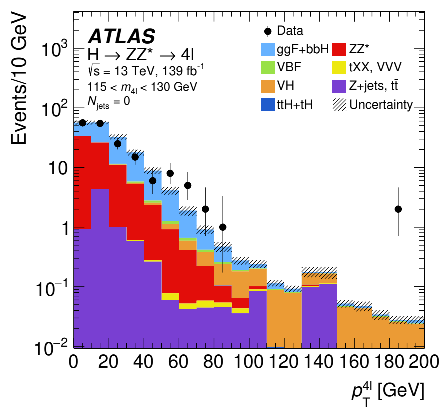

(b) $p_T^{4\ell}$ with zero jets

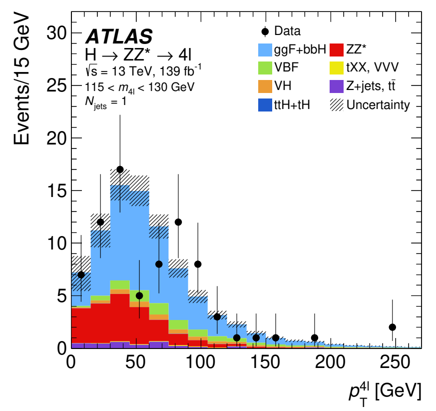

(c) $p_T^{4\ell}$ with one jet

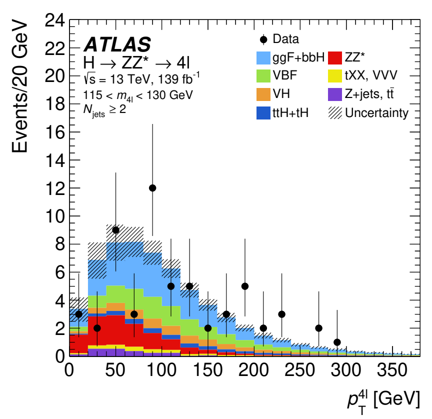

(d) $p_T^{4\ell}$ with at least two jets

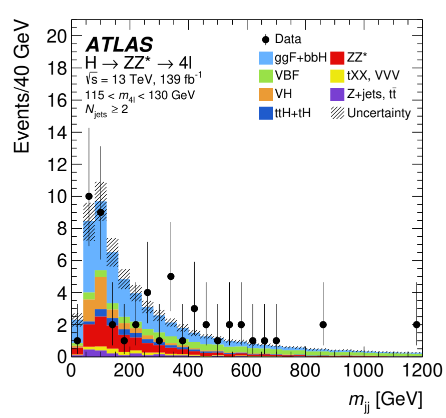

(e) m_{jj}

Figure 4.11: The observed and expected distributions (post-fit) of (a) the jet multiplicity N_{jets} after the inclusive event selection, the four-lepton transverse momenta $p_T^{4\ell}$ for events with (b) exactly zero jets, (c) with exactly one jet and (d) with at least two jets and (e) the dijet invariant mass m_{jj} for events with at least two jets. The SM Higgs boson signal is assumed to have a mass $m_H = 125$ GeV. The uncertainty in the prediction is shown by the hatched band, calculated as described in Section 4.7, and includes the theoretical uncertainties on the SM cross section for the signal and the background processes.

Table 4.7: The expected (prefit) and observed numbers of events for an integrated luminosity of 140 fb^{-1} and at $\sqrt{s} = 13$ TeV in the signal region $115 < m_{4\ell} < 130$ GeV and sideband region $105 < m_{4\ell} < 115$ GeV or $130 < m_{4\ell} < 160$ GeV (350 GeV for tXX-enriched) in each reconstructed event category assuming the SM Higgs boson signal with a mass $m_H = 125$ GeV. The sum of the expected number of SM Higgs boson events and the estimated background yields is compared to the data. Combined statistical and systematic uncertainties are included for the predictions. Expected contributions that are below 0.2% of the total yield in each reconstructed category are not shown and are replaced by "-".

Reconstructed event category	Signal	ZZ^* background	tXX background	Other backgrounds	Total expected	Observed
Signal			$115 < m_{4\ell} < 130$ GeV			
$0j$-$p_T^{4\ell}$-Low	24.2 ± 3.5	30 ± 4	–	0.93 ± 0.13	55 ± 5	56
$0j$-$p_T^{4\ell}$-Med	76 ± 8	37 ± 4	–	6.5 ± 0.6	120 ± 9	117
$0j$-$p_T^{4\ell}$-High	0.355 ± 0.031	0.020 ± 0.012	0.0094 ± 0.0027	0.30 ± 0.05	0.69 ± 0.06	1
$1j$-$p_T^{4\ell}$-Low	34 ± 4	15.5 ± 2.7	–	1.91 ± 0.29	52 ± 5	41
$1j$-$p_T^{4\ell}$-Med	20.8 ± 2.8	4.0 ± 0.7	0.114 ± 0.013	1.02 ± 0.19	26.0 ± 2.9	31
$1j$-$p_T^{4\ell}$-High	4.7 ± 0.8	0.48 ± 0.10	0.043 ± 0.008	0.27 ± 0.04	5.5 ± 0.8	4
$1j$-$p_T^{4\ell}$-BSM-Like	1.23 ± 0.23	0.069 ± 0.031	0.0067 ± 0.0031	0.062 ± 0.012	1.37 ± 0.23	2
$2j$	38 ± 5	9.1 ± 2.7	0.95 ± 0.08	2.13 ± 0.31	50 ± 6	48
$2j$-BSM-like	3.3 ± 0.6	0.18 ± 0.06	0.032 ± 0.005	0.091 ± 0.017	3.6 ± 0.6	6
VH-Lep-enriched	1.29 ± 0.07	0.156 ± 0.025	0.039 ± 0.009	0.0194 ± 0.0032	1.50 ± 0.08	1
ttH-Had-enriched	1.02 ± 0.18	0.058 ± 0.025	0.252 ± 0.032	0.119 ± 0.033	1.45 ± 0.18	2
ttH-Lep-enriched	0.42 ± 0.04	0.002 ± 0.005	0.0157 ± 0.0023	0.0028 ± 0.0029	0.44 ± 0.04	1
Sideband			$105 < m_{4\ell} < 115$ GeV or $130 < m_{4\ell} < 160$ GeV			
SB-$0j$	4.5 ± 0.5	150 ± 13	–	16.2 ± 2.2	171 ± 13	183
SB-$1j$	2.80 ± 0.30	51 ± 7	1.29 ± 0.16	8.4 ± 1.2	63 ± 7	64
SB-$2j$	2.02 ± 0.27	25 ± 7	4.4 ± 0.5	6.0 ± 0.9	38 ± 7	41
SB-VH-Lep-enriched	0.273 ± 0.015	0.48 ± 0.06	0.125 ± 0.018	0.126 ± 0.019	1.00 ± 0.07	3
			$105 < m_{4\ell} < 115$ GeV or $130 < m_{4\ell} < 350$ GeV			
SB-ttV-enriched	0.071 ± 0.012	0.32 ± 0.12	12.1 ± 1.3	0.84 ± 0.33	13.3 ± 1.4	19

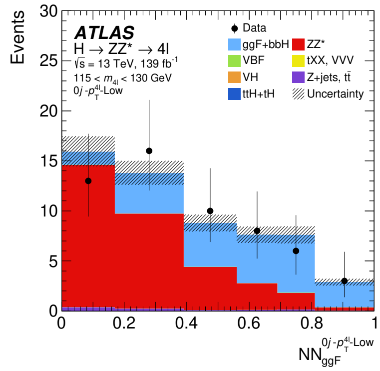

(a) $\mathrm{NN_{ggF}}$

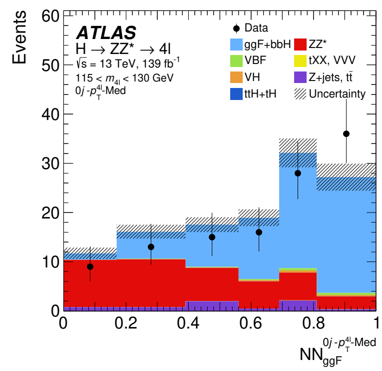

(b) $\mathrm{NN_{ggF}}$

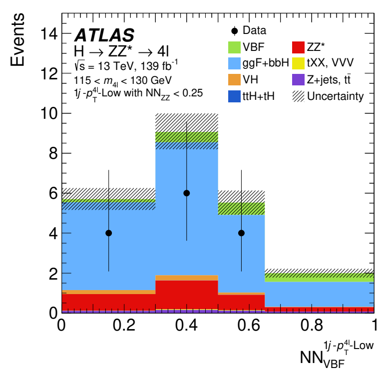

(c) $\mathrm{NN_{VBF}}$

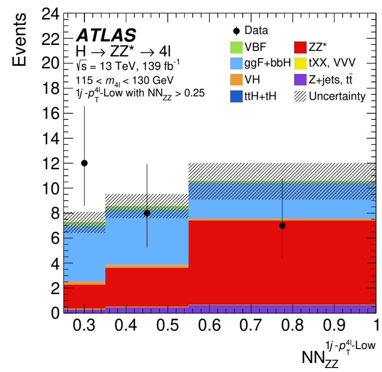

(d) $\mathrm{NN_{ZZ}}$

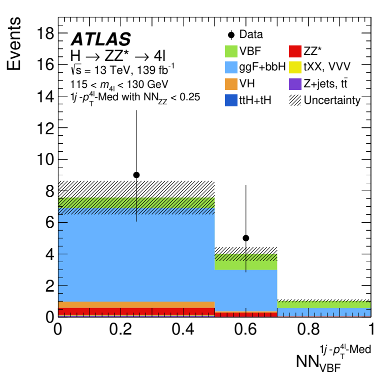

(e) $\mathrm{NN_{VBF}}$

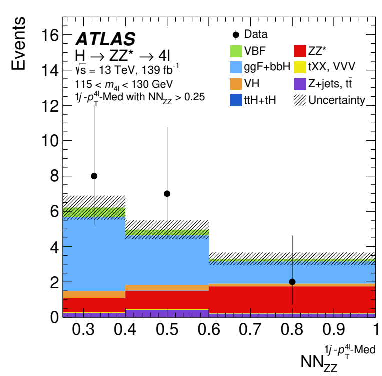

(f) $\mathrm{NN_{ZZ}}$

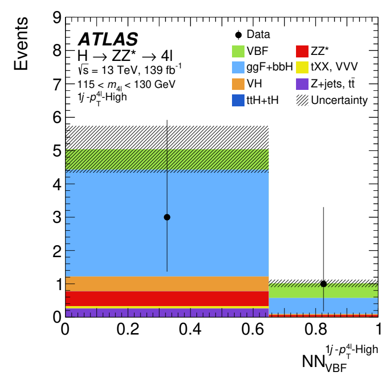

(g) $\mathrm{NN_{VBF}}$

Figure 4.12: The observed and expected NN output (post-fit) distributions for an integrated luminosity of 140 fb^{-1} and at $\sqrt{s}$ = 13 TeV in the different categories: (a) $\mathrm{NN_{ggF}}$ in $0j$-$p_{\mathrm{T}}^{4\ell}$-Low, (b) $\mathrm{NN_{ggF}}$ in $0j$-$p_{\mathrm{T}}^{4\ell}$-Med, (c) $\mathrm{NN_{VBF}}$ $1j$-$p_{\mathrm{T}}^{4\ell}$-Low with $\mathrm{NN_{ZZ}}$ <0.25, (d) $\mathrm{NN_{ZZ}}$ in $1j$-$p_{\mathrm{T}}^{4\ell}$-Low with $\mathrm{NN_{ZZ}}$ >0.25, (e) $\mathrm{NN_{VBF}}$ in $1j$-$p_{\mathrm{T}}^{4\ell}$-Med with $\mathrm{NN_{ZZ}}$ <0.25, (f) $\mathrm{NN_{ZZ}}$ in $1j$-$p_{\mathrm{T}}^{4\ell}$-Med with $\mathrm{NN_{ZZ}}$ >0.25, (g) $\mathrm{NN_{VBF}}$ in $1j$-$p_{\mathrm{T}}^{4\ell}$-High. The SM Higgs boson signal is assumed to have a mass of m_H = 125 GeV. The uncertainty in the prediction is shown by the hatched band, calculated as described in Section 4.7, and includes the theoretical uncertainties on the SM cross section for the signal and the background processes. The bin boundaries are chosen to maximize the significance of the targeted signal in each category.

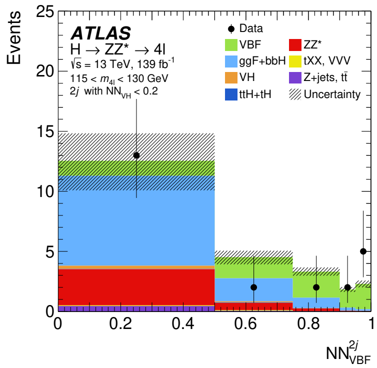

(a) $\mathrm{NN_{VBF}}$

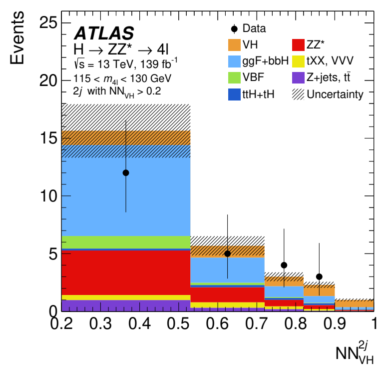

(b) $\mathrm{NN_{VH}}$

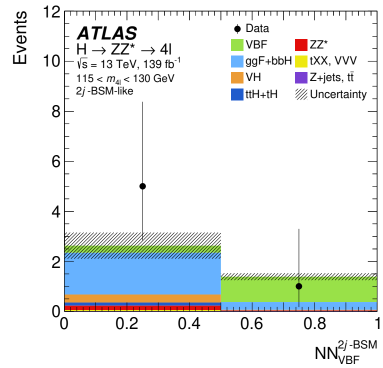

(c) $\mathrm{NN_{VBF}}$

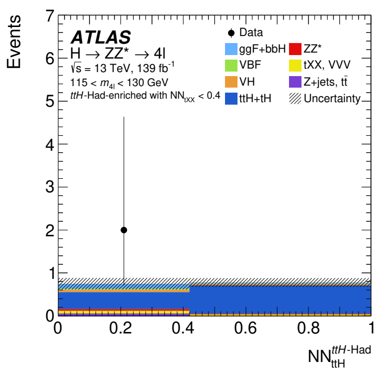

(d) $\mathrm{NN_{ttH}}$

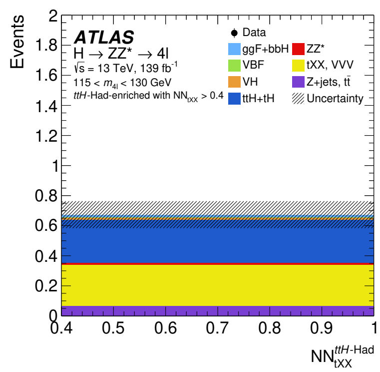

(e) $\mathrm{NN_{tXX}}$

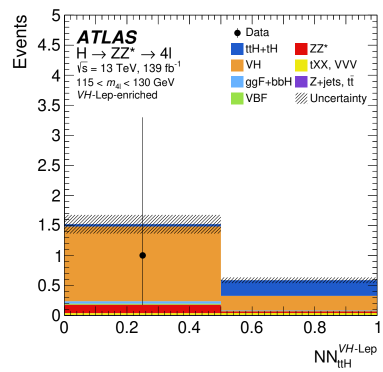

(f) $\mathrm{NN_{ttH}}$

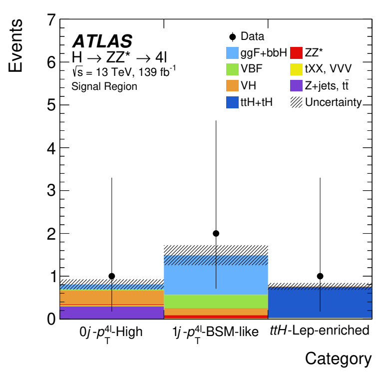

(g) Counting signal regions

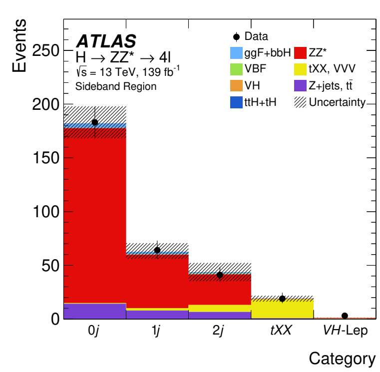

(h) Sideband categories

Figure 4.13: The observed and expected NN output (post-fit) distributions for an integrated luminosity of 140 fb^{-1} and at $\sqrt{s} = 13$ TeV in the different categories: (a) $\mathrm{NN_{VBF}}$ $2j$ with $\mathrm{NN_{VH}}$ <0.2, (b) $\mathrm{NN_{VH}}$ in $2j$ with $\mathrm{NN_{VH}}$ >0.2, (c) $\mathrm{NN_{VBF}}$ in $2j$-BSM-like, (d) $\mathrm{NN_{ttH}}$ in ttH-Had-enriched with $\mathrm{NN_{tXX}}$ <0.4, (e) $\mathrm{NN_{tXX}}$ in ttH-Had-enriched with $\mathrm{NN_{tXX}}$ >0.4 and (f) $\mathrm{NN_{ttH}}$ in VH-Lep-enriched. The categories where no NN discriminant is used are also shown (g), together with the sidebands used to constrain the ZZ^* and tXX backgrounds (h). The SM Higgs boson signal is assumed to have a mass of $m_H = 125$ GeV. The uncertainty in the prediction is shown by the hatched band, calculated as described in Section 4.7, and includes the theoretical uncertainties on the SM cross section for the signal and the background processes. The bin boundaries are chosen to maximize the significance of the targeted signal in each category.

optimization.

4.9.2 Measurement of production mode cross sections

Assuming that the relative signal fractions in each production bin are given by the predictions for the SM Higgs boson, the inclusive $H \to ZZ^*$ production cross section for $|y_H| < 2.5$ is measured to be:

$$\sigma \cdot B \equiv \sigma \cdot B(H \to ZZ^*) \;=\; 1.34 \pm 0.11(\text{stat.}) \pm 0.04(\text{exp.}) \pm 0.04(\text{th.})\ \text{pb} \;=\; 1.34 \pm 0.12\ \text{pb},$$

The SM prediction is $(\sigma \cdot B)_{\text{SM}} \equiv (\sigma \cdot B(H \to ZZ^*))_{\text{SM}} = 1.33 \pm 0.08$ pb. The data are also interpreted in terms of the global signal strength, yielding

$$\mu = 1.01 \pm 0.08(\text{stat.}) \pm 0.04(\text{exp.}) \pm 0.05(\text{th.}) = 1.01 \pm 0.11.$$

The measured cross section and signal strength are in a good agreement with the SM prediction, with a p-value of 98.9% for both consistency tests.

The corresponding likelihood functions are shown in Figure 4.14. The dominant systematic uncertainty in the cross section measurement is the experimental uncertainty in the lepton efficiency and integrated luminosity measurements. The signal strength measurement is also equally affected by the theoretical uncertainty of the ggF signal yield due to QCD scale variations.

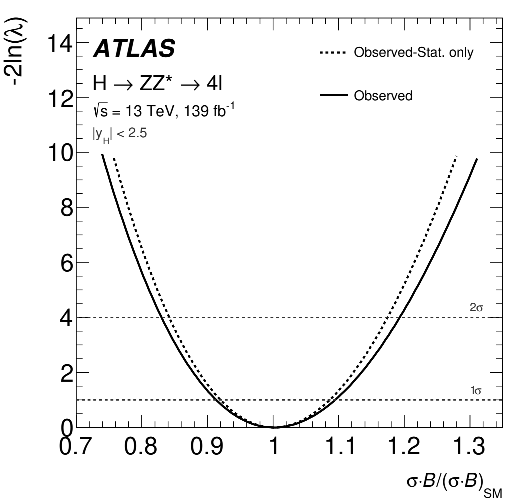

(a) $\sigma \cdot B(H \to ZZ^*)$

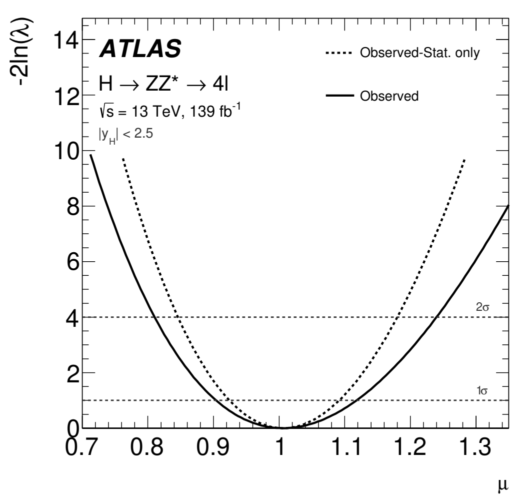

(b) μ

Figure 4.14: Observed profile likelihood as a function of (a) $\sigma \cdot B(H \to ZZ^*)$ normalized by the SM expectation and (b) the inclusive signal strength μ; the scans are shown both with (solid line) and without (dashed line) systematic uncertainties.

The expected SM cross sections, the observed values of $\sigma \cdot B(H \to ZZ^*)$, and their ratio for the inclusive production and in each bin of the Production Mode Stage and the reduced Stage-1.1 are shown in Table 4.8.

The corresponding values are summarized in Figure 4.15. The bbH production process is treated as a part of the ggF production bins. In the ratio calculation, uncertainties on the SM expectation are not taken into account. The Production Mode Stage and reduced Stage-1.1 measurements agree with the predictions for the SM Higgs boson. The p-values of the consistency tests are 91.3% and 76.5%, respectively.

Table 4.8: The expected SM cross section $(\sigma \cdot B)_{\mathrm{SM}}$, the observed value of $\sigma \cdot B$, and their ratio $(\sigma \cdot B)/(\sigma \cdot B)_{\mathrm{SM}}$ for the inclusive production and for each Production Mode and reduced Stage-1.1 production bin for the $H \to ZZ^*$ decay for an integrated luminosity of 140 fb^{-1} at $\sqrt{\mathrm{s}} = 13$ TeV. The bbH (tH) contribution is included in the ggF (ttH) production bins. The uncertainties are given as (stat.)+(exp.)+(th.) for the inclusive cross section and Production Mode Stage, and as (stat.)+(syst.) for the Reduced Stage 1.1. The Stage 1.1 results are dominated by the statistical uncertainty and the impact of theory uncertainties is smaller compared to the Production Mode Stage. The impact of the theory uncertainties for Stage-1.1 is smaller than the rounding.

Production bin	Cross section $(\sigma \cdot B)$ [pb]		$(\sigma \cdot B)/(\sigma \cdot B)_{\mathrm{SM}}$
	SM expected	Observed	Observed
Inclusive production, $\lvert y_H \rvert < 2.5$			
	1.33 ± 0.08	$1.34 \pm 0.11 \pm 0.04 \pm 0.03$	$1.01 \pm 0.08 \pm 0.03 \pm 0.02$
Production bins of the Production Mode Stage, $\lvert y_H \rvert < 2.5$			
ggF	1.17 ± 0.08	$1.12 \pm 0.12 \pm 0.04 \pm 0.03$	$0.96 \pm 0.10 \pm 0.03 \pm 0.03$
VBF	0.0920 ± 0.0020	$0.11 \pm 0.04 \pm 0.01 \pm 0.01$	$1.21 \pm 0.44\ ^{+0.13}_{-0.08}\ ^{+0.07}_{-0.05}$
VH	$0.0524^{+0.0027}_{-0.0049}$	$0.075^{+0.059}_{-0.047}\ ^{+0.011}_{-0.007}\ ^{+0.013}_{-0.009}$	$1.44^{+1.13}_{-0.90}\ ^{+0.21}_{-0.14}\ ^{+0.24}_{-0.17}$
ttH	$0.0154^{+0.0010}_{-0.0013}$	$0.027^{+0.026}_{-0.017} \pm 0.002 \pm 0.002$	$1.8^{+1.7}_{-1.2} \pm 0.2 \pm 0.2$
Reduced Stage-1.1 production bins, $\lvert y_H \rvert < 2.5$			
gg2H-0j-p_{T}^{H}-Low	0.176 ± 0.025	$0.17 \pm 0.05 \pm 0.02$	$0.96 \pm 0.30 \pm 0.09$
gg2H-0j-p_{T}^{H}-High	0.55 ± 0.04	$0.63 \pm 0.09 \pm 0.06$	$1.15 \pm 0.17 \pm 0.11$
gg2H-1j-p_{T}^{H}-Low	0.172 ± 0.025	$0.05 \pm 0.07\ ^{+0.04}_{-0.06}$	$0.3 \pm 0.4\ ^{+0.2}_{-0.3}$
gg2H-1j-p_{T}^{H}-Med	0.119 ± 0.018	$0.17 \pm 0.05\ ^{+0.02}_{-0.01}$	$1.4 \pm 0.4 \pm 0.1$
gg2H-1j-p_{T}^{H}-High	0.020 ± 0.004	$0.009^{+0.016}_{-0.011} \pm 0.002$	$0.5^{+0.8}_{-0.6} \pm 0.1$
gg2H-2j	0.127 ± 0.027	$0.04 \pm 0.07 \pm 0.04$	$0.3 \pm 0.5 \pm 0.3$
gg2H-p_{T}^{H}-High	0.015 ± 0.004	$0.038^{+0.021}_{-0.016}\ ^{+0.003}_{-0.002}$	$2.5^{+1.3}_{-1.0}\ ^{+0.2}_{-0.1}$
qq2Hqq-VH	$0.0138^{+0.0004}_{-0.0006}$	$0.021^{+0.037}_{-0.029}\ ^{+0.009}_{-0.006}$	$1.5^{+2.7}_{-2.1}\ ^{+0.6}_{-0.4}$
qq2Hqq-VBF	$0.1076^{+0.0024}_{-0.0035}$	$0.15 \pm 0.05\ ^{+0.02}_{-0.01}$	$1.4 \pm 0.5\ ^{+0.2}_{-0.1}$
qq2Hqq-BSM	0.00420 ± 0.00018	$0.0005^{+0.0079}_{-0.0047} \pm 0.008$	$0.1^{+1.9}_{-1.1} \pm 0.2$
VH-Lep	0.0164 ± 0.0004	$0.022^{+0.028}_{-0.018}\ ^{+0.003}_{-0.001}$	$1.3^{+1.7}_{-1.1}\ ^{+0.2}_{-0.1}$
ttH	$0.0154^{+0.0010}_{-0.0013}$	$0.026^{+0.026}_{-0.017}\ ^{+0.005}_{-0.003}$	$1.7^{+1.7}_{-1.1}\ ^{+0.3}_{-0.2}$

The dominant contribution to the measurement uncertainty in the ggF Production Mode bin originates from the same sources as in the inclusive measurement. In the remaining three production bins of the Production Mode Stage, similar sources of uncertainty are relevant for both the cross section and the signal strength measurements: the jet energy scale or resolution uncertainties in all production bins and, additionally, theoretical jet bin migrations in the ggF process. For the reduced Stage-1 categories the

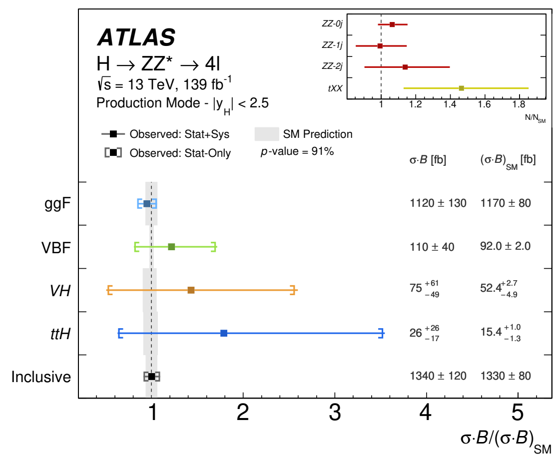

(a)

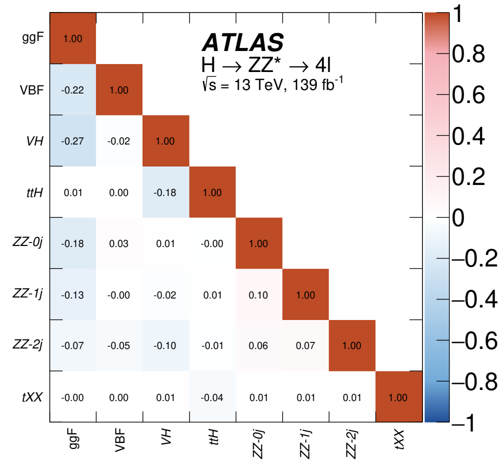

(b)

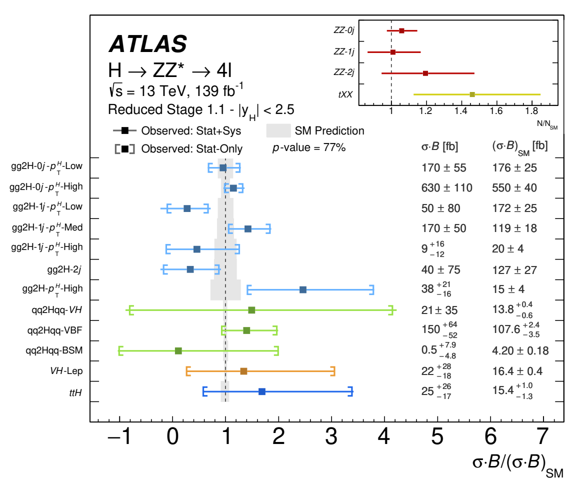

(c)

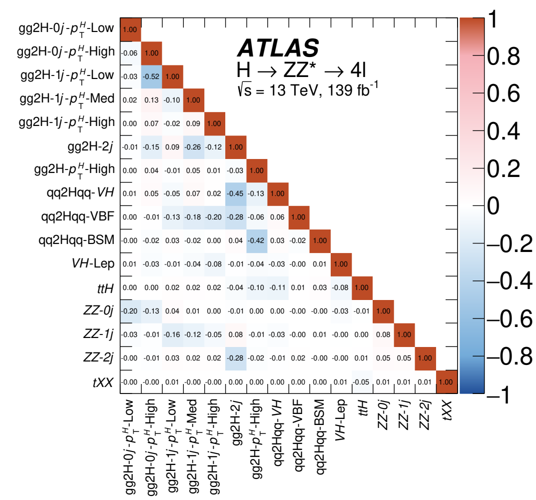

(d)

Figure 4.15: The observed and expected SM values of the cross sections $\sigma \cdot B$ normalized by the SM expectation $(\sigma \cdot B)_{\text{SM}}$ for (a) the inclusive production and in the Production Mode Stage and (c) the reduced Stage-1.1 production bins for an integrated luminosity of 140 fb^{-1} at $\sqrt{s} = 13$ TeV. The fitted normalization factors for the the ZZ and tXX background are shown in the inserts. Different colours indicate different Higgs boson production modes (or background sources). The gray vertical band represents the theory uncertainty in the signal prediction. The correlation matrices between the measured cross-sections and the ZZ and tXX normalization factors are shown for (b) Production Mode Stage and (d) reduced Stage-1.1.

dominant cross section uncertainties are the integrated luminosity and lepton efficiency measurements for the VH-Lep bin and the jet energy scale or resolution for all other categories. The gg2H-1j-p_{T}^{H}-Med, gg2H-1j-p_{T}^{H}-High, qq2Hqq-VH and ttH bins are additionally affected by parton shower uncertainties, while the uncertainties related to the top-quark mass treatment have a dominant impact on the qq2Hqq-BSM bin.

Figure 4.16 shows the likelihood contours in the (ggF, VBF), (ggF, VH), (VBF, VH) and (gg2H-0j-p_{T}^{H}-Low, gg2H-0j-p_{T}^{H}-High) plane. The other cross section parameters are left free in the fit, i.e. they are not treated as parameters of interest. The compatibility with respect to the Standard Model expectation is at the level of 0.22, 0.25, 0.19 and 0.33 standard deviations respectively.

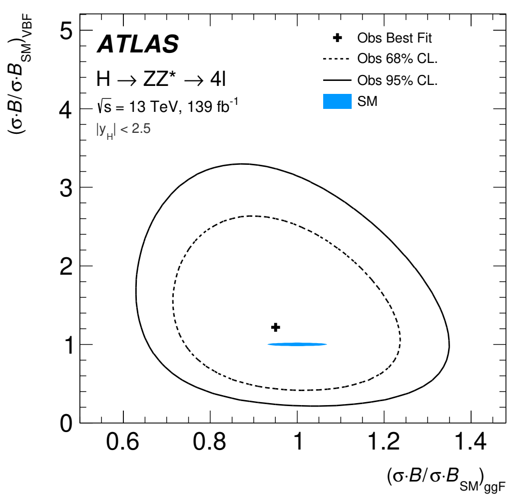

(a)

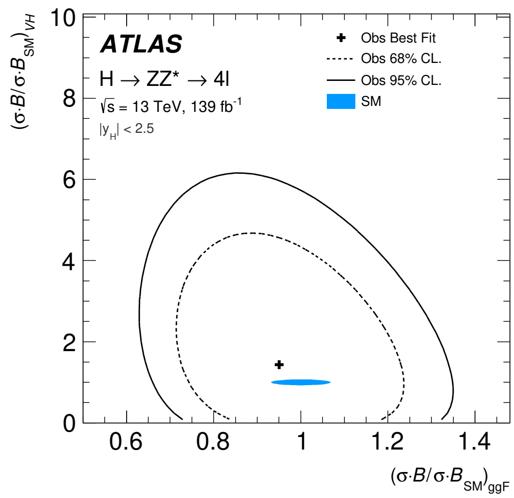

(b)

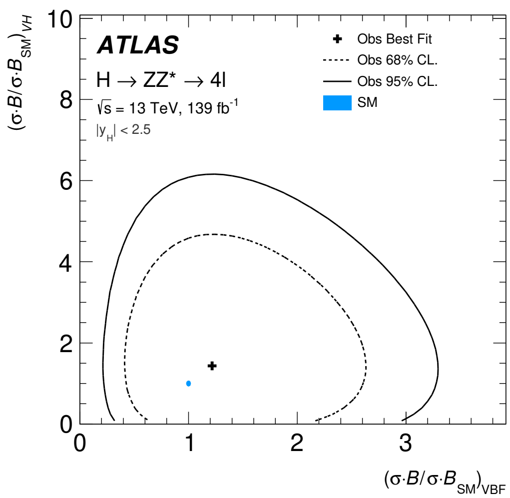

(c)

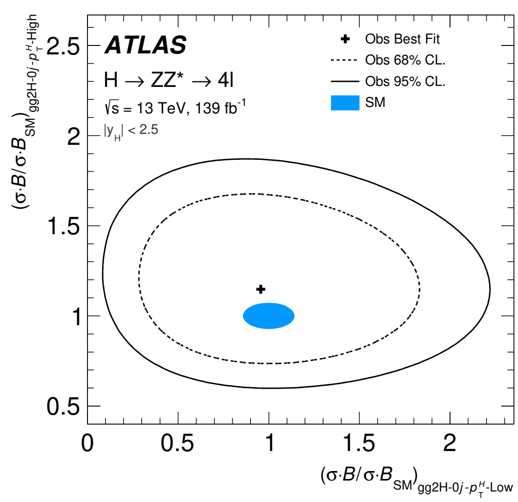

(d)

Figure 4.16: Likelihood contours at 68% CL (dashed line) and 95% CL (solid line) in the (a) (ggF, VBF), (b) (ggF, VH), (c) (VBF, VH) and (d) (gg2H-0j-p_{T}^{H}-Low, gg2H-0j-p_{T}^{H}-High) cross-section plane. The SM prediction is shown together with its theory uncertainty (filled blue ellipse). The VH parameter of interest is constrained to positive values.

4.9.3 Tensor structure of the Higgs boson

The fit results with only one Wilson coefficient fitted at a time are summarized in Fig. 4.17 and in Table 4.9. The results are in good agreement with the SM predictions. The measurements are dominated by the statistical uncertainty.

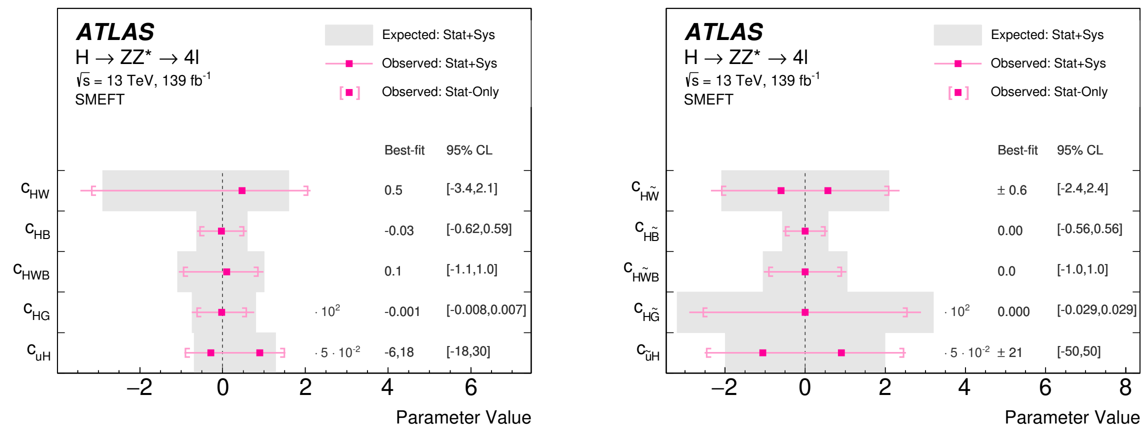

(a) (b)

Figure 4.17: The observed and expected values of SMEFT Wilson coefficients from (a) CP-even and (b) CP-odd operators obtained for an integrated luminosity of 140 fb^{-1} at $\sqrt{s} = 13$ TeV. Only one Wilson coefficient is fit at a time while all others are set to the SM expectation of zero. The gray vertical band represents the expected measurement uncertainty.

Table 4.9: The expected and observed confidence intervals at 68% and 95% CL on the SMEFT Wilson coefficients for an integrated luminosity of 139 fb^{-1} at $\sqrt{s} = 13$ TeV. Only one Wilson coefficient is fitted at a time while all others are set to zero.

EFT coupling	Expected		Observed		Best-fit value	Best-fit
parameter	68% CL	95% CL	68% CL	95% CL		p-value
c_{HG}	[-0.004,0.004]	[-0.007,0.008]	[-0.005,0.003]	[-0.008,0.007]	-0.001	0.79
c_{uH}	[-8,20]	[-14,26]	[-12,6]	[-18,30]	$-6, 18$	0.50
c_{HW}	[-1.6,0.9]	[-2.9,1.6]	[-1.5,1.3]	[-3.4,2.1]	0.5	0.66
c_{HB}	[-0.43,0.38]	[-0.62,0.60]	[-0.42,0.37]	[-0.62,0.59]	-0.03	0.98
c_{HWB}	[-0.75,0.63]	[-1.09,0.99]	[-0.71,0.63]	[-1.06,0.99]	0.1	0.93
$c_{H\widetilde{G}}$	[-0.022,0.022]	[-0.031,0.031]	[-0.019,0.019]	[-0.029,0.029]	0.000	1.00
$c_{\widetilde{u}H}$	[-26,26]	[-40,40]	[-37,37]	[-50,50]	±21	0.48
$c_{H\widetilde{W}}$	[-1.3,1.3]	[-2.1,2.1]	[-1.5,1.5]	[-2.4,2.4]	±0.6	0.84
$c_{H\widetilde{B}}$	[-0.39,0.39]	[-0.57,0.57]	[-0.37,0.37]	[-0.56,0.56]	0.00	1.00
$c_{H\widetilde{W}B}$	[-0.71,0.71]	[-1.05,1.05]	[-0.69,0.689]	[-1.03,1.03]	0.0	1.00

The strongest constraint, driven mostly by the ggF reconstructed event categories, is obtained on the

c_{HG} coefficient related to the CP-even Higgs boson interactions with gluons. The next-strongest constraints are obtained on the c_{HB}, c_{HWB}, $c_{H\widetilde{B}}$ and $c_{H\widetilde{W}B}$ coefficients which mostly affect the $H \to ZZ^*$ decay. The c_{HW} and $c_{H\widetilde{W}}$ parameters are less constrained since they are mainly measured in the production vertex of the VBF and VH production modes. These are less sensitive due to smaller cross sections. Finally, looser constraints are set on the top-Yukawa coupling parameters c_{uH} and $c_{\widetilde{u}H}$.

The results from simultaneous fits of two Wilson coefficients are shown in Figure 4.18 for several combinations of two CP-even EFT parameters and in Figure 4.19 for the corresponding CP-odd operators. Good agreement with the SM predictions is observed for all such possible combinations.

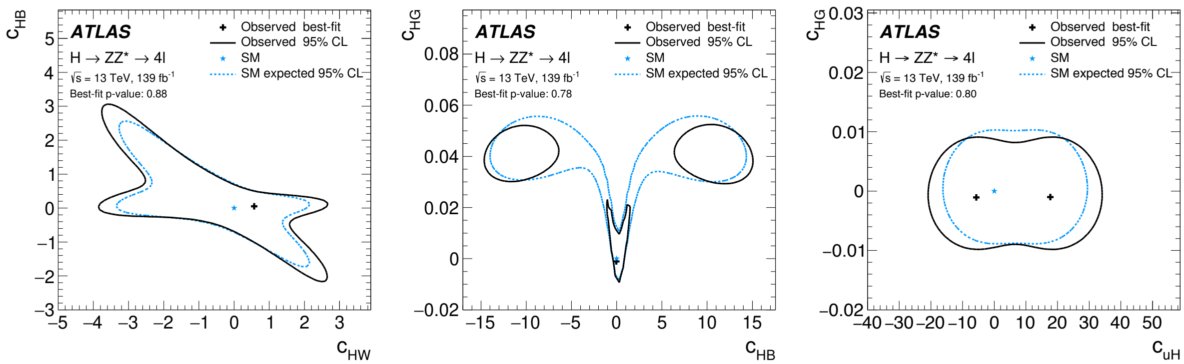

(a) (b) (c)

Figure 4.18: Expected (light blue) and observed (black) 2D-fit likelihood curves at the 68% CL (dashed lines) and 95% CL (full lines) for the SMEFT Wilson coefficients of CP-even operators at an integrated luminosity of 140 fb^{-1} and $\sqrt{s} = 13$ TeV. The best fit to the data (solid cross) and the SM prediction (star) are also indicated. Except for the two fitted Wilson coefficients, all others are set to zero.

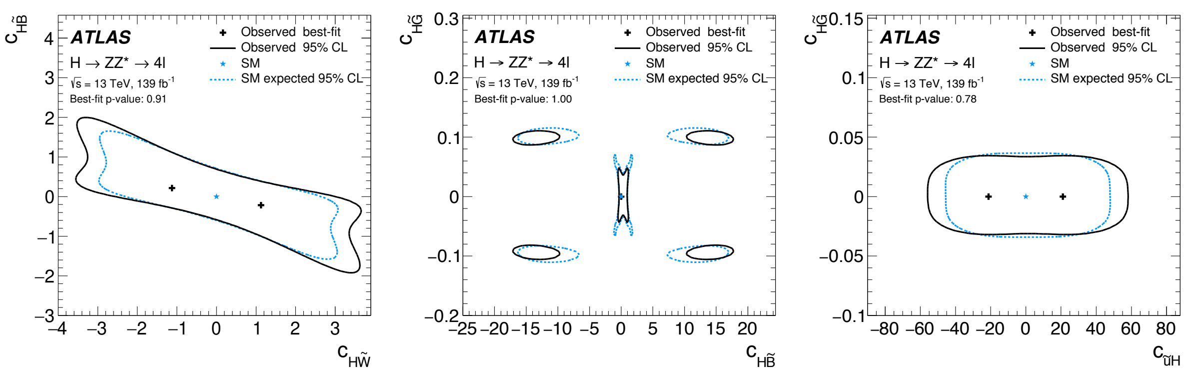

(a) (b) (c)

Figure 4.19: Expected (light blue) and observed (black) 2D-fit likelihood curves at the 68% CL (dashed lines) and 95% CL (full lines) for the SMEFT Wilson coefficients of CP-odd operators at an integrated luminosity of 140 fb^{-1} and $\sqrt{s} = 13$ TeV. The best fit to the data (solid cross) and the SM prediction (star) are also indicated. Except for the two fitted Wilson coefficients, all others are set to zero.

The anti-correlation between the c_{HW} and c_{HB}, as well as between the $c_{H\widetilde{W}}$ and $c_{H\widetilde{B}}$ parameters is driven by their impact on the signal acceptance. The non-ellipsoidal shape is caused by the acceptance correction that lowers the sensitivity for increasing coefficient values. However, this sensitivity is partially compensated by the VBF production vertex.

The v-shaped correlation between the c_{HG} and c_{HB} parameters is due to an interplay of changes to the Higgs boson decay fractions and acceptance corrections. The ggF production vertex provides the constraint on the c_{HG} parameter alone. Due to acceptance corrections for the decay vertex, this constrained range increases with larger values of c_{HB}, with the VBF production mode providing additional constraints. Sensitivity to intermediate values of the c_{HB} parameter is provided by the acceptance corrections, resulting in two additional allowed parameter regions that are disjoint from the region around the SM point. Similar arguments hold also for the CP-odd case with the $c_{H\widetilde{G}}$ and $c_{H\widetilde{B}}$ parameters.

The correlation between the c_{HG} and c_{uH} ($c_{H\widetilde{G}}$ and $c_{\widetilde{u}H}$) parameters is introduced through the interference term in the ttH vertex. However, the impact of this term on the final result is negligible since the c_{HG} ($c_{H\widetilde{G}}$) parameter is already constrained to very small values compared with c_{uH} ($c_{\widetilde{u}H}$). Therefore, the ttH production vertex is mainly constraining the c_{uH} and $c_{\widetilde{u}H}$ parameters, while the ggF vertex is constraining only the other two.

4.10 Conclusions and Next Steps

This analysis probes the properties of the Higgs boson using the $H \to ZZ^* \to 4\ell$ decay channel. Specifically, the coupling of the Higgs boson and other SM particles is studied by measuring the production cross-sections, which are also extended by measuring them in differential phase bins. Using the 140 fb^{-1} dataset collected by the ATLAS detector at the LHC, these results are the most precise measurements of the properties of the Higgs boson to date and provide stringent tests of the SM. These measurements are also used to test for contributions from BSM physics using the κ and EFT frameworks. All results are consistent with the SM and no evidence of new physics is found with the current sensitivity.

As most of the presented results are limited by the available data statistics, these results can be improved by statistically combining similar measurements from different decay channels. Furthermore, as ATLAS collects more data, this analysis can be extended to probe new or finer phase space bins. Additionally, many analysis techniques, such as the accuracy of MC simulation, the use of NNs to improve classification and the use of data driven methods to estimate background contributions to reduce model dependency, can be improved to further extend the sensitivity of this analysis.

Chapter 5

Conclusion

The Standard Model is a theoretical framework that describes the fundamental particles and the interactions between them. This framework has been successfully tested to an unprecedented level of precision. The Higgs boson, one of the predicted fundamental particles, was experimentally observed in 2012 by the ATLAS and CMS collaborations at the Large Hadron Collider. This new discovery provides a new portal to test the predictions of the Standard Model and look for any contributions from new physics.

Once the mass of the Higgs boson is specified, the SM has well defined predictions for the interaction strength between the Higgs boson and other fundamental particles. This coupling can be measured through probing different properties of the Higgs boson, with one being the measurement of the production cross sections at a proton-proton collider. The four main production modes at the LHC provide access to the Higgs boson to vector boson and to fermion couplings. Additionally, differential cross sections for each production mode can provide a further way to test the SM predictions.

These measurements are performed using the $H \to ZZ^* \to 4\ell$ decay channel, which has a fully reconstructible final state. Despite the low predicted branching ratio, this channel has a high signal to background ratio which allows properties of the Higgs boson to be probed with a high precision. For measuring the cross sections, kinematic and topological differences are used to classify the reconstructed events into categories targeting the different production modes. The measurement sensitivity is further improved by using boosted decisions trees or neural networks to create discriminating observables.

Using these methods, the inclusive production cross section is measured to be 1.34 ± 0.12 pb, which is in good agreement with the SM prediction of 1.33 ± 0.08 pb. The ggF, VBF, VH and ttH cross sections are measured to be 1.12 ± 0.12 pb, 110 ± 40 fb, 75^{+61}_{-49} fb and 27^{+26}_{-17} fb, respectively. The differential production cross sections are also measured using the Simplified Template cross sections framework. All measurements are in good agreement with the Standard Model predictions. The measurement errors are largely dominated by the limited data statistics. The leading systematic errors are the uncertainty in the luminosity measurement, lepton identification, jet energy scale and missing higher order corrections to the ggF prediction.

These results are also used to measure the Higgs boson couplings to vector bosons and to fermions using the κ-framework. No significant deviations from the SM predictions are observed. To further probe for contributions from new physics, the measurements are also used to constrain the Wilson coefficients of dimension 6 operators in an EFT model with the Higgs Characterization and the SMEFT basis.

Contributions from both the CP-even and the CP-odd operators are probed and no significant deviations from the SM are observed.

The research carried out in this thesis has provided results that improve our understanding of the mechanism for the Electroweak symmetry breaking. At the beginning of 2015, only the discovery of the Higgs boson and a few measurements of the inclusive properties were established. This research contributes to the set of new results that probe the couplings properties in many previously unexplored regions of this Higgs boson phase space. These results agree well with the SM, providing more evidence for the range of phenomena that this model can predict, and no evidence of contributions from BSM physics is observed. As the LHC delivers more data and the analysis techniques are improved, more stringent tests of the SM will be carried out and searches for even smaller contributions from new physics can be performed.

Appendix A

Contributions to other analyses and projects

My PhD thesis research built upon my previous contributions to analyses using the $H \to ZZ^* \to 4\ell$ ($H4\ell$) decay channel [24, 27, 30, 32, 33, 163–165]. While the main topic for this thesis was probing the Higgs boson couplings to other particles, I have contributed to other analyses and projects. These are described below.

$H4\ell$ Coupling

For the $H4\ell$ coupling analysis, there were several preliminary publications to which I also contributed. In addition to these being the first Higgs bosons results, these also provided a method for the ATLAS collaboration to improve the understanding of the detector in a new data taking environment and benchmark its performance.

At the beginning of Run 2, I optimized the event selection cuts for the $H4\ell$ channel to accommodate the different data-taking conditions of Run 2. I conducted studies to improve fake-lepton rejection using isolation and $d0$-significance requirements. The resulting criteria are part of the ATLAS-wide definition for prompt leptons. These studies were crucial for the first results with $\sqrt{s} = 13$ TeV [100, 166].

With the 14.8 fb^{-1} dataset, first detailed studies of the Higgs boson properties were carried out [52] at the new centre of mass energy. I had a supporting role in recreating Run 1 measurements for the differential cross section and couplings measurements. I further optimized the event selection criteria, category definitions and the boosted decision tree discriminants to benefit from the larger available data statistics. I also contributed to the first studies and interpretation of the measurements in the EFT framework.

After the published results with the 36.1 fb^{-1} dataset, preliminary results for the coupling analysis were also published using the 80 fb^{-1} dataset [129]. I collaborated on several improvements such generating new theoretical predictions, improved electron reconstruction, new categories to target VH and ttH processes, and new background estimating procedures. These improvements were crucial in the discovery of the ttH process and formed the basis for the final Run 2 publications.

$H4\ell$ Differential Cross Section

As a complement to the coupling measurements, I have also collaborated on the fiducial and differential cross section measurements of the Higgs boson [52, 100, 151, 167, 168] within the $H4\ell$ decay channel. While these results are limited to being with respect to one or two variables, these are more model-independent when compared to the couplings results and provide an independent method to isolate and test specific parts of the SM.

One of the methods to limit the model dependency is to only measure the Higgs boson cross sections within a fiducial volume, which matches the sensitivity of the detector. This reduces the reliance on theory to extrapolate the results to the full phase space. I have collaborated on constructing and validating the definition of this fiducial volume. I also coordinated the development of the likelihood matrix based unfolding method and the data-driven estimate for the ZZ^* background. These allow for an improved description of bin-to-bin migration effects and further reduce model dependency by relaxing the assumptions that background processes follow the SM predictions.

For the final Run 2 results [168], I coordinated the expansion of the differential cross sections results to include over 35 variables. These provide new ways to test for the CP properties for the Higgs boson, the description of QCD at low energies, effects of theoretical assumptions such as infinite top mass and to search for new physics.

I also coordinated and developed the methodology to constrain various BSM models using these results. The pseudo-observable framework provides a method at the quantum mechanical amplitude level to test for direct decays of the Higgs boson to two leptons and a Z and for lepton flavour violation in the decay. Additionally, the p_{T}^{H} differential cross section results are also used to derive constraints on the charm quark Yukawa coupling. For these interpretations, I initiated collaborations with theorists, developed new MC simulations, created new analytical parameterizations and developed new statistical methods for deriving results [168].

Higgs Statistical Combination

A combination of analyses targeting similar underlying processes is routinely performed to improve the statistical precision of the final results. I contributed to several such statistical combinations.

I developed a common fitting model for the analyses using the $H \to ZZ \to 4\ell$ and $H \to \gamma\gamma$ decay channels. Using this, I was the main analyzer for the combination of the Higgs boson mass and differential cross section measurements between the two channels [169–172]. These were the most precise measurements of the Higgs properties with the 36.1 fb^{-1} dataset.

I was the primary contributor to the Run 1+2 $H \to b\bar{b}$ (Hbb) combination analysis. I developed and validated the systematic correlation scheme between 3 Hbb analyses using datasets collected at multiple different centre of mass energies. This work established the discovery of this process at 5σ level [173–176].

I also contributed to the discovery of the ttH process [177–179]. I lead the optimization of the ttH-like category in the $H4\ell$ decay channel, which allowed the expected statistical significance to surpass the 5σ level. I was the liaison to the ttH statistical combination.

Other Analyses

As part of the $H \to ZZ^*$ analysis group, I had a supporting role in the search for heavy BSM scalar particles [180, 181], constraining Higgs boson width through off-shell interference effects [182] and measuring the ZZ^* production cross-section as a function of the four lepton mass [183].

Software

All analyses require extensive software frameworks to process and analyze the large dataset collected by ATLAS and the large MC simulation datasets. I have developed and maintained many such frameworks, which have been extensively used by other students and researchers.

With the start of Run 2, ATLAS introduced a new object oriented event data model called xAOD [184]. As such, I led the upgrade of the $H4\ell$ software infrastructure to use this new xAOD data format for Run 2 measurements. I designed, developed, and maintained the main $H4\ell$ analysis code. This framework combines official ATLAS and custom software tools to calibrate all physics objects, apply relevant event selection criteria and output processed n-tuples for further statistical analysis. This software is the starting point for all analyses using $H \to ZZ^*$ decay mode: couplings, differential cross section, Spin-CP and mass measurements, and searches for heavy scalar particles with $H \to ZZ^* \to 4\ell$ and $H \to ZZ^* \to 2\ell 2\nu$ decays. I served as the coordinator of the $H4\ell$ n-tuple production team and was responsible for providing starting n-tuples for all $H4\ell$ analyses. These n-tuples have been used in over 20 published conference proceedings and scientific papers.

I collaborated on developing a framework that provides an easy way to apply different statistical procedures, such as likelihood scans, measuring the impact of systematics uncertainties, performing bootstrapping studies and measuring statistical correlations. This software package has been extensively used by many analyses within the overall ATLAS Higgs group to produce the published results.

As part of introducing neural network based discriminants for the coupling analysis, I collaborated on the development of a software framework to process generic input n-tuples and train a Keras-based NN. This software is extensively used for $H4\ell$ couplings, as described in this thesis, and mass measurements [185] and for search for heavy scalar particles.

ATLAS upgrade

The LHC intends to start its new upgraded accelerator, the High Luminosity LHC (HL-LHC), in 2027, which will allow it to deliver approximately 4 ab^{-1} of data to each experiment and ultimately increase its physics reach. With this upgrade, the data taking conditions will become harsher and the number of pile-up events per bunch crossing will increase. For the ATLAS detector, the current inner tracker will not be able to survive this high expected radiation environment and the high particle density will increase detector occupancy above acceptable levels at the HL-LHC. As such, the ATLAS collaboration intends to upgrade the current inner detector with the new ITk detector, an all silicon-based tracker. This new detector consists of pixel and microstrip technologies and is designed to provide tracking measurements in the harsh conditions.

I led the development of ITk module construction capabilities at the University of Toronto [186]. I coordinated the development of local facilities for module construction and the fabrication of end-cap assembly tooling. I defined the assembly procedures and ensured that they met the criteria and constraints specified by the ATLAS collaboration. I also worked with Celestica Inc., a multinational corporate partner, to set up and demonstrate industrial ITk module wire-bonding capabilities to the collaboration. We successfully assembled and tested the first ABC250 and ABC130 end-cap module in Canada.

I was also involved in characterizing and developing silicon strip sensors for the ITk detector [187]. I led the design and construction of a silicon sensor test system that uses a β source or a laser for charge deposition. I coordinated the collection and analysis of measurements to extract the characteristics of irradiated sensors, such as charge collection efficiency, which helps predict the end-of-life performance of the ITk detector. Additionally, I collaborated in the local development of IV/CV probing of ATLAS sensors.

I investigated the mechanical properties of SE4445 glue for my authorship task [188]. This adhesive is proposed as a means of mounting ITk strip modules onto support structures. I designed procedures and fabricated testing setups to evaluate the glue's properties under stresses similar to those imposed in HL-LHC conditions. I also developed simulations of sensor deformation caused by thermal stress using the measured properties of the glue.

Appointed Roles

I have served in numerous appointed roles within the ATLAS collaboration. I was the analysis contact for the final Run 2 couplings and differential cross section analyses [131, 168], contact editor for Ref. [129, 131] and support note editor for Ref. [52, 100, 189]. I was also the contact person for ATLAS Higgs combination group [190–193], ATLAS ttH combination group and xAOD development for the $H \to ZZ^*$ Group.

Bibliography

[1] K. Olive et al., *Review of Particle Physics*, Chin.Phys. **C38** (2014) 090001 (cit. on pp. 1, 2).

[2] D. Tong, *Lectures of Quantum Field Theory*, (2016), Avaliable at http://www.damtp.cam.ac.uk/user/tong/qft.html (cit. on p. 3).

[3] D. Griffiths, *Introduction to Elementary Particles*, Physics textbook, Wiley, 2008, ISBN: 9783527406012 (cit. on pp. 3, 9).

[4] M. Thomson, *Modern Particle Physics*, Modern Particle Physics, Cambridge University Press, 2013, ISBN: 9781107034266 (cit. on pp. 3, 9).

[5] L. N. Cooper, *Bound Electron Pairs in a Degenerate Fermi Gas*, Phys. Rev. **104** (4 1956) 1189, URL: https://link.aps.org/doi/10.1103/PhysRev.104.1189 (cit. on p. 7).

[6] J. Bardeen, L. N. Cooper, and J. R. Schrieffer, *Microscopic Theory of Superconductivity*, Phys. Rev. **106** (1 1957) 162, URL: https://link.aps.org/doi/10.1103/PhysRev.106.162 (cit. on p. 7).

[7] J. Bardeen, L. N. Cooper, and J. R. Schrieffer, *Theory of Superconductivity*, Phys. Rev. **108** (5 1957) 1175, URL: https://link.aps.org/doi/10.1103/PhysRev.108.1175 (cit. on p. 7).

[8] J. Ellis, M. K. Gaillard, and D. V. Nanopoulos, *A Historical Profile of the Higgs Boson*, (2012), arXiv: 1201.6045 [hep-ph] (cit. on p. 7).

[9] F. Englert and R. Brout, *Broken Symmetry and the Mass of Gauge Vector Mesons*, Phys. Rev. Lett. **13** (9 1964) 321, URL: http://link.aps.org/doi/10.1103/PhysRevLett.13.321 (cit. on p. 7).

[10] P. W. Higgs, *Broken Symmetries and the Masses of Gauge Bosons*, Phys. Rev. Lett. **13** (16 1964) 508, URL: http://link.aps.org/doi/10.1103/PhysRevLett.13.508 (cit. on p. 7).

[11] G. S. Guralnik, C. R. Hagen, and T. W. B. Kibble, *Global Conservation Laws and Massless Particles*, Phys. Rev. Lett. **13** (20 1964) 585, URL: http://link.aps.org/doi/10.1103/PhysRevLett.13.585 (cit. on p. 7).

[12] L. Alvarez-Gaume and J. Ellis, *Eyes on a prize particle*, Nat Phys **7** (2011) 2 (cit. on p. 7).

[13] I. van Vulpen, *The Standard Model Higgs Boson*, (2014), Avaliable at http://web.mst.edu/~hale/courses/Physics_357_457/Notes/Lecture.17.Higgs.Mechanism/HiggsLectureNote.pdf (cit. on p. 9).

[14] A. Pich, *The Standard Model of Electroweak Interactions*, (2005) 1, arXiv: hep-ph/0502010 [hep-ph] (cit. on p. 9).

[15] B. W. Lee, C. Quigg, and H. B. Thacker, *Weak Interactions at Very High-Energies: The Role of the Higgs Boson Mass*, Phys. Rev. **D16** (1977) 1519 (cit. on p. 10).

[16] M. Shaposhnikov, *Cosmology: theory*, PoS (2013) 155, arXiv: `1311.4979 [hep-ph]` (cit. on p. 11).

[17] A. R. Vieira, B. Hiller, M. D. R. Sampaio, and M. C. Nemes, *Naturalness and Theoretical Constraints on the Higgs Boson Mass*, Int. J. Theor. Phys. **52** (2013) 3494, arXiv: `1207.4088 [hep-ph]` (cit. on p. 11).

[18] T. Hambye and K. Riesselmann, "SM Higgs mass bounds from theory," *e+ e- linear colliders: Physics and detector studies. Proceedings, Workshops, ECFA/DESY, Frascati, Italy, February 5-6, 1996, London, UK, July 4-6, 1996, Munich, Germany, September 16-18, 1996 and Hamburg, Germany, November 20-22, 1996. Pt.E*, 1997, arXiv: `hep-ph/9708416 [hep-ph]` (cit. on p. 11).

[19] M. Baak, M. Goebel, J. Haller, A. Hoecker, D. Ludwig, et al., *Updated Status of the Global Electroweak Fit and Constraints on New Physics*, Eur.Phys.J. **C72** (2012) 2003, arXiv: `1107.0975 [hep-ph]` (cit. on pp. 11, 12).

[20] D. de Florian et al., *Handbook of LHC Higgs Cross Sections: 4. Deciphering the Nature of the Higgs Sector*, (2016), arXiv: `1610.07922 [hep-ph]` (cit. on pp. 12, 13, 34).

[21] R. Barate et al., *Search for the standard model Higgs boson at LEP*, Phys.Lett. **B565** (2003) 61, arXiv: `hep-ex/0306033 [hep-ex]` (cit. on p. 14).

[22] *Updated Combination of CDF and D0 Searches for Standard Model Higgs Boson Production with up to 10.0 fb^{-1} of Data*, (2012), arXiv: `1207.0449 [hep-ex]` (cit. on p. 14).

[23] ATLAS Collaboration, *Observation of a new particle in the search for the Standard Model Higgs boson with the ATLAS detector at the LHC*, Phys. Lett. B **716** (2012) 1, arXiv: `1207.7214 [hep-ex]` (cit. on p. 14).

[24] ATLAS Collaboration, *Measurements of Higgs boson production and couplings in the four-lepton channel in pp collisions at center-of-mass energies of 7 and 8 TeV with the ATLAS detector*, Phys. Rev. D **91** (2015) 012006, arXiv: `1408.5191 [hep-ex]` (cit. on pp. 14, 29, 30, 48, 49, 51, 53, 61, 106, 129).

[25] ATLAS Collaboration, *Measurement of Higgs boson production in the diphoton decay channel in pp collisions at center-of-mass energies of 7 and 8 TeV with the ATLAS detector*, Phys. Rev. D **90** (2014) 112015, arXiv: `1408.7084 [hep-ex]` (cit. on p. 14).

[26] ATLAS Collaboration, *Observation and measurement of Higgs boson decays to WW^* with the ATLAS detector*, Phys. Rev. D **92** (2015) 012006, arXiv: `1412.2641 [hep-ex]` (cit. on p. 14).

[27] ATLAS Collaboration, *Measurement of the Higgs boson mass from the $H \to \gamma\gamma$ and $H \to ZZ^* \to 4\ell$ channels in pp collisions at center-of-mass energies of 7 and 8 TeV with the ATLAS detector*, Phys. Rev. D **90** (2014) 052004, arXiv: `1406.3827 [hep-ex]` (cit. on pp. 14, 36, 129).

[28] ATLAS and CMS Collaborations, *Combined Measurement of the Higgs Boson Mass in pp Collisions at $\sqrt{s} = 7$ and 8 TeV with the ATLAS and CMS Experiments*, Phys. Rev. Lett. **114** (2015) 191803, arXiv: `1503.07589 [hep-ex]` (cit. on pp. 14, 15, 28, 36, 77).

[29] ATLAS and CMS Collaborations, *Measurements of the Higgs boson production and decay rates and constraints on its couplings from a combined ATLAS and CMS analysis of the LHC pp collision data at* $\sqrt{s} = 7$ *and* 8 *TeV*, JHEP **08** (2016) 045, arXiv: `1606.02266 [hep-ex]` (cit. on pp. 15, 16, 28).

[30] ATLAS Collaboration, *Study of the spin and parity of the Higgs boson in diboson decays with the ATLAS detector*, Eur. Phys. J. C **75** (2015) 476, arXiv: `1506.05669 [hep-ex]` (cit. on pp. 15, 129), Erratum: Eur. Phys. J. C **76** (2016) 152.

[31] ATLAS Collaboration, *Measurements of the Total and Differential Higgs Boson Production Cross Sections Combining the* $H \to \gamma\gamma$ *and* $H \to ZZ^* \to 4\ell$ *Decay Channels at* $\sqrt{s} = 8$ *TeV with the ATLAS Detector*, Phys. Rev. Lett. **115** (2015) 091801, arXiv: `1504.05833 [hep-ex]` (cit. on p. 15).

[32] ATLAS Collaboration, *Fiducial and differential cross sections of Higgs boson production measured in the four-lepton decay channel in pp collisions at* $\sqrt{s} = 8$ *TeV with the ATLAS detector*, Phys. Lett. B **738** (2014) 234, arXiv: `1408.3226 [hep-ex]` (cit. on pp. 15, 129).

[33] ATLAS Collaboration, *Constraints on the off-shell Higgs boson signal strength in the high-mass* ZZ *and* WW *final states with the ATLAS detector*, Eur. Phys. J. C **75** (2015) 335, arXiv: `1503.01060 [hep-ex]` (cit. on pp. 15, 129).

[34] O. S. Brüning et al., *LHC Design Report*, CERN, 2004 (cit. on p. 17).

[35] L. Evans and P. Bryant, *LHC Machine*, Journal of Instrumentation **3** (2008) S08001, URL: `http://stacks.iop.org/1748-0221/3/i=08/a=S08001` (cit. on p. 17).

[36] L. Rossi, *The LHC superconducting magnets*, Conf. Proc. **C030512** (2003) 141 (cit. on pp. 17, 18).

[37] R. Bruce et al., *LHC Run 2: Results and Challenges*, tech. rep. CERN-ACC-2016-0103, CERN, 2016, URL: `https://cds.cern.ch/record/2201447` (cit. on p. 20).

[38] T. A. Collaboration, *Luminosity Public Results Run2*, (2010), Avaliable at `https://twiki.cern.ch/twiki/bin/view/AtlasPublic/LuminosityPublicResultsRun2?rev=23` (cit. on pp. 20, 35).

[39] ATLAS Collaboration, *The ATLAS Experiment at the CERN Large Hadron Collider*, JINST **3** (2008) S08003 (cit. on pp. 20, 21).

[40] *ATLAS Inner Detector: Technical Design Report, 1*, Technical Design Report ATLAS, CERN, 1997 (cit. on p. 21).

[41] T. A. Collaboration, *ATLAS Insertable B-Layer Technical Design Report*, tech. rep. CERN-LHCC-2010-013. ATLAS-TDR-19, 2010, URL: `https://cds.cern.ch/record/1291633` (cit. on p. 21).

[42] H. Spieler, *Semiconductor detector systems*, Semiconductor Science and Technology, Oxford Univ. Press, 2005 (cit. on p. 23).

[43] ATLAS Collaboration, *Performance of the ATLAS trigger system in 2015*, Eur. Phys. J. C **77** (2017) 317, arXiv: `1611.09661 [hep-ex]` (cit. on pp. 27, 45).

[44] LHC Higgs Cross Section Working Group et al., *Handbook of LHC Higgs Cross Sections: 4. Deciphering the nature of the Higgs sector*, (CERN, Geneva, 2016), arXiv: `1610.07922 [hep-ph]` (cit. on pp. 28, 31–33, 36, 77, 90, 95, 96).

[45] M. Grazzini, A. Ilnicka, M. Spira, and M. Wiesemann, *Modeling BSM effects on the Higgs transverse-momentum spectrum in an EFT approach*, JHEP **03** (2017) 115, arXiv: 1612.00283 [hep-ph] (cit. on pp. 28, 29).

[46] F. Bishara, U. Haisch, P. F. Monni, and E. Re, *Constraining Light-Quark Yukawa Couplings from Higgs Distributions*, Phys. Rev. Lett. **118** (2017) 121801, arXiv: 1606.09253 [hep-ph] (cit. on pp. 28, 29).

[47] I. Brivio, Y. Jiang, and M. Trott, *The SMEFTsim package, theory and tools*, JHEP **12** (2017) 070, arXiv: 1709.06492 [hep-ph] (cit. on pp. 29, 95, 97).

[48] C. Degrande, B. Fuks, K. Mawatari, K. Mimasu, and V. Sanz, *Electroweak Higgs boson production in the standard model effective field theory beyond leading order in QCD*, Eur. Phys. J. C **77** (2017) 262, arXiv: 1609.04833 [hep-ph] (cit. on p. 29).

[49] J. Ellis, D. S. Hwang, K. Sakurai, and M. Takeuchi, *Disentangling Higgs-Top Couplings in Associated Production*, JHEP **04** (2014) 004, arXiv: 1312.5736 [hep-ph] (cit. on p. 29).

[50] F. Maltoni, K. Mawatari, and M. Zaro, *Higgs characterisation via vector-boson fusion and associated production: NLO and parton-shower effects*, Eur. Phys. J. C **74** (2014) 2710, arXiv: 1311.1829 [hep-ph] (cit. on p. 29).

[51] ATLAS Collaboration, *Measurement of the Higgs boson coupling properties in the $H \to ZZ^* \to 4\ell$ decay channel at $\sqrt{s} = 13$ TeV with the ATLAS detector*, JHEP **03** (2018) 095, arXiv: 1712.02304 [hep-ex] (cit. on pp. 29, 30, 33, 48, 53, 54, 101, 109).

[52] ATLAS Collaboration, *Study of the Higgs boson properties and search for high-mass scalar resonances in the $H \to ZZ^* \to 4\ell$ decay channel at $\sqrt{s} = 13$ TeV with the ATLAS detector*, ATLAS-CONF-2016-079, 2016, URL: https://cds.cern.ch/record/2206253 (cit. on pp. 29, 33, 37, 129, 130, 132).

[53] A. Hoecker et al., *TMVA: Toolkit for Multivariate Data Analysis*, (2007), arXiv: physics/0703039 [physics.data-an] (cit. on pp. 31, 55, 57).

[54] ATLAS Collaboration, *Measurements of the Higgs boson production and decay rates and coupling strengths using pp collision data at $\sqrt{s} = 7$ and 8 TeV in the ATLAS experiment*, Eur. Phys. J. C **76** (2016) 6, arXiv: 1507.04548 [hep-ex] (cit. on p. 32).

[55] CMS Collaboration, *Precise determination of the mass of the Higgs boson and tests of compatibility of its couplings with the standard model predictions using proton collisions at 7 and 8 TeV*, Eur. Phys. J. C **75** (2015) 212, arXiv: 1412.8662 [hep-ex] (cit. on p. 32).

[56] ATLAS and CMS Collaborations, *Measurements of the Higgs boson production and decay rates and constraints on its couplings from a combined ATLAS and CMS analysis of the LHC pp collision data at $\sqrt{s} = 7$ and 8 TeV*, JHEP **08** (2016) 045, arXiv: 1606.02266 [hep-ex] (cit. on p. 32).

[57] M. Cacciari, G. P. Salam, and G. Soyez, *The anti-k_t jet clustering algorithm*, JHEP **04** (2008) 063, arXiv: 0802.1189 [hep-ph] (cit. on p. 33).

[58] M. Cacciari, G. P. Salam, and G. Soyez, *FastJet User Manual*, Eur. Phys. J. C **72** (2012) 1896, arXiv: 1111.6097 [hep-ph] (cit. on p. 33).

[59] S. Heinemeyer et al., *Handbook of LHC Higgs Cross Sections: 3. Higgs Properties*, (2013), ed. by S. Heinemeyer, arXiv: 1307.1347 [hep-ph] (cit. on pp. 34, 90).

[60] LHC Higgs Cross Section Working Group, *Handbook of LHC Higgs Cross Sections: 3. Higgs Properties*, CERN-2013-004 (2013), arXiv: `1307.1347 [hep-ph]` (cit. on p. 34).

[61] P. Artoisenet, P. de Aquino, F. Demartin, R. Frederix, S. Frixione, et al., *A framework for Higgs characterisation*, JHEP **11** (2013) 043, arXiv: `1306.6464 [hep-ph]` (cit. on pp. 34, 35).

[62] P. Nason and C. Oleari, *NLO Higgs boson production via vector-boson fusion matched with shower in POWHEG*, JHEP **02** (2010) 037, arXiv: `0911.5299 [hep-ph]` (cit. on pp. 36, 38, 78, 98).

[63] G. Luisoni, P. Nason, C. Oleari, and F. Tramontano, *$HW^{\pm}/HZ$ + 0 and 1 jet at NLO with the POWHEG BOX interfaced to GoSam and their merging within MiNLO*, JHEP **10** (2013) 083, arXiv: `1306.2542 [hep-ph]` (cit. on pp. 36, 78, 98).

[64] D. J. Lange, *The EvtGen particle decay simulation package*, Nucl. Instrum. Meth. **A462** (2001) 152 (cit. on pp. 36–38, 42, 98).

[65] J. Butterworth et al., *PDF4LHC recommendations for LHC Run II*, J. Phys. G **43** (2016) 023001, arXiv: `1510.03865 [hep-ph]` (cit. on p. 36).

[66] K. Hamilton, P. Nason, E. Re, and G. Zanderighi, *NNLOPS simulation of Higgs boson production*, JHEP **10** (2013) 222, arXiv: `1309.0017 [hep-ph]` (cit. on p. 36).

[67] S. Catani and M. Grazzini, *An NNLO subtraction formalism in hadron collisions and its application to Higgs boson production at the LHC*, Phys. Rev. Lett. **98** (2007) 222002, arXiv: `hep-ph/0703012` (cit. on p. 36).

[68] M. Grazzini, *NNLO predictions for the Higgs boson signal in the $H \to WW \to \ell\nu\ell\nu$ and $H \to ZZ \to 4\ell$ decay channels*, JHEP **02** (2008) 043, arXiv: `0801.3232 [hep-ph]` (cit. on p. 36).

[69] K. Hamilton, P. Nason, C. Oleari, and G. Zanderighi, *Merging H/W/Z + 0 and 1 jet at NLO with no merging scale: a path to parton shower + NNLO matching*, JHEP **05** (2013) 082, arXiv: `1212.4504 [hep-ph]` (cit. on p. 36).

[70] J. Alwall et al., *The automated computation of tree-level and next-to-leading order differential cross sections, and their matching to parton shower simulations*, JHEP **07** (2014) 079, arXiv: `1405.0301 [hep-ph]` (cit. on pp. 36, 51, 99).

[71] M. Wiesemann et al., *Higgs production in association with bottom quarks*, JHEP **02** (2015) 132, arXiv: `1409.5301 [hep-ph]` (cit. on p. 36).

[72] H.-L. Lai, M. Guzzi, J. Huston, Z. Li, P. M. Nadolsky, et al., *New parton distributions for collider physics*, Phys. Rev. D **82** (2010) 074024, arXiv: `1007.2241 [hep-ph]` (cit. on p. 36).

[73] R. D. Ball et al., *Parton distributions for the LHC Run II*, JHEP **04** (2015) 040, arXiv: `1410.8849 [hep-ph]` (cit. on pp. 36, 98, 99).

[74] T. Sjöstrand, S. Mrenna, and P. Z. Skands, *A brief introduction to PYTHIA 8.1*, Comput. Phys. Commun. **178** (2008) 852, arXiv: `0710.3820 [hep-ph]` (cit. on pp. 36, 99).

[75] ATLAS Collaboration, *Measurement of the Z/γ^* boson transverse momentum distribution in pp collisions at $\sqrt{s} = 7$ TeV with the ATLAS detector*, JHEP **09** (2014) 145, arXiv: `1406.3660 [hep-ex]` (cit. on pp. 36, 78).

[76] M. Bahr et al., *Herwig++ physics and manual*, Eur. Phys. J. C **58** (2008) 639, arXiv: `0803.0883 [hep-ph]` (cit. on p. 36).

[77] M. H. Seymour and A. Siodmok, *Constraining MPI models using σ_{eff} and recent Tevatron and LHC Underlying Event data*, JHEP **10** (2013) 113, arXiv: 1307.5015 [hep-ph] (cit. on p. 36).

[78] A. Djouadi, J. Kalinowski, and M. Spira, *HDECAY: A Program for Higgs boson decays in the Standard Model and its supersymmetric extension*, Comput. Phys. Commun. **108** (1998) 56, arXiv: hep-ph/9704448 (cit. on p. 36).

[79] A. Bredenstein, A. Denner, S. Dittmaier, and M. Weber, *Precise predictions for the Higgs-boson decay $H \to WW/ZZ \to 4$ leptons*, Phys. Rev. D **74** (2006) 013004, arXiv: hep-ph/0604011 (cit. on pp. 36, 78).

[80] A. Bredenstein, A. Denner, S. Dittmaier, and M. Weber, *Radiative corrections to the semileptonic and hadronic Higgs-boson decays $H \to WW/ZZ \to 4$ fermions*, JHEP **02** (2007) 080, arXiv: hep-ph/0611234 (cit. on pp. 36, 78).

[81] R. Frederix and S. Frixione, *Merging meets matching in MC@NLO*, JHEP **12** (2012) 061, arXiv: 1209.6215 [hep-ph] (cit. on pp. 36, 99).

[82] T. Gleisberg et al., *Event generation with SHERPA 1.1*, JHEP **02** (2009) 007, arXiv: 0811.4622 [hep-ph] (cit. on pp. 37, 99).

[83] T. Gleisberg and S. Höche, *Comix, a new matrix element generator*, JHEP **12** (2008) 039, arXiv: 0808.3674 [hep-ph] (cit. on pp. 37, 99).

[84] F. Cascioli, P. Maierhofer, and S. Pozzorini, *Scattering Amplitudes with Open Loops*, Phys. Rev. Lett. **108** (2012) 111601, arXiv: 1111.5206 [hep-ph] (cit. on pp. 37, 99).

[85] S. Schumann and F. Krauss, *A Parton shower algorithm based on Catani-Seymour dipole factorisation*, JHEP **03** (2008) 038, arXiv: 0709.1027 [hep-ph] (cit. on p. 37).

[86] S. Höche, F. Krauss, M. Schönherr, and F. Siegert, *QCD matrix elements + parton showers: The NLO case*, JHEP **04** (2013) 027, arXiv: 1207.5030 [hep-ph] (cit. on p. 37).

[87] B. Biedermann, A. Denner, S. Dittmaier, L. Hofer, and B. Jäger, *Electroweak corrections to $pp \to \mu^+\mu^-e^+e^- + X$ at the LHC: a Higgs background study*, Phys. Rev. Lett. **116** (2016) 161803, arXiv: 1601.07787 [hep-ph] (cit. on pp. 37, 40).

[88] B. Biedermann, A. Denner, S. Dittmaier, L. Hofer, and B. Jager, *Next-to-leading-order electroweak corrections to the production of four charged leptons at the LHC*, JHEP **01** (2017) 033, arXiv: 1611.05338 [hep-ph] (cit. on pp. 37, 40).

[89] N. Kauer, C. O'Brien, and E. Vryonidou, *Interference effects for $H \to W\ W \to \ell\nu q\bar{q}'$ and $H \to ZZ \to \ell\bar{\ell}q\bar{q}$ searches in gluon fusion at the LHC*, JHEP **10** (2015) 074, arXiv: 1506.01694 [hep-ph] (cit. on pp. 37, 42).

[90] F. Caola, K. Melnikov, R. Röntsch, and L. Tancredi, *QCD corrections to ZZ production in gluon fusion at the LHC*, Phys. Rev. D **92** (2015) 094028, arXiv: 1509.06734 [hep-ph] (cit. on pp. 37, 42, 99).

[91] F. Caola, K. Melnikov, R. Röntsch, and L. Tancredi, *QCD corrections to W^+W^- production through gluon fusion*, Phys. Lett. B **754** (2016) 275, arXiv: 1511.08617 [hep-ph] (cit. on pp. 37, 42, 99).

[92] J. M. Campbell, R. K. Ellis, M. Czakon, and S. Kirchner, *Two Loop Correction to Interference in $gg \to ZZ$*, JHEP **08** (2016) 011, arXiv: 1605.01380 [hep-ph] (cit. on pp. 37, 42, 99).

[93] K. Melnikov and M. Dowling, *Production of two Z-bosons in gluon fusion in the heavy top quark approximation*, Phys. Lett. B **744** (2015) 43, arXiv: `1503.01274 [hep-ph]` (cit. on pp. 37, 42, 99).

[94] M. Bonvini, F. Caola, S. Forte, K. Melnikov, and G. Ridolfi, *Signal-background interference effects for $gg \to H \to W^+W^-$ beyond leading order*, Phys. Rev. D **88** (2013) 034032, arXiv: `1304.3053 [hep-ph]` (cit. on pp. 37, 42, 99).

[95] C. S. Li, H. T. Li, D. Y. Shao, and J. Wang, *Soft gluon resummation in the signal-background interference process of $gg(\to h^*)\to ZZ$*, JHEP **08** (2015) 065, arXiv: `1504.02388 [hep-ph]` (cit. on pp. 37, 42, 99).

[96] S. Frixione, V. Hirschi, D. Pagani, H.-S. Shao, and M. Zaro, *Electroweak and QCD corrections to top-pair hadroproduction in association with heavy bosons*, JHEP **06** (2015) 184, arXiv: `1504.03446 [hep-ph]` (cit. on pp. 37, 99).

[97] T. Sjöstrand, S. Mrenna, and P. Z. Skands, *PYTHIA 6.4 physics and manual*, JHEP **05** (2006) 026, arXiv: `hep-ph/0603175` (cit. on p. 37).

[98] ATLAS Collaboration, *The ATLAS Simulation Infrastructure*, Eur. Phys. J. C **70** (2010) 823, arXiv: `1005.4568 [physics.ins-det]` (cit. on p. 37).

[99] S. Agostinelli et al., *GEANT4: a simulation toolkit*, Nucl. Instrum. Meth. **A 506** (2003) 250 (cit. on p. 37).

[100] ATLAS Collaboration, *Measurements of the Higgs boson production cross section at $7, 8$ and 13 TeV centre-of-mass energies and search for new physics at 13 TeV in the $H \to ZZ^* \to \ell^+\ell^-\ell'^+\ell'^-$ final state with the ATLAS detector*, ATLAS-CONF-2015-059, 2015, URL: `https://cds.cern.ch/record/2114825` (cit. on pp. 37, 129, 130, 132).

[101] ATLAS Collaboration, *Multi-Boson Simulation for 13 TeV ATLAS Analyses*, ATL-PHYS-PUB-2017-005, 2017, URL: `https://cds.cern.ch/record/2261933` (cit. on pp. 38, 42, 110).

[102] ATLAS Collaboration, *Measurement of the $Z/\gamma*$ boson transverse momentum distribution in pp collisions at $\sqrt{s} = 7$ TeV with the ATLAS detector*, JHEP **2014** (2014) 55, arXiv: `1406.3660 [hep-ex]` (cit. on p. 38).

[103] J. Pumplin et al., *New generation of parton distributions with uncertainties from global QCD analysis*, JHEP **07** (2002) 012, arXiv: `hep-ph/0201195 [hep-ph]` (cit. on p. 38).

[104] M. Grazzini, S. Kallweit, and D. Rathlev, *ZZ production at the LHC: fiducial cross sections and distributions in NNLO QCD*, Phys. Lett. **B750** (2015) 407, arXiv: `1507.06257 [hep-ph]` (cit. on p. 41).

[105] S. Alioli, F. Caola, G. Luisoni, and R. Röntsch, *ZZ production in gluon fusion at NLO matched to parton-shower*, Phys. Rev. **D95** (2017) 034042, arXiv: `1609.09719 [hep-ph]` (cit. on p. 42).

[106] ATLAS Collaboration, *Electron efficiency measurements with the ATLAS detector using 2012 LHC proton–proton collision data*, Eur. Phys. J. C **77** (2017) 195, arXiv: `1612.01456 [hep-ex]` (cit. on p. 45).

[107] ATLAS Collaboration, *Electron efficiency measurements with the ATLAS detector using the 2015 LHC proton–proton collision data*, ATLAS-CONF-2016-024, 2016, URL: `https://cds.cern.ch/record/2157687` (cit. on pp. 45, 46).

[108] ATLAS Collaboration, *Performance of the ATLAS Silicon Pattern Recognition Algorithm in Data and Simulation at $\sqrt{s} = 7$ TeV*, ATLAS-CONF-2010-072, 2010, URL: `https://cds.cern.ch/record/1281363` (cit. on p. 46).

[109] ATLAS Collaboration, *Electron and photon energy calibration with the ATLAS detector using LHC Run 1 data*, Eur. Phys. J. C **74** (2014) 3071, arXiv: `1407.5063 [hep-ex]` (cit. on pp. 46, 74, 112).

[110] ATLAS Collaboration, *Muon reconstruction performance of the ATLAS detector in proton–proton collision data at $\sqrt{s} = 13$ TeV*, Eur. Phys. J. C **76** (2016) 292, arXiv: `1603.05598 [hep-ex]` (cit. on pp. 46, 47, 74, 101, 112).

[111] T. Alexopoulos, M. Bachtis, E. Gazis, and G. Tsipolitis, *Implementation of the Legendre Transform for track segment reconstruction in drift tube chambers*, Nuclear Instruments and Methods in Physics Research Section A: Accelerators, Spectrometers, Detectors and Associated Equipment **592** (2008) 456, ISSN: 0168-9002 (cit. on p. 46).

[112] ATLAS Collaboration, *Jet energy scale and its systematic uncertainty in proton–proton collisions at $\sqrt{s} = 7$ TeV with ATLAS 2011 data*, ATLAS-CONF-2013-004, 2013, URL: `https://cds.cern.ch/record/1509552` (cit. on p. 47).

[113] ATLAS Collaboration, *Jet energy scale measurements and their systematic uncertainties in proton–proton collisions at $\sqrt{s} = 13$ TeV with the ATLAS detector*, Phys. Rev. D **96** (2017) 072002, arXiv: `1703.09665 [hep-ex]` (cit. on p. 47).

[114] ATLAS Collaboration, *Tagging and suppression of pileup jets with the ATLAS detector*, ATLAS-CONF-2014-018, 2014, URL: `https://cds.cern.ch/record/1700870` (cit. on p. 47).

[115] ATLAS Collaboration, *Selection of jets produced in* 13 *TeV proton–proton collisions with the ATLAS detector*, ATLAS-CONF-2015-029, 2015, URL: `https://cds.cern.ch/record/2037702` (cit. on p. 47).

[116] ATLAS Collaboration, *Optimisation of the ATLAS b-tagging performance for the 2016 LHC Run*, ATL-PHYS-PUB-2016-012, 2016, URL: `https://cds.cern.ch/record/2160731` (cit. on p. 47).

[117] K. S. Cranmer, *Kernel estimation in high-energy physics*, Comput. Phys. Commun. **136** (2001) 198, arXiv: `hep-ex/0011057` (cit. on p. 69).

[118] ATLAS Collaboration, *Luminosity determination in pp collisions at $\sqrt{s} = 8$ TeV using the ATLAS detector at the LHC*, Eur. Phys. J. C **76** (2016) 653, arXiv: `1608.03953 [hep-ex]` (cit. on p. 74).

[119] ATLAS Collaboration, *Measurement of the Inelastic Proton–Proton Cross Section at $\sqrt{s} = 13$ TeV with the ATLAS Detector at the LHC*, Phys. Rev. Lett. **117** (2016) 182002, arXiv: `1606.02625 [hep-ex]` (cit. on p. 74).

[120] ATLAS Collaboration, *Electron efficiency measurements with the ATLAS detector using the 2012 LHC proton–proton collision data*, ATLAS-CONF-2014-032, 2014, URL: `https://cds.cern.ch/record/1706245` (cit. on pp. 74, 112).

[121] ATLAS Collaboration, *Jet energy measurement with the ATLAS detector in proton–proton collisions at $\sqrt{s} = 7$ TeV*, Eur. Phys. J. C **73** (2013) 2304, arXiv: `1112.6426 [hep-ex]` (cit. on pp. 77, 112).

[122] ATLAS Collaboration, *Jet Calibration and Systematic Uncertainties for Jets Reconstructed in the ATLAS Detector at* $\sqrt{s} = 13$ *TeV*, ATL-PHYS-PUB-2015-015, 2015, URL: `https://cds.cern.ch/record/2037613` (cit. on pp. 77, 112).

[123] ATLAS Collaboration, *Performance of b-jet identification in the ATLAS experiment*, JINST **11** (2016) P04008, arXiv: `1512.01094 [hep-ex]` (cit. on p. 77).

[124] Campbell, J. M. and Ellis, R. K. and Williams, C., *Vector boson pair production at the LHC,* JHEP **07** (2011) 018, arXiv: `1105.0020 [hep-ph]` (cit. on p. 78).

[125] J. Bendavid et al., *Les Houches 2017: Physics at TeV Colliders Standard Model Working Group Report*, 2018, arXiv: `1803.07977 [hep-ph]` (cit. on pp. 78, 112).

[126] M. Cacciari, F. A. Dreyer, A. Karlberg, G. P. Salam, and G. Zanderighi, *Fully Differential Vector-Boson-Fusion Higgs Production at Next-to-Next-to-Leading Order*, Phys. Rev. Lett. **115** (2015) 082002, arXiv: `1506.02660 [hep-ph]` (cit. on p. 78).

[127] G. Cowan, K. Cranmer, E. Gross, and O. Vitells, *Asymptotic formulae for likelihood-based tests of new physics*, Eur. Phys. J. C **71** (2011) 1554, arXiv: `1007.1727 [hep-ex]`, Erratum: Eur. Phys. J. C **73** (2013) 2501 (cit. on p. 85).

[128] A. L. Read, *Presentation of the search results: the CLs technique*, J. Phys. G **28** (2002) 2693 (cit. on p. 86).

[129] ATLAS Collaboration, *Measurements of the Higgs boson production, fiducial and differential cross sections in the* 4ℓ *decay channel at* $\sqrt{s} = 13$ *TeV with the ATLAS detector*, ATLAS-CONF-2018-018, 2018, URL: `https://cds.cern.ch/record/2621479` (cit. on pp. 94, 101, 109, 129, 132).

[130] ATLAS Collaboration, *Measurements of the Higgs boson inclusive, differential and production cross sections in the* 4ℓ *decay channel at* $\sqrt{s} = 13$ *TeV with the ATLAS detector*, ATLAS-CONF-2019-025, 2019, URL: `https://cds.cern.ch/record/2682107` (cit. on p. 94).

[131] ATLAS Collaboration, *Higgs boson production cross section measurements and their EFT interpretation in the* 4ℓ *decay channel at* $\sqrt{s}$ *=13 TeV with the ATLAS detector*, 2020, arXiv: `2004.03447 [hep-ex]` (cit. on pp. 94, 132).

[132] B. Grzadkowski, M. Iskrzynski, M. Misiak, and J. Rosiek, *Dimension-Six Terms in the Standard Model Lagrangian*, JHEP **10** (2010) 085, arXiv: `1008.4884 [hep-ph]` (cit. on pp. 95, 97).

[133] N. Berger et al., *Simplified Template Cross Sections - Stage 1.1*, (2019), arXiv: `1906.02754 [hep-ph]` (cit. on p. 96).

[134] C. Hays, V. Sanz Gonzalez, and G. Zemaityte, *Constraining EFT parameters using simplified template cross sections*, (2017), URL: `https://cds.cern.ch/record/2290628` (cit. on p. 98).

[135] ATLAS Collaboration, *Luminosity determination in pp collisions at* $\sqrt{s} = 13$ *TeV using the ATLAS detector at the LHC*, ATLAS-CONF-2019-021, 2019, URL: `https://cds.cern.ch/record/2677054` (cit. on p. 98).

[136] B. Cabouat and T. Sjöstrand, *Some dipole shower studies*, The European Physical Journal C **78** (2018), ISSN: 1434-6052, URL: `http://dx.doi.org/10.1140/epjc/s10052-018-5645-z` (cit. on p. 99).

[137] ATLAS Collaboration, *Validation of signal Monte Carlo event generation in searches for Higgs boson pairs with the ATLAS detector*, ATL-PHYS-PUB-2019-007, 2019, URL: `https://cds.cern.ch/record/2665057` (cit. on p. 99).

[138] ATLAS Collaboration, *Modelling of the vector boson scattering process $pp \to W^{\pm}W^{\pm}jj$ in Monte Carlo generators in ATLAS*, ATL-PHYS-PUB-2019-004, 2019, URL: `https://cds.cern.ch/record/2655303` (cit. on p. 99).

[139] I. Brivio, Y. Jiang, and M. Trott, *The SMEFTsim package, theory and tools*, JHEP **12** (2017) 070, arXiv: `1709.06492 [hep-ph]` (cit. on p. 99).

[140] *Standard Model Effective Field Theory – The SMEFTsim package*, URL: `https://feynrules.irmp.ucl.ac.be/wiki/SMEFT` (cit. on p. 99).

[141] E. Bothmann et al., *Event Generation with Sherpa 2.2*, (2019), arXiv: `1905.09127 [hep-ph]` (cit. on p. 99).

[142] ATLAS Collaboration, *ATLAS Pythia 8 tunes to 7 TeV data*, ATL-PHYS-PUB-2014-021, 2014, URL: `https://cds.cern.ch/record/1966419` (cit. on p. 99).

[143] ATLAS Collaboration, *Studies on top-quark Monte Carlo modelling for Top2016*, ATL-PHYS-PUB-2016-020, 2016, URL: `https://cds.cern.ch/record/2216168` (cit. on p. 99).

[144] ATLAS Collaboration, *Electron and photon reconstruction and performance in ATLAS using a dynamical, topological cell clustering-based approach*, ATL-PHYS-PUB-2017-022, 2017, URL: `https://cds.cern.ch/record/2298955` (cit. on pp. 100, 101).

[145] ATLAS Collaboration, *Electron reconstruction and identification in the ATLAS experiment using the 2015 and 2016 LHC proton–proton collision data at $\sqrt{s} = 13$ TeV*, Eur. Phys. J. C **79** (2019) 639, arXiv: `1902.04655 [hep-ex]` (cit. on p. 100).

[146] ATLAS Collaboration, *Improved electron reconstruction in ATLAS using the Gaussian Sum Filter-based model for bremsstrahlung*, ATLAS-CONF-2012-047, 2012, URL: `https://cds.cern.ch/record/1449796` (cit. on p. 100).

[147] ATLAS Collaboration, *Jet reconstruction and performance using particle flow with the ATLAS Detector*, Eur. Phys. J. C **77** (2017) 466, arXiv: `1703.10485 [hep-ex]` (cit. on p. 100).

[148] ATLAS Collaboration, *Topological cell clustering in the ATLAS calorimeters and its performance in LHC Run 1*, Eur. Phys. J. C **77** (2017) 490, arXiv: `1603.02934 [hep-ex]` (cit. on p. 100).

[149] ATLAS Collaboration, *Expected performance of the ATLAS b-tagging algorithms in Run-2*, ATL-PHYS-PUB-2015-022, 2015, URL: `https://cds.cern.ch/record/2037697` (cit. on p. 100).

[150] ATLAS Collaboration, *Measurements of b-jet tagging efficiency with the ATLAS detector using $t\bar{t}$ events at $\sqrt{s} = 13$ TeV*, JHEP **08** (2018) 089, arXiv: `1805.01845 [hep-ex]` (cit. on p. 100).

[151] ATLAS Collaboration, *Measurement of inclusive and differential cross sections in the $H \to ZZ^* \to 4\ell$ decay channel in pp collisions at $\sqrt{s} = 13$ TeV with the ATLAS detector*, JHEP **10** (2017) 132, arXiv: `1708.02810 [hep-ex]` (cit. on pp. 101, 109, 130).

[152] ATLAS Collaboration, *Electron and photon performance measurements with the ATLAS detector using the 2015-2017 LHC proton–proton collision data*, JINST **14** (2019) P12006, arXiv: `1908.00005 [hep-ex]` (cit. on p. 102).

[153] ATLAS Collaboration, *Measurement of the photon identification efficiencies with the ATLAS detector using LHC Run 2 data collected in 2015 and 2016*, Eur. Phys. J. C **79** (2019) 205, arXiv: `1810.05087 [hep-ex]` (cit. on p. 102).

[154] Martin Abadi et al., *TensorFlow: Large-Scale Machine Learning on Heterogeneous Systems*, Software available from tensorflow.org, 2015, URL: `https://www.tensorflow.org/` (cit. on p. 104).

[155] D. Guest, K. Cranmer, and D. Whiteson, *Deep Learning and Its Application to LHC Physics*, Annual Review of Nuclear and Particle Science **68** (2018) 161, eprint: `https://doi.org/10.1146/annurev-nucl-101917-021019`, URL: `https://doi.org/10.1146/annurev-nucl-101917-021019` (cit. on p. 104).

[156] F. Chollet et al., *Keras*, `https://keras.io`, 2015 (cit. on p. 104).

[157] ATLAS Collaboration, *Evidence for the spin-0 nature of the Higgs boson using ATLAS data*, Phys. Lett. B **726** (2013) 120, arXiv: `1307.1432 [hep-ex]` (cit. on p. 106).

[158] D. Rainwater, R. Szalapski, and D. Zeppenfeld, *Probing color-singlet exchange inZ+2-jet events at the CERN LHC*, Physical Review D **54** (1996) 6680, ISSN: 1089-4918, URL: `http://dx.doi.org/10.1103/PhysRevD.54.6680` (cit. on p. 106).

[159] ATLAS Collaboration, *Measurement of the $t\bar{t}Z$ and $t\bar{t}W$ cross sections in proton–proton collisions at $\sqrt{s} = 13$ TeV with the ATLAS detector*, Phys. Rev. D **99** (2019) 072009, arXiv: `1901.03584 [hep-ex]` (cit. on p. 109).

[160] ATLAS Collaboration, *Measurement of the $t\bar{t}Z$ and $t\bar{t}W$ production cross sections in multilepton final states using $3.2\,fb^{-1}$ of pp collisions at $\sqrt{s} = 13$ TeV with the ATLAS detector*, Eur. Phys. J. C **77** (2017) 40, arXiv: `1609.01599 [hep-ex]` (cit. on p. 109).

[161] ATLAS Collaboration, *Evaluation of theoretical uncertainties for simplified template cross section measurements of V-associated production of the Higgs boson*, ATL-PHYS-PUB-2018-035, 2018, URL: `https://cds.cern.ch/record/2649241` (cit. on p. 112).

[162] *Measurements of properties of the Higgs boson in the four-lepton final state in proton-proton collisions at* $\sqrt{s} = 13$ TeV, (2019), URL: `https://cds.cern.ch/record/2668684` (cit. on p. 115).

[163] ATLAS Collaboration, *Search for an additional, heavy Higgs boson in the $H \to ZZ$ decay channel at $\sqrt{s} = 8$ TeV in pp collision data with the ATLAS detector*, Eur. Phys. J. C **76** (2016) 45, arXiv: `1507.05930 [hep-ex]` (cit. on p. 129).

[164] ATLAS Collaboration, *Inclusive and differential fiducial cross sections of Higgs boson production measured in the $H \to ZZ^* \to 4\ell$ decay channel using $\sqrt{s} = 8$ TeV pp collision data recorded by the ATLAS detector*, ATLAS-CONF-2014-044, 2014, URL: `https://cds.cern.ch/record/1741017` (cit. on p. 129).

[165] ATLAS Collaboration, *Centrality and rapidity dependence of inclusive jet production in $\sqrt{s_{NN}} = 5.02$ TeV proton–lead collisions with the ATLAS detector*, ATLAS-CONF-2014-024, 2014, URL: `https://cds.cern.ch/record/1702986` (cit. on p. 129).

[166] ATLAS Collaboration, *Measurements of the total cross sections for Higgs boson production combining the $H \to \gamma\gamma$ and $H \to ZZ^* \to 4\ell$ decay channels at $7, 8$ and 13 TeV center-of-mass energies with the ATLAS detector*, ATLAS-CONF-2015-069, 2015, URL: `https://cds.cern.ch/record/2114841` (cit. on p. 129).

[167] ATLAS Collaboration, *Measurement of inclusive and differential cross sections in the $H \to ZZ^* \to 4\ell$ decay channel at 13 TeV with the ATLAS detector*, ATLAS-CONF-2017-032, 2017, URL: https://cds.cern.ch/record/2265796 (cit. on p. 130).

[168] ATLAS Collaboration, *Measurements of the Higgs boson inclusive and differential fiducial cross sections in the 4ℓ decay channel at $\sqrt{s} = 13$ TeV*, 2020, arXiv: 2004.03969 [hep-ex] (cit. on pp. 130, 132).

[169] ATLAS Collaboration, *Measurement of the Higgs boson mass in the $H \to ZZ^* \to 4\ell$ and $H \to \gamma\gamma$ channels with $\sqrt{s} = 13$ TeV pp collisions using the ATLAS detector*, Phys. Lett. B **784** (2018) 345, arXiv: 1806.00242 [hep-ex] (cit. on p. 130).

[170] ATLAS Collaboration, *Measurement of the Higgs boson mass in the $H \to ZZ^* \to 4\ell$ and $H \to \gamma\gamma$ channels with $\sqrt{s} = 13$ TeV pp collisions using the ATLAS detector*, ATLAS-CONF-2017-046, 2017, URL: https://cds.cern.ch/record/2273853 (cit. on p. 130).

[171] ATLAS Collaboration, *Combined measurement of differential and inclusive total cross sections in the $H \to \gamma\gamma$ and the $H \to ZZ^* \to 4\ell$ decay channels at $\sqrt{s} = 13$ TeV with the ATLAS detector*, ATLAS-CONF-2018-002, 2018, URL: https://cds.cern.ch/record/2308390 (cit. on p. 130).

[172] ATLAS Collaboration, *Combined measurement of differential and total cross sections in the $H \to \gamma\gamma$ and the $H \to ZZ^* \to 4\ell$ decay channels at $\sqrt{s} = 13$ TeV with the ATLAS detector*, Phys. Lett. B **786** (2018) 114, arXiv: 1805.10197 [hep-ex] (cit. on p. 130).

[173] ATLAS Collaboration, *Observation of $H \to b\bar{b}$ decays and VH production with the ATLAS detector*, ATLAS-CONF-2018-036, 2018, URL: https://cds.cern.ch/record/2630338 (cit. on p. 130).

[174] ATLAS Collaboration, *Measurements of VH, $H \to b\bar{b}$ production as a function of the vector boson transverse momentum in 13 TeV pp collisions with the ATLAS detector*, ATLAS-CONF-2018-053, 2018, URL: https://cds.cern.ch/record/2649082 (cit. on p. 130).

[175] ATLAS Collaboration, *Observation of $H \to b\bar{b}$ decays and VH production with the ATLAS detector*, Phys. Lett. B **786** (2018) 59, arXiv: 1808.08238 [hep-ex] (cit. on p. 130).

[176] ATLAS Collaboration, *Measurement of VH, $H \to b\bar{b}$ production as a function of the vector-boson transverse momentum in 13 TeV pp collisions with the ATLAS detector*, JHEP **05** (2019) 141, arXiv: 1903.04618 [hep-ex] (cit. on p. 130).

[177] ATLAS Collaboration, *Evidence for the associated production of the Higgs boson and a top quark pair with the ATLAS detector*, ATLAS-CONF-2017-077, 2017, URL: https://cds.cern.ch/record/2291405 (cit. on p. 130).

[178] ATLAS Collaboration, *Evidence for the associated production of the Higgs boson and a top quark pair with the ATLAS detector*, Phys. Rev. D **97** (2018) 072003, arXiv: 1712.08891 [hep-ex] (cit. on p. 130).

[179] ATLAS Collaboration, *Observation of Higgs boson production in association with a top quark pair at the LHC with the ATLAS detector*, Phys. Lett. B **784** (2018) 173, arXiv: 1806.00425 [hep-ex] (cit. on p. 130).

[180] ATLAS Collaboration, *Search for heavy ZZ resonances in the $\ell^+\ell^-\ell^+\ell^-$ and $\ell^+\ell^-\nu\bar{\nu}$ final states using proton–proton collisions at $\sqrt{s} = 13$ TeV with the ATLAS detector*, ATLAS-CONF-2017-058, 2017, URL: https://cds.cern.ch/record/2273874 (cit. on p. 131).

[181] ATLAS Collaboration, *Search for heavy ZZ resonances in the $\ell^+\ell^-\ell^+\ell^-$ and $\ell^+\ell^-\nu\bar{\nu}$ final states using proton–proton collisions at $\sqrt{s} = 13$ TeV with the ATLAS detector*, Eur. Phys. J. C **78** (2018) 293, arXiv: `1712.06386 [hep-ex]` (cit. on p. 131).

[182] ATLAS Collaboration, *Constraints on off-shell Higgs boson production and the Higgs boson total width in $ZZ \to 4\ell$ and $ZZ \to 2\ell 2\nu$ final states with the ATLAS detector*, Phys. Lett. B **786** (2018) 223, arXiv: `1808.01191 [hep-ex]` (cit. on p. 131).

[183] ATLAS Collaboration, *Measurement of the four-lepton invariant mass spectrum in* 13 *TeV proton–proton collisions with the ATLAS detector*, JHEP **04** (2019) 048, arXiv: `1902.05892 [hep-ex]` (cit. on p. 131).

[184] A. Buckley et al., *Implementation of the ATLAS Run 2 event data model*, Journal of Physics: Conference Series **664** (2015) 072045 (cit. on p. 131).

[185] *Measurement of the Higgs boson mass in the $H \to ZZ^* \to 4\ell$ decay channel with $\sqrt{s} = 13$ TeV pp collisions using the ATLAS detector at the LHC*, tech. rep. ATLAS-CONF-2020-005, CERN, 2020, URL: `http://cds.cern.ch/record/2714883` (cit. on p. 131).

[186] C. G. Argos et al., *Assembly and electrical tests of the first full-size forward module for the ATLAS ITk Strip detector*, Nuclear Instruments and Methods in Physics Research Section A: Accelerators, Spectrometers, Detectors and Associated Equipment **924** (2019) 112, 11th International Hiroshima Symposium on Development and Application of Semiconductor Tracking Detectors, ISSN: 0168-9002 (cit. on p. 131).

[187] R. Hunter et al., *First bulk and surface results for the ATLAS ITk Strip stereo annulus sensors*, Nuclear Instruments and Methods in Physics Research Section A: Accelerators, Spectrometers, Detectors and Associated Equipment **924** (2019) 142, 11th International Hiroshima Symposium on Development and Application of Semiconductor Tracking Detectors, ISSN: 0168-9002 (cit. on p. 132).

[188] ATLAS Collaboration, *Technical Design Report for the ATLAS Inner Tracker Pixel Detector*, tech. rep. CERN-LHCC-2017-021. ATLAS-TDR-030, CERN, 2017, URL: `https://cds.cern.ch/record/2285585` (cit. on p. 132).

[189] ATLAS Collaboration, *Measurement of the Higgs boson coupling properties in the $H \to ZZ^* \to 4\ell$ decay channel at $\sqrt{s} = 13$ TeV with the ATLAS detector*, ATLAS-CONF-2017-043, 2017, URL: `https://cds.cern.ch/record/2273849` (cit. on p. 132).

[190] ATLAS Collaboration, *Combined measurements of Higgs boson production and decay in the $H \to ZZ^* \to 4\ell$ and $H \to \gamma\gamma$ channels using $\sqrt{s} = 13$ TeV proton–proton collision data collected with the ATLAS experiment*, ATLAS-CONF-2017-047, 2017, URL: `https://cds.cern.ch/record/2273854` (cit. on p. 132).

[191] ATLAS Collaboration, *Combined measurements of Higgs boson production and decay using up to 80 fb^{-1} of proton–proton collision data at $\sqrt{s} = 13$ TeV collected with the ATLAS experiment*, ATLAS-CONF-2018-031, 2018, URL: `https://cds.cern.ch/record/2629412` (cit. on p. 132).

[192] ATLAS Collaboration, *Combined measurements of Higgs boson production and decay using up to 80 fb^{-1} of proton–proton collision data at $\sqrt{s} = 13$ TeV collected with the ATLAS experiment*, ATLAS-CONF-2019-005, 2019, URL: `https://cds.cern.ch/record/2668375` (cit. on p. 132).

[193] ATLAS Collaboration, *Combined measurements of Higgs boson production and decay using up to* $80\,fb^{-1}$ *of proton–proton collision data at* $\sqrt{s} = 13$ *TeV collected with the ATLAS experiment*, Phys. Rev. D **101** (2020) 012002, arXiv: `1909.02845 [hep-ex]` (cit. on p. 132).